

School of Physics
University of Dublin, Trinity College

DOCTORAL THESIS

Optical Transmitters based on High-Order Surface Grating Lasers for Applications in Communication Systems

---

Author:
Gaurav Jain

Supervisor:
Prof. John Donegan

A thesis submitted to the University of Dublin
for the degree of Doctor of Philosophy

January 18, 2021

Declaration of Authorship

I declare that this thesis has not been submitted as an exercise for a degree at this or any other university and that it is entirely my own work.

I agree to deposit this thesis in the University's open access institutional repository or allow the Library to do so on my behalf, subject to Irish Copyright Legislation and Trinity College Library conditions of use and acknowledgement.

I have read and I understand the plagiarism provisions in the General Regulations of the University Calendar for 2019–20, found at http://www.tcd.ie/calendar. I have also completed the Online Tutorial on avoiding plagiarism 'Ready, Steady Write', located at http://tcd-ie.libguides.com/plagiarism/ready-steady-write.

Gaurav Jain
14337528
January 18, 2021

School of Physics
University of Dublin, Trinity College

Abstract

Optical Transmitters based on High-Order Surface Grating Lasers for Applications in Communication Systems

by Gaurav Jain

Optical communication is the forefront of modern communication systems and is unarguably the leading technology for information sharing and transmission of large amounts of data over longer distances with low latency. Since its inception in early 1970s, the transmission capacity of optical networks have experienced an exceptional growth, thanks to various technological advancements. Alongside, the information age is thriving with the advent of personal computers and more recently media-rich applications and services. It is expected that within a decade, the continuous exponential growth in the data traffic will outrun the system capacity. To keep pace with the rapidly increasing data traffic, continual industry innovation is needed to increase the system capacity. This calls for technologies and photonic components able to continually improve the spectral efficiency of the already deployed optical networks. In that endeavour, in this thesis we have explored three unique transmitter designs. The first transmitter is based on non-uniform high-order surface gratings which enable simple and high-yield fabrication along with superior operation at higher temperatures compared to previous designs. The second transmitter is an optical frequency comb based on the gain-switching of an externally injected laser diode. External injection allows for the generation of multiple discernible comb tones with high spectral purity. The third transmitter considered in this thesis is a unique directly modulated Photonic Integrated Circuit (PIC) utilising optical injection by incorporating a master-slave configuration. Optical injection reduces the frequency chirp of the directly modulated PIC and allows the transmission of the optical signal up to longer distances by mitigating the dispersion effects in the standard single mode fiber.

Summary

Optical communication is the forefront of modern communication systems and is unarguably the leading technology for information sharing and transmission of large amounts of data over longer distances with low latency. Since its inception in early 1970s, the transmission capacity of optical networks have experienced an exceptional growth, thanks to various technological advancements. Alongside, the information age is thriving with the advent of personal computers and more recently media-rich applications and services. It is expected that within a decade, the continuous exponential growth in the data traffic will outrun the system capacity. To keep pace with the rapidly increasing data traffic, continual industry innovation is needed to increase the system capacity. This calls for technologies and photonic components able to continually improve the spectral efficiency of the already deployed optical networks. In that endeavour, in this thesis we have explored three unique transmitter designs.

The first transmitter studied in this thesis is a semiconductor laser based on high-order surface gratings which were previously developed in the Semiconductor Photonics group of Trinity College Dublin. Such structures simplifies the fabrication process as complex regrowth steps and high resolution e-beam lithography become obsolete. These lasers showed stable single mode operation at lower temperature, but their side mode suppression ratio (SMSR) significantly degraded with increased temperature due to the small free spectral range associated with a high-order grating that causes mode competition with increased temperature and resulted in SMSR reduction and even mode hoping beyond 60 ^{o}C. This hinders the usefulness of such structures, so tackling this issue by improving the grating design is the focus of this research. We designed gratings with non-uniform periods (2, 3 and 4 period) to suppress the undesired modes to insure stable single-mode performance over larger temperature range. At fixed temperature, a single period device should work best while temperature tuning requires a multi-period device. We found that the 2 period grating structure works best among the multi-period devices. A follow-on study with the scattering matrix model shows that the slope efficiency while quite low in this study (about 0.1 mW/mA at best) can be improved to a value of up to 0.17 mW/mA by reducing the number of slots used to form the grating from the present design which has 24 slots to 18.

The second transmitter considered in this thesis is externally injected gain switched optical frequency comb sources (GS-OFCS) as a potential candidate for flexible and elastic optical networks. We presented an extensive experimental development and investigation of these sources. These sources take advantage of optical external injection to generate OFC with clear discernible comb tones with high spectral purity. The free spectral range (FSR) of the generated OFC solely depends on the frequency of applied gain-switching signal, so a precise and wide range of FSR is achieved. We took advantage of the mode selectivity offered by optical injection and achieved a quasi continuous wavelength tunability of 31 nm by injecting into various longitudinal modes of a Fabry-Pérot laser. We investigated optical injection in great detail and experimentally verified various benefits reaped from it including single mode performance with high SMSR, high power, low noise and enhanced modulation response.

The third transmitter considered in this thesis is a directly modulated Photonic Integrated Circuit (PIC). Direct modulation, despite being simple, small footprint, cost and energy efficient suffers from frequency chirp imposed on the signal which reduces the overall reach of the transmission. Optical injection is known to improve output characteristics of the injected laser including frequency chirp. The presented PIC utilises optical injection by incorporating a unique master-slave configuration. As a result, an error-free transmission of a 10 Gb/s on-off keyed signal over 37 km of fiber, with a receiver sensitivity of -17.9 dBm, has been achieved. The device also offers wavelength tunability, enabling the generation of 8 channels placed on a 50 GHz grid. For optical networks working at a closer grid spacing, wavelength stability is critical. In current systems, this is achieved by continuous temperature control of the lasers using thermoelectric coolers (TEC). This increases the cost and power profile of the system significantly. In this thesis we developed a current-based athermal transmitter for TEC-free operation. We showed an error-free transmission of a 2.5 Gb/s on-off keyed signal over 37 km of fiber over a temperature range of 10-45 ^{o}C, with a receiver sensitivity of -16 dBm at 30 ^{o}C and a wavelength stability of $\pm$ 5 pm ($\pm$ 625 MHz). We then developed an algorithm to automate the process which has reduced the overall time to obtain look up tables of required bias current versus device temperature from several hours to few minutes.

Acknowledgements

First and foremost, my special thanks goes to my supervisor Professor John Donegan for introducing me to the wonderful world of photonics by first hiring me as a summer intern and later by giving me the opportunity to pursue this research. His invaluable guidance, constructive advice, constant encouragement and kindness over the past four years has made this work possible. His patience and understanding accompanied by freedom to pursue own research has made this industrial PhD a very enjoyable learning experience, I thank him for that.

I will always be indebted to my industrial partner, Pilot Photonics, for providing me with the knowledge, guidance, freedom and means to pursue the industrial PhD. I would like to express my sincerest appreciation to Jules Braddell and Dr. Sean O'Duill for sharing their incredible knowledge and ideas through countless discussions. My deepest appreciation goes to Dr. Frank Smyth for being an inspiration over the past four years through his exceptional mentorship, enthusiasm, trust, and encouragement. A special thanks to Dr. Prince Anandarajah, Dr. Deseada Gutierrez Pascual, and Dr. Michael Wallace for introducing me to the experimental aspect of the conducted research. I thank them for their unconditional help and supervision, for their incredible insights, for looking after me so well during the writing process and for their friendship. I would also like to thank Professor Liam Barry with providing me uninterrupted access to the labs in Dublin City University and for all the meaningful discussions. I would also like to thank Dr. Colm Browning and Dr. Eamonn Martin for their incredible help in the lab especially with the transmission experiments.

I would like to thank the Photonics group and School of Physics of Trinity College Dublin. I thank Robert McKenna for his help with characterisation in the lab along with all the informative discussions on the conducted research. I would like to thank Dr. Frank Bello for all his insights on device modelling and for his friendship. I thank all the members of the Donegan's group for making working in the lab so much more enjoyable. I would also like to thank Irish Research Council for providing the funding for this research.

Though not directly associated with the research, there are those without whom this journey would not have been possible. I will always be indebted to my Father Ashok Kumar

Jain, and my mother Prabha Jain for providing me with a loving home, for their constant care, for believing in me and for their financial and moral support, I thank them for it. I would like to thank my sisters Swati and Pragati and my brother-in-law Vinurse for their constant encouragement and for being there for me when I didn't even know I needed it.

I would like to thank all the past and present inhabitants of office - 4.22 (CRANN) in Trinity College Dublin and SB10 and Pilot Photonic's office in Dublin City University. I would like to specially thank Jane, Stephen, Joao, Chuan, Akshara, Robbie, Prajwal, Mohab, Aleksandra, Nicola, and Gavin for making the desk job not so boring. I would also like to thank my housemates: Pritish, Samarth, Chandan, Arpit, and Anuj. Thank you for your company and making my years in Dublin so much memorable. Then there are those who became family: Jorge, Anais, Subhayan, Brian, Ross, Jack, Dovydas, Katja, Katarzyna, Carolyn, Calin, Alison, Devika, and Vishesh – thank you for looking after me all along and keeping me always above threshold to make sure that I lase coherently.

Contents

Declaration of Authorship iii

Abstract v

Summary vii

Acknowledgements ix

List of Figures xv

List of Tables xxi

Keywords and Abbreviations xxiii

1 Introduction 1
- 1.1 History . . . 1
- 1.2 Evolution of Lightwave Systems . . . 2
- 1.3 Optical Network Architecture . . . 5
  - 1.3.1 Long-Haul Networks . . . 5
  - 1.3.2 Metropolitan Network . . . 6
  - 1.3.3 Access Networks . . . 6
- 1.4 Challenges with Modern Optical Communication System . . . 7
- 1.5 Thesis Scope and Goal . . . 9
  - 1.5.1 Array of Independent Lasers . . . 10
  - 1.5.2 Optical Frequency Comb Source . . . 11
  - 1.5.3 Single Mode Lasers with Injection-Locking Enabled . . . 11

2 Semiconductor Laser Fundamentals 13
- 2.1 Introduction . . . 13
- 2.2 Optical Processes in Semiconductors . . . 13
- 2.3 Fabry-Pérot Resonator . . . 15
- 2.4 Semiconductor Laser Diode Rate Equations . . . 18
- 2.5 Light-Current Characteristics and Threshold . . . 20
- 2.6 Gratings and Slotted Fabry-Pérot Laser . . . 23
- 2.7 2D Scattering Matrix Method . . . 26
- 2.8 High Order Surface Grating Semiconductor Lasers . . . 27
  - 2.8.1 Device Design and Fabrication . . . 27
- 2.9 Basic Laser Output Characteristics . . . 33
  - 2.9.1 Threshold Current and Slope Efficiency . . . 33
  - 2.9.2 SMSR . . . 34
  - 2.9.3 Tunability . . . 34
  - 2.9.4 Modulation Response . . . 36
  - 2.9.5 Laser Linewidth . . . 38
  - 2.9.6 Phase Noise . . . 41
- 2.10 Conclusion . . . 43

3 Semiconductor Lasers based on High Order Surface Gratings with Non-Uniform Period 45
3.1 Introduction . . . 45
3.2 Device Characterisation . . . 46
3.2.1 Experimental Setup . . . 46
3.2.2 Characterisation . . . 47
3.3 Multi Period Grating Design, Fabrication and Temperature Performance . . . 52
3.4 Device Characteristics of 2, 3 and 4 Period Devices . . . 58
3.5 Optimized Design Simulation Results . . . 60
3.6 Conclusion . . . 66

4 Gain Switched Optical Frequency Comb 67
4.1 Introduction . . . 67
4.2 Gain Switching and Injection Locking . . . 69
4.3 Optical External Injection . . . 71
4.3.1 Experimental Set Up . . . 73
4.3.2 Spectral Characterisation . . . 75
4.3.3 Enhancement of Resonance Peak and Modulation Response . . . 79
4.3.4 Noise Reduction . . . 84
4.4 Gain Switched Optical Frequency Comb . . . 87
4.4.1 Experimental Set Up and Device Characterisation . . . 87
4.4.2 Generation of GS-OFC without External Optical Injection . . . 88
4.4.3 Generation of GS-OFC with External Optical Injection . . . 90
4.4.4 FSR Tunability . . . 92
4.4.5 Wavelength Tunability . . . 95
4.4.6 Phase Noise . . . 95
4.5 Conclusion . . . 98

5 Chirp Compensated Directly Modulated PIC for Next Generation Access Networks and Uncooled DWDM 99
5.1 Introduction . . . 99
5.2 Direct Modulation and it's Challenges . . . 102
5.3 Photonic Integrated Circuit (PIC) Design . . . 105
5.3.1 CW Characterisation . . . 107
5.4 Transmission - *Towards improved Bl* . . . 110
5.4.1 Transmission System . . . 110
5.4.2 Transmission Performance . . . 113
5.5 Athermalised Wavelength Stabilization under Direct Modulation . . . 115
5.5.1 CW Athermalisation . . . 116
5.5.1.1 Experimental Setup . . . 116
5.5.1.2 Tuning Maps and Athermalisation Scheme . . . 117
5.5.1.3 CW Athermalisation of PIC . . . 122
5.5.2 Athermal Transmission . . . 124
5.6 Automation Of Athermalisation . . . 126
5.6.1 Determination of Athermal Path . . . 126
5.6.2 Power Maps . . . 128

5.6.3 Generating Look-Up Table through Vector Analysis 130
5.6.4 TEC Free Operation 134
5.7 Conclusion 139

6 Conclusions & Future Work **141**
6.1 Conclusions 141
6.2 Future Work and Other Applications 145
6.2.1 Dynamic Free Spectral Range Sweep 145
6.2.2 Dual-Comb Spectrometer 146
6.2.3 Improved PIC Design 148
6.2.4 Burst Mode Operation 149
6.2.5 Automation of Athermalised Transmission 149

Bibliography **151**

Appendix A **165**

List of Figures

1.1 Increase in the *BL* product over the period 1975 to 2000. *Source:* [8] 3
1.2 WDM architecture. 4
1.3 Optical Network Architecture. *Image courtesy: Vidak Vujicic* [15] 5
1.4 Global internet traffic growth, estimation (1990-2017), and prediction (2018-2022). 8

2.1 Optical processes in semiconductors. 14
2.2 (a) Forward biased double-heterostructure diode laser: (a) Band diagram, and (b) refractive index profile. 15
2.3 Schematic diagram of a Fabry-Pérot Laser Resonators showing the guided-mode profile. 16
2.4 Fabry-Pérot cavity's possible longitudinal modes and gain curve (top). Measured 400 μm Fabry-Pérot lasing spectrum at 60mA (bottom). *Image courtesy: Michael Wallace* [35] 17
2.5 Gain Process. 19
2.6 Optical spectra of a 200 μm long Fabry-Pérot laser diode showing multimode operation. 22
2.7 Schematic diagram of (a) DBR laser, and (b) DFB laser. 24
2.8 Schematic diagram of a slotted single mode laser. 24
2.9 Scattering Matrix Junction. 26
2.10 Schematic diagram of a slotted single mode laser. 28
2.11 Schematic diagram of the slotted laser diode fabrication process. 29
2.12 SEM image of (a) ridge and group of slots; (b) a single slot. *Image Courtesy: Robert McKenna* 31
2.13 Variation of threshold current and slope efficiency with transmission, α_i, and mirror, α_m, losses. Here, $\nu = 193.356$ THz (1550 nm), $V = L \times w \times d$ (400 μm $\times$ 2 μm $\times$ 20 nm), $B = 10^{-10}$ cm^3/s, $N_{tr} = 1.8{\times}10^{36}$ cm^{-3}, $\eta_i = 1$, and $\Gamma g_o = 50$ cm^{-1} 33
2.14 Experimentally measured modulation response variation of a commercial Fabry-Perot laser diode for the mentioned biases. 38
2.15 Experimental set up for linewidth measurement using the modified delay self heterodyne detection method. SSMF: standard single mode fiber; PC: polarization controller; SG: signal generator; RF AMP: RF amplifier; Phase mod: phase modulator; PD: photodiode, ESA: electrical spectrum analyser. 40

3.1 Experimental set up to measure the LI curve and optical spectrum. 47
3.2 (a) Measured LI curves for HR and AR coated slotted laser (red) and FP laser fabricated on the same chip (dotted line), and (b) Measured optical spectra of the 11 channels covering wavelengths from 1535 nm to 1565 nm at an interval of $\sim$ 3 nm. 48
3.3 (a) Measured optical spectra of the laser array showing C-band coverage using temperature tuning, and (b) Wavelength tuning characteristics of all the devices on the laser array with temperature showing overlap with neighbouring laser on the array. 49
3.4 SMSR of the measured array temperature-tuned over the C-band. 50

3.5 Schematic structure of a high order surface grating single mode laser. Both the front and back sections are active (current is injected to both front and back section) and the front section consists of the slotted structure which acts as an active DBR to provide necessary feedback for single mode operation. The slotted front section is based on 3 period grating structure. The three different periods in the front section (grating) are clearly indicated. 52
3.6 Optical spectrum of lasers with one (top), two (middle) and three (bottom) period grating structure at 50°C, demonstrating the much improved side mode suppression in the two and three period case. 54
3.7 SMM (Scattering Matrix Method) simulated reflection spectrum of one (top), two (middle) and three (bottom) period grating structures. The suppression in the undesired side reflection peaks can be clearly seen in the two and three period grating structures. 55
3.8 Performance comparison of lasers with 1, 2 and 3 period grating structure in terms of (a) SMSR, (b) peak wavelength, and (c) output power versus operating temperature. 57
3.9 (a) Threshold vs Slope Efficiency for all the measured uncoated devices, (b) Threshold and Slope Efficiency vs Device-Count, and (c) Comparison between the performance of 2 Period Coated Laser and 2 Period Uncoated Laser. . . . 58
3.10 Comparison between the simulated performance of 2 period slotted laser with 3 and 4 period slotted laser in terms of (a) threshold, and (b) slope efficiency, (c) Comparison between the experimental performance of 2 Period (with SS1 = 7.384 μm and SS2 = 8.353 μm) Coated Laser, Uncoated Laser and Simulation, and (d) Simulated Amplitude Reflection and Transmission vs Design for 2 Period slotted laser (with SS1 = 7.384 μm and SS2 = 8.353 μm). 60
3.11 (a) Simulated SMSR vs Slot configuration for 18, 20, 22 and 24 slots (SS1 = 7.384 μm and SS2 = 8.353 μm) at 20 °C, and (b) Simulated Amplitude reflection and transmission for 2-Period slotted laser vs slot configuration with 18 slots (SS1 = 7.384 μm and SS2 = 8.353 μm) 63
3.12 Simulated slope efficiency and threshold versus slot configuration for a 2 period slotted laser with 18 slots (SS1 = 7.384 μm and SS2 = 8.353 μm). 64
3.13 (Top) Amplitude reflection for 2 period grating structure (SS1 = 7.384 μm and SS2 = 8.353 μm) with 18 slots and slot configuration $\{9, 9\}$. (Bottom) The undesired left and right reflection peak suppression (which are one FSR away from the desired reflection peak at 1550 nm) plotted against slot configuration for 2 period grating structure (SS1 = 7.384 μm and SS2 = 8.353 μm) with 18 slots and slot configuration $\{9, 9\}$. 65

4.1 (a) Transient photon density dynamics under the application of a step current, and (b) Gain switching dynamics. 70
4.2 Optical external injection. 71
4.3 Cavity resonant condition under injection locking. 73
4.4 Experimental setup to obtain locking maps of SMSR, peak wavelength, peak power, peak resonance, modulation bandwidth, and linewidth for various detuning and injected power. 74
4.5 Locking map showing steady state SMSR for (a) low injected power, and (b) high injected power, for the mentioned detuning. 76
4.6 Locking Range of the slave laser vs injected power from master laser. 77

4.7 Locking map showing steady state peak wavelength for (a) low injected power, and (b) high injected power, for the mentioned detuning. 78
4.8 Variation of slave laser's output wavelength versus injected wavelength during injection locking at a constant injection power of 13.5 dBm. 79
4.9 Locking map showing steady state peak power for (a) low injected power, and (b) high injected power, for the mentioned detuning. 80
4.10 Locking map showing the resonance peak for (a) low injected power, and (b) high injected power, for the mentioned detuning. 82
4.11 Locking map showing 3 dB modulation bandwidth for (a) low injected power, and (b) high injected power, for the mentioned detuning. 83
4.12 Experimental set up for phase noise measurements using the modified delay selfheterodyne detection method. SSMF: standard single mode fiber; PC: polarization controller; SG: signal generator; RF AMP: RF amplifier; Phase mod: phase modulator; PD: photodiode, RTO: real time oscilloscope. 84
4.13 Measured FM-noise spectrum of (a) Free running slave laser, and (b) master laser, and injection locked slave laser. 86
4.14 Locking map for various detuning and injection ratio, showing steady state (a) SMSR, and (b) linewidth. 87
4.15 Schematic diagram of the experimental set-up used to generate Gain-Switched Optical Frequency Comb (GS-OFC). 88
4.16 FP laser CW characterisation at 20 ^{o}C: (a) LI curve, (b) Optical spectrum at 50 mA, and (c) small-signal modulation response at 20, 40 and 60 mA. 89
4.17 Optical Spectrum of the Tunable laser used as master for optical injection, at 1530, 1540, 1550, and 1560 nm. 90
4.18 Optical spectra of gain switched optical frequency comb at a gain switching frequency of 12.5 GHz: (a) without external injection, (b) without external injection, focussing on the non-dominating mode of the FP laser, (c) with optical injection, showing the excellent mode selectivity, and (d) with optical injection, focussing on the generated optical frequency comb with 9 lines in the 3 dB bandwidth. 91
4.19 Injection locked master-slave laser, showing excellent mode selectivity with an SMSR of $>$ 60 dB. 92
4.20 Optical spectra of the GS-OFCS generated with different FSRs: (a) 6.25 GHz, (b) 10 GHz, (c) 14 GHz, (d) 18 GHz, (e) 22 GHz, and (f) 25 GHz. OSA resolution is 0.16 pm. 93
4.21 Variation of (a) number of comb tones in the 3 dB bandwidth, and (b) 3 dB bandwidth versus free spectral range (FSR). 94
4.22 Optical spectra of: (a) overlapped GS-OFCs with an FSR = 20 GHz covering wavelength range from 1552 nm to 1583 nm, and (b) GS-OFC with an FSR = 20 GHz with a central wavelength around 1576.5 nm having 5 lines in the 3 dB bandwidth. 95
4.23 Optical spectra of GS-OFC with external optical injection optimised for (a) flatness, and (b) low noise. 96
4.24 Measured FM-noise spectrum for (a) master laser and the 3 comb tones marked in Figure 4.23 (a), and (b) comparison of the phase of the cenral comb tone of the 2 combs shown in Figure 4.23 (marked with red arrow). 97

5.1 Transmission loss of silica fiber and optical communication wavelength bands. *Image courtesy: Laser 2000* 100
5.2 (a) Typical WDM grid with channel spacing of 50 GHz. The length of the channel signify the *BL* product, and (b) improved grid with narrower channel spacing and increased *BL* product enhancing the overall system efficiency. . . 101
5.3 Schematic diagram of a laser under direct modulation. 103
5.4 Schematic diagram of the 4 section InP PIC 106
5.5 Continuous Wave (CW) optical spectrum of the two integrated lasers, Master section biased at 40 mA, Slave section biased at 70 mA. 107
5.6 (a) Wavelength, (b) SMSR, and (c) Wavelength (for SMSR > 30) tuning maps at 20 ^{o}C for the master gain = 34 mA, and slave gain = 65 mA. 108
5.7 Overlapped optical spectra of 8 operating channels with emission wavelengths separated by 50 GHz 109
5.8 Measured (a) modulation response, and (b) linewidth 110
5.9 (a) Experimental, and (b) Schematic diagram of the set-up for the Transmission system. 111
5.10 An ideal eye diagram. 113
5.11 BER versus received power for back-to-back case, and after transmission through 37 km of SSMF, inset: eye diagram. 113
5.12 Measured (a) chirp vs applied master gain current, and (b) optical spectrum at 2 different master gain current 114
5.13 Eye-diagram measured back-to-back for (a) without, and (b) with optical injection. 114
5.14 Experimental set up. 117
5.15 Wavelength tuning map of the slave laser at (a) 20 ^{o}C, (b) 25 ^{o}C, (c) 30 ^{o}C, (d) 35 ^{o}C, (e) 40 ^{o}C, and (f) 45 ^{o}C. 118
5.16 SMSR tuning map of the slave laser at (a) 20 ^{o}C, (b) 25 ^{o}C, (c) 30 ^{o}C, (d) 35 ^{o}C, (e) 40 ^{o}C, and (f) 45 ^{o}C. 119
5.17 Comparison of (a) wavelength stability, and (b) SMSR, with (red) and without (black) athermal control. 121
5.18 CW Athermalisation results: (i) applied Currents, (ii) emission wavelength, and (iii) SMSR versus Temperature 122
5.19 Optical Linewidth measurement; (a) Linewidth reduction through optical injection at 20 ^{o}C, and (b) Linewidth with optical injection at 20, 40, 60 ^{o}C for the operating currents shown in Figure 5.18(i) for the respective temperatures. 123
5.20 Athermal transmission results: (a) applied currents, and (b) emission wavelength versus temperature 124
5.21 BER vs received power for back-to-back, and after transmission through 37 km of SSMF, at 30 and 40 ^{o}C, inset: Back-to-back eye diagram measured at 10, 20, 30, 40, 45 ^{o}C 125
5.22 Wavelength map of the slave laser at 20 ^{o}C. The *black dot* points at the injection current required at mentioned temperature to keep the wavelength unchanged. 126
5.23 Contour plot of the SMSR map of slave laser at 20 ^{o}C. 127
5.24 Power map of the slave laser at 20 ^{o}C. 128
5.25 Variation of wavelength and peak power of slave laser with the reflector current at 20 ^{o}C, while the gain section is biased at 175 mA. 129
5.26 Experimental setup to determine the power map of the slave laser. 129

5.27 Generated power map of the slave laser at 20 ^{o}C using the experimental set up shown in Figure 5.26, which doesn't require any spectral measurement. . . 130
5.28 Determination of A and B parameter. 132
5.29 Variation of Parameter (a) A, and (b) B with the gain current at the mentioned temperatures. 133
5.30 Variation of Parameter C with the gain current. 133
5.31 Variation of the wavelength of the slave laser along the athermal path at 15 ^{o}C. 134
5.32 Performance of the developed athermalisation algorithm at a constant ambient temperature of 20 ^{o}C, athermalising 5 wavelengths on the DWDM grid spaced by 50 GHz/ 0.4 nm. 136
5.33 Performance of the developed athermalisation algorithm at a constant ambient temperature of 20 ^{o}C, athermalising 5 wavelengths spaced by 12.5 GHz/ 0.1 nm, confirming the suitability of the developed algorithm for finer grid spacing. 137
5.34 Performance of the developed algorithm with varying ambient temperature with and without adjustment of the look-up table. 138

6.1 (a) Measured optical comb spectra for four different frequencies from the VCO. Note how one comb line (the master laser) remains fixed throughout the VCO sweep, marked with an arrow. (b) Zoom in on the relevant spectral region over which the linear frequency sweep will take place. 145
6.2 (a) Measured optical comb spectra for four different frequencies from the VCO. Note how one comb line (the master laser) remains fixed throughout the VCO sweep, marked with an arrow. (b) Zoom in on the relevant spectral region over which the linear frequency sweep will take place. 146
6.3 Experimental setup to create a dual comb spectrometer. 147
6.4 Improved PIC utilising optical injection through master-slave configuration with an attenuator section for improved isolation between master and slave laser. 148

List of Tables

2.1 Specifications on the various epitaxial layers of the IQE wafer. 32

3.1 Design Specifications for all the fabricated multi period slotted lasers. SS"X" refers to the slot spacing of slot group "X" in micrometers (μm) used in the design, "X" refers to position of slot group relative to the back section with X=1 being the closest and so on, and $\{N\}$ refers to number of slots in each period. 56

5.1 Bias Currents for the various sections for the channels presented in Figure 5.7 109
5.2 Look-up table found to athermalise DWDM channel at 1550.12 nm. 135

Keywords and Abbreviations

Keywords

Multicarrier transmitter, single mode laser, high-order surface grating, multi period slotted Fabry-Pérot laser, optical frequency comb, gain switching, optical external injection, injection locking, photonic integrated circuit, direct modulation, transmission, athermalisation, automation.

Abbreviations

AlN	Aluminium Nitride	**APD**	Avalanche Photo Diode
AR	Anti Reflective	**BER**	Bit Error Rate
C-band	Conventional band	**CW**	Continuous Wave
DBR	Distributed Bragg Reflector	**DFB**	Distributed Feedback
DML	Directly Modulated Laser	**DSH**	Delayed Self Heterodyne
DWDM	Dense Wavelength Division Multiplexing	**EDFA**	Erbium Doped Fiber Amplifier
FP	Fabry-Pérot	**FSR**	Free Spectral Range
FWHM	Full Width at Half Maximum	**HR**	High Reflective
ITU	International Telecommunication Union	**NGPON2**	Next Generation Passive Optical Network 2
OFC	Optical Frequency Comb	**OSA**	Optical Spectrum Analyser
PIC	Photonic Integrated Circuit	**PON**	Passive Optical Network
PRBS	Pseudo Random Bit Sequence	**PSD**	Power Spectral Density
ROP	Received Optical Power	**SMM**	Scattering Matrix Method
SMSR	Side Mode Suppression Ratio	**SSMF**	Standard Single Mode Fiber
TEC	ThermoElectric Cooler	**VOA**	Variable Optical Attenuator
WDM	Wavelength Division Multiplexing	**VCO**	Voltage Controlled Oscillator

Chapter 1

Introduction

1.1 History

Communication is the transfer of information from one place to another. In modern communication system the transfer of information is achieved by the superimposition (modulation) of the information (message) onto an electromagnetic wave (carrier). The modulated carrier is then launched in a medium for it's transmission to the required destination. The received signal at the destination is then processed (demodulated), and the original message signal is recovered.

The era of modern communication system began with the emergence of *electrical telegraphs* in 1840s, which essentially used coded pulses of electric current through dedicated wires to transmit information over long distances [1]. By the adoption of coding techniques like *morse-code*, and using intermediate relay stations, a bit-rate of ~ 10 b/s is achieved while transmitting information to ~ 1000 km [2]. The invention of the *telephone* in 1876 by *Alexander Graham Bell*, enabled people to talk directly across larger distance for the very first time in the human history [3]. Soon, the telephone network became available worldwide and has seen many technical advances. In order to improve the capacity of the telephone network, twisted-pair cables were replaced by coaxial-cables. This improved the system capacity up to certain extent but was limited by the frequency-dependent losses of coaxial-cable, which at that time were unsustainable beyond 10 MHz. This led to the development of microwave communication system. Such system uses an electromagnetic wave in the frequency range of 1 to 10 GHz as a carrier to transmit a message signal. With the implementation of microwave communication system, the system capacity was significantly improved but the bit rate of such system is limited by the carrier frequency.

In the second half of the 20th century, it was realised that the system capacity can be increased multiple times if an optical signal is used as a carrier. But there was a lack of coherent optical sources and a suitable transmission medium in 1950s. This has pushed the development of semiconductor lasers significantly and the breakthrough came in 1962, when

the lasing action was first observed by Robert Hall [4] in a forward biased GaAs p-n junction laser diode. Soon, laser diodes with other semiconductor materials, such as GaAsP, GaInAs, InAs, and InP were made to generate optical light at different wavelengths. These early devices required high threshold current density which restricted their continuous-wave (CW) operation at room temperature. It was suggested in 1963 [5] that the performance of these devices can be significantly enhanced by heterostructure design, where the active layer of semiconductor material is sandwiched between two cladding layers of wider bandgap semiconductor material. With the development of liquid phase epitaxy, growth of such structures became possible and in 1970 [6], CW operation of semiconductor laser based on double heterostructure has been shown at room temperature. At about the same time, the development of low loss silica fibers was speeding up. In 1966, Charles K. Kao and George Hockham proposed the use of optical fibers as a new form of high capacity communication medium [7]. In 1970, Corning Glass Works started to manufacture optical fibers with 20 dB/km attenuation, low enough for transmission. The introduction of double heterostructure laser diode and low-loss fiber developed the field of optical communications from the status of a curiosity into a proper technology.

1.2 Evolution of Lightwave Systems

The performance of a communication system can be evaluated by the *bit rate-distance product*, BL, where B is the bit-rate and L is the repeater spacing. Development of first semiconductor laser in 1962 and low-loss optical fiber in 1970 marks the beginning of the research phase of fiber-optic communication system. Over the years immense technological advancements have been made to continually improve the BL product. This era of technological advancements can be categorised into 4 main generations as illustrated in Figure 1.1 [8]. The straight line corresponds to doubling of BL product every year.

The first generation of fiber-optic communication systems were based on GaAs semiconductor lasers and operated near 0.8 μm. They became commercially available in 1980 and operated at a bit rate of 45 Mb/s with a repeater spacing of $\sim$ 10 km [9]. This was a huge improvement compared to contemporary coaxial-cable network which required a repeater spacing of 1 km and had reduced the installation, operating and maintenance cost of the overall system.

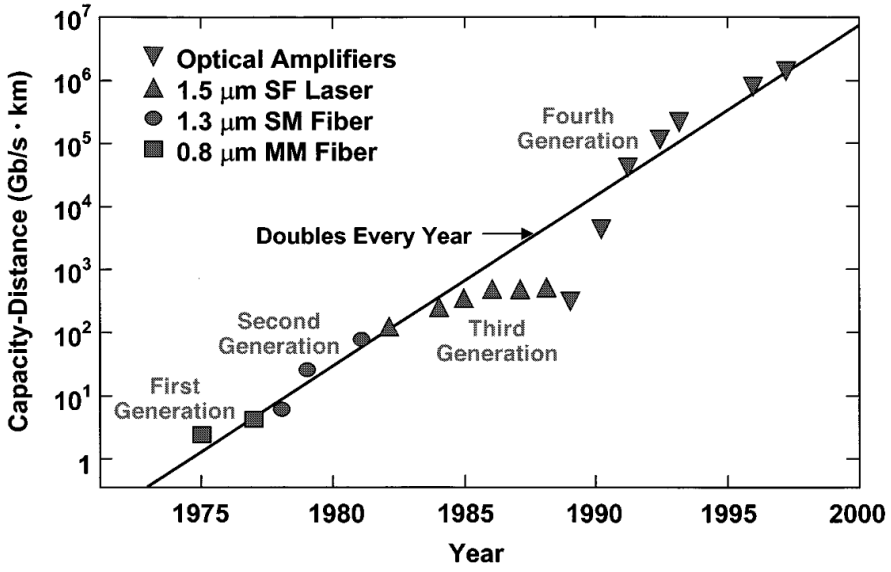


Figure 1.1: Increase in the *BL* product over the period 1975 to 2000. *Source:* [8]

Soon, it was realised that the repeater spacing can be considerably improved by moving towards the low-loss region of optical fiber. This gave a huge push towards the development of InGaAsP semiconductor lasers and detectors that operate near 1.3 μm, where the fiber loss (1 dB/km) and especially the dispersion is low. In order to further reduce the dispersion and improve the *BL* product, a switch from multi-mode fiber towards single-mode fiber was made. These advancements mark the second generation of lightwave communication systems and a bit-rate of 1.7 Gb/s with a repeater spacing of 50 km became commercially available by 1987.

In 1979, optical fiber with a very low loss of 0.2 dB/km at 1.55 μm was realised [10]. This attracted both research and industry to move towards 1.55 μm. But this migration from 1.3 μm towards 1.5 μm was delayed due to the large dispersion at such wavelengths. In order to counter this, a significant effort was made to develop single mode lasers at 1.55 μm [11] and dispersion shifted fiber designed to have minimum dispersion at 1.55 μm [12]. In 1990, these third generation lightwave system operating at 1.55 μm became available at a bit-rate of 2.5 Gb/s.

Development of erbium doped fiber amplifiers (EDFA) [13] and adoption of wavelength division multiplexing (WDM) in 1990s marks the fourth generation of optical communication and significantly boosted the capacity of optical communications systems. EDFAs increase the spacing between repeaters or, in some system completely eliminate them by compensating

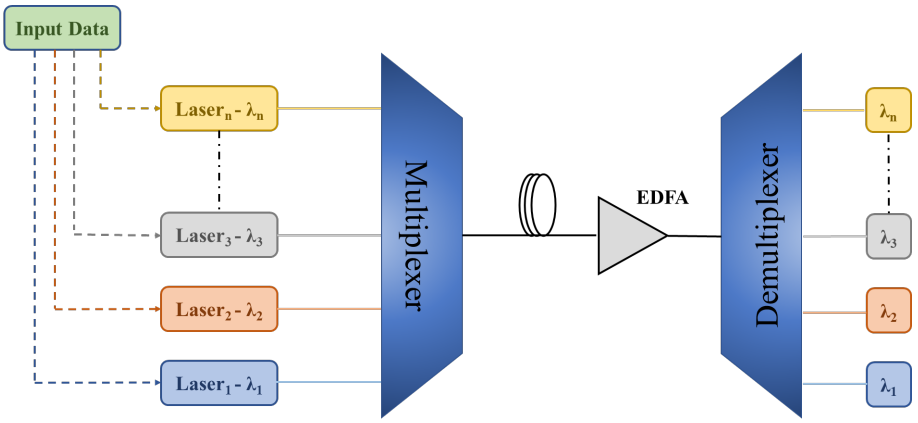


Figure 1.2: WDM architecture.

for the signal attenuation (0.2 dB/km) due to its propagation over optical fiber. WDM has revolutionised the modern optical communication systems by facilitating the development of high bandwidth communications. WDM combines multiple individual channels at different wavelengths for its transmission along the single optical fiber as shown in Figure 1.2. Individual channel comprises of a single mode laser that generates an optical carrier on which data is encoded either directly or externally. These optical carriers with encoded data on them are combined together on a single optical fiber for their transmission. The receiver is comprised of a demultiplexer, which separates the received signal into an individual channel. These individual channels are then detected using a photo-receiver to recover the encoded information on the optical carrier. The ability to send multiple signals bidirectionally over a single fiber has yielded dramatic increases in data rates. These innovations have substantially fostered the *information age* and as illustrated in Figure 1.1, resulted in doubling of system capacity every six months or so and led to lightwave system operating at a bit-rate of 10 Tb/s by 2001.

Post 2000, the major concern in the lightwave systems was to improve the capacity of the WDM systems by extending the wavelength range over which WDM system can operate simultaneously. The conventional operating window, also known as the C-band, is being extended to both shorter (S-band) and longer (L-band) wavelengths in order to increase the number of simultaneous operating channels. Though the EDFAs have gain profile in the C-band, techniques like Raman amplification can be used for wavelengths in all the three bands. Another concern of current lightwave system is to increase the spectral efficiency of the WDM systems. This idea is employed by using advanced modulation formats in which

the message signal is encoded in both amplitude and phase of the optical carrier. In 2010, in a record experiment a bit-rate of 64 Tb/s was achieved over 320 km using 640 WDM channels spaced by 12.5 GHz in C and L band employing advance modulation format (PDM-36QAM) [14]. This is 10^{13} times more faster than the electrical telegraphs deployed in 1840s. Communication systems have come a long way.

1.3 Optical Network Architecture

The architecture of a typical network is illustrated in Figure 1.3 [15]. The nodes in the network are termed as *central offices*, and are usually linked through multiple fiber pairs. Based on their geometrical extension, functionality and requirements, the optical network can be categorised as *long-haul (core)*, *metropolitan (metro)*, and *access networks* [16].

1.3.1 Long-Haul Networks

Long-haul networks, also known as core networks, are the backbone of global communications system. These networks connects continents and countries through terrestrial and submarine links and spans over thousands of kilometres. Long-haul networks transport large amount of aggregated data from millions of users, so system reliability and robustness is paramount. In long-haul networks, cost and power consumption are less critical compared to their short-haul (metro and access networks) counterparts instead maximising system capacity by improving the spectral efficiency and transmission distances is of greater focus. Since the deployment

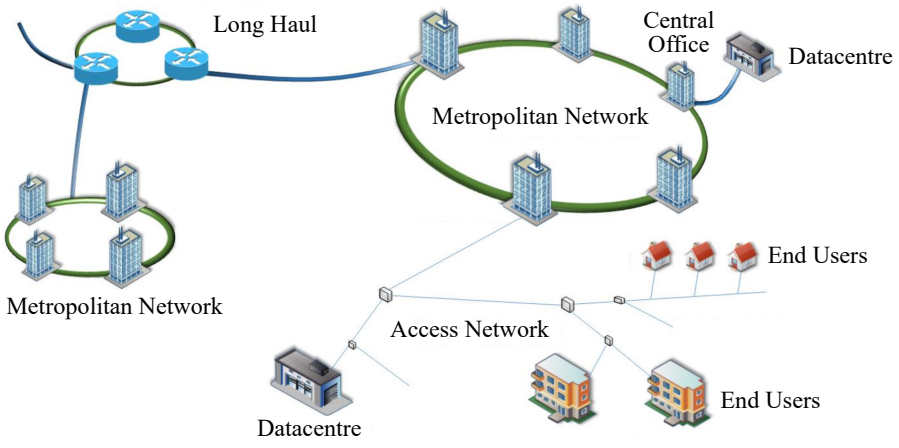


Figure 1.3: Optical Network Architecture. *Image courtesy: Vidak Vujicic* [15]

of long-haul networks is an expensive affair, the majority of the advances in this regard is to develop technologies to utilise the current infrastructure more efficiently.

1.3.2 Metropolitan Network

Metropolitan network acts as bridge between core-network and the end users by interconnecting long-haul networks and access networks. Metro networks usually spans from tens to few hundreds of kilometres. Network traffic is continuously growing due to emergence of information age, the metro network must evolve as well to support the demand for bandwidth of end users in the access network.

1.3.3 Access Networks

The access network typically connects the end user (individual businesses or homes) to the first node (central office) of the metro network, as shown in Figure 1.3. Access network are often referred as last/first mile of the network and usually spans up to several kilometres. Currently, the dominant access technologies are Digital Subscriber Loop (DSL) (ITU-T G.922), coaxial cable (ITU-T J.112/122), and wireless access technologies such as Wi-Fi (IEEE 802.11) and WiMax (IEEE 802.16) [17]. DSL uses copper twisted pairs, originally designed to carry 4 kHz voice data, by assigning certain frequency bands for voice and data transmission. Several DSL techniques exist such as Asymmetric Digital Subscriber Loop (ADSL) and Very high-bit-rate Digital Subscriber Loop (VDSL). ADSL offer speeds of up to 24 Mb/s, while VDSL can increase the data rate to above 100 Mb/s. Another widely deployed broadband connection is coaxial (coax) copper cable, initially used for the transmission of analog TV signals. As coaxial cables typically provide higher bandwidth than twisted copper pairs, higher data rates up to 100 Mb/s and longer transmission distances can be achieved. Common wireless access network designs to reach end users include Wireless Fidelity (WiFi), Worldwide Interoperability for Microwave Access (WiMAX), and Long-Term Evolution (LTE). Although wireless technologies provide flexible mobile access solution, these techniques are fundamentally limited by the unreliability of the wireless channel and also have a limited access range.

Optical access networks can be realised using two common topologies: point-to-point (home run) and point-to-multipoint (star) [18]. In the point-to-point architecture, a single fiber is

dedicated to each end user, which provides huge amount of bandwidth to each subscriber. However, deployment of a separate fiber from the central-office to each optical network unit (ONU) requires large capital expenditure, which is the main disadvantage of this topology. A more economical solution is point-to-multipoint architecture, where an optical fiber is deployed from the central office to the remote node which can be active or passive, and which is located near to the user premises. Point-to-multipoint access networks which use active remote node are referred as active optical networks (AON), whilst the access networks which use passive remote nodes are classified as passive optical networks (PON). In both AONs and PONs, the end users are connected with the remote node using optical fibers, where a single fiber is required for each end user. Passive optical networks can employ TDM technology, WDM technology, or a hybrid TDM-WDM approach [18].

1.4 Challenges with Modern Optical Communication System

Since it's inception, the transmission capacity of fiber-optic communication system has seen a tremendous growth, thanks to the technological advancement made over the years. The major breakthrough came with the introduction of EDFAs and WDM system which gave a significant boost to the system capacity as illustrated in Figure 1.1.

Parallelly, the information age was booming with the introduction of personal computers and the evolution of data transmission services. This explosion in the information age drove a rapid traffic growth and created a demand for higher system capacity. Post 2000s, the dissemination of the internet, through smartphones and other devices, and the rapid growth of high speed data transmission services like cloud, video streaming, online gaming etc. is exhausting the network capacity [19, 20]. The extensive increase in bandwidth usage shows no sign of abating. Figure 1.4 plots the trends of global internet traffic for 1990-2017 [21] and the forecast from 2018 - 2022 published in the Cisco Visual Networking Index: Forecasts and trends [20]. As illustrated, the internet traffic is increasing very rapidly with a 23 % increment every year in the recent times. According to Cisco Visual Networking Index: Forecasts and trends, by the year 2022, the global IP traffic will double from its current value of 201 Exabytes per month to 396 Exabytes per month [20] – 1 Exabyte = 10^{18} bytes!!! So far the system capacity enabled by WDM has exceeded the requirements of network bandwidth.

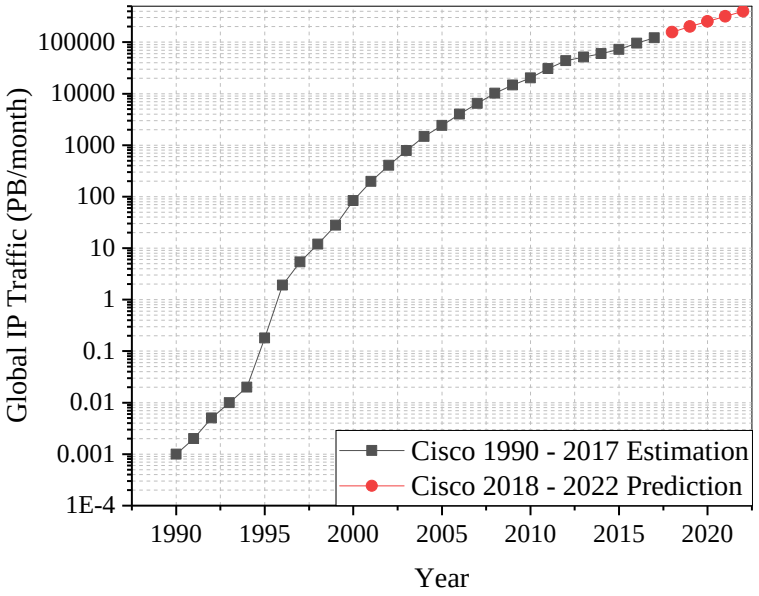


Figure 1.4: Global internet traffic growth, estimation (1990-2017), and prediction (2018-2022).

But the current trend of system capacity and internet traffic suggests that in the next decade the system capacity will fall behind the internet traffic by a factor of 10 [19].

Continual industry innovation is needed to keep pace with rapidly increasing internet traffic. In order to keep meeting the demand for bandwidth, optical networks must evolve towards higher performance, throughput, spectral efficiency, and reduced power consumption [22, 23]. An important measure of the performance of a lightwave system is its spectral efficiency, which is the information rate that can be transmitted over a given bandwidth or channel spacing. Improved spectral efficiency can be attained by two main scaling methods:

- Increasing the data rate per optical channel, and
- Reducing the channel spacing which implies a larger number of usable channels.

Achieving improved spectral efficiency requires an optical transmitter capable of creating single/multiple, stable, low-noise optical carriers. Realisation of such transmitters are the focus of this thesis and are discussed briefly in next section and in greater detail in later chapters.

1.5 Thesis Scope and Goal

In lightwave systems, the role of an optical transmitter is to convert the message signal (electrical) into optical form for its transmission along the optical fiber. An optical transmitter constitutes an optical source, a modulator (in case of external modulation), and a channel coupler. Semiconductor lasers are the primary device used as an optical source in modern lightwave systems. As discussed in the previous section, in order to continuously meet the demand of rapidly growing global internet traffic, lightwave systems must move towards higher spectral efficiency. This requires transmitter with certain stringent requirements including:

1. Number of carriers: A large number of equally spaced carriers. This reduces cost of the transmitter.

2. Flatness: Flatness means number of carriers in the top 3 dB window of the optical spectrum. Flatness of the spectrum ensures the similar performance on all the sub-channels, which makes detection easy and efficient.

3. Flexible channel spacing: In order to be compatible with different modulation formats, the channel spacing needs to be tunable.

4. Wavelength tunability: In order to cover the entire C-band the transmitter must be wavelength tunable.

5. Low linewidth: Low linewidth is required to have superior phase noise performance and efficient detection at the receiver end.

6. High Side Mode Suppression Ratio (SMSR)[1]: In order to be able to transmit data over long distances, the sub-channels should be single mode with high SMSR.

7. Stability and durability: Stability and durability is the most critical requirement of any real time system which operates continuously 24x7. The source needs to be stable in terms of all the attributes discussed above for long durations.

8. Cost efficient: When it comes to large optical networks, a large number of transmitters need to be deployed. So, in order for a transmitter to be commercially viable, it needs to be cost and power efficient.

[1]SMSR - The ratio of power between the lasing mode and the next strongest mode.

In this thesis we explore 3 such transmitters:

1.5.1 Array of Independent Lasers

A bank or array of discrete lasers bundled together can be used to implement a multi carrier transmitter. Previously in the Semiconductor Photonics group of Trinity College Dublin led by Prof. John Donegan, research into single mode laser designs based on simple fabrication has been undertaken [24–26]. These devices utilises high-order surface grating for their single mode operation and which reduces the complexity of the fabrication as it eliminates the regrowth and high resolution requirements from the fabrication process. The right wavelength lasers are designed by carefully choosing the periodicity of these surface Bragg mirrors and then the tunability is achieved by temperature tuning the laser diodes individually [25, 27, 28]. Easy integration of these devices allow us to fabricate a high number of channels on a photonic integrated circuit (PIC). However, due to incorporation of high-order surface grating for single mode operation, the free spectral range (separation between adjacent reflection modes, decided by the periodicity of the grating) of the device reduces. This hinders the performance of these device as the temperature is varied. The increment/reduction in temperature causes the gain curve of the material to redshift/blueshift causing increased gain experienced by the modes adjacent to desired wavelength. This causes reduction in the SMSR and can also lead to mode hopping if the temperature is varied significantly which is undesirable for a lightwave system. In this thesis we:

- Develop devices based on simple fabrication, however utilising a non uniform grating to suppress the adjacent reflection modes to maintain performance at a larger temperature range.
- Experimentally and through simulation characterise the performance of the developed devices to ascertain what level of complexity is required in the structure of grating to obtain the best performance.
- Optimise the design of the grating through simulation to develop an improved version of the device with superior slope efficiency, threshold, throughput, and operating temperature range while maintaining a high SMSR.

This work is presented in detail in chapter 3.

1.5.2 Optical Frequency Comb Source

In 2005, Optical Frequency Comb Source (OFCS) came into spotlight, when the Nobel prize in Physics was awarded to John L. Hall and Theodor W. Hänsch for their groundbreaking work in the field of spectroscopy using optical frequency combs [29, 30]. An OFCS can be defined as laser or laser subsystem, capable of generating multiple precisely spaced discreet optical carriers that share a strong phase correlation [31]. The inherently precise and stable frequency spacing of OFCS enables the reduction of guard band and hence improving the spectral efficiency of a lightwave system utilising advanced multicarrier modulation technique. A good survey on various OFCS and their applicability in elastic optical network can be found in this article [31]. The most commonly used and relevant configurations for OFC generation are Mode-locked lasers (MLL), Microresonator based Kerr OFCS, Electro-optic Modulator based OFCS, and Gain Switched OFCS. In this thesis, we have chosen gain switching of laser diodes as our method to generate OFCS. In this thesis we:

- Discuss in detail the process of generating OFCS using gain switching.
- Discuss the importance of injection locking in generation of a wide OFC with multiple carriers sharing a very high phase correlation.
- Assess the quality of the generated comb lines through phase noise and linewidth measurements.
- Present a detailed study of the effect of optical injection on the injected laser and experimentally characterise its output performance wavelength, SMSR, Modulation Response, Relaxation oscillation peak, linewidth and phase noise.
- Characterise the effect of optical external injection on the overall bandwidth and phase noise of the generated optical frequency comb.

This work is presented in detail in chapter 4.

1.5.3 Single Mode Lasers with Injection-Locking Enabled

Single mode lasers operating under direct modulation provide a simple, and cost efficient, optical transmitters for use in access network. However, the chirp imposed on the optical

carrier under direct modulation limits the bit rate distance product, BL, achievable in such systems. This eclipses the benefits of the direct modulation and makes it unsuitable for next generation access network where transmission distances of more than 20 km are required at a data rate of 10 Gb/s. Externally modulated lasers comfortably meet most of the requirements imposed, but their high insertion loss and requirement of extra optical component adds to the cost and complexity of the transmitter, rendering this technique unsuitable for cost-sensitive applications. External optical injection has been shown earlier to significantly reduce the chirp [32] under direct modulation, and thereby increase the transmission reach [33]. In this thesis, we will present a Photonic Integrated Circuit (PIC) as a directly modulated transmitter which utilises the optical-injection. In this thesis we:

- Present a directly modulated Photonic Integrated Circuit (PIC) for access network applications utilising optical injection for error free performance up to longer distances.
- Present the athermalisation of this PIC in CW and under direct modulation.
- Develop an algorithm to automate the athermalisation process.

This work is presented in detail in chapter 5. In the next chapter, we will develop a basic understanding of the working of laser diodes and its various performance indicator including SMSR, threshold, slope efficiency, modulation response, linewidth, and phase noise.

Chapter 2

Semiconductor Laser Fundamentals

2.1 Introduction

The basic ingredients that constitutes a diode laser are – *gain medium*, *pump source*, *feedback mechanism i.e., mirrors*, and *wavelength selective structures* (to allow single mode operation). The gain medium consists of a material which absorbs the incident radiation over certain bandwidth, but under right pump conditions (either electrical or optical) the electrons within the material can be excited to a higher energy state which can then be de-excited by stimulated recombination process producing additional radiation, resulting in gain. In order for lasing to occur, the net gain for some resonant mode should overcome the losses – the corresponding mode is said to have reached *threshold*. In order to establish and sustain lasing oscillations above threshold, a feedback mechanism is required. To this end, mirrors are used which provides the necessary feedback and results in the formation of resonant cavity for the lateral confinement of the radiation. This resonant cavity supports multiple longitudinal modes within the gain bandwidth of the material. In order to attain single mode operations, wavelength selective structures such as gratings are used. In this chapter, we will discuss these concepts in more details. We will also develop an insight about the fabrication process and explore various output characteristics of the fabricated laser diode.

2.2 Optical Processes in Semiconductors

The semiconductor valence band is formed by multiple splitting of the highest occupied atomic energy of the constituent atoms and is entirely filled with no external excitation at $T = 0$ K. The next higher-lying atomic level splits apart into the conduction band and is entirely empty at $T = 0$ K, with no external injection. Electrons in the valence band can be excited to the conduction band when thermal or other energy is added to the system. Following the excitation process there are three major radiative processes in a semiconductor material, as illustrated in Figure 2.1. In absorption, a photon with energy greater or equal to the band-gap energy gets absorbed in the material stimulating the transition of an electron

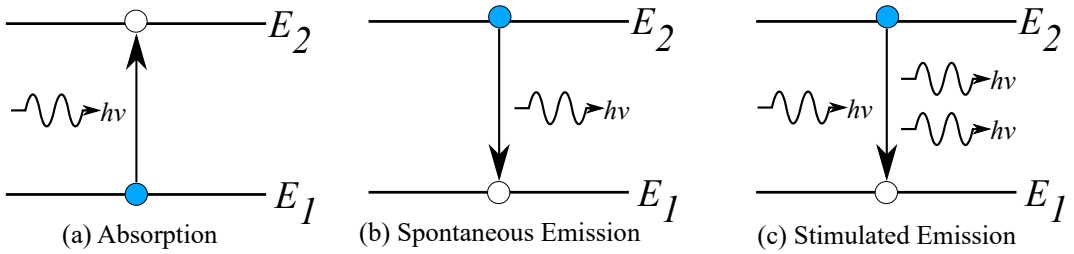


Figure 2.1: Optical processes in semiconductors.

from the conduction band to the valence band. In spontaneous emission, an electron in the conduction band jumps down to the valence band and recombines spontaneously with a hole to generate a photon. Such emission is incoherent in nature since the emission time and direction are random. The Rate of spontaneous emission requires presence of an electron hole pair, hence can be quantified as BN^2, where N is the carrier density and B is the *bimolecular recombination coefficient*. In stimulated emission, an incident photon perturbs the system, stimulating the recombination of an electron and hole and generating a new photon. The generated photon matches the frequency and phase of the incident photon and contributes to coherent emission.

The basic structure of a semiconductor laser is a double-heterostructure, i.e., the undoped active region is sandwiched between two wide-bandgap materials (one n-doped and other p-doped). A band diagram of a forward-biased double-heterostructure *p-i-n diode* is shown in Figure 2.2(a). When the diode is forward biased, electrons and holes from the n-doped, and p-doped region respectively are injected into the active region. Since the active region is surrounded by high bandgap material from both sides, the injected electrons and holes remain confined in the active region and are forced to recombine and generate photons. When the bias becomes sufficiently high such that the two quasi-Fermi levels enter the conduction and valence band of active region ($E_{Fc} - E_{Fv} \geq E_g$), stimulated recombination takes over the spontaneous recombination and lasing occurs. The bias condition at which lasing occurs is known as threshold of the laser. Decreasing the width of the active region close to the de-Broglie wavelength results in a quantum well (QW) structure which helps in achieving low lasing threshold and large material gain. Double-heterostructure provides a transverse confinement for the optical energy. The lower band-gap active region also usually have higher index of refraction, n, than the cladding as shown in Figure 2.2(b). In order to maintain the photon density (necessary for stimulated emission) in the active region, a longitudinal

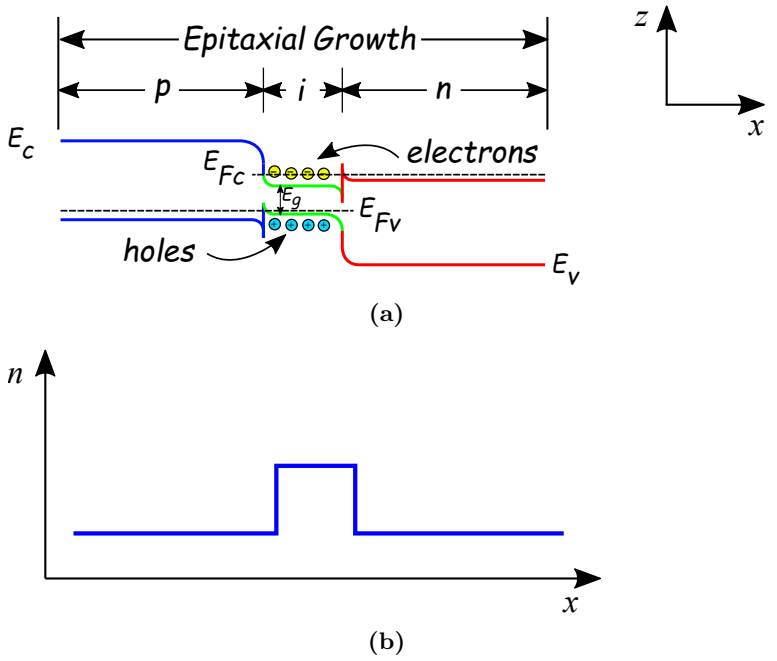


Figure 2.2: (a) Forward biased double-heterostructure diode laser: (a) Band diagram, and (b) refractive index profile.

confinement is also required. The simplest way to achieve this is through a Fabry-Pérot resonator.

2.3 Fabry-Pérot Resonator

As illustrated in Figure 2.3, the optical energy of a diode laser propagates in a dielectric waveguide mode which is confined both transversely and laterally and is defined by a transverse electric field profile, *U(x, y)*. The propagation of this mode in the axial direction is defined by a complex propagation constant, β, and is given by equation 2.1. The time and space varying electric field can be given by equation 2.2:

$$\beta = \frac{2\pi n}{\lambda} + \frac{j}{2}(\Gamma_{xy} g - \alpha_i) \tag{2.1}$$

$$E = E_o U(x, y) e^{j(\omega t - \beta z)} \tag{2.2}$$

where n is the mode effective index of refraction, λ is the wavelength of propagation, Γ_{xy} is the transverse confinement factor, g is the modal gain, α_i is the internal loss, and E_o is the

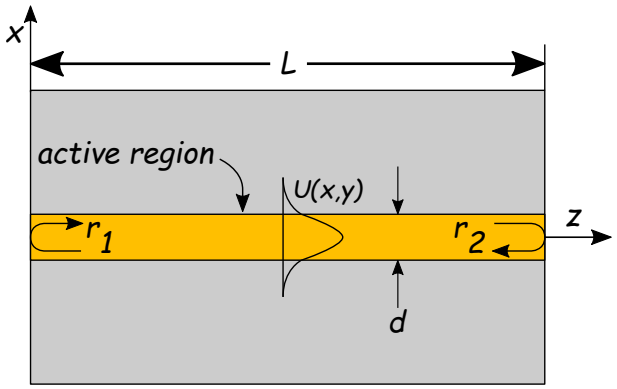


Figure 2.3: Schematic diagram of a Fabry-Pérot Laser Resonators showing the guided-mode profile.

magnitude of the field. A resonant cavity for the propagating mode is provided by the end mirrors, which have amplitude reflection coefficient of r_1 and r_2 respectively. For a mode to attain threshold, the gain should compensate for all the losses (propagation and mirror) and the electric field should replicate itself after one round trip. This will translate to equation 2.3:

$$r_1 r_2 e^{-2j\beta_{th}L} = 1 \tag{2.3}$$

where β_{th} denotes the threshold value of complex propagation coefficient. Separating and solving the above equation for magnitude, gain condition can be achieved as illustrated in equation 2.4 , here g_{th} is the gain value at the threshold.

$$\Gamma_{xy} g_{th} = \alpha_i + \alpha_m \tag{2.4}$$

where, α_m is the mirror loss and can be written as equation 2.5:

$$\alpha_m = \frac{1}{L} ln\left[\frac{1}{r_1 r_2}\right] \tag{2.5}$$

Solving for phase leads to equation 2.6:

$$\lambda_m = \frac{2nL}{m} \tag{2.6}$$

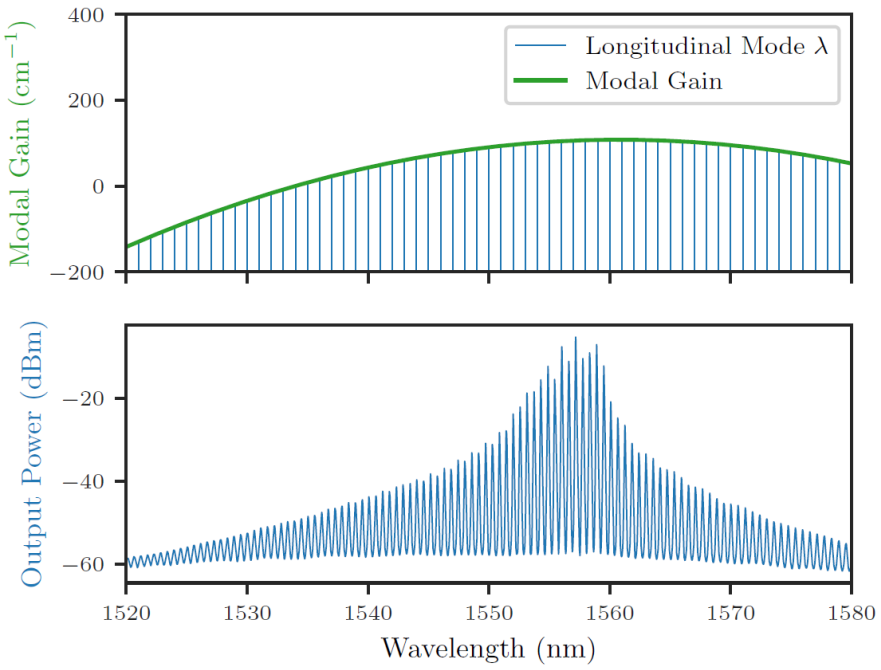


Figure 2.4: Fabry-Pérot cavity's possible longitudinal modes and gain curve (top). Measured 400 μm Fabry-Pérot lasing spectrum at 60mA (bottom). *Image courtesy: Michael Wallace* [35]

where m ($\in$ Z) is the mode order and λ is the wavelength of emission. This equation is known as the phase condition of lasing. As the optical mode resonates in the cavity, it interferes with itself constructively and destructively creating a standing wave pattern. Constructive interference leads to generation of discrete resonant modes, known as longitudinal modes, while all the other frequencies get suppressed by destructive interference. The vertical lines in Figure 2.4(top) represents the solutions to the equation 2.6 for an arbitrary cavity length. The modal gain curve is represented in green and is calculated using parabolic approximation [34]. The wavelength of the longitudinal mode determined by equation 2.4 relative to the gain curve determine the power in each longitudinal mode. An experimentally measured spectrum of a Fabry-Pérot laser with cavity length of 400 μm is illustrated in Figure 2.4(bottom). The steady state gain in a laser running above threshold must be equal to its threshold value as given by equation 2.4, since if the gain were higher than g_{th}, then the field amplitude would increase without bound, which is not sustainable. Also since carrier density and gain are monotonically related, the carrier density is also clamped to its threshold value and all the additional carrier injected recombines coherently. More detailed analyses of lasing threshold and output power can be performed using the semiconductor laser rate equations.

2.4 Semiconductor Laser Diode Rate Equations

In order to attain lasing in a diode laser, the quasi-Fermi levels (denoted by E_{Fc} and E_{Fv} in Figure 2.2(a)) must penetrate the conduction and valence band of the active region - the probability of occurrence of electrons and holes in conduction and valence band respectively should be more than half. In solid state lasers this condition is called population inversion. In diode lasers, this is achieved by the application of electrical current in a forward-bias fashion. A fraction of this current gets lost due to possible shunt paths around the active region. The rest of the current enters the active region and leads to an increase in carrier density given by:

$$G_{gen} = \frac{\eta_i I}{qV} \tag{2.7}$$

here, η_i denotes the fraction of the total current, I, entering the active region of volume, V. The generated carrier density is then depleted through various radiative and non-radiative recombination processes. Radiative processes are dictated by spontaneous and stimulated recombination rate (absorption and emission) and are denoted by R_{sp}, and R_{st}, respectively. Non-radiative processes constitute of nonradiative recombination and carrier leakage and the rates associated with these processes are denoted by R_{nr}, and R_l, respectively. Thus the net carrier density decay/recombination rate is given by:

$$R_{rec} = R_{sp} + R_{nr} + R_l + R_{st} \tag{2.8}$$

Spontaneous and nonradiative recombination processes are natural decay processes and can be described by a carrier lifetime, τ. Then equation 2.8 can be simplified to:

$$R_{rec} = \frac{N}{\tau} + R_{st} \tag{2.9}$$

R_{st} represents the photon-stimulated net electron-hole recombination which generates more photons. This is a gain process and is illustrated in Figure 2.5. The incoming photon density, S, passing through a small length of active region, Δz, grows to an exiting value of $S + \Delta S$. This growth can also be described in terms of a gain per unit length, g as:

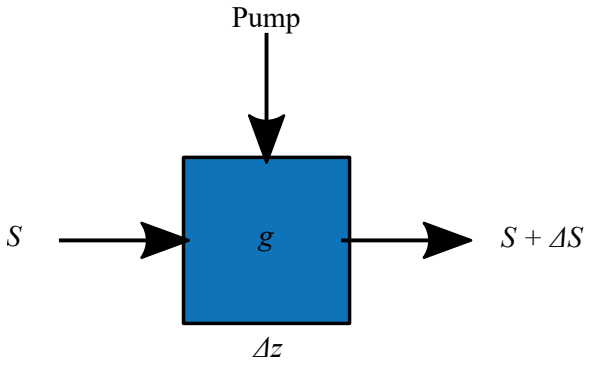


Figure 2.5: Gain Process.

$$S + \Delta S = Se^{g\Delta z} \tag{2.10}$$

For sufficiently small value of Δz, $e^{g\Delta z} \approx (1 + g\Delta z)$. Also, for a group velocity of v_g, $\Delta z = v_g \Delta t$. This gives, $\Delta S = S g v_g \Delta t$. Then, stimulated recombination rate can be written as:

$$R_{st} = \frac{\Delta S}{\Delta t} = v_g g S \tag{2.11}$$

In a double heterostructure laser diode, the injected current contributes to the generation of carrier density (N) in the conduction band while various optical processes like radiative and nonradiative recombination as well as carrier leakage leads to the depletion of carrier density. Hence, the carrier density rate equation can be written as equation 2.13:

$$\frac{dN}{dt} = G_{gen} - R_{rec} \tag{2.12}$$

using equation 2.7, 2.9, and 2.11, equation 2.12 can be written as:

$$\frac{dN}{dt} = \frac{\eta_i I}{qV} - \frac{N}{\tau} - v_g g S \tag{2.13}$$

Radiative recombination processes like spontaneous and stimulated recombination results in building of photon density (S) in the active region of a double heterostructure laser diode. Photon loss occurs in the cavity due to optical absorption, scattering out of the mode and coupling out at the facets etc. These losses can be quantified through a photon lifetime, τ_p.

Hence, the photon density rate equation can be written as equation 2.14:

$$\frac{dS}{dt} = \Gamma v_g g S + \Gamma \beta_{sp} \frac{N}{\tau} - \frac{S}{\tau_p} \tag{2.14}$$

This equation describes the evolution of the photon density of a single mode laser. It is formed by three terms. The first term is the contribution of stimulated emission, here Γ is the confinement factor and denotes the fraction of the volume of photon density which overlaps with the volume of active region. The second term is the contribution of spontaneous recombination ($\frac{N}{\tau}$) to the photon generation rate for a particular mode. Here, the spontaneous recombination rate is multiplied by β_{sp} (spontaneous emission factor) to acknowledge the fact that there are typically thousands of possible optical modes in a diode laser cavity, and only a fraction contributes to the mode in question. The third term describes the decay of photon density due to losses and imperfection in the cavity.

2.5 Light-Current Characteristics and Threshold

Below threshold, spontaneous emission is the main radiative process responsible for the generation of photons. The spontaneous photon generation rate per unit volume is exactly equal to the spontaneous electron recombination rate, R_{sp}. Under steady-state condition, the generation rate becomes equal to the recombination rate. From equation 2.8, 2.12 and neglecting R_{st}, we get:

$$\frac{\eta_i I}{qV} = R_{sp} + R_{nr} + R_l \tag{2.15}$$

Since, only radiative processes leads to generation of photons and contribute to useful light output, it is wise to define a radiative efficiency, η_r - it is the measure of what percentage of total recombinations (radiative and nonradiative) leads to the generation of photon. η_r can be written as:

$$\eta_r = \frac{R_{sp}}{R_{sp} + R_{nr} + R_l} \tag{2.16}$$

The spontaneously generated optical power, P_{sp}, is obtained by multiplying the number of photons generated per unit volume, R_{sp}, by the energy per photon, $h\upsilon$, and the volume of the active region, V. This relationship is given by equation 2.17, and as can be seen the spontaneously generated power, P_{sp}, is directly proportional to the drive current, I.

$$P_{sp} = h\upsilon V R_{sp} = \eta_i \eta_r \frac{h\upsilon}{q} I \tag{2.17}$$

Now, since below threshold the major contribution in depleting the carrier density comes from spontaneous recombination, so by neglecting the contribution of stimulated recombination at threshold, carrier density and rate of spontaneous recombination at threshold ($R_{sp,th}$) can be written as equation 2.18:

$$\frac{\eta_i I_{th}}{qV} = \frac{N_{th}}{\tau} \tag{2.18}$$

As discussed earlier in section 2.3, the carrier density and gain above threshold clamps to it threshold value and all the additional injected carrier contributes to photon generation through stimulated emission. Therefore, using the threshold carrier density found in equation 2.18, and using equation 2.14 at steady state, the photon density can be obtained and is given by equation 2.19:

$$S = \frac{\eta_i (I - I_{th})}{q \upsilon_g g_{th} V} \tag{2.19}$$

Now, the relationship between gain and carrier density can be well approximated using the transparency carrier density (N_{tr}) by equation 2.20:

$$g = g_o ln \left[\frac{N}{N_{tr}} \right] \tag{2.20}$$

where g_o is the gain coefficient. Solving the equation 2.20 at threshold, the threshold carrier density can be written as equation 2.21:

$$N_{th} = N_{tr} e^{(\alpha_i + \alpha_m)/\Gamma g_o} \tag{2.21}$$

Now, using $R_{sp} = BN^2$ and equation 2.4, 2.18 and 2.21, lasing threshold of a semiconductor laser can be quantified as equation 2.22:

$$I_{th} = \frac{qVBN_{tr}^2}{\eta_i} e^{2(\alpha_i+\alpha_m)/\Gamma g_o} \tag{2.22}$$

also, the total power out (P_o) from the laser can be calculated by multiplying the stored optical energy (i.e., $E_{os} = Sh\nu V_p$) in the cavity by the energy loss rate (i.e., $v_g\alpha_m$), and is given by equation 2.23:

$$P_o = \eta_i \frac{\alpha_m}{\alpha_i + \alpha_m} \frac{h\nu}{q}(I - I_{th}) = \eta_d \frac{h\nu}{q}(I - I_{th}) \tag{2.23}$$

here, η_d is known as the *differential quantum efficiency* and dictates how responsive is the output power to the applied bias current. A more detailed explanation of this can be found in [36]. Figure 2.6 shows the optical spectrum of a typical Fabry-Pérot laser. As can be seen in Figure 2.6 the spectrum is highly multimode, usually unstable (high mode-partition noise), and can fluctuate with changes in temperature and current, therefore not such a suitable device for lightwave communications. These lasers can be modified to lase at single frequency by either integrating a grating section in the design or by external optical injection. The

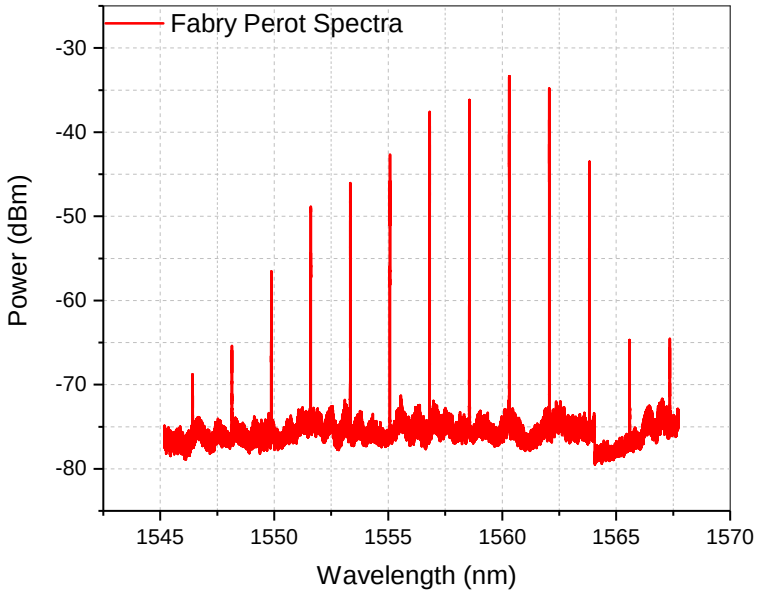


Figure 2.6: Optical spectra of a 200 μm long Fabry-Pérot laser diode showing multimode operation.

effect of external optical injection are studied in greater detail in section 4.3. In the next section we will see how integrating a grating structure in a laser diode forces the laser to lase at single wavelength.

2.6 Gratings and Slotted Fabry-Pérot Laser

Modern diode lasers incorporate gratings for one or both the mirrors to use their frequency selectivity for single mode operation. Gratings consist of a periodic array of index variation. From this periodic variation of refractive index, reflections add up constructively for certain wavelengths defined by Bragg condition:

$$\lambda_{Bragg} = \frac{2n_{eff}\Lambda}{m} \tag{2.24}$$

where, λ_{Bragg} is the Bragg wavelength, Λ is the grating period and m ($\in Z$) is known as the grating order. At the Bragg condition, the period of the grating is half of the wavelength in the medium. The basic idea of a grating is that many reflections can add up to a large net reflection. For frequencies defined by the Bragg condition, the reflections and fields add up constructively and their field grows while others frequencies adds up destructively and their field diminishes.

Distributed Bragg reflector (DBRs) based and distributed Feedback (DFB) based gratings are the most popular examples of gratings used in modern diode lasers. Figure 2.7(a) and 2.7(b) shows the schematic diagram of DBR and DFB grating based laser respectively. In a DBR laser, single mode performance is achieved by replacing one or both of the mirrors with a grating. Maximum reflection will be attained by the wavelength which satisfies the Bragg Condition. In DFB based lasers, single mode performance is achieved by fabricating a grating over the entire active region and the frequency which satisfies the Bragg condition results in laser action.

DBR and DFB lasers are the most commercially successful optical light source in the modern communication system. They exhibit single mode performance with high side mode suppression ratio (SMSR), high power, low linewidth, low threshold and excellent tunability

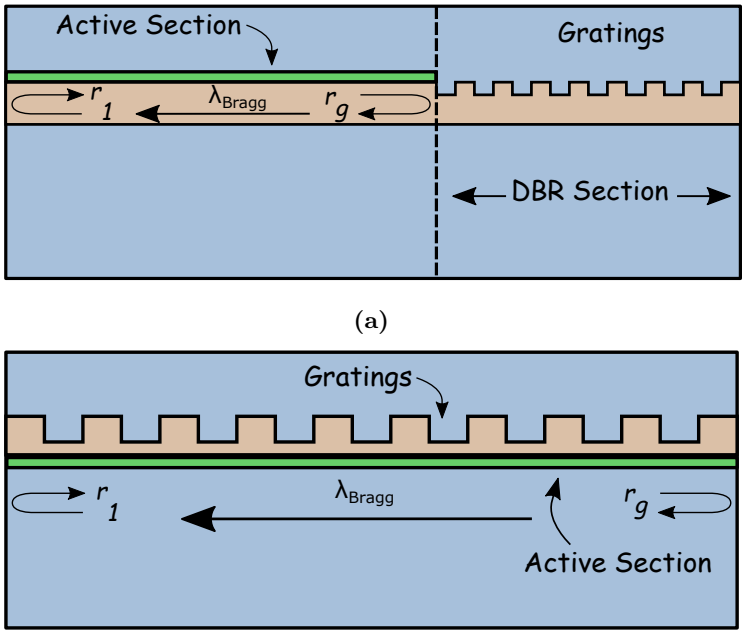


Figure 2.7: Schematic diagram of (a) DBR laser, and (b) DFB laser.

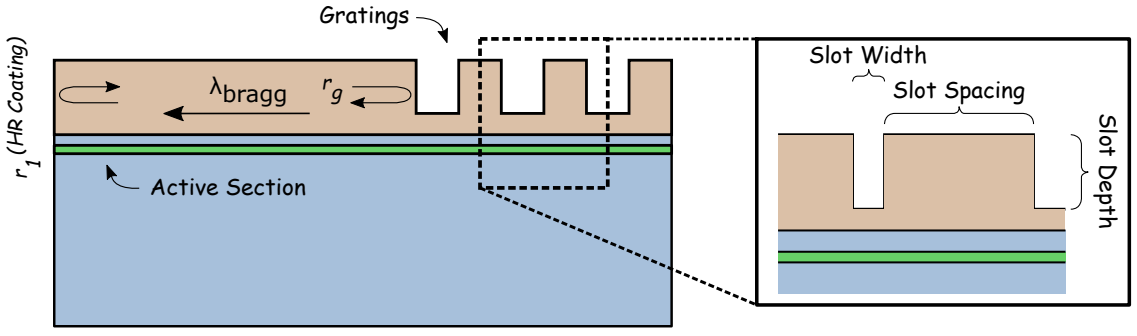


Figure 2.8: Schematic diagram of a slotted single mode laser.

over C-band (1530 nm to 1565 nm) makes it ideal for data transmission. However, as illustrated in Figure 2.7 they are fabricated with buried gratings with low order (m = 1 or 2, generally) which makes them costly as the fabrication process require both high resolution lithography and complex regrowth steps. Thus, realising a single mode laser with simple fabrication i.e., with no regrowth steps has attracted a lot of interest. One of the solutions is the use of high order ($m >> 1$) surface grating [26, 37–39] etched into the ridge waveguide structure [40]. Figure 2.8 shows the schematic diagram of a slotted single mode laser. The change in the structure relative to conventional DBR and DFB lasers requires careful modelling of various grating parameters including slot width, and slot spacing and total number of slots to produce sufficient reflection and a narrow bandwidth. The grating period is defined

by the Bragg condition from equation 2.24 for a defined wavelength. The slot width, Λ_w, and slot spacing, Λ_s can then be written as:

$$\Lambda = \Lambda_w + \Lambda_s \tag{2.25}$$

The slot width and spacing are chosen to satisfy the Bragg condition,

$$\begin{aligned} \Lambda_w &= (m_w)\frac{\lambda_{Bragg}}{2n_w} \\ \Lambda_s &= (m_s)\frac{\lambda_{Bragg}}{2n_s} \end{aligned} \tag{2.26}$$

where m_s, and m_w are half integers and are slot spacing and width order respectively. n_w, and n_s are the effective indices of slotted and un-slotted waveguide respectively. In depth analysis of optimising various grating parameters can be found in [25]. High order grating can be fabricated with cheaper photo-lithography and does not require any regrowth step. The surface grating etched into the ridge waveguide acts as a mode selection mechanism to obtain single mode performance. One major issue with using high order surface grating is their lower free spectral range. The free spectral range (FSR) is the distance between two successive Bragg wavelength, and is given by:

$$\Delta\lambda = \frac{\lambda^2}{2n_g\Lambda} \tag{2.27}$$

where n_g is group refractive index. For a high-order grating (37^{th} order), the FSR is only 40 nm. As a result 3 wavelength peaks in the reflection spectrum of these lasers overlaps with the gain spectrum of the laser. This can cause a mode-hop when the laser operating temperature is changed. This issue is addressed in chapter 3. The analysis of these grating sections are done using 2D scattering matrix model (2D-SMM) and is the next topic of discussion. We used the open source python library called CAvity Modelling FRamework (CAMFR[1]) which uses optimised C++ code called through python to implement the SMM [41].

[1]CAMFR is developed by the photonics group of the Department of Information Technology (INTEC) at Ghent University in Belgium.

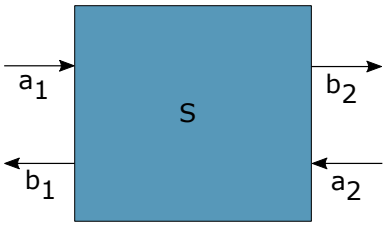


Figure 2.9: Scattering Matrix Junction.

2.7 2D Scattering Matrix Method

Modern semiconductor lasers use a variety of cavity structures (e.g. gratings) to achieve desirable performance. In order to design an efficient laser, various laser parameters such as reflectivity, transmission and losses (transmission and scattering) needs to be modelled and optimized before fabricating the real structures. The 2D Scattering Matrix Method (2D-SMM) is used to model the device performance. The 2D-SMM is based on the principle of eigenmode expansion and the use of scattering matrices. 2D-SMM works with normalized amplitudes, a_j, which have a magnitude equal to the square root of the power flow and a phase equal to a selected observable. In the case of semiconductor lasers, choosing an electric field given by equation 2.2 to reference the phase is apt. Then, a_j is defined by equation 2.28.

$$a_j = \frac{E_o}{\sqrt{2\eta_j}} e^{-j\beta z} \tag{2.28}$$

where, η_j is the mode impedance (the ratio of Transverse Electric (TE) to Transverse Magnetic (TM) field magnitudes of the mode). If the wave is propagating in the z direction then, $a_j a_j^* = P_j^+$, the power flowing in the positive z direction.

Figure 2.9 shows a scattering matrix junction with power flowing in and out of both the ports. Here, a_1 and a_2 are the normalized amplitude of incident waves (inputs) and b_1 and b_2 are the normalised amplitude of reflecting waves (outputs). Using 2D-SMM, the outward propagating field can be related to inward propagating field as in equation 2.29:

$$\begin{bmatrix} b_1 \\ b_2 \end{bmatrix} = \begin{bmatrix} S_{11} & S_{12} \\ S_{21} & S_{22} \end{bmatrix} \begin{bmatrix} a_1 \\ a_2 \end{bmatrix} \tag{2.29}$$

S_{11}, S_{12}, S_{21} and S_{22} are the scattering coefficients and have physical significance. S_{11} and

S_{22} signifies the reflection while S_{12} and S_{21} signifies the transmission. Scattering coefficients for DBR, DFB, slotted laser etc. can be directly obtained by applying 2D-SMM to the respective structure. An in-depth detailed description of 2D-SMM can be obtained in [35, 36].

2.8 High Order Surface Grating Semiconductor Lasers

The simple fabrication introduced in section 2.6 is realised by employing surface gratings [42, 43] along with ridge waveguide structure to realize the single mode laser. These structures can be realized by either etching the grating on the side of the ridge [44–48] or by etching the grating into the ridge of the laser waveguide [40, 49, 50]. Etching the grating on the side of the ridges generally results in weak coupling and current leakage. Etching the grating into the top of the ridge avoids these drawbacks, however making low order gratings in this case requires a very high etching aspect ratio which is difficult to achieve. Therefore, surface gratings of high-order etched into the ridge waveguide have generated significant research [37–39, 50–52]. In these devices single-mode operation is obtained by etching the slots that form the grating onto the ridge of a conventional Fabry-Pérot (FP) laser cavity. These slots manipulate the FP cavity mirror loss spectrum by enhancing one FP mode and suppressing the others and therefore single mode emission can be achieved. In [37, 39, 51], slots were etched in the middle of the ridge waveguide to attain single mode performance. Even though these devices have shown a good single mode performance with a SMSR in access of 40 dB with a narrow linewidth [53, 54], they are not suitable for photonic integration. This is due to their requirement of cleaved facets to attain sufficient reflection to sustain the fundamental Fabry-Perot cavity. In order to attain photonic integration through simple fabrication, the dependence of reflectivity on the cleaved facets had to be reduced. In [25, 38, 50], it has been shown that sufficient reflection and filtering for single mode operation can be achieved by placing multiple distributed slots on the ridge waveguide. This makes the dependence on cleaved facets for single mode operation redundant and allows photonic integration.

2.8.1 Device Design and Fabrication

The schematic structure of the slotted single mode laser with a high-order surface grating is shown in Figure 2.10. The laser has a 2 μm wide surface ridge waveguide structure. The epitaxial structure of the laser is the same as that used in [39]. The cavity length of the

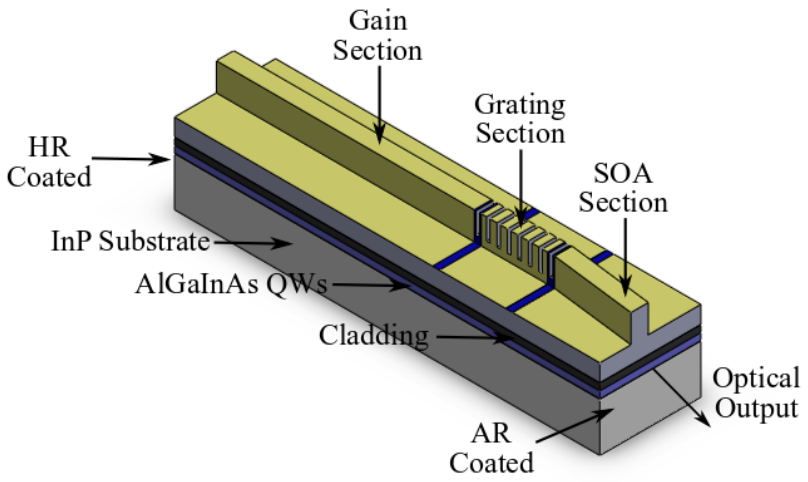


Figure 2.10: Schematic diagram of a slotted single mode laser.

device is $\sim$ 400 μm. The laser is divided electrically into a front section (grating), and a back section (gain), as in [55] by the first slot to avoid the single mode yield problem due to the uncertainty of the cleaving facet position (back facet). Adjustment of the two currents can be used to ensure high SMSR when the cleaving error results in poor single mode operation [56]. The front section of the laser has multiple uniformly distributed slots etched into the ridge waveguide which act as an active DBR of the laser for single mode operation. Etching the slots into the surface removes the requirement of re-growth during fabrication. In order to adopt simpler lithography techniques like photolithography which require low lithographic resolution, a high-order surface grating is designed. To minimize the threshold current and increase output power anti-reflection (AR) and high-reflection (HR) coatings should be applied to the front and back facets, respectively. The key parameters (slot depth, slot width, slot spacing and slot number) that are critical to the performance of the laser were optimised in [25] using the scattering matrix model (SMM) and incorporated in the design used for the fabricated devices in this study. It is shown in [25] for a slot depth of 1.35 μm, the optimised slot width and slot spacing are 1.1 μm (slots can be fabricated using standard photolithography at this feature size) and 7.87 μm respectively. For the trade-off between maximizing the reflectivity and minimizing the bandwidth of the reflection peaks and keeping the laser cavity length to a minimum, 24 slots are used. For 24 slots the reflection was 0.43 with transmission around 0.4 and the 3 dB bandwidth of the reflection

spectrum is around 2.5 nm (covering only 2∼3 longitudinal modes and ensuring good single mode operation).

The epitaxial layers of the fabricated laser diode is based on a commercial 1550 nm laser diode wafer structure which was provided by the British semiconductor company, *IQE PLC*. The active region of the wafer consists of a multi quantum-well structure, with 5 $AlGaInAs$ quantum-wells. The emission peak of the active region is centered around 1550 nm. The active region of the wafer is sandwiched between p (above) and n (below) regions. The p-region is grown above the active region and consists of a 1.6 μm-thick p-doped InP layer, a 50 nm-thick p-doped InGaAsP layer, and a 200 nm-thick InGaAs. The n-region is grown below the active region and consists of a 800 nm-thick Si-doped InP layer. A detailed specifications of the various epitaxial layers of the wafer including the mole fraction, strain, thickness, dopant and doping concentration is tabulated in Table 2.1.

All devices presented in this thesis which are based on this simple fabrication were fabricated in an external foundry based in Glasgow (UK), Compound Semiconductor Technologies. For the fabrication run, e-beam lithography was used to pattern the slots. Although these devices could be fabricated with standard photolithography given the 1 μm width of the slots, the fabrication process used e-beam lithography as a stepper was not available at the external foundry. Recently, researchers of University of Science and Technology (Wuhan,

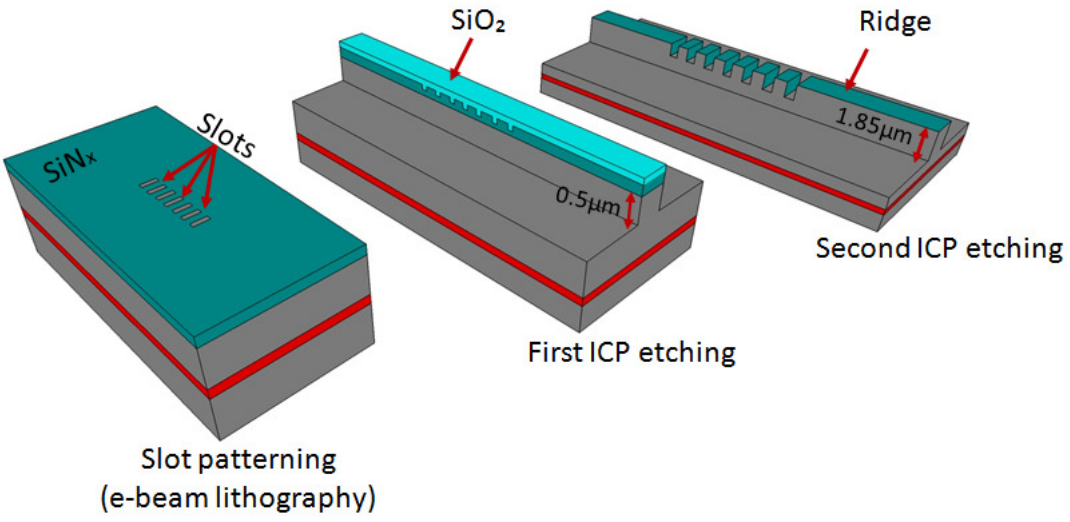
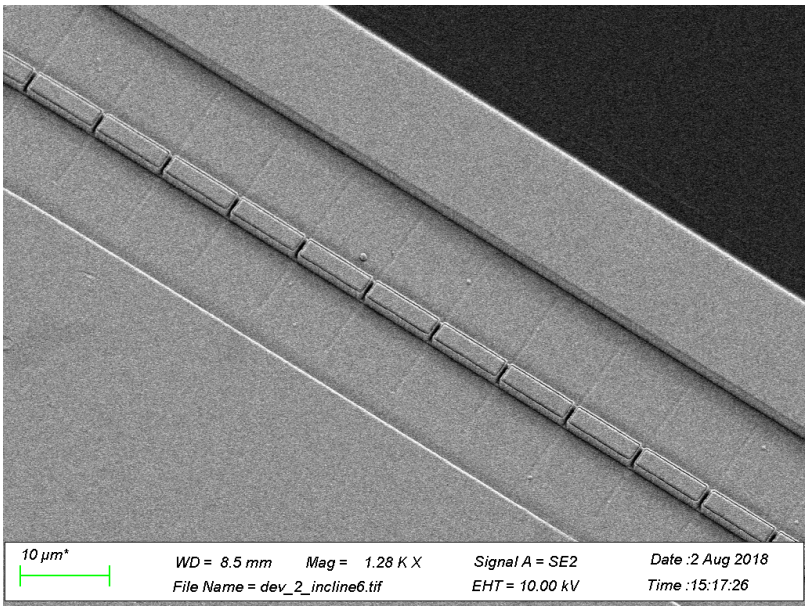


Figure 2.11: Schematic diagram of the slotted laser diode fabrication process.

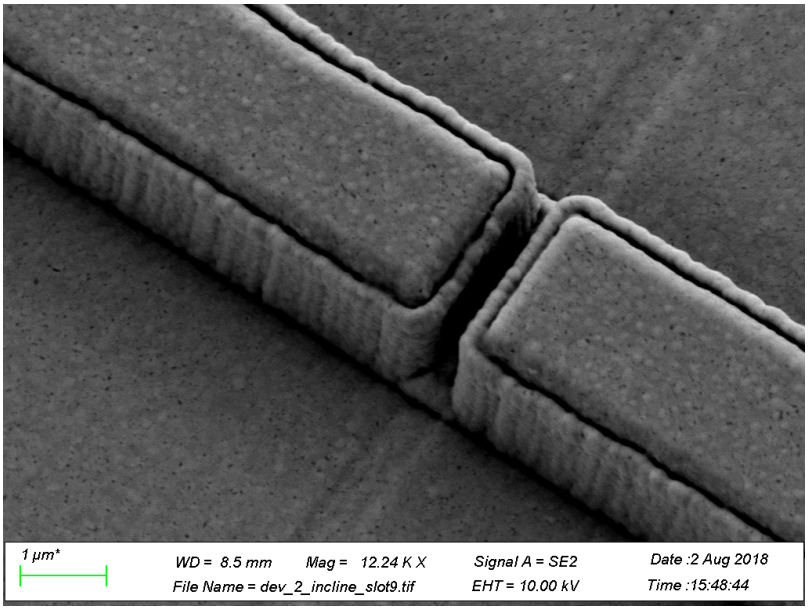
China) and Trinity college Dublin (Dublin, Ireland) fabricated devices based on high order surface gratings with narrow slot-widths $\sim$ 100 nm through standard photolithography [57]. The author reported a single mode performance with an SMSR in excess of 40 dB while achieving a threshold of 27 mA and a slope-efficiency of $\sim$ 0.1 mW/mA. The fabrication of these slots was carried out by carefully controlling the V-shape profile, which is similar to the fabrication process reported by Hans Wenzel et. al., [58] on GaAs materials. However, these slotted lasers are based on InP, the details of which can be found in [59].

The fabrication process for the single mode slotted laser presented in this thesis is illustrated in Figure 2.11. The major steps involved in the fabrication process are:

1. Silicon Nitride (SiN) layer deposition using plasma enhanced chemical vapour deposition technique (PECVD).
2. Patterning slots and alignment marks using e-beam lithography.
3. Etching the SiN layer using hard dry etch process.
4. Silicon dioxide (SiO_2) layer deposition using plasma enhanced chemical vapour deposition technique (PECVD). This is to protect the slot area during the first inductively coupled plasma (ICP) dry etching process.
5. First ICP dry etch to a depth of 0.5 μm to form the ridge.
6. Selective removal of (SiO_2) layer to start the second ICP dry etching process to etch the slots on the ridge.
7. Second ICP dry etch to a depth of 1.35 μm to deepen the ridge and etch the slots on the ridge. This resulted in a ridge depth of 1.85 μm and slot depth of 1.35 μm.
8. After completing the two ICP dry etching process, the ridge was passivated by depositing an SiO_2 layer by PECVD. Then, the ridge was p-metal deposited and the metal was lift off.
9. Finally, the laser bars were cleaved, where every bar consisted of a Fabry-Pérot laser and 11 slotted Fabry-Pérot laser. Theses were then coated with high-reflection (HR) and anti-reflection (AR) coating films. Then the chip was bonded onto an Aluminium Nitride (AlN) carrier for subsequent measurements.



(a)



(b)

Figure 2.12: SEM image of (a) ridge and group of slots; (b) a single slot. *Image Courtesy: Robert McKenna*

Figures 2.12(a) and 2.12(b), show the scattering electron microscope (SEM) images of the ridge and the single slot of the fabricated device. It is evident from the SEM images that there is some residue left on the lateral faces of the ridge waveguide which has in turn increased the surface roughness. This might increase the loss from the slots and might reduce the performance. However, the four corners of etched slot are quite sharp. A detailed characterisation of these devices is presented in chapter 3.

Table 2.1: Specifications on the various epitaxial layers of the IQE wafer.

Layer	Material	Group	Repeat	Mole Fraction (x)	Mole Fraction (y)	Strain (ppm)	PL (nm)	Thickness (μm)	Dopant	Type	CV Level (cm^{-3})
16	GaIn(x)As			0.530		0		0.2000	Zinc	P	>1.50E19
15	GaIn(x)As(y)P			0.710	0.620	0	1300 +/-50	0.0500	Zinc	P	>3.00E18
14	InP							0.1000	Zinc	P	>1.50E18
13	InP							1.5000	Zinc	P	= 1.00E18
12	GaIn(x)As(y)P			0.850	0.330	0	1100 +/-20	0.0200	Zinc	P	= 1.00E18
11	InP							0.0500	Zinc	P	= 7.00E17
10	[Al(x)Ga]In(y)As			0.900	0.530	0		0.0600	Zinc	P	= 4.00E17
9	[Al(x)Ga]In(y)As			0.720 to 0.900	0.530	0		0.0600	Undoped	U/D	
8	[Al(x)Ga]In(y)As			0.440	0.490	-3000	1100 +/-20	0.0100	Undoped	U/D	
7	[Al(x)Ga]In(y)As	1	5	0.240	0.710	12000	1530	0.0060	Undoped	U/D	
6	[Al(x)Ga]In(y)As	1	5	0.440	0.490	-3000	1100 +/-20	0.0100	Undoped	U/D	
5	[Al(x)Ga]In(y)As			0.900 to 0.720	0.530	0		0.0600	Undoped	U/D	
4	[Al(x)Ga]In(y)As			0.900	0.530	0		0.0600	Silicon	N	= 1.00E18
3	[Al(x)Ga]In(y)As			0.860 to 0.900	0.530	0		0.0100	Silicon	N	= 1.00E18
2	InP							0.5000	Silicon	N	= 1.00E18
1	InP							0.3000	Silicon	N	= 3.00E18
	SUBSTRATE										

2.9 Basic Laser Output Characteristics

2.9.1 Threshold Current and Slope Efficiency

By rearranging equation 2.23, and substituting the value of threshold current using equation 2.22, a relationship between the required bias current to attain a given output power, P_0, can be found as shown in equation 2.30.

$$I = \frac{qP_o(\alpha_i + \alpha_m)}{\eta_i h\nu\alpha_m} + \frac{qVBN_{tr}^2}{\eta_i} e^{2(\alpha_i+\alpha_m)/\Gamma g_o} \tag{2.30}$$

here, the first term is the additional current required above threshold (second term) to attain output power P_0. In order to minimise the threshold, it is desirable to increase the differential gain, g_0, and reduce the transparency carrier density, N_{tr}. Both of this can be achieved by the use of strained-layer quantum well active layers. Equation 2.30, also give important insight for cavity design. It suggests that in order to reduce the threshold of laser, it is desirable

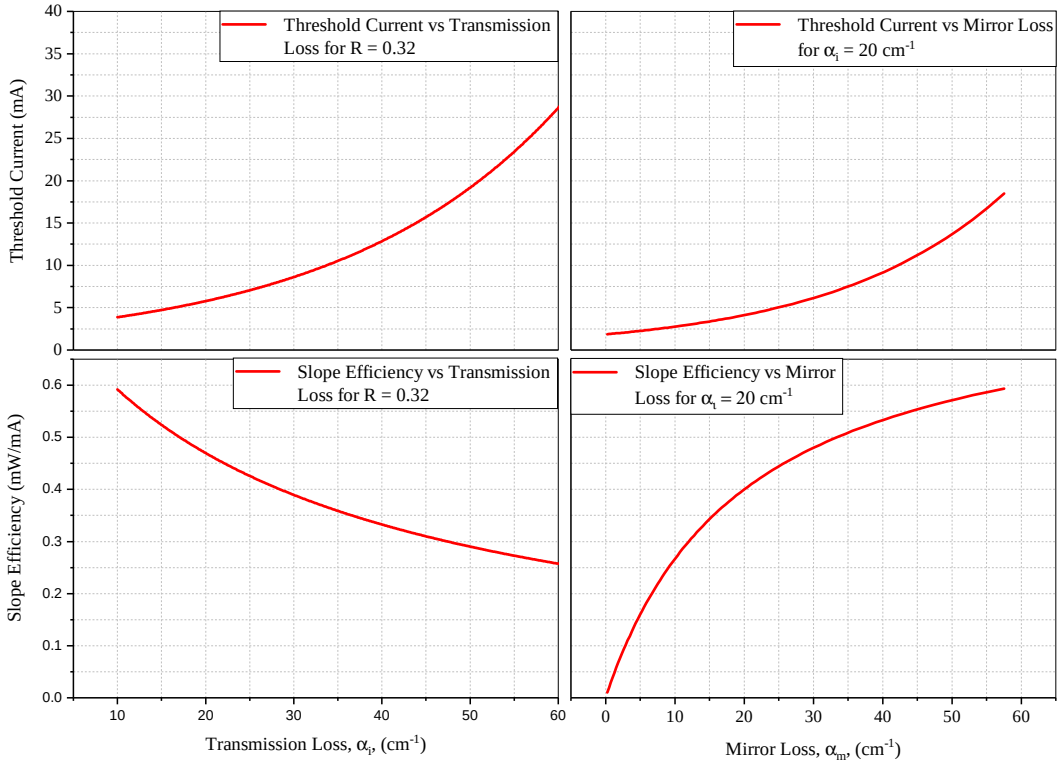


Figure 2.13: Variation of threshold current and slope efficiency with transmission, α_i, and mirror, α_m, losses. Here, ν = 193.356 THz (1550 nm), $V = L \times w \times d$ (400 μm × 2 μm × 20 nm), $B = 10^{-10}$ cm^3/s, $N_{tr} = 1.8{\times}10^{36}$ cm^{-3}, $\eta_i = 1$, and $\Gamma g_o = 50$ cm^{-1}

to reduce the cavity losses, $\alpha_i + \alpha_m$, and volume, V. This can be achieved by using short-cavity lasers with carefully designed grating and appropriately coated facets. The variation of threshold current with transmission and mirror losses is presented in Figure 2.13. A high value of internal quantum efficiency, η_i, is also desirable to attain lower threshold and higher efficiency. This can be attained by carefully removing the shunt paths to avoid carrier leakage and loss.

Equation 2.23 suggests that above threshold power increases linearly with applied current with a slope $= \eta_d \frac{h\nu}{q}$. In laser physics, this slope is commonly termed as *slope efficiency*, as it dictates how efficiently the laser diode convert the input current into useful optical output. In order to improve the slope efficiency of the device, it is desirable to improve the differential quantum efficiency, $\eta_d = \eta_i \frac{\alpha_m}{\alpha_i + \alpha_m}$, of the device. This also suggests to reduce the total cavity loss and improve the internal quantum efficiency for improved overall efficiency. The variation of slope efficiency with transmission and mirror losses is shown in Figure 2.13. More discussion on this is presented in chapter 3.

2.9.2 SMSR

The primary goal of incorporating a grating structure in the laser design is to attain a single-frequency operation. Since single-frequency is a relative term, the purity of a single-mode laser is measured through side-mode suppression ratio (SMSR). It is simply the ratio of output power in the primary laser mode, λ_0 to that in the next strongest mode, λ_1. SMSR is usually measured in decibels (dB) and is given by equation 2.31. High SMSR is achieved by designing the grating with narrow reflection bandwidth. This is further discussed in chapter 3.

$$SMSR = 10 \times log_{10} \left[\frac{P(\lambda_0)}{P(\lambda_1)} \right] \tag{2.31}$$

2.9.3 Tunability

Wavelength tunability is one of the major requirements from most single mode semiconductor laser diodes for various applications including optical communication, spectroscopy etc. According to equation 2.24, for a semiconductor laser employing Bragg gratings for their single mode operation, the operating wavelength of the fabricated device can be tuned by

changing the effective refractive index. n_{eff}, of the active region. The variation in the refractive index can be achieved by various mechanism including free-carrier plasma effect [60], quantum-confined Stark effect [61], and thermal tuning [62].

Free-Carrier Plasma Effect

Free-carrier plasma effect changes the refractive index by the injection of electrons and holes into a semiconductor [63]. This effect reduces the refractive index of the semiconductor, therefore causes a blue-shift in the operating wavelength. The reduction of refractive index is caused by the polarisation of the injected carriers, and the shift in the absorption edge [64]. This effect is usually utilised by passivating a section of the laser diode to enable the injection of higher carrier densities to attain larger variation in refractive indexes, ~ 0.04 [63]. One of the disadvantage associated with such tuning mechanism is the increased device temperature due to carrier injection which leads to thermal-tuning which reduces the overall refractive index variation.

Quantum Confined Stark Effect

In quantum confined Stark effect (QCSE), the application of reverse bias across a *pn*-junction produces an electric field within the quantum-wells. This results in reduced band-gap which in turn reduces the refractive index of the active region. The main advantage of the QCSE over the free-carrier plasma is the operation in reverse bias. This will not increase the temperature of the device. However the refractive index variations are relatively smaller, typically of the order of 10^{-3} to 10^{-2} [65].

Thermal Tuning

Thermal tuning is one of the most widely used wavelength tuning mechanism for single mode laser diodes. The change in device temperatures increases the refractive index, and red-shifts the gain spectrum. Longitudinal-mode and Bragg peak varies at a rate ~ 0.1 nm/^{o}C with thermal-tuning, while the gain curve redshifts at a rate ~ 0.5 nm/^{o}C. Thermoelectric coolers based on the peltier effect along with thermistor (for precise temperature measurement) are typically used to thermally-tune the laser diode. On chip heating elements have also been implemented for precise temperature control [66]

2.9.4 Modulation Response

Small signal analysis of the rate equation presented in section 2.4 and given by equation 2.13, and 2.14 can provide much information about the dynamic response of the semiconductor diode lasers [36, 67]. Equation 2.32, gives the total current, i.e., the above threshold dc current, I_0, superimposed with a small ac current, applied across the laser diode. Under steady-state conditions the laser's carrier density and photon density responds similarly as presented by equation 2.33, and 2.34, respectively.

$$I = I_0 + I_1 e^{jwt} \tag{2.32}$$

$$N = N_0 + N_1 e^{jwt} \tag{2.33}$$

$$S = S_0 + S_1 e^{jwt} \tag{2.34}$$

Under small-signal conditions, the gain of the active region can be approximated as a linear function of carrier density above transparency, provided the local slope is used - $g = g_0(N - N_{tr})$. Since, the applied laser bias is above threshold, neglecting the spontaneous emission term in equation 2.13, and 2.14, and substituting the linear approximation for gain, the carrier and photon density rate equation can be written as:

$$\frac{dN}{dt} = \frac{\eta_i I}{qV} - \frac{N}{\tau} - v_g g_0 (N - N_{tr}) S \tag{2.35}$$

$$\frac{dS}{dt} = \Gamma v_g g_0 (N - N_{tr}) S - \frac{S}{\tau_p} \tag{2.36}$$

Now, by substituting equation 2.32, 2.33, and 2.34 in equation 2.35, and 2.36, and recognizing that $g_0(N_0 - N_{tr})$, is the threshold value of gain, $g_{th} = \dfrac{1}{\Gamma v_g \tau_p}$, and setting the steady-state dc components to zero, we get:

$$j\omega N_1 = \frac{\eta_i I_1}{qV} - \frac{N_1}{\tau} - \frac{S_1}{\Gamma\tau_p} - v_g g_0 N_1 S_0 \tag{2.37}$$

$$j\omega S_1 = \Gamma v_g g_0 N_1 S_0 \tag{2.38}$$

The coupling between the small signal carrier density, N_1, and small signal photon density, S_1, can be understood from equation 2.37, and 2.38. If we consider the time-derivative of these equation, then by equation 2.38 as N_1 increases and becomes positive, S_1 increases in time due to increased gain in the laser according to linear gain approximation. However, from the third term in equation 2.37, as S_1 increases and becomes positive, N_1 decrease, due to increased stimulated emission. As N_1 decreases and becomes negative, S_1 also decreases and once its becomes negative, this produces an increase in N_1. At this point this cycle repeats itself. This coupling between the carrier and photon density produces ringing in the output power when a sudden change is applied to the bias current of the laser. The frequency of such ringing is commonly known as *Relaxation Oscillation Frequency* (ROF), and can be found by multiplying equation 2.37, and 2.38, ignoring all but the third term of equation 2.37. The ROF is then given by:

$$\omega_R^2 = \frac{v_g g_0 S_0}{\tau_p} \tag{2.39}$$

The modulation response of a laser diodes tells about the responsivity of the device to the applied ac signal. It is given by $\frac{P_{ac}(\omega)}{I_1(\omega)}$, where P_{ac} is the power coupled out of the laser and can be written as,

$$P_{ac} = v_g \alpha_m S_1 h\nu V_p \tag{2.40}$$

Substituting S_1 in equation 2.40 from equation 2.38, and eliminating N_1 by using equation 2.37, and using equation 2.39, the modulation response can be written as:

$$\frac{P_{ac}(\omega)}{I_1(\omega)} = \frac{\eta_d h\nu/q}{1-(\omega/\omega_R)^2 + j(\omega/\omega_R)[\omega_R\tau_p + 1/\omega_R\tau]} \tag{2.41}$$

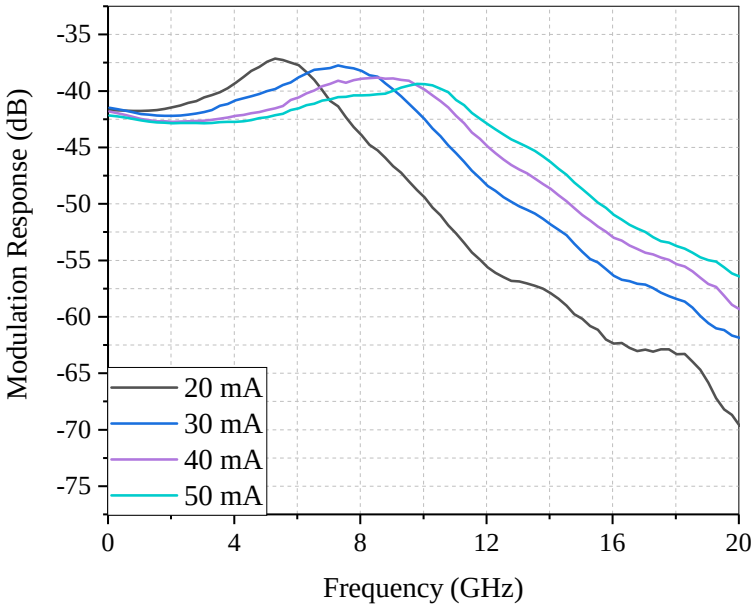


Figure 2.14: Experimentally measured modulation response variation of a commercial Fabry-Perot laser diode for the mentioned biases.

Figure 2.14 plots the experimentally measured modulation response of a commercial Fabry-Perot laser diode for the mentioned biases. According to equation 2.41, for sufficiently low frequencies, the denominator reduces to one and the modulation response becomes the ac version of equation 2.23. As the modulation frequency is increased the real part of the denominator creates a strong resonance in the response up to the relaxation oscillation frequency is reached. Beyond the relaxation oscillation frequency, the response starts to degrade. Also, as given by equation 2.39, the ROF increase continuously with the applied current (above threshold, $I \propto S_0$).

2.9.5 Laser Linewidth

Two of the most distinctive feature of laser emission are *spatial coherence* and *spectral coherence* [68]. While spatial coherence is related to beam divergence, spectral coherence is determined by measuring the linewidth of the laser emission and it is a measure of spectral purity/noise characteristics of the semiconductor laser. Linewidth is defined as full width at half maximum (FWHM) of the lasing mode optical spectra. The noise of an optical transmitter is a crucial parameter when advanced modulation formats are employed for coherent communication applications [69]. The noise requirements for system transmissions depends on the modulation format and baud rate employed, as well as the phase recovery algorithms

implemented at the receiver. For example, the linewidth requirements according to [70] for 10 Gbaud are 10 MHz for QPSK and 500 kHz for 16-QAM using a decision-directed phase-locked loop. In [71], the linewidth requirements for 10 Gbaud QPSK and 16-QAM are 4.1 MHz and 1.4 MHz, respectively, employing a digital feedforward carrier recovery algorithm. Also, since the optical signal undergoes dispersion along their transmission on an optical fiber, narrow linewidth becomes one critical property required from a transmitter in a communication systems and needs proper attention while designing a laser diode.

Spontaneous emission events discontinuously alters the phase and intensity of the laser's optical field and broadens the optical spectra of a laser diode. Coupling of spontaneous emission into laser field causes an instantaneous, and a delayed phase change [72]. While the instantaneous phase change is caused by alteration of the optical field phase by spontaneous emission event, the delayed phase change results from instantaneous intensity variation due to spontaneous emission event. Instantaneous intensity variation results in laser undergoing relaxation oscillations, which causes change in the carrier density. This change in the carrier density causes fluctuations in the refractive index (both real and imaginary component) of the active region. In 1958, A. L. Schawlow, and C. H. Townes calculated the fundamental limit for linewidth considering instantaneous phase variation caused by the spontaneous emission event [73]. However, in order to fully account for all the contibuting processes, the effect of refractive index variation due to carrier density fluctuations need to be properly accounted for. In 1982, C. Henry, modified the Schawlow-Townes equation by introducing a linewidth enhancement factor, α, to give the *modified* Schawlow-Townes equation [72]. The *modified* Schawlow-Townes equation [72] with respect to output power is given by equation 2.42, and accounts for both phase and carrier density fluctuations.

$$\Delta\nu = \frac{v_g^2 h\nu(\alpha_m + \alpha_i)\beta_{sp}\alpha_m}{8\pi P_0}(1+\alpha^2) \tag{2.42}$$

here, v_g is the group velocity, h is the Planck's constant, ν is the operating frequency, β_{sp} is the spontaneous emission factor, α_i, and α_m are the waveguide and mirror losses, and P_0 is the output power. α is the linewidth enhancement factor and is defined as, $\alpha = \frac{-4\pi\nu}{c}\frac{dn/dN}{dg/dN}$. Here, n and g stand for refractive index and gain, respectively. Equation 2.42 also suggests reduced cavity losses for lower linewidth. Also, as suggested by equation

2.5, longer cavity lengths are desirable for lower linewidth applications. The linewidth of the laser is experimentally characterised using delayed self-heterodyne method and is discussed next.

Delayed Self-Heterodyne Technique

Linewidth is the FWHM of the optical spectra of the laser diode at a given bias, and usually varies within several kilohertz to several megahertz depending on the design of the laser diode. Grating based optical spectrum analysers (OSAs) and other conventional spectroscopy techniques do not offer the measurement resolution required to accurately determine the linewidth of such a sharp spectrum. Electronic components such as electrical spectrum analyser (ESA) on the other hand provides superior resolution. So it was realised that down-conversion of the terahertz optical signal to a gigahertz electrical signal will improve the accuracy of the linewidth measurement given the phase information is preserved. The delayed self-heterodyne (DSH) is one such technique [74].

The experimental setup of the DSH technique is illustrated in Figure 2.15. In DSH, the optical output of the laser is divided into two paths using a 50:50 coupler. One branch of the divided optical signal is used as a local oscillator and is passed through a delay line (12 km of standard single mode fiber (SSMF)) to make it decorrelated, if the delay is longer than the coherence length of the laser, the 2 combining beams interfere as if they are from 2 independent lasers. The typical length of the delay line used to measure a linewidth of $\Delta\nu$ is given by equation 2.43, where c is the speed of light. In order to down-convert the optical

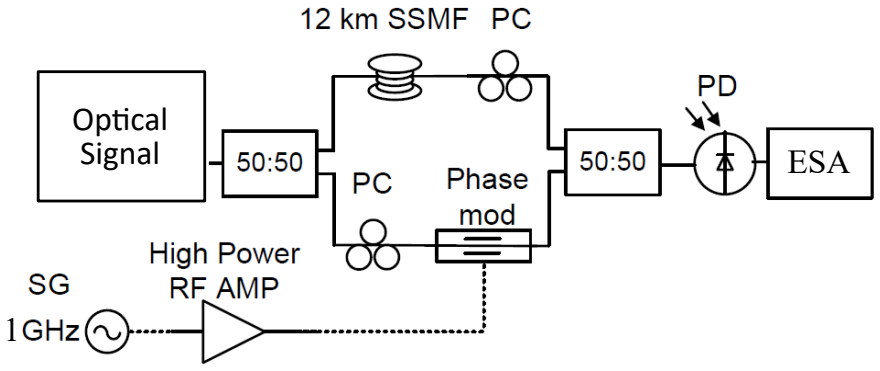


Figure 2.15: Experimental set up for linewidth measurement using the modified delay self heterodyne detection method. SSMF: standard single mode fiber; PC: polarization controller; SG: signal generator; RF AMP: RF amplifier; Phase mod: phase modulator; PD: photodiode, ESA: electrical spectrum analyser.

signal from terahertz frequency to a lower electrical frequency, the 2 branches are combined and produce a beat signal on a photodiode. Since, the ESA have a poor response near DC, the beat frequency is shifted by phase modulating the other half of the optical signal at 1 GHz, which is much higher than the spectral spread to be measured. The combined delayed and phase-modulated signal on the photodetector are then fed to an electrical spectrum analyser (ESA) for linewidth estimation. The FWHM of the measured electrical spectrum on the ESA is twice that of the actual linewidth as the signal and local oscillator light outputs are equally noisy.

$$L_{delay\ line} > \frac{c}{\pi \Delta \nu} \tag{2.43}$$

2.9.6 Phase Noise

The linewidth is an important criteria to measure the spectral coherence of the optical output. However it doesn't capture the full extent of the noise associated with the laser and associated electronics. The measured optical linewidth using conventional techniques as DSH can appear significantly broadened, due to the presence of low frequency noise associated with the electronics, and can mask the intrinsic linewidth of the laser diode caused by spontaneous emission [75, 76]. This low frequency noise is commonly referred to as 1/f noise as it presents a power spectral density inversely proportional to the noise frequency, and thus has a slope of 1/f. For communication network employing coherent communication and high order optical modulation formats, low phase noise becomes one of the major requirements and needs to be properly characterised. In this thesis, the phase noise of the optical signal is characterised by measuring the Frequency Modulated (FM) - noise spectrum which fully describes the noise processes contributing to the overall phase noise [75, 77]. The method used in this thesis to measure the FM-noise spectrum is based on the technique previously developed by T. N. Huynh *et.al.,* [75] and is briefly discussed below.

The experimental setup used to measure the phase noise is based on the modified delayed self-heterodyne technique as used for linewidth determination above. The beat signal from the photodiode is passed to a real time oscilloscope where the time variation of the received signal is recorded and then the phase information is recovered through offline digital signal

processing. The electric field of the optical output from a single mode laser can be expresses as:

$$E(t) = \sqrt{P_0 + \Delta P(t)} e^{j[\omega_0 t + \phi_n(t)]} \tag{2.44}$$

where, $P_0 + \Delta P(t)$, ω_0, and $\phi_n(t)$ are optical output power, angular optical frequency and laser phase noise, respectively. The delayed and phase modulated electric field incident on the photodetector can be written as:

$$\begin{aligned} E_i(t) &= \frac{1}{2}\left[\gamma E(t-T) - E(t) e^{j[bsin(\omega_c t + \phi_c)]}\right] \\ &= \frac{1}{2} E(t)\left[\gamma e^{-j[\omega_0 T + \phi_n(t) - \phi_n(t-T)]} - e^{j[bsin(\omega_c t + \phi_c)]}\right] \end{aligned} \tag{2.45}$$

where, γ is amplitude ratio between delayed and phase-modulated branch, T is the time delay of the SSMF, b is the phase modulator (PM) index, ω_c and ϕ_c are the frequency and phase of the driving signal at the input of phase modulator. The intensity fluctuation is considered to be constant over the delay time. For a photodetector of responsivity ρ, the generated photocurrent can be written as, $i_{pd}(t) = \rho E_i(t) E_i^*(t)$. Using equation 2.44, and 2.45, and denoting $\phi_n(t) - \phi_n(t-T) = \Delta\phi_n(t)$, *differential phase noise*, and ignoring the DC term, $i_(pd)(t)$ can be written as:

$$\begin{aligned} i_{pd}(t) = &-\frac{\gamma\rho[P_0 + \Delta P(t)]}{2} cos[\Delta\phi_n(t) + \omega_0 T] \times cos[bsin(\omega_c t + \phi_c)] \\ &+\frac{\gamma\rho[P_0 + \Delta P(t)]}{2} sin[\Delta\phi_n(t) + \omega_0 T] \times sin[bsin(\omega_c t + \phi_c)] \end{aligned} \tag{2.46}$$

Using Bessel coefficient expansion:

$$\begin{aligned} cos[bsin(\omega_c t + \phi_c)] &= J_0(b) + 2\sum_{k-even}^{\infty} J_k(b) cos[k(\omega_c t + \phi_c)] \\ sin[bsin(\omega_c t + \phi_c)] &= 2\sum_{k-odd}^{\infty} J_k(b) sin[k(\omega_c t + \phi_c)] \end{aligned} \tag{2.47}$$

where, $J_k(b)$ is the Bessel function of first kind with integer order k. Using equation 2.47, the in-phase ($I(t)$), and quadrature ($Q(t)$) component of the differential phase noise can be found at even and odd harmonics of the detected photocurrent signal. At first and second

harmonic, respectively we can write:

$$\begin{aligned} Q(t) &= J_1(b)\gamma\rho[P_0 + \Delta P(t)] \times sin[\Delta\phi_n(t) + \omega_0 T] \times sin(\omega_c t + \phi_c) \\ I(t) &= -J_2(b)\gamma\rho[P_0 + \Delta P(t)] \times cos[\Delta\phi_n(t) + \omega_0 T] \times cos[2(\omega_c t + \phi_c)] \end{aligned} \tag{2.48}$$

Equation 2.48 suggests that the differential phase noise, $\Delta\phi_n(t)$, can be recovered by coherently demodulating the detected photocurrent, $i_{pd}(t)$. The phase of the driving signal can be estimated using a simple phase recovery algorithm. The polarisation is of the delayed and phase modulated path is adjusted using polarisation controller to increase the amplitude of the beat components (I and Q). The equalisation of I and Q component is done in the DSP (digital signal processing) by measuring the RMS (root mean square) value of both the components and then scaling them accordingly to recover the phase information. FM-noise spectrum is defined as the power spectral density of the instantaneous frequency which can be obtained by differentiating the phase noise. Procedure to determine FM-noise spectrum and then estimation of linewidth through FM-noise spectrum is presented in section 4.3.4.

2.10 Conclusion

In this chapter, we introduced the fundamentals of semiconductor laser diodes. We first discussed various radiative processes associated with the generation or loss of photons. We established the threshold condition for lasing using a Fabry-Pérot resonator. We also established a relationship between input current and output power using rate equations. We then introduced the concept of gratings to attain single mode operation and a brief introduction to scattering matrix method (SMM) to analyse various grating structure has also been introduced. We then presented in detail the design and fabrication of semiconductors lasers based on high order surface gratings. Various important properties of lasers including threshold, slope efficiency, SMSR, modulation response, linewidth, and phase noise have also been described.

Chapter 3

Semiconductor Lasers based on High Order Surface Gratings with Non-Uniform Period

3.1 Introduction

As discussed in chapter 1, the dissemination of internet, through smartphones and other devices, and all the services that use telecommunication networks such as video streaming have driven the need for higher capacity optical networks. One of the key technologies developed to improve the capacity of optical networks is Dense Wavelength Division Multiplexing (DWDM). DWDM is a key technology that combines multiple individual channels at different wavelength for its transmission along a single optical fiber. In a DWDM system, different carriers at different wavelengths are treated individually. The emergence of services like cloud and video streaming is exhausting the available bandwidth, and is pushing service providers to improve the spectral efficiency of the network by increasing the capacity per channel and also by reducing the inter-channel spacing. This calls for multi-wavelength transmitters capable of generating multiple, closely spaced and stable optical carriers. The reduction of inter-channel guard bands puts certain stringent requirements on the transmitters including flexible channel spacing, flatness, wavelength tunability, low linewidth, high Side Mode Suppression Ratio (SMSR), stability, and cost efficiency. In this chapter we will discuss design aspect of one such transmitter - *Array of independent lasers*, based on high order surface grating semiconductor lasers.

Single mode semiconductor lasers are the critical components in many fields including optical communications and gas sensing. Wavelength stability with high SMSR, low threshold and high slope efficiency are the vital attributes required from these devices. As discussed in section 2.6, both distributed Bragg reflector (DBR) and distributed feedback (DFB) lasers employ periodic variations of refractive index to form a low order grating and thereby to generate single mode emission. But these devices are fabricated with low order buried gratings

which makes them expensive as the fabrication process require both high resolution lithography and complex regrowth steps. Thus, realizing single mode lasers using simple fabrication i.e., with no regrowth has attracted strong interest. Surface gratings [42, 43] are generally employed along with ridge waveguide structure to realize this simple fabrication process. These structures can be realized by either etching the grating on the side of the ridge [44–48] or by etching the grating into the top of the ridge of the laser waveguide [40, 49, 50]. Etching the grating on the side of the ridges generally results in weak coupling and current leakage. Etching the grating into the ridge avoids these drawbacks, however making low order gratings in this case requires a very high etching aspect ratio which is difficult to achieve. Therefore, surface gratings of high order, etched into the ridge waveguide have generated significant research [37–39, 50, 52]. In our designs, the high order gratings are formed by etching slots into the ridge waveguide. Detailed discussion on the design and fabrication of these devices are presented in section 2.8.1. In the next section we will present experimental characterisation of these devices.

3.2 Device Characterisation

3.2.1 Experimental Setup

Figure 3.1 shows the experimental set up used for characterization of the slotted Fabry-Pérot (FP) laser diode to obtain the spectral and light-current characteristics. The fabricated devices are mounted on Aluminium-Nitride (AlN) carriers and kept on a copper heat sink which in turn was mounted on a peltier based ThermoElectric Cooler (TEC) for precise temperature control. The device temperature was monitored using a 10 kΩ thermistor and kept constant at 20 ^{o}C (unless mentioned otherwise) by a temperature controller (ILXLightwave LDC-3742). The laser diode was electrically pumped using a current source (Keithley-2400).

For spectral measurement, the output light from the laser diode was coupled with a lensed optical fiber which is coated with an anti-reflection coating to avoid back-reflections. The lensed fiber has a focal spot which has a Gaussian profile and has a diameter of 5 μm. The gathered light is then fed to a 90/10 optical splitter. 10 percent of the light was fed to a photodetector which in turn was connected to a picoammeter (Keithley-6485) to optimise

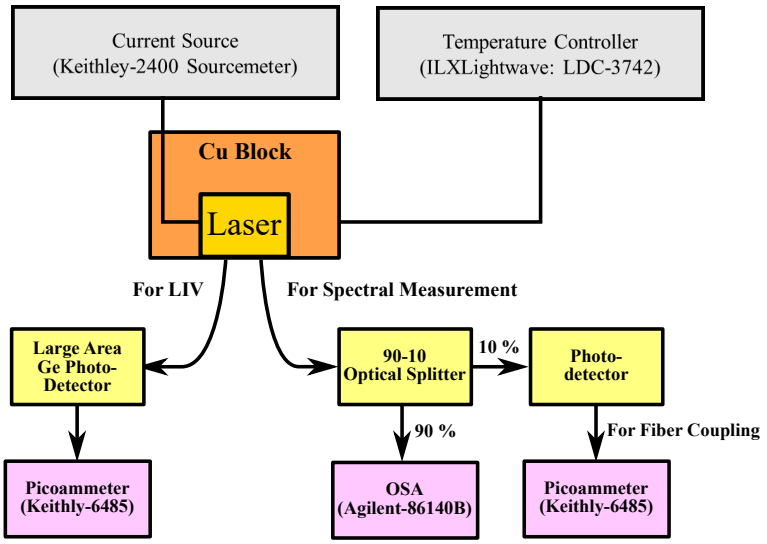
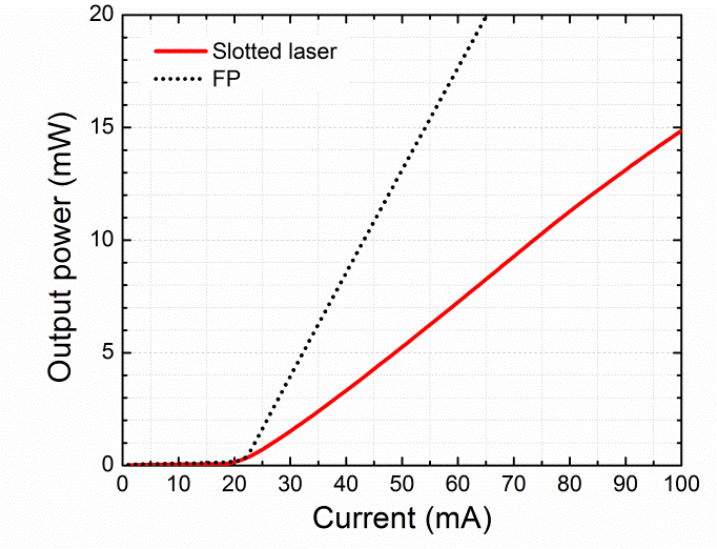


Figure 3.1: Experimental set up to measure the LI curve and optical spectrum.

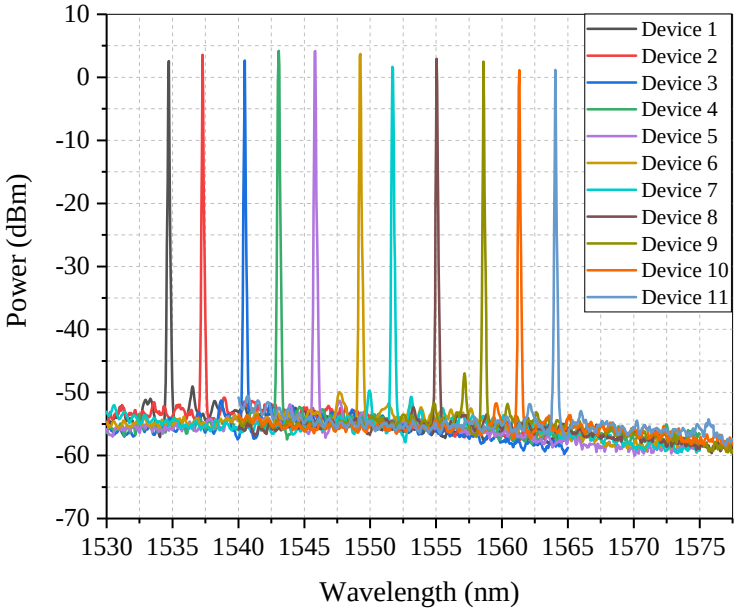
the fiber coupling. 90 percent of the light was fed to the optical spectrum analyser (Agilent-86140B) with a resolution bandwidth of 0.06 nm and a sensitivity of -75 dBm, for spectrum measurement. For obtaining the light-current (LI) characteristics of the laser diode, the laser diode output light was directly coupled to a large area (5mm×5mm) Germanium (Ge) detector, which was connected to a picoammeter (Keithley-6485).

3.2.2 Characterisation

The cleaved and coated laser bar characterised here consisted of a FP laser and 11 individual slotted single mode lasers. The cavity length of each laser is $\sim$ 400 μm. The slotted single mode lasers were divided into a front (grating) and back (gain) section as shown in Figure 2.10. Figure 3.2(a) shows the measured LI curve of one of the fabricated slotted laser with appropriate Anti-Reflective (AR) and High-Reflective (HR) coating. The front and back section of the laser are biased in such a way that the same current density goes into the both sections. In general, the two currents in the front and back sections should be set differently. However, here the front and back section of the laser are biased in such a way that the same current density goes into the both sections. This is due to in many of the devices we have characterised to date, the front and back sections were electrically connected in order to measure LI curves, threshold and slope efficiency of the individual devices. We did the same to be consistent with the previous measurements for a fair comparison. This generally provides SMSR around or better than 30 dB, but much higher values require a



(a)



(b)

Figure 3.2: (a) Measured LI curves for HR and AR coated slotted laser (red) and FP laser fabricated on the same chip (dotted line), and (b) Measured optical spectra of the 11 channels covering wavelengths from 1535 nm to 1565 nm at an interval of $\sim$ 3 nm.

separate current source for the two sections. We measured a threshold current of 19 mA with a slope efficiency of 0.17 mW/mA. Figure 3.2(a) also shows the measured LI curve of a FP laser diode, fabricated on the same chip for comparison. The threshold of the FP laser was comparable to the slotted laser and is measured to be $\sim$ 22 mA, but the slope efficiency was far superior. This was due to the increased transmission losses experienced by the filtered longitudinal mode due to the etched slots in the case of slotted laser.

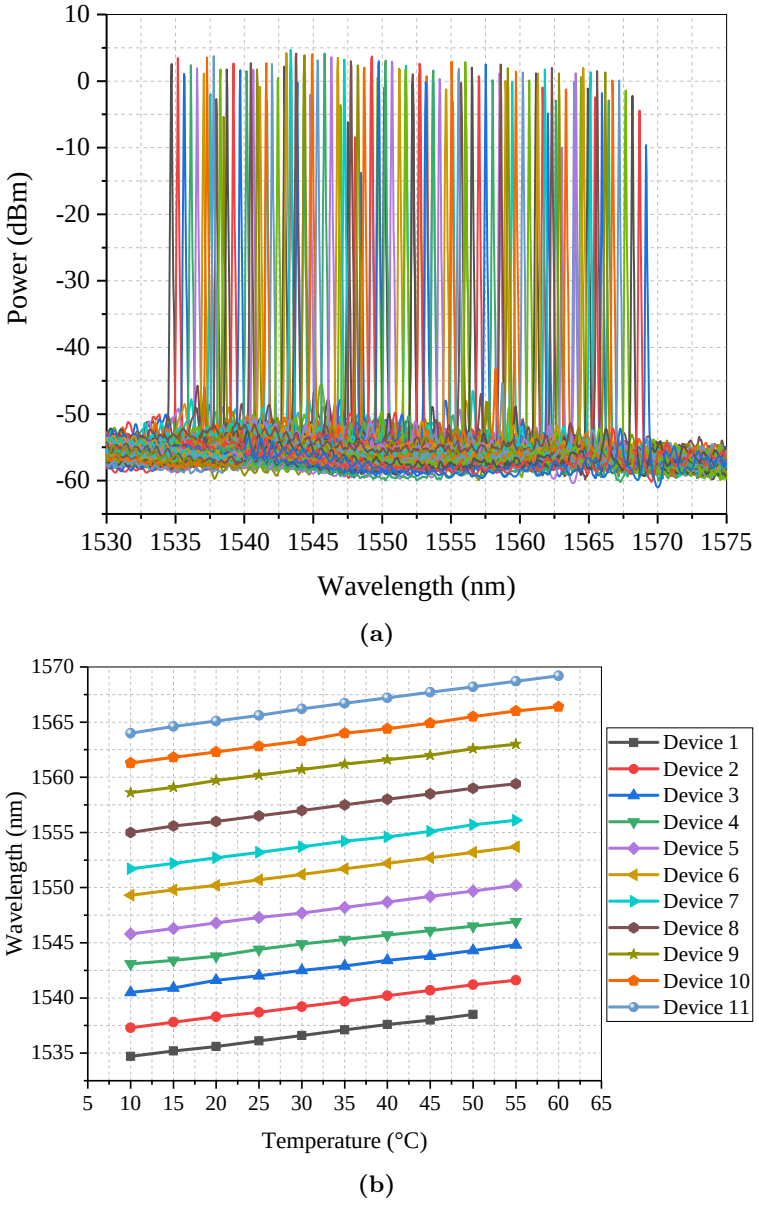


Figure 3.3: (a) Measured optical spectra of the laser array showing C-band coverage using temperature tuning, and (b) Wavelength tuning characteristics of all the devices on the laser array with temperature showing overlap with neighbouring laser on the array.

The slot-width (width of the slot), and slot-spacing (spacing between two consecutive slots), of the slotted-lasers on the bar were optimised to cover the C-band. The slot-separation were selected in such a way that the emission wavelength of the adjacent channels differs by $\sim$ 3 nm. Figure 3.2(b) shows the optical spectra, at 130 mA, of all the 11 slotted lasers, covering wavelengths from 1535 nm to 1565 nm at an interval of $\sim$ 3 nm. In order to achieve a complete C-band coverage with fine resolution, temperature tuning is used. The laser pump current for all the lasers on the bar was kept constant at 130 mA throughout. The wavelength

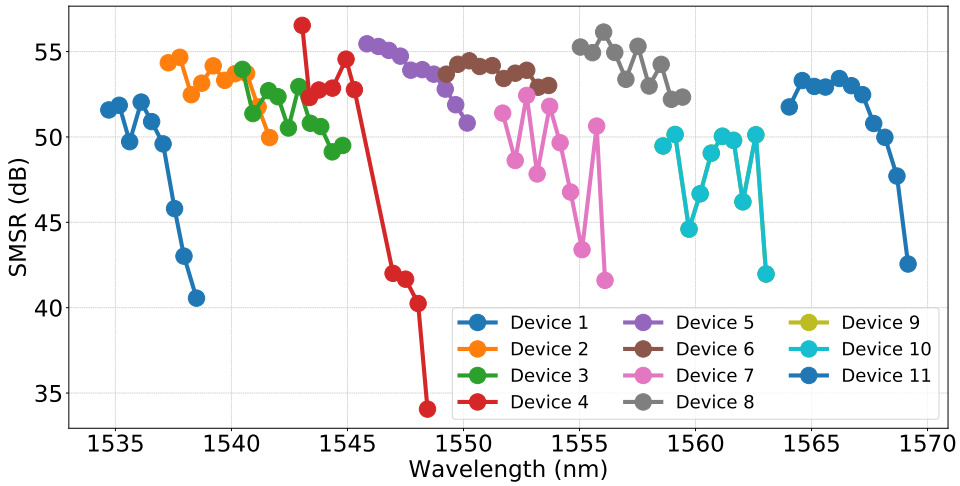


Figure 3.4: SMSR of the measured array temperature-tuned over the C-band.

tunability is achieved by tuning the temperature of the chip using TEC. Figure 3.3(a) shows the complete C-band coverage using temperature tuning in the range of 10-60 ^{o}C. The detailed wavelength tuning characteristics of each laser in the array is shown in Figure 3.3(b). The slotted single mode laser array covers a wavelength range of about 34.5 nm from 1534.7 to 1569.2 nm over a 50 ^{o}C (10 ^{o}C to 60 ^{o}C) temperature range. The measured wavelength tunability with temperature is $\sim$ 0.095 nm/^{o}C.

Despite showing single mode performance with good tunability there is a major disadvantage associated with these high order surface grating structures that hinders their operation at higher temperatures. Due to having a larger grating structure, these devices exhibit a narrower Free Spectral Range[1] (FSR) and additional losses over the DFB lasers. These uniform period grating laser devices show stable single mode performance with SMSR $>$ 50 dB at 10 °C, but the SMSR drops significantly as the temperature is increased. Figure 3.4 records this variation.

Here the degradation in the SMSR with increased temperature is not attributed to the competition from the modes adjacent to the lasing mode but from the mode which is one FSR longer, where the FSR is determined by the slot period. The calculated FSR for a group of slots with uniform slot period (slot width + slot spacing) of $\sim$ 9 μm, is approximately 37 nm [26], which implies that there are 3 reflection peaks in the 1500 nm to 1600 nm wavelength

[1]FSR - Spacing between two adjacent reflection peaks, determined by the Bragg condition.

range for a laser cavity designed to operate at 1550 nm. The mode competition becomes more severe when the lasers are temperature tuned. The gain peak shifts to higher wavelengths with increased temperature. This causes increased gain being experienced by other modes when the device operating temperature is changed and results in SMSR reduction and even mode hopping.

In order to suppress these side-modes which are one FSR away from the desired mode, the designs of slotted single mode laser diode structure reported in [25–27, 78] have been modified [28] by employing a high order surface grating with non-uniformly spaced slots. A 12-channel laser array, covering the full C-band, with a 3 period slotted single mode laser has been demonstrated [28] and a stable single-mode performance with SMSR $>$ 45 dB had been achieved over a wide temperature range. Multi period slotted lasers have better wavelength stability with changing temperature while maintaining a high SMSR over that of the single period slotted lasers because of their ability to suppress the reflection peaks which are one FSR away from the desired peak.

In [27], lasers with a single period grating structure showed poor temperature performance. This issue was solved by the introduction of a 3 period grating [28]. This generated interest in further studying these devices in detail and to compare the performance of different number of periods in the grating. In [28], the SMSR was key parameter to optimize. In the rest of this chapter, we are looking at significantly improving the slope efficiency of our devices.

In this chapter, we compared the performance of various uncoated (2, 3 and 4) multi period slotted lasers in terms of their lasing threshold and slope efficiency. We found that the performance of these multi period slotted lasers degrades when we use a higher number of periods with the 2 period lasers performing best in terms of threshold and slope efficiency. We also compared the performance of uncoated (only cleaved) two period slotted lasers with HR and AR coated two period slotted laser and found a significant performance improvement in the latter case. In addition to the experimental study, we also present a detailed modelling investigation in which we find very good agreement with the experiments. We find also, that the slope efficiency can be significantly improved with a reduction in the number of slots used in the high-order grating over our present design.

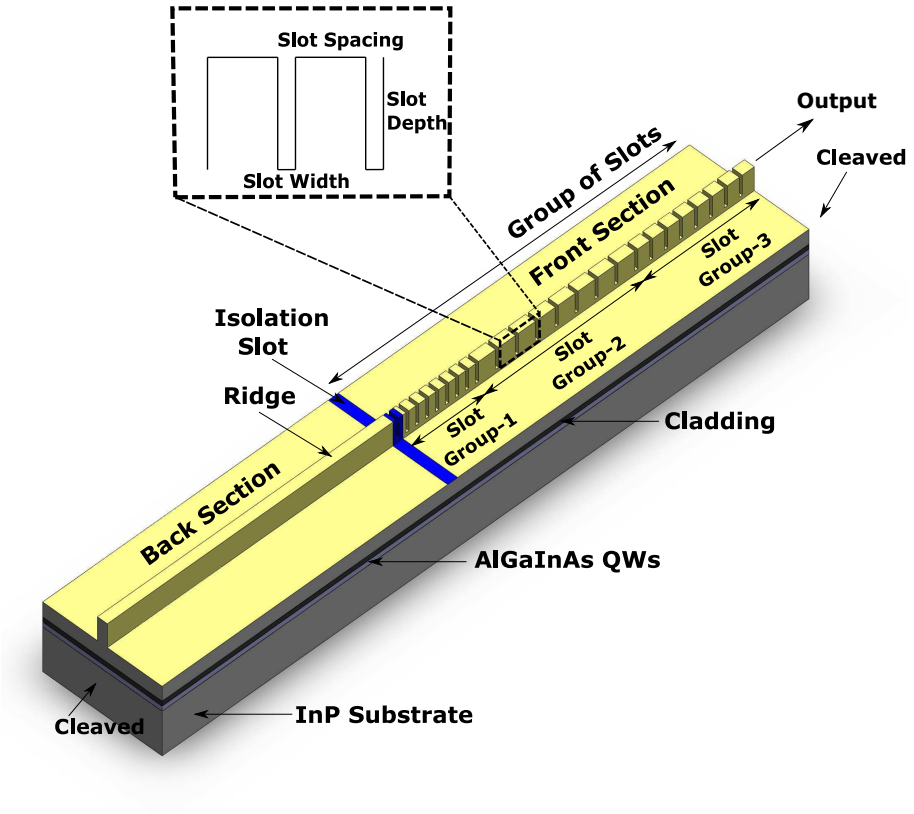


Figure 3.5: Schematic structure of a high order surface grating single mode laser. Both the front and back sections are active (current is injected to both front and back section) and the front section consists of the slotted structure which acts as an active DBR to provide necessary feedback for single mode operation. The slotted front section is based on 3 period grating structure. The three different periods in the front section (grating) are clearly indicated.

3.3 Multi Period Grating Design, Fabrication and Temperature Performance

The schematic design of a 3 period slotted single mode laser is shown in Figure 3.5. Designs with 2 and 4 periods are easily adapted from this. The laser has a 2 μm wide surface ridge waveguide structure. The epitaxial structure of the laser is the same as that used in [39] and explained in detail in section 2.8.1. The active layer consists of 5 AlGaInAs quantum well structure and has the emission peak at $\sim$ 1550 nm. The laser is divided electrically into a front section and a back section as in [55] by the first slot to avoid the single mode yield problem due to the uncertainty of the cleaving facet position (back facet). Adjustment of the two currents can be used to ensure high SMSR when the cleaving error results in poor single mode operation [56]. Both, front and back sections are active and the front section consists of the slotted structure which acts as an active DBR and provides the necessary feedback

for the laser to work in single mode. Both the ends (front/back) of the laser are cleaved and could be coated (HR/AR) for improved performance. The total length of the laser is 400 μm. The key parameters (slot depth, slot width, slot spacing and slot number) that are critical to the performance of laser were optimised in [25] using the scattering matrix model (see section 2.7) and incorporated in the design used for the fabricated devices in this study. The side reflection peaks are suppressed due to the introduction of high order surface grating with non-uniformly spaced slots [28]. This results in a wavelength-stable (mode-hopping free) performance of the laser.

In previous work [27] and [28], we have demonstrated a laser array with tunability across the C-band. In [27], we used a single period laser, but found that lasers at the blue end in particular had a decreased SMSR with temperature tuning. In [28], this situation was much improved with the use of a three-period grating, showing an SMSR $>$ 45 dB across the full C-band with temperature tuning of the individual devices in the array. The improved SMSR arose due to the much suppressed reflectivity of the grating one FSR away from peak near 1550 nm. We then designed a set of lasers to be fabricated with 2, 3 and 4 periods in order to determine which of these multi-period devices would work best in particular to improve the slope efficiency. For the designs, we kept the 1.35 μm depth slots, a 37th order grating and 24 slots. We then adjusted the periods to strongly reduce the reflectivity at one FSR away from 1550 nm. These designs also took into account the requirements of the fabrication itself, so that the smallest slot spacing produced in these cases would not cause difficulties in the fabrication.

Figure 3.6 shows a comparison between the lasing spectrum of a single period grating laser and the new two and three period grating lasers at 50 °C. The single period grating laser suffers from mode competition at $\sim$ 1590 nm reducing its SMSR. The mode competition becomes more severe when the lasers are temperature tuned. The gain curve shifts to larger wavelengths resulting in an increased gain experienced by the 1590 nm mode. The two and three period grating lasers on the other hand have little to no mode competition from the adjacent reflection peak which is one FSR away. This is a result of the reflection peak at one FSR away being suppressed by using several periods in the grating as shown in Figure 3.7, and as discussed in [28]. The Vernier effect is responsible for the suppression in the

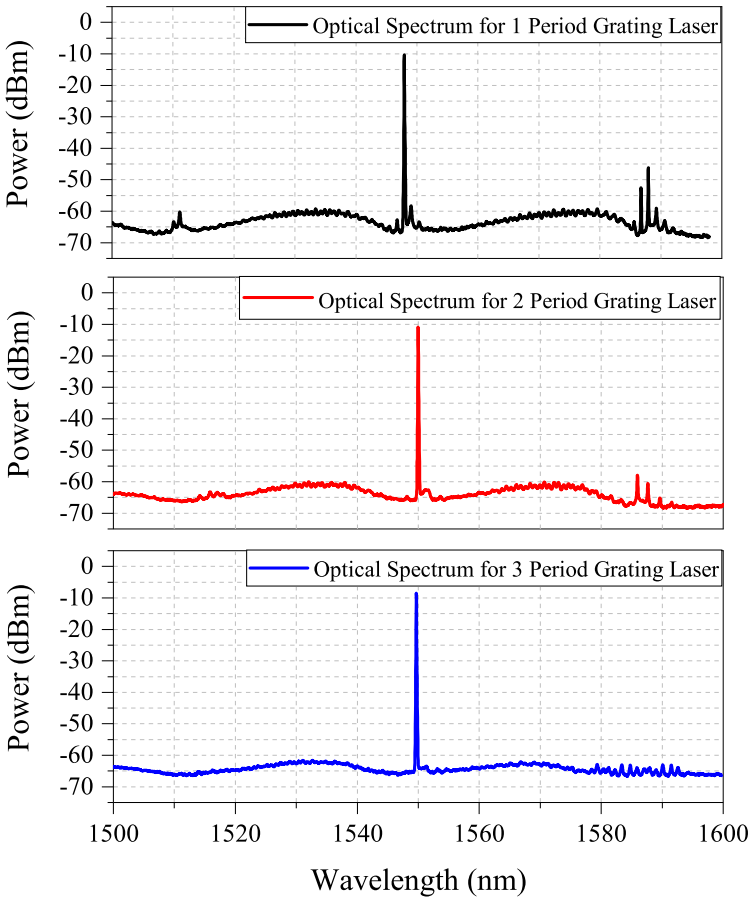


Figure 3.6: Optical spectrum of lasers with one (top), two (middle) and three (bottom) period grating structure at 50°C, demonstrating the much improved side mode suppression in the two and three period case.

reflectivity of the adjacent modes. The periods of the gratings is chosen such that they all reflect the desired mode but the FSR associated with them varies slightly. This reduces the overall feedback associated with modes which are adjacent to the central mode.

We have designed, characterised and studied the performance of these multi period lasers in more detail in this study. The dimensions used for slot width, slot depth and slot number are 1.089 μm, 1.37 μm and 24 respectively as designed in [25]. The slot spacing is varied to introduce multi slot periods. The slot spacing is varied around the optimum value (7.87 μm) to get high reflection and transmission. In our current work, we have designed lasers with 2, 3 and 4 slot periods. In Table 3.1, the design specifications for all the measured multi period slotted lasers are tabulated. Here, SS1 represents the slot spacing of those slots which are closest to the back section followed by SS2 and so on. The repetition column indicates the number of slots with slot spacing SS1 followed by SS2 and so on with the total always close

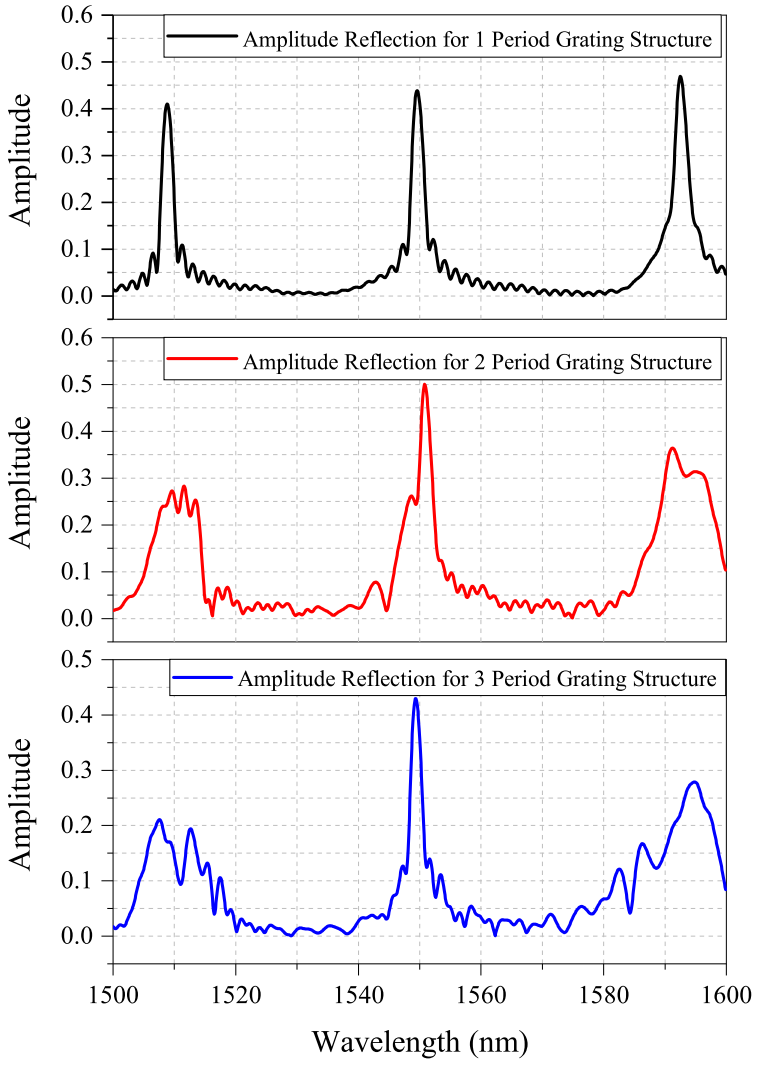


Figure 3.7: SMM (Scattering Matrix Method) simulated reflection spectrum of one (top), two (middle) and three (bottom) period grating structures. The suppression in the undesired side reflection peaks can be clearly seen in the two and three period grating structures.

to the optimised value of 24 e.g. $\{5, 19\}$ for a two period case. The designed devices were fabricated using a two-step dry etching process in an external foundry as described in section 2.8.1 earlier. The ridge was etched to a depth of about 1.8 μm. The slot depth was about 0.5 μm shallower than the ridge as determined by the two-step etching process. The length of the fabricated devices was around 400 μm with a back section length of $\sim$ 210 μm and a front grating section of $\sim$ 190 μm. The ridge was passivated and metal contacted, and then the devices were cleaved. The cleaved devices should have been HR coated at the back facet for better reflectivity and AR coated at the front facet to avoid feedback. However, this was not done and the cleaved devices were directly mounted on AlN carriers for measurements without

Table 3.1: Design Specifications for all the fabricated multi period slotted lasers. SS"X" refers to the slot spacing of slot group "X" in micrometers (μm) used in the design, "X" refers to position of slot group relative to the back section with X=1 being the closest and so on, and $\{N\}$ refers to number of slots in each period.

2 Period Grating Laser		3 Period Grating Laser		4 Period Grating Laser	
Slot Spacing (μm)	Repetition	Slot Spacing (μm)	Repetition	Slot Spacing (μm)	Repetition
SS1=7.384, SS2=8.353	{5,19}, {6,18}, {7,17}, {8,16}, {9,15}, {10,14}	SS1=7.384, SS2=8.595, SS3 = 9.806	{7,9,9}, {7,9,10}, {7,8,10}, {8,9,9}	SS1=7.385, SS2=8.353, SS3=9.079, SS4=10.532	{7,5,6,6}, {6,6,7,5}, {6,6,6,6}
SS1=7.868, SS2=8.837	{6,18}, {7,17}, {8,16}, {9,15}, {10,14}	SS1=7.626, SS2=8.837, SS3=10.290	{9,8,8}, {8,8,9}, {8,9,9}, {7,9,9}	SS1=7.142, SS2=8.353, SS3=9.321, SS4=10.048	{7,7,6,5}, {8,6,6,5}, {6,6,6,6}, {7,6,6,6}
SS1=8.595, SS2=7.385	{5,19}, {6,18}, {7,17}, {8,16}, {9,15}, {10,14}	SS1=7.626, SS2=8.837, SS3=10.290	{7,8,10}, {8,8,8}, {9,7,7}	SS1=7.142, SS2=8.111, SS3=8.837, SS4=9.806	{6,7,7,5}, {7,6,7,5}
SS1=7.384, SS2=9.079	{7,17}, {8,16}, {9,15}	-	-	SS1=7.142, SS2=8.111, SS3=9.079, SS4=10.048	{7,7,5,6}, {8,6,5,6}, {6,6,6,6}

any coating being applied. Even without coatings, we can carry out a relative comparison of lasers with 2, 3 and 4 periods. Later, some of the lasers with 2 period grating structure were coated and mounted on AlN carriers for measurements. The experimental performance of these devices is presented in section 3.4.

Figure 3.8 compares the experimental temperature performance of these multi period lasers with 2 and 3 period grating structure with 1 period grating structure laser. All 3 lasers shown in Figure 3.8 operate near 1550 nm at the gain peak. Lasers with single period grating structure showed relatively low SMSR compared with earlier reported devices [15], this was possibly because of the ageing of the device. As mentioned earlier, lasers with 1

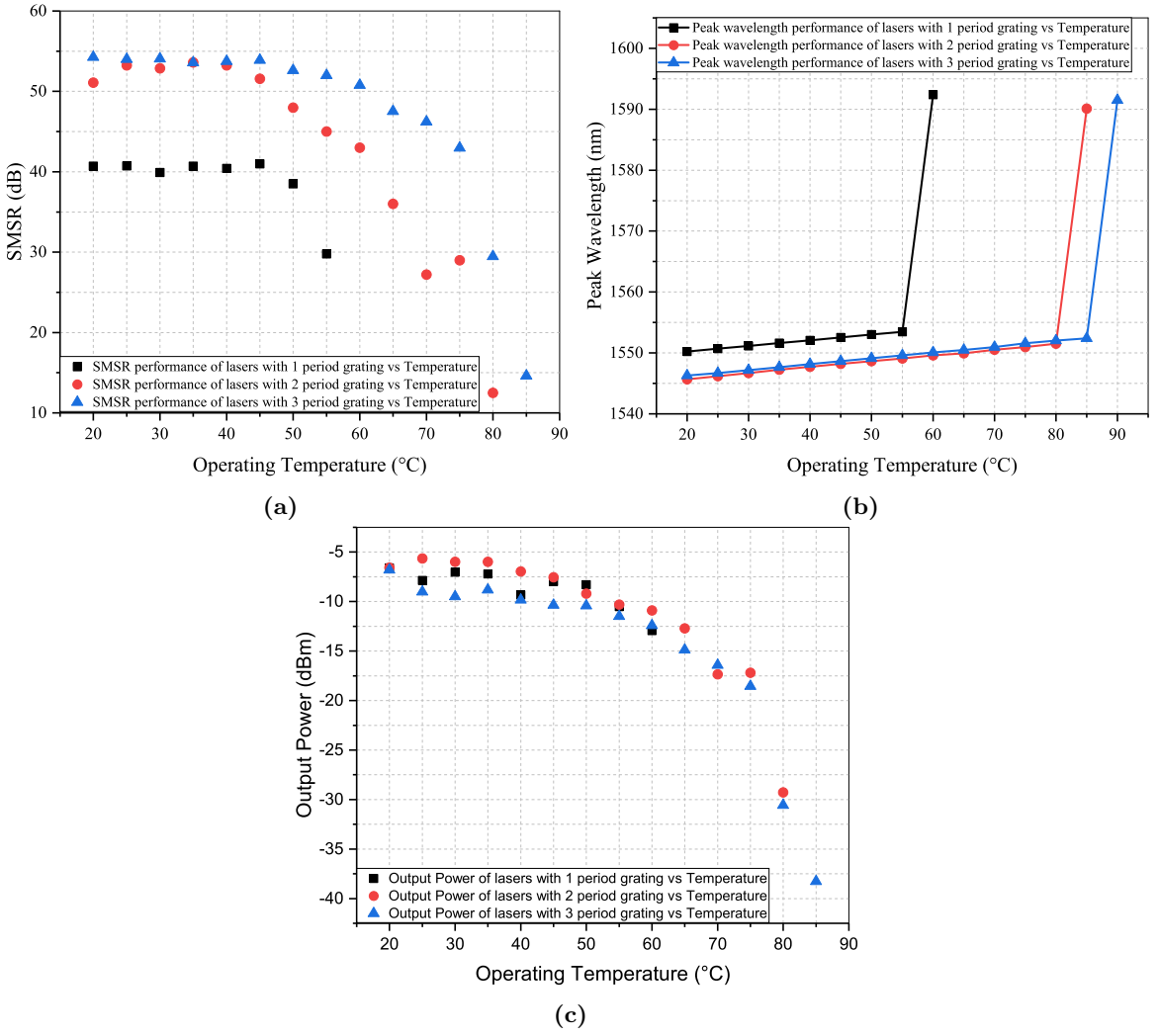


Figure 3.8: Performance comparison of lasers with 1, 2 and 3 period grating structure in terms of (a) SMSR, (b) peak wavelength, and (c) output power versus operating temperature.

period grating structure struggle with mode competition between desired longitudinal mode and the longitudinal modes which are one FSR away. As the operating temperature of the devices increases, the gain curve red shifts which causes an increase in the gain experienced by the adjacent longitudinal mode which is one FSR away, this results in SMSR reduction and eventually mode-hopping as shown in Figure 3.8(a), and 3.8(b). As shown in Figure 3.8(b), the laser with 1 period grating structure encounters a mode-hop at 60 °C when the main mode jumps from $\sim$ 1555 nm to 1592 nm. This puts a limitation on the operating temperature range of lasers with 1 period grating structure. The operating temperature range can be extended with the introduction of non uniform grating structure as it suppresses the undesired reflection peaks, as shown in Figure 3.7. The output power is shown in Figure

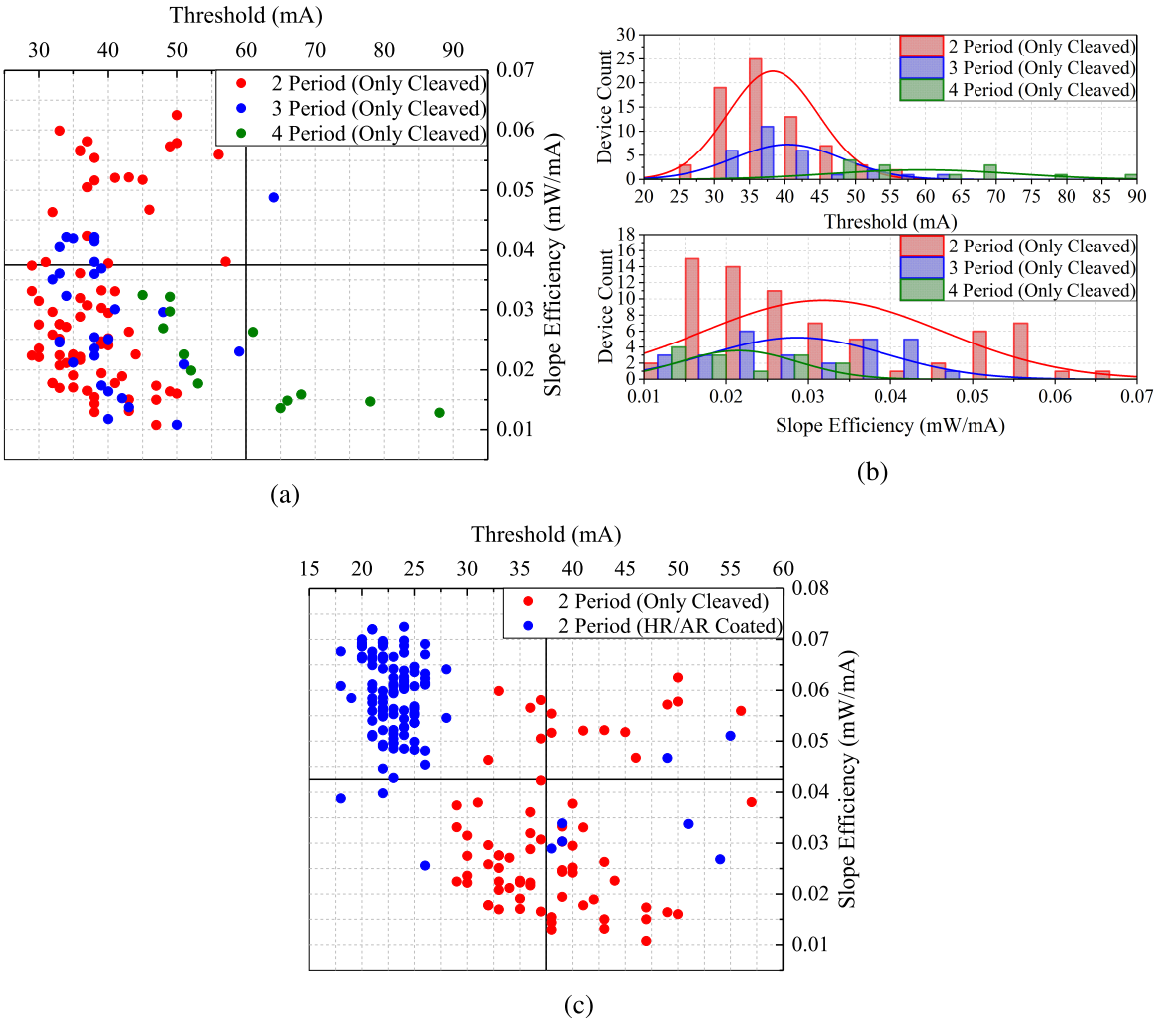


Figure 3.9: (a) Threshold vs Slope Efficiency for all the measured uncoated devices, (b) Threshold and Slope Efficiency vs Device-Count, and (c) Comparison between the performance of 2 Period Coated Laser and 2 Period Uncoated Laser.

3.8(c). Figure 3.8(b) shows that the introduction of 2 and 3 period grating structure extend the occurrence of mode-hop to 85 °C and 90 °C respectively. Also as shown in Figure 3.8(a), a SMSR of greater than 27 dB can be maintained upto 75 °C and 80 °C for 2 and 3 period grating structure respectively. This provides an extended operating temperature range of 15-20 °C which can prove critical in operation for energy efficient performance [79].

3.4 Device Characteristics of 2, 3 and 4 Period Devices

The fabricated uncoated 2, 3 and 4 period devices were mounted on AlN carriers and kept on a copper heat sink which in turn was mounted on a Peltier based TEC for precise temperature control. The temperature was kept constant at 20 °C and the measurement were carried

out in continuous wave (CW) mode. The front and back sections of the laser have separate contacts, but were connected together and were driven by the same current source to apply the same current density. In general, the two currents in the front and back sections should be set differently. However, in many of the devices we have fabricated to date, the front and back sections were electrically connected in order to measure LI curves, threshold and slope efficiency of the individual devices. This generally provides SMSR around or better than 30 dB, but much higher values require a separate current source for the two sections. The output spectrum was measured by a lensed fiber and recorded by an Agilent 86140B Optical Spectrum Analyser (OSA). The resolution of the OSA was set at 0.06 nm with sensitivity of -75 dBm. A single mode performance at $\sim$ 1550 nm with a SMSR $>$ 45 dB was achieved at 100 mA of injection current for all the measured devices. The LI curve is measured by varying the input current from 1 to 100 mA in the steps of 1 mA. The output power was measured from the front facet as shown in Figure 3.5 using a large Ge detector. Figure 3.9(a) shows the measured threshold vs slope-efficiency plot for uncoated (only cleaved) 2, 3 and 4 period grating lasers. It can be seen that most of the uncoated 2, 3 and 4 period devices performed in the bottom left quadrant of the plot. A few of the 2 period designs also performed in the top left quadrant with low threshold and high slope-efficiency. In Figure 3.9(b), the measured laser thresholds and slope efficiency against the device-count and their respective normal distribution for uncoated 2, 3, and 4 period grating lasers is plotted. The threshold peak for the uncoated 2, 3 and 4 period lasers were around 38, 41 and 59 mA respectively and the slope efficiency peak for the 2, 3 and 4 period lasers were around 0.031, 0.028 and 0.02 mW/mA respectively. It is evident that the performance of these devices degrades as the number of periods are increased, with the 2 period grating laser performing the best. The slope efficiency measured for most devices is low because the measured fabricated devices were only cleaved and not HR/AR coated. We also measured a set of 2 period grating lasers with HR/AR coated facets. Figure 3.9(c) compares the performance of those HR and AR coated 2 period slotted devices with only cleaved (uncoated) 2 Period slotted devices. A threshold of $\sim$ 20-25 mA with a slope efficiency $>$ 0.05 mW/mA have been observed for most of the HR and AR coated devices. The performance of HR and AR coated devices have significantly improved over the uncoated devices but there is clear room for improvement in the threshold and slope efficiency as we will see later in the simulation section. Taking into account the

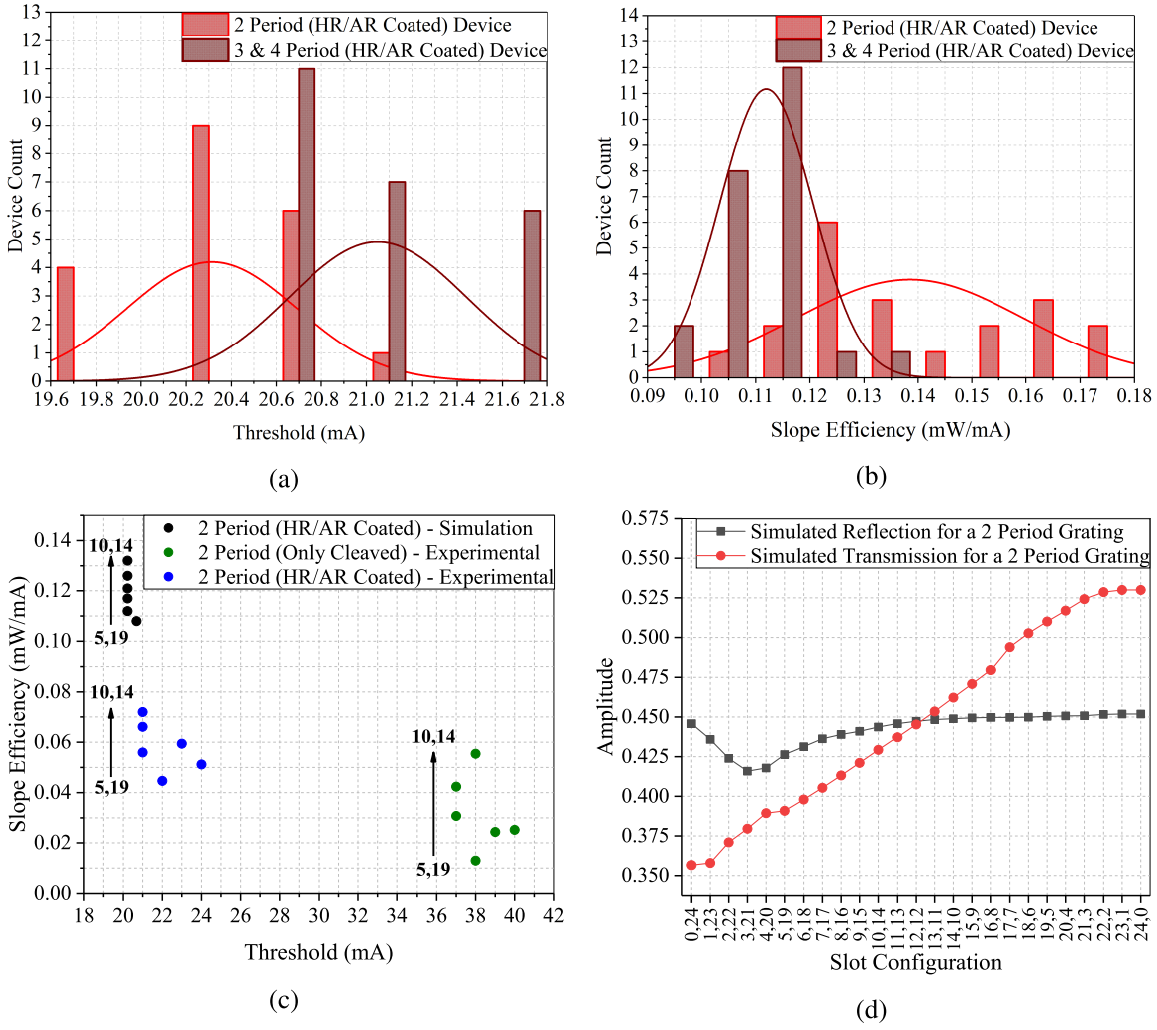


Figure 3.10: Comparison between the simulated performance of 2 period slotted laser with 3 and 4 period slotted laser in terms of (a) threshold, and (b) slope efficiency, (c) Comparison between the experimental performance of 2 Period (with SS1 = 7.384 μm and SS2 = 8.353 μm) Coated Laser, Uncoated Laser and Simulation, and (d) Simulated Amplitude Reflection and Transmission vs Design for 2 Period slotted laser (with SS1 = 7.384 μm and SS2 = 8.353 μm).

results from Figures 3.6, 3.7, 3.8 and 3.9, we can conclude that the best operation of our high order grating laser in terms of threshold, slope efficiency and temperature is with a two period grating laser. However, if the device is kept at a constant temperature and operates near the peak of the gain at 1550 nm, then a single period will suffice for the grating.

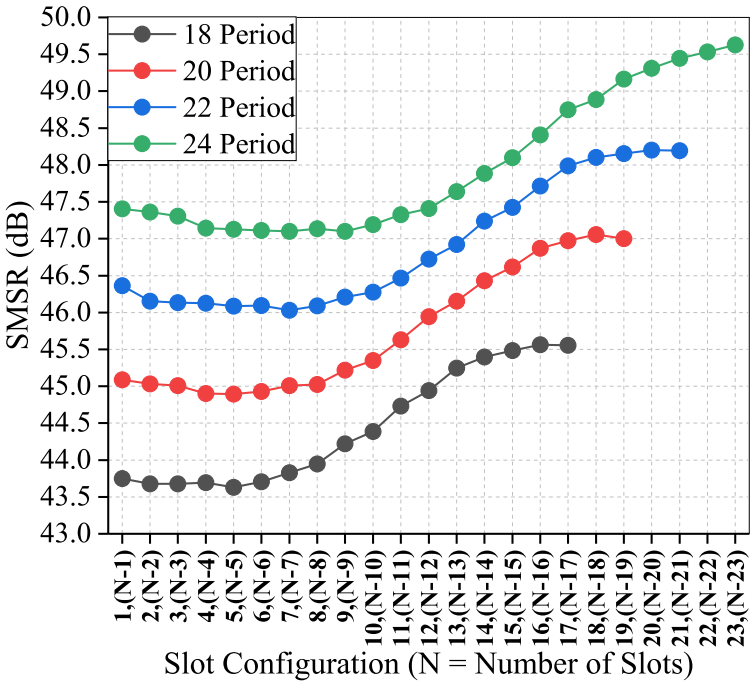
3.5 Optimized Design Simulation Results

We seek now to elucidate the results found in the experimental section and further optimize our design using high order grating with 2 period lasers in particular to achieve a higher slope

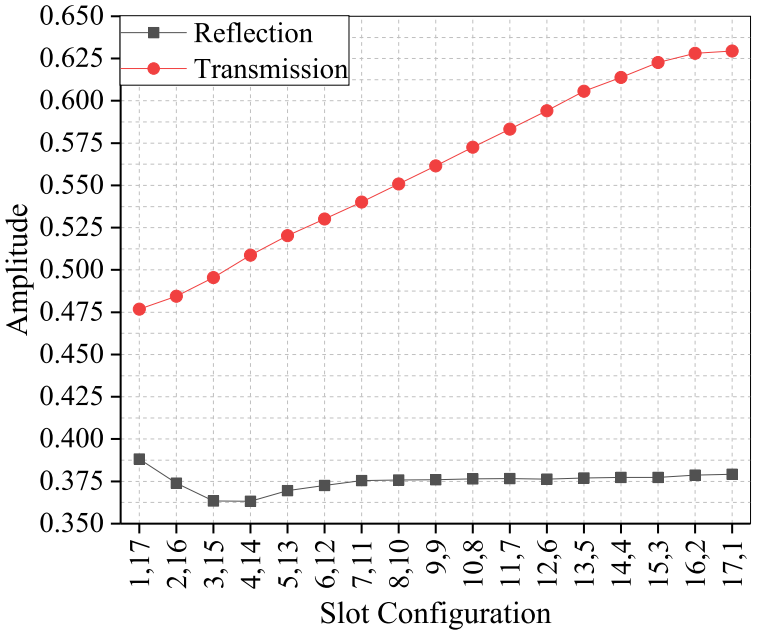
efficiency. The scattering matrix method (SMM) [24] is used to simulate the performance of these multi period slotted lasers, and the interaction between these slots are accounted for properly by applying the SMM directly in 2-D. The slot width is set to 1.09 μm and the slot depth is set to 1.37 μm. To investigate the effects of the multi period grating on the slope efficiency, threshold, reflection and transmission of the device, we kept total number of slots constant at 24. The slot spacing and slot configuration used in the simulation are the same as the measured devices and are shown in Table 3.1. In Figure 3.10(a) and 3.10(b) the simulated performance of HR/AR coated 2 period slotted lasers are compared with HR/AR coated 3 and 4 period slotted lasers. Here, the device count corresponds to the devices with different slot spacing and slot configuration. As found experimentally, the performance of the two period slotted lasers are superior compared to other higher number of periods with a lower threshold and higher slope efficiency. Also, the calculated threshold ($<$ 21.7 mA) and calculated slope efficiency ($>$ 0.09 mW/mA) for all the devices is much better than the measured case, which suggests that by decreasing the losses (scattering, transmission, fabrication etc.) the performance of these devices can be subsequently improved. Figure 3.10(c) compares the simulated threshold and slope-efficiency results for HR/AR coated 2 period slotted lasers (with SS1 = 7.384 μm and SS2 = 8.353 μm) with the corresponding experimental results (both HR/AR coated and uncoated). It is evident that the performance of two period HR/AR coated slotted lasers are very close to their optimum values (as determined from simulation) in terms of threshold but there is a big mismatch in terms of slope-efficiency. The discrepancy in the model and experiments is due to the fact that the out of plane scattering is not directly accounted for in the model. The 2D model assumes infinite length in the perpendicular direction. During the homogeneous parts of the model, the model assumes no scattering as the mode is guided. In the lasers model (Time domain transfer matrix model - TDTMM), we used an internal loss to account for scattering at the waveguide walls, etc. The scattering comes in at the slot boundaries. CAMFR (Cavity Modelling Framework) works by matching the modes in the two sections at the boundary. The main reason for using the 2D model is for simulation time, a 3D model though more accurate would take an incredibly long time to run. In Figure 3.10(c), it is evident that as the slot period is changed from $\{5, 19\}$ (followed by $\{6, 18\}$ and so on) to $\{10, 14\}$, the slope efficiency increases while the threshold remains almost the same which is because of the strong dependence of

the threshold on reflection and the strong dependence of the slope efficiency on transmission. By changing the slot configuration from $\{5, 19\}$ (followed by $\{6, 18\}$ and so on) to $\{10, 14\}$, the length of the front section has also been changed. Here, SS1 < SS2, hence the length of the front section decreases as the configuration is changed from $\{5, 19\}$ to $\{10, 14\}$. Both the front and back sections are active and current injected. The front section grating consists of slots with a large period, which gives rise to increased scattering losses when compared with a DFB for example. This is the disadvantage of using high-order gratings and we must therefore optimise the grating structure including controlling the number of slots so that we get the best possible performance from the laser. Figure 3.10(d) shows that the simulated transmission amplitude increases linearly as we move from slot configuration $\{0, 24\}$ towards $\{24, 0\}$ because the length of front section decreases as we change the slot configuration from $\{0, 24\}$ to $\{24, 0\}$, which reduces the transmission losses in the front section and hence increases the transmission amplitude. An increment in transmission amplitude increases the slope efficiency. On the other hand, the reflection amplitude varies very little as the slot configuration is changed. The threshold depends strongly on the reflectivity which is almost constant in this case, hence there is very little change in threshold.

As discussed above, a shorter front section will lower the transmission loss and increases the slope efficiency of the laser. For slot width and spacing optimised in [25], a shorter front section can be achieved by reducing the number of slots. A front section with less slots would also results in reduced out of plane scattering losses and results in lower transmission losses. This results in an increment in transmission amplitude which improves the slope efficiency. However, as shown in [25], the 3-dB reflection bandwidth increases as the number of slots decreases. This increment in the 3-dB reflection bandwidth results in an increased gain experienced by the longitudinal cavity mode adjacent to the desired longitudinal cavity mode. This leads to mode competition between the longitudinal cavity modes and leads to reduction in SMSR. Hence, there is a trade-off between a higher slope efficiency and a higher SMSR. Figure 3.11(a) shows that for a 2 period slotted laser with SS1 = 7.384 μm and SS2 = 8.353 μm as the number of slots reduces from 24 to 18, the simulated SMSR decreases by 4 dB. In Figure 3.11(b), as expected the transmission increases significantly as compared to the case with 24 slots. Also, the reflectivity decreases slightly since the total number of reflecting slots has been reduced but is almost constant for all the slots configuration for the



(a)



(b)

Figure 3.11: (a) Simulated SMSR vs Slot configuration for 18, 20, 22 and 24 slots (SS1 = 7.384 μm and SS2 = 8.353 μm) at 20 °C, and (b) Simulated Amplitude reflection and transmission for 2-Period slotted laser vs slot configuration with 18 slots (SS1 = 7.384 μm and SS2 = 8.353 μm)

18 slots, 2 period laser. In Figure 3.12, it can be seen that higher transmission caused by a shorter front section leads to a higher slope efficiency for 18 slots compared to 24 slots, and a simulated slope efficiency of as high as 0.2 mW/mA is achieved which is closer to the

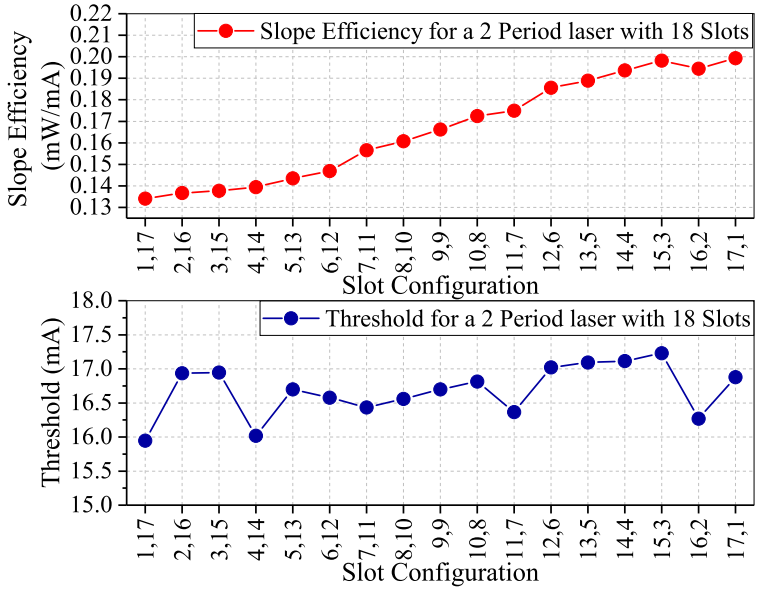


Figure 3.12: Simulated slope efficiency and threshold versus slot configuration for a 2 period slotted laser with 18 slots (SS1 = 7.384 μm and SS2 = 8.353 μm).

performance of a DFB laser. This best performance in terms of improved slope efficiency is associated with a one period device. However, as we have shown earlier, this performance can only be maintained provided that the temperature is constant and laser operates near the peak of gain spectrum. Also, as shown in Figure 3.12, threshold is almost constant as expected from the reflection data in Figure 3.11b.

Figure 3.13 suggests a way to select the optimum slot configuration for these 2 period lasers with 18 slots, so that a high value of slope efficiency can be achieved with a good suppression in the undesired reflection peaks which are one FSR away from the desired reflection peak at 1550 nm. Figure 3.13 (bottom) plots the simulated suppression in the undesired left and right reflection peaks with respect to the desired peak at 1550 nm against different slot configuration. The left/right side reflection peak suppression is the difference between the amplitude of desired reflection peak at 1550 nm and the left/right reflection peaks which are one FSR away as clearly marked in Figure 3.13 (top). As expected the undesired left/right reflection peak suppression first increases as the slot configuration changes from $\{1, 17\}$ towards $\{17, 1\}$, attains a maximum for the slot configuration $\{9, 9\}$ and then reduces. This is because, the slot configuration like $\{1, 17\}$, $\{2, 16\}$, $\{16, 2\}$, $\{17, 1\}$ etc., doesn't have a dominating vernier effect and hence leads to little to no suppression in the undesired reflection peaks. So even though Figure 3.12 suggests that for the slot configurations like $\{16, 2\}$, $\{17, 1\}$

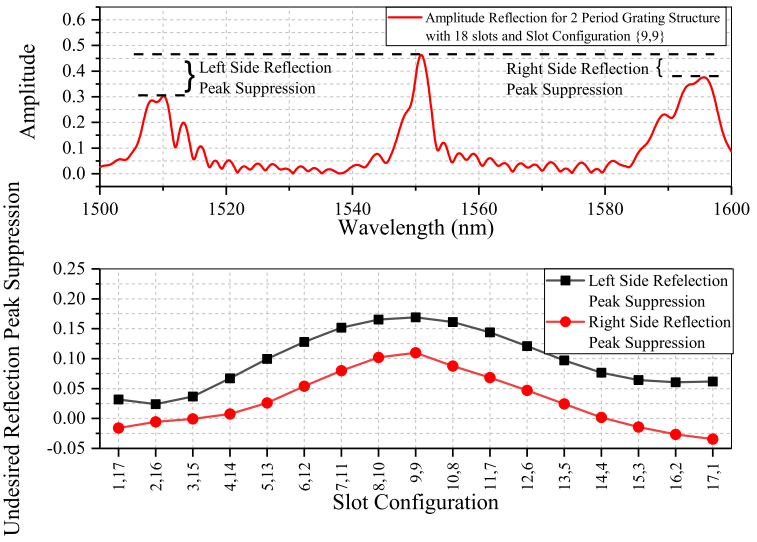


Figure 3.13: (Top) Amplitude reflection for 2 period grating structure (SS1 = 7.384 μm and SS2 = 8.353 μm) with 18 slots and slot configuration $\{9, 9\}$. (Bottom) The undesired left and right reflection peak suppression (which are one FSR away from the desired reflection peak at 1550 nm) plotted against slot configuration for 2 period grating structure (SS1 = 7.384 μm and SS2 = 8.353 μm) with 18 slots and slot configuration $\{9, 9\}$.

etc., the slope efficiency will be optimum, these slot configurations will have poor SMSR performance when the temperature is changed. The reduction in the SMSR will be because of the mode competition between the desired longitudinal mode and the modes which is one FSR away. On the other hand for slot configurations like $\{7, 11\}$, $\{8, 10\}$, $\{9, 9\}$, $\{10, 8\}$ etc., where the proportion of the slot number for the 2 slot groups used are comparable, the vernier effect is strong and leads to a good suppression of the undesired reflection peaks at one FSR away. By reducing the number of slots from 24 to 18, and incorporating the slot configurations in the laser design with strong vernier effect, lasers with simulated slope efficiency of ~ 0.17 mW/mA can be achieved. Also, since these slot configurations have a strong vernier effect, the undesired reflection peaks at one FSR away on either side are substantially suppressed which leads to an increase in the operating temperature range without mode hopping.

Shortening the length of the front section by reducing the number of slots, the slope efficiency can be increased significantly. Reducing the number of slots results in degradation of SMSR but the obtained value for 18 slots was > 43.5 dB which is still far better than the industrially acceptable SMSR limit of 30 dB. So, it can be deduced that the performance of these multi period devices can be significantly improved by reducing the number of slots.

3.6 Conclusion

In this chapter, we first presented a ridge waveguide semiconductor laser, which achieve a single mode performance by employing high order surface slots onto the ridge waveguide. These structures eliminate the need of regrowth and higher resolution lithography techniques in the fabrication process, so can potentially reduce the cost and complexity of the manufacturing. We presented a detailed characterisation of these devices and showed a full C-band coverage by thermally tuning the devices on the laser array. Even though these devices were performing in single mode with an SMSR $>$ 50 dB at lower temperature, the performance at higher temperature was significantly degraded due to the nature of higher order grating. Gratings with larger period support simpler fabrication but they also reduce the FSR of the Bragg peaks. At higher temperature the adjacent undesired modes start to experience enough gain to overcome the cavity losses and starts to lase. This causes mode competition and reduces the SMSR and even cause mode hopping when the temperature is increased significantly. We then improved the design of our device by employing non-uniform grating which utilise the vernier effect to reduce the reflectivity of adjacent FSR modes and hence increases the overall operating temperature range with high SMSR. We compared the performance of various (2, 3 and 4) multi period slotted lasers in terms of their lasing threshold and slope efficiency. We found that the performance of these multi period slotted lasers degrades when we use a higher number of periods with the 2 period lasers performing best in terms of threshold and slope efficiency. We also compared the performance of uncoated two period slotted lasers with HR and AR coated two period slotted laser and found a significant performance improvement in the latter case. We also found out that the performance of these devices can be further enhanced by shortening the slot section of the laser by reducing the number of slots from 24 to 18. For our laser grating design near 1550 nm at 20 °C, the best performance is found for a device with a single period grating structure. However, when temperature tuning is used, a device with two period grating structure provides improved performance due to suppression of modes one FSR away from main lasing mode.

Chapter 4

Gain Switched Optical Frequency Comb

4.1 Introduction

In the last two decades, network traffic has seen a significant increase due to the evolution of the information age. The unprecedented growth in the network traffic is continuously increasing the demand for bandwidth. In parallel, the advancement in optical communication technology has kept pace with the bandwidth requirement of the existing and newly emerging applications. The emergence of optical amplifiers, especially erbium doped fiber amplifier (EDFA) and the development of wavelength division multiplexing (WDM) technique has revolutionised the modern optical communication systems by enabling the deployment of high capacity system. WDM combines multiple individual channels at different wavelengths for its transmission along the single optical fiber. In the last decade, due to rapid growth of high speed data transmission services like cloud, video streaming etc. optical transmissions systems are facing a capacity crunch due to filling up of the entire C-band [80]. The immense increase in bandwidth usage is showing no sign of stopping and forcing the industry as well as research to develop newer technologies to further improve the system capacity.

Use of advanced modulation format over ON-OFF Keyed formats are gaining a lot of attention due to their ability to provide better spectral efficiency [81]. Currently, systems incorporating dense wavelength division multiplexing utilise a minimum channel spacing of 50 GHz, and can support data rates of up to 100 Gb/s [82]. In order to achieve further spectral efficiency, even closer channel spacing is required. One such technology which can efficiently operate at such narrow channel spacing without any interference is orthogonal frequency division multiplexing, and hence gained a lot of interest [83–85]. Due to the orthogonality of the adjacent channels, data signal can be overlapped without any intersymbol interference. This combined with its flexibility and tolerance to impairments can significantly improve the system efficiency.

Another important consideration in the system implementation is the cost of wavelength dependent transmitter and receiver subsystems in both access networks and user premises.

Currently in a WDM based passive optical network (PON), each user is assigned a specific wavelength. This is fulfilled by using either a bank of independent lasers or a bank of externally injected Fabry-Perot laser diodes. Such systems requires a dedicated temperature control for wavelength stabilisation. This along with the large inventory significantly increases the power budget and the overall cost of the system.

Implementation of spectrally efficient technologies at closer grid spacing at lower cost calls for innovative multicarrier transmitters. One such transmitter, optical frequency comb sources (OFCS) can play a vital role in the implementation of narrow channel spacing grid at significantly lower cost due to its ability to reduce or eliminate the guard bands by ensuring constant frequency spacing between the carriers. An OFCS can simply be described as a device or subsystem, capable of generating multiple wavelengths which are equally spaced and share strong phase correlation. The generated optical frequency comb can then be demultiplexed into individual channels for independent modulation [86, 87]. Due to reduction/elimination of guard bands these multicarrier transmitters are required to have certain attributes including – number of carriers, flatness, flexible channel spacing, wavelength tunability, low linewidth, high SMSR, and cost-efficiency among others. A very good survey on various OFCS and their applicability in elastic optical network can be found in this article [31]. The most commonly used and relevant configurations for OFC generation are:

- Mode-locked lasers (MLL)
- Microresonator based Kerr OFCS
- Electro-optic Modulator based OFCS
- Gain Switched OFCS

In this work we have chosen Gain Switching of laser diodes as our method to generate OFCS and is discussed next [88]. In the rest of the chapter we will discuss in detail the process of generating OFCS using gain switching. We will also talk about the importance of injection locking in generation of a wide OFC with multiple carriers sharing a very high phase correlation. We will assess the quality of the generated comb lines through phase noise and linewidth measurements. We will also present a detailed study of the effect of

optical injection on the injected laser and experimentally characterise its output performance including wavelength, SMSR, modulation response, relaxation oscillation frequency, linewidth and phase noise. We will also discuss how optical injection affects the overall bandwidth and the phase noise of the OFC.

4.2 Gain Switching and Injection Locking

Gain switching is the direct modulation of a DC biased (above threshold) laser diode with a large amplitude RF signal. The large electrical signal (DC + RF) drives the laser diode above and below the threshold current. Figure 4.1(a), shows the transient photon density dynamics of a laser diode. When the laser's bias conditions are changed during operation, the photon density oscillates before achieving the steady state. The frequency of oscillation is known as the relaxation oscillation frequency (f_r) and was first observed in 1980 [89]. The frequency of gain switching signal (f_o) is chosen to be greater than half the relaxation oscillation frequency ($f_r/2$) to suppress the second oscillation of the photon density, thus creating an optical pulse. Repetition of this results in an optical pulse train of the same frequency as that of the applied sinewave, as shown in Figure 4.1(b).

As shown in Figure 4.1(a), the photon density does not start to build up as soon as the electrical signal is applied but starts after a time duration of t_d. This is because the carrier density has to first increase above the threshold value for the stimulated emission to start. This delay shortens the generated gain switched optical pulse, which is convenient for creating a multi-carrier transmitter. Since, $f_o > f_r/2$, this limits the minimum FSR achievable, which is typically around 5 GHz. The maximum FSR obtainable is limited by the modulation bandwidth, which is typically around 10 GHz.

The modulation bandwidth of a semiconductor laser is inversely proportional to the length of the device, so the modulation response can be improved by reducing the overall length of the device. But, shortening the length of a semiconductor laser increases its linewidth, which degrades the quality of light output. Also, in gain-switching the laser is driven above and below threshold continuously, this gives rise to frequency chirp. The frequency chirp is defined as a variation of the instantaneous emission frequency due to fluctuations on the carrier density during direct modulation. Also, since we are switching off all the photon density

in the negative cycle of gain-switching signal, the adjacent pulses are not phase correlated, which gives rise to temporal jitter.

Both of these issues can be solved by externally injecting the gain switched device [90]. Optical external injection consists in coupling light from an external light source optically isolated and usually named as master laser, into the cavity of a slave laser (gain switched laser in this case), as shown in Figure 4.2. Generally, a low linewidth laser is used as the master. External injection adds an out-of-phase contribution from the master laser to the lasing mode (considering a single mode laser) of the slave laser. Therefore the injected photon density, if it succeeds to dominate in the cavity, may provoke the appearance of photons at the same oscillating frequency and with the same phase through stimulated emission. Hence, a reduction in linewidth and chirp can be achieved using a low linewidth master laser for external injection. We will present detailed experimental verification of this in section 4.3.

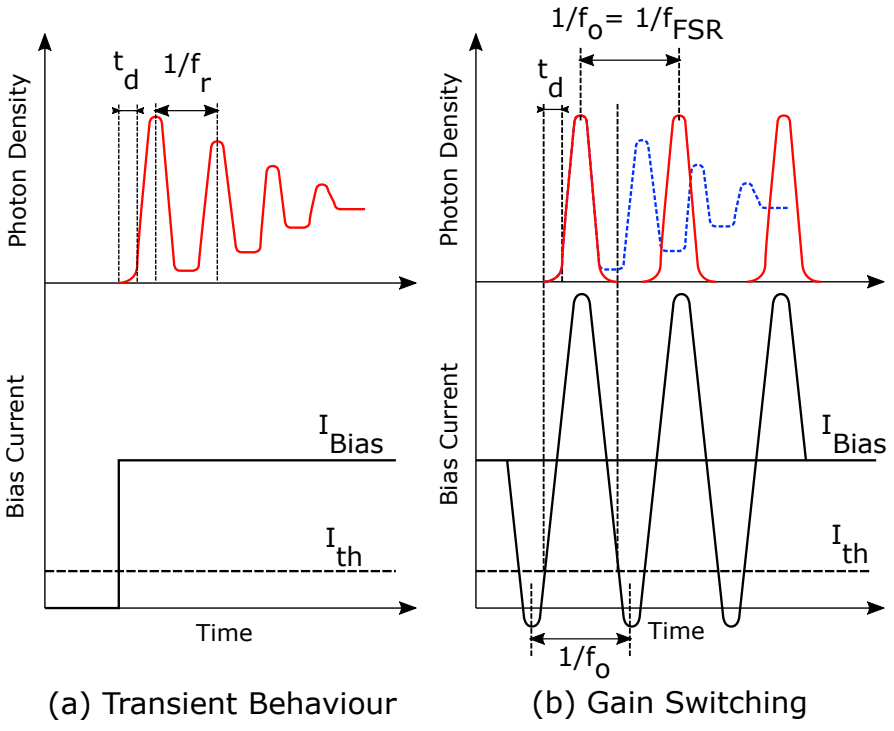


Figure 4.1: (a) Transient photon density dynamics under the application of a step current, and (b) Gain switching dynamics.

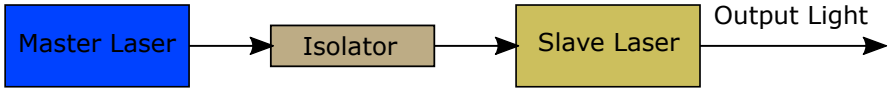


Figure 4.2: Optical external injection.

4.3 Optical External Injection

Optical external injection consists in coupling light from an optically isolated external laser source, usually named as master laser, into the cavity of a laser known as slave [91–94]. Optical external injection has been studied in detail and is known to improve the slave laser performance, typically in terms of mode selectivity [95], resonance peak and modulation bandwidth enhancement [94, 96], and noise reduction [97, 98]. In this section we will present experimental verification of this along with some theoretical insights.

The dynamics of an injection-locked laser can be understood by the steady-state analysis of the rate equation of semiconductor lasers with optical injection. The standard optical injection locking (OIL) rate equations are [91, 93, 94, 96]:

$$\frac{dS(t)}{dt} = g_o[N(t) - N_{th}]S(t) + 2\kappa\sqrt{S_{inj}S(t)}cos(\phi(t)) \tag{4.1}$$

$$\frac{d\phi(t)}{dt} = \frac{\alpha}{2}g_o[N(t) - N_{th}] - \kappa\sqrt{\frac{S_{inj}}{S(t)}}sin(\phi(t)) - \Delta\omega_{inj} \tag{4.2}$$

$$\frac{dN(t)}{dt} = J(t) - \tau N(t) - \{\tau_p + g_o[N(t) - N_{th}]\}S(t) \tag{4.3}$$

where *S(t)*, and *N(t)* are slave laser's photon, and carrier number. *ϕ(t)* is the phase difference between the internal and injected field from the master. g_o, N_{th}, α, J, τ, and τ_p are slave laser's differential gain, threshold carrier number, linewidth enhancement factor, pump current normalised by electron charge, carrier recombination rate, and photon decay rate, respectively. κ, S_{inj}, and $\Delta\omega_{inj}$ denotes the injection terms and stands for the coupling rate, injected photon number, and detuning frequency, respectively. The coupling rate is the rate at which the injected photons enter into the cavity and distribute themselves along the cavity length. The detuning frequency, $\Delta\omega_{inj}$, is the difference between the master laser's frequency

and slave laser's free running frequency (without injection): $\Delta\omega_{inj} = \omega_{master}$ - ω_{fr}.

Equation 4.2 qualitatively explains the locking condition of the slave laser. It describes the differential of the phase, namely, it is a formula for the emission frequency of the laser [96]. The relative change in frequency induced by the resonance shift which is caused due to the reduction of the carrier number under injection is denoted by the first term on the right hand side. The second term captures the shift caused due to the coupling between internal and injected fields. When the sum of the relative changes in frequency changes caused due to reduction of carrier number under injection and the coupling between internal-injected fields is equal to the detuned frequency, $\Delta\omega_{inj}$, the slave laser is injection locked. This is the steady state solution of the equation 4.2. By substituting the steady state solution for various parameters in equation 4.2, and solving for the detuned frequency, we obtain:

$$\Delta\omega_{inj} = \frac{\alpha}{2} g_o [N_s - N_{th}] - \kappa \sqrt{\frac{S_{inj}}{S_s}} sin(\phi_s) \tag{4.4}$$

For a free running Fabry-Perot (FP) laser, the m^{th} longitudinal modes corresponding to the FP cavity resonance can be written as:

$$\upsilon_{fr} = \frac{mc}{2\mu l} \tag{4.5}$$

here, υ_{fr} is the free running frequency of the m^{th} longitudinal mode, c is the speed of light in vacuum, μ is the refractive index of the active layer and l is the cavity length. Equation 4.5 shows that the frequency of emission is inversely proportional to the refractive index of the laser material. Also, refractive index is a material property and shares a inversely proportional relationship with the carrier number, N, in the cavity. Hence, the increase (decrease) in the carrier number, increases (decreases) the emission frequency. This relationship can be expressed as [91]:

$$\Delta\omega(N) = \frac{\alpha}{2} g_o \Delta N \tag{4.6}$$

here, α is the linewidth enhancement factor, g_o is the differential gain, and $\Delta N = N$ - N_{th}, N_{th} is the threshold carrier number. Figure 4.3 considers the case of external optical

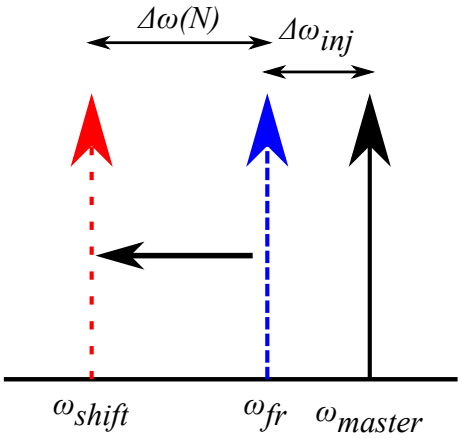


Figure 4.3: Cavity resonant condition under injection locking.

injection. Here, ω_{fr} is the free running frequency of the m^{th} longitudinal mode of the FP cavity resonance, and ω_{master} is the frequency of the injected field (master-laser). Due to the increased number of photons in the slave laser's cavity, the steady state carrier number goes below the threshold value, this redshifts the cavity mode as per equation 4.6. This change is depicted in Figure 4.3 by the frequency ω_{shift}. But under injection locking, the frequency of the output light is ω_{master}, not ω_{shift}. From Figure 4.3, and equation 4.4, we can deduce that despite being injection locked, the slave laser continues to emit photons at a frequency which corresponds to its cavity resonance condition, ω_{shift}. Under injection locking, the injected master light continuously shift the phase of the slave laser's light such that the slave laser's output appear to lase at the frequency of the injected light (master-laser). These phase-shifted photons undergo stimulated emission and creates more photons which are phase correlated to the new phase [94].

4.3.1 Experimental Set Up

Figure 4.4 shows the experimental setup used to assess the effect of injection locking on the output characteristics of the slave laser. The FP laser characterised in the next section and also used for gain-switched OFC generation is used as a slave laser. The slave laser was biased at 26.3 mA and kept at 15.3 ^{o}C. The free running longitudinal mode at 1563.76 nm of the FP laser cavity resonance is selected to study the injection properties of the slave laser. A low-linewidth tunable laser, wavelength tunable in the C-band is used as a master laser, injecting light in the cavity of the slave laser using a PM circulator. The tunable laser is sourced

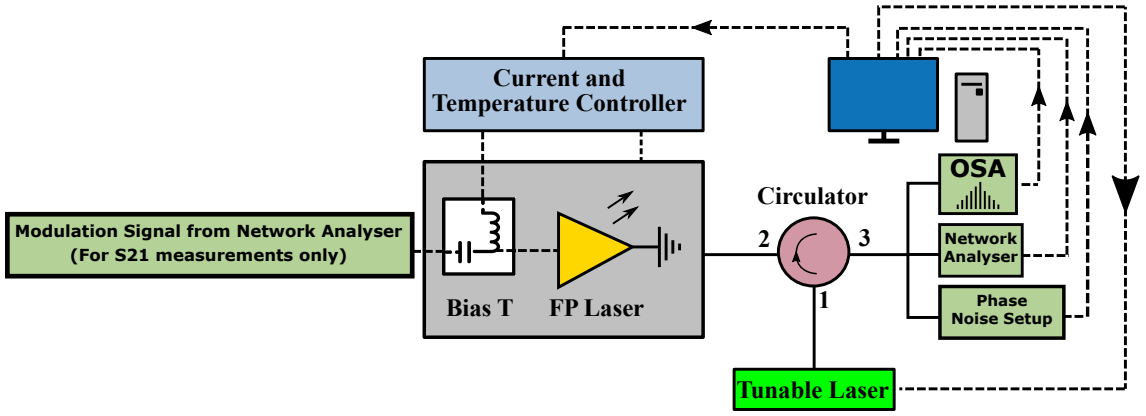


Figure 4.4: Experimental setup to obtain locking maps of SMSR, peak wavelength, peak power, peak resonance, modulation bandwidth, and linewidth for various detuning and injected power.

from Pure Photonics and shows a complete full C-band coverage with a narrow linewidth ($<$ 80 kHz).The master laser is encased in a module with a PM fiber pigtail and a barrel plug for +12V supply. The underlying technology is an External Cavity Laser design, with tunable filters embedded in the cavity for frequency control. The used master laser allowed communication through the RS-232 port. The emission wavelength of the master laser is varied from 1563.6 nm to 1564.4 nm in steps of 0.01 nm to vary the detuning frequency, $\Delta\omega_{inj}$. Also the emission power of the master laser is varied from -2 dBm to 13.5 dBm in steps of 0.5 dB to emulate injection ratio variation. In this study, the injected power into the slave laser is kept relatively high due to various reasons including -

- For OFC generation through gain switching, relatively high optical injection (typically $>$ -5 dBm) is required.
- The suitable output characteristics required for various applications are achieved at higher injection, the benefits of injection locking can be seen at lower injection power too but the enhancements are limited e.g., small locking range, low modulation response, relatively higher linewidth etc.
- Here the slave laser is a FP laser which suffer from high mode partition noise so relatively high injection is required for injection locking. DFB and DBR lasers can be injection locked at much lower output power to produce desired output characteristics.

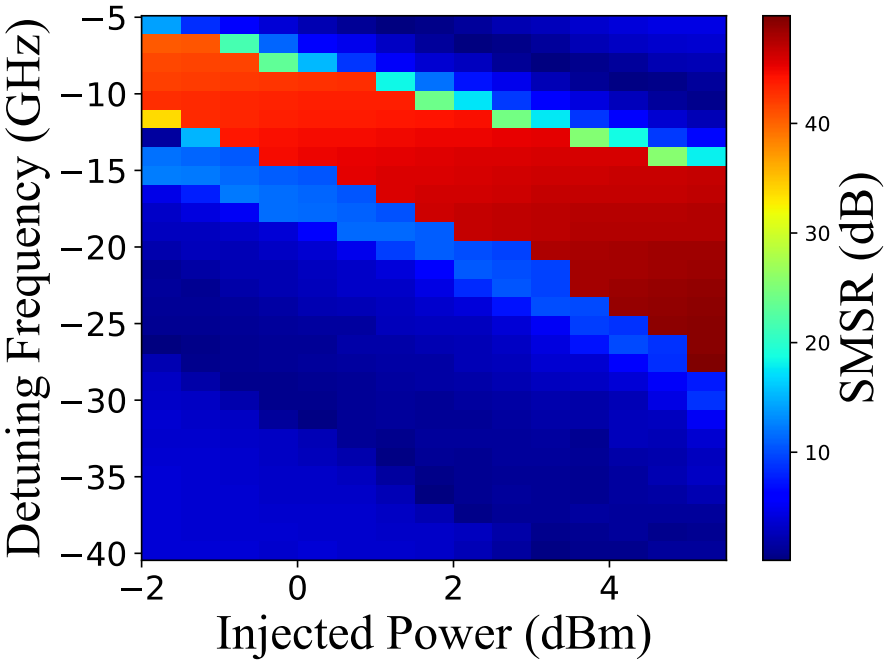
The output of the externally injected slave laser is then passed to an Optical Spectrum Analyser (Yokagawa, AQ6370), Network Analyser (Hewlett-Packard 8510C), and phase noise setup for spectral, modulation response and noise measurements, respectively.

4.3.2 Spectral Characterisation

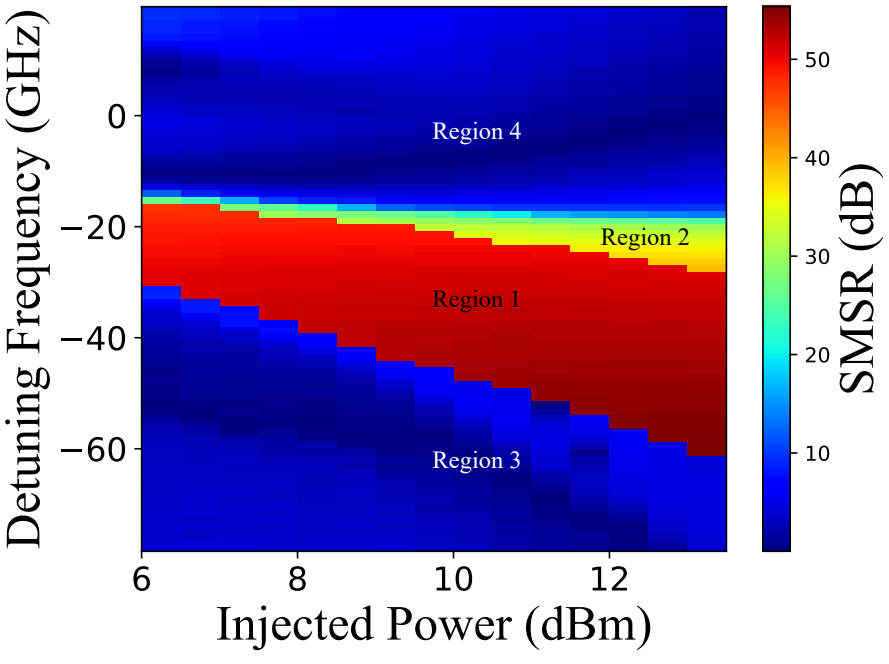
Figure 4.5, shows the SMSR map of the slave laser under external optical injection. The vertical axis shows the optical frequency detuning between master laser and free-running slave laser (1563.78 nm), and the horizontal axis denotes the wide range of injected master power in the cavity of slave laser. Figure 4.5(b), shows different operating regimes under external optical injection. Region-1 signifies the stable injection locking regime, which is the most important regime for all the major applications including direct and coherent communications. Region-2 denotes the chaotic regime. In this region the oscillation undergoes amplitude and frequency non-linear modulation, which leads to phenomenon like self-pulsation. Region-3, and Region-4 corresponds to the regime where four-wave mixing between internal and injected fields occurs in the laser cavity. These non-linear behaviour in Region-2,3 and 4 has been extensively studied by many authors [99–102]. In this work we mainly focus our attention on the stable injection locking regime (Region-1), which is the most important regime as in this region we see the enhancement in various slave laser output characteristics including bandwidth broadening and noise-reduction. In the rest of the chapter, injection locking regime will refer to the stable locking regime unless specified otherwise.

Figure 4.5(a), and (b) shows that in the injection locking regime, all the longitudinal modes of the FP cavity are suppressed except for the one under optical injection. Locking range is defined as the range of frequency of injected light from the master-laser at a given injected power into the the cavity of the slave-laser over which the slave-laser is injection locked with the injected light. This corresponds to a very good single mode performance with an SMSR in excess of 45 dB. In Figure 4.6, the observed locking range for different levels of injection power is plotted. From Figure 4.6, it can be deduced that the locking range can be continually increased with increased injected power. We have achieved a maximum 32.5 GHz of locking range at 13.5 dBm of optical injection.

Figure 4.7(a) and (b) shows the corresponding output peak wavelength maps under external optical injection. As discussed earlier, even though the FP cavity resonance condition



(a)



(b)

Figure 4.5: Locking map showing steady state SMSR for (a) low injected power, and (b) high injected power, for the mentioned detuning.

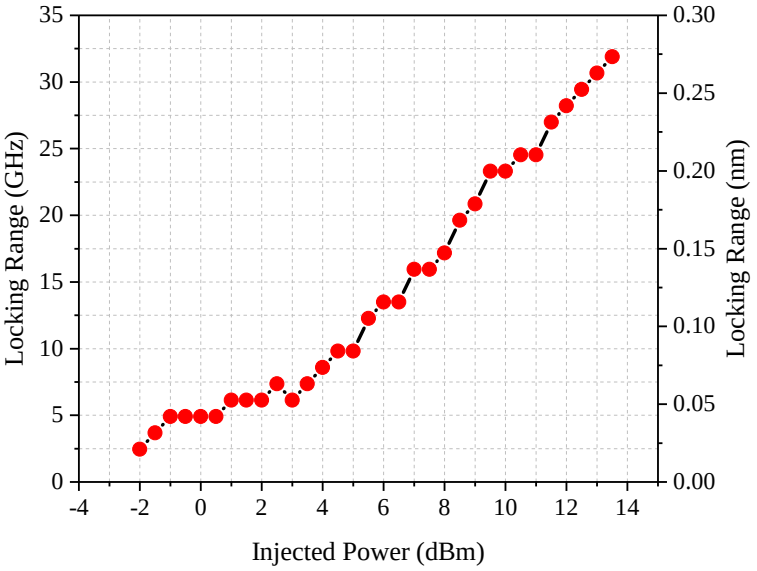
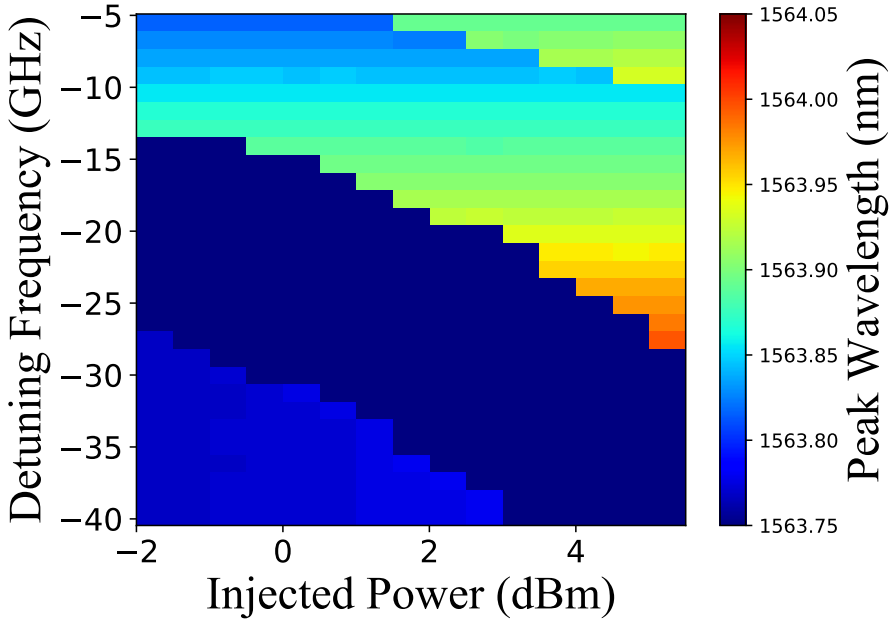
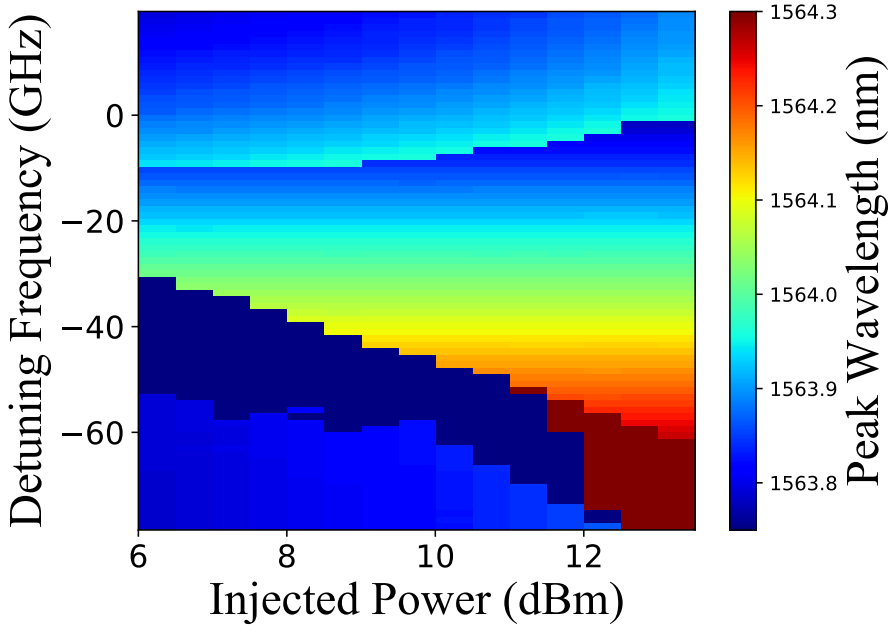


Figure 4.6: Locking Range of the slave laser vs injected power from master laser.

redshifts the slave laser's resonant cavity frequency under external optical injection, the output of the slave laser follows the master laser wavelength, once injection locked. It can be clearly seen in Figure 4.7(a), and (b), that the output wavelength from the slave laser follows the wavelength of the injected light in the region of injection locking. This is more clearly presented in the Figure 4.8. In Figure 4.8, the variation of the peak output wavelength of the slave laser under injection locking with varying injected wavelength at a constant injection power of 13.5 dBm is plotted. It can be clearly seen that the output wavelength of the slave laser follows the wavelength of the injected light under injection locking. The slight difference in the output wavelength and the injected wavelength is due to the discrepancy between set and actual wavelength of the tunable laser used as the master-laser for external injection. The observed variation difference between the set and actual wavelength of the tunable laser was $\sim$ 0.016 nm, which accounts for the variation between output and injected wavelength. Finally the corresponding maps for the peak power is presented in Figure 4.9(a), and (b). In a Fabry-Pérot spectrum, the power gets distributed among many longitudinal modes. However under injection locking, the single mode emission wins and captures most of the gain. As is clearly evident, the peak power significantly improves under injection locking.



(a)



(b)

Figure 4.7: Locking map showing steady state peak wavelength for (a) low injected power, and (b) high injected power, for the mentioned detuning.

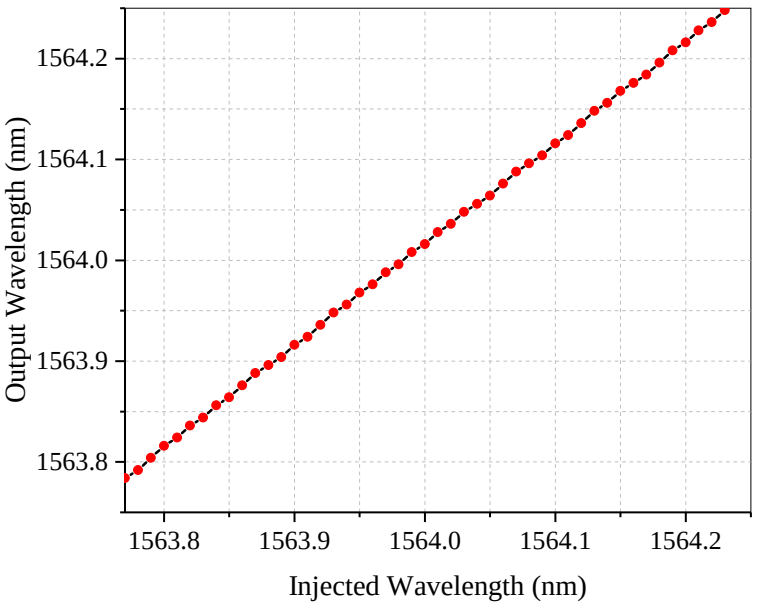
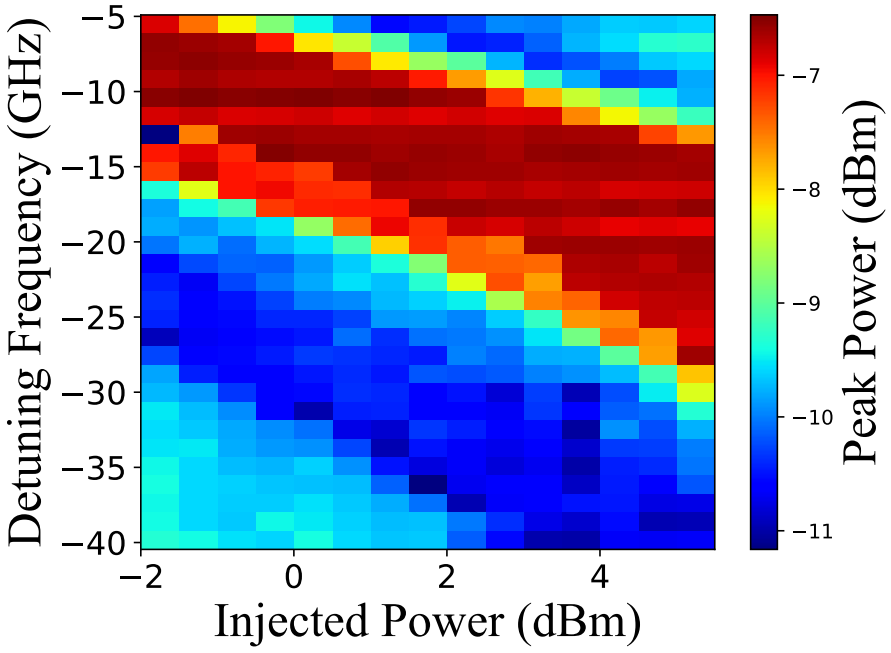


Figure 4.8: Variation of slave laser's output wavelength versus injected wavelength during injection locking at a constant injection power of 13.5 dBm.

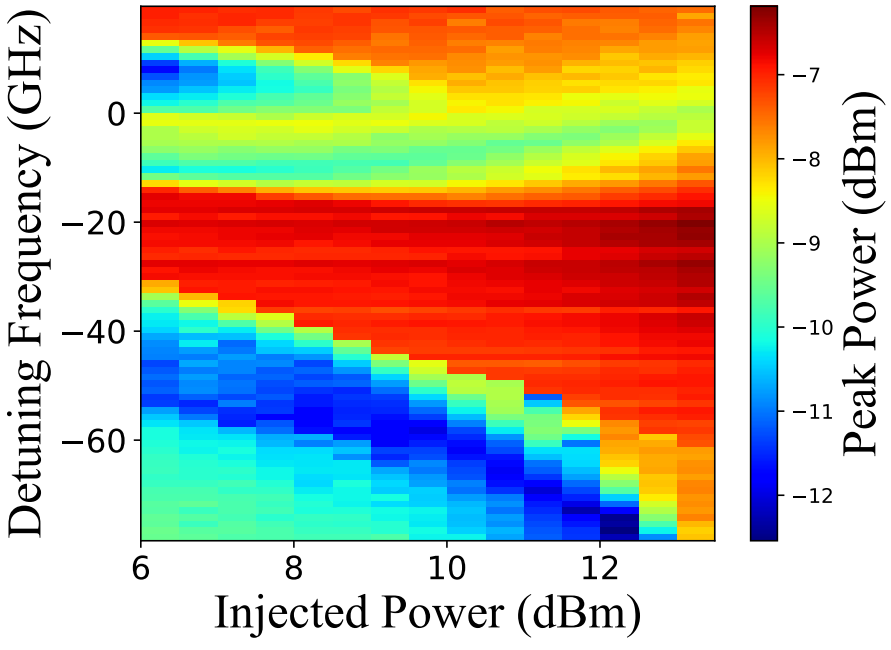
4.3.3 Enhancement of Resonance Peak and Modulation Response

When the slave laser is injection-locked, it emits all the power at the injected frequency, ω_{master}. However, since the carrier number are reduced below its threshold value due to external optical injection, the cavity resonance condition redshifts as given by the equation 4.6. As shown in Figure 4.7(a), and (b), once locked, the slave laser lases at ω_{master} and not at its cavity resonance condition, ω_{shift}. This frequency detuning between the cavity resonance condition, ω_{shift}, and the lasing wavelength, ω_{master}, influences the modulation response [103]. In [96], the author has shown that during the transient processes, the field corresponding to the cavity resonance condition is generated. This field then interferes with the injection locked field. Due to this interference, the output laser intensity exhibits a beat at the detuned frequency. Such transient field diminishes in the steady state, as all the optical gain is provided to the locked field. The resonance frequency (ω_{res}) produced by this interaction can be given by the difference between injected field frequency, ω_{master}, and the cavity resonance condition, ω_{shift}: $\omega_{res} = \omega_{master}$ - ω_{shift}. From Figure 4.3, and equation 4.6, this can be further written as:

$$\omega_{res} = \Delta\omega_{inj} - \frac{\alpha}{2} g_o \Delta N \tag{4.7}$$



(a)



(b)

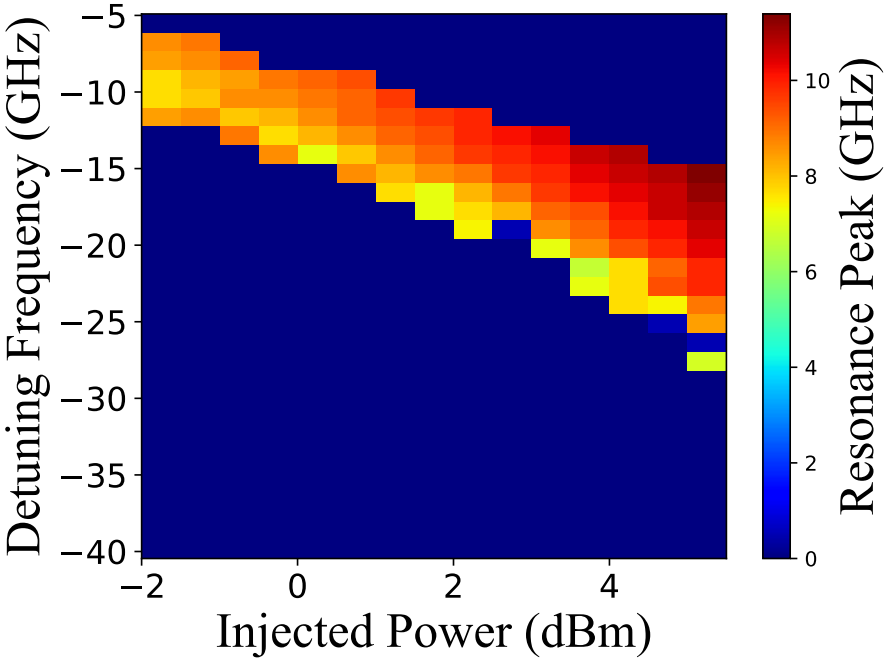
Figure 4.9: Locking map showing steady state peak power for (a) low injected power, and (b) high injected power, for the mentioned detuning.

Figure 4.10(a), and (b), shows the corresponding maps of resonance frequency of slave laser under optical injection. The resonance frequency is experimentally measured by locating the peak in the modulation response of the slave laser under optical injection. In figure 4.10(a), and (b), the resonance frequency is considered only in the locking range (Region-1). However, resonance peak will also exist outside locking range due to the interaction between ω_{master} and ω_{shift}, these interaction are not considered in this work. The maps show 2 profound variations:

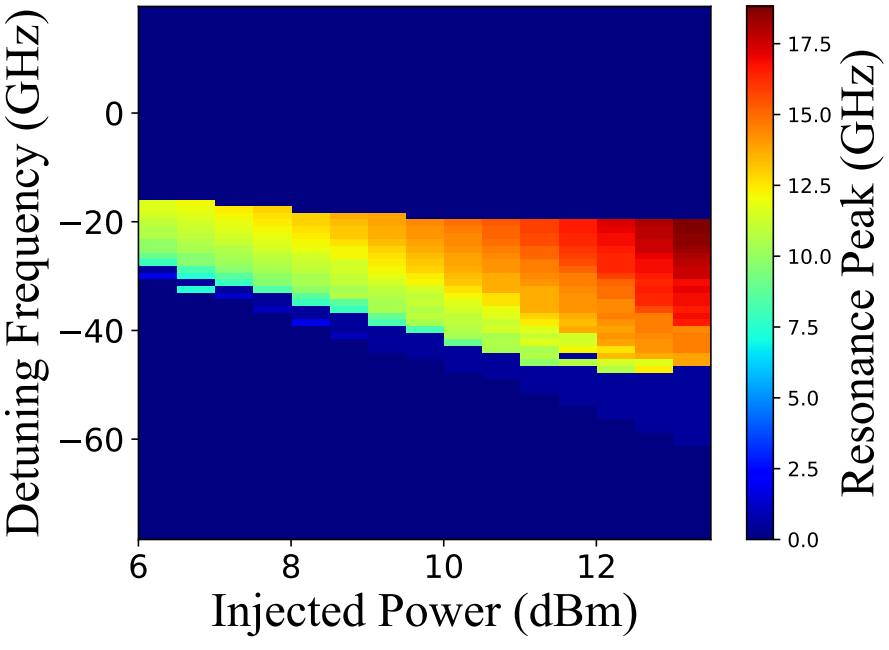
- **Frequency of resonance increases with injected power:** This variation can be easily understood from equation 4.7. For a given detuning, as the injected power in the slave laser cavity increases, the carrier number decreases. This reduction in carrier number further redshifts the cavity mode, ω_{shift}, as given by equation 4.6. This increases the detuning between the injected frequency, ω_{master} and the cavity mode, ω_{shift} and results in the increment of the resonance frequency, ω_{res}.

- **Frequency of resonance increases (decreases) with positive (negative) detuning:** For increasingly negative detuning frequencies, the master laser frequency approaches the cavity mode (see Figure 4.3) and the resonance frequency enhancement decreases. However, for positive detunings, the master moves in the opposite direction of the cavity mode migration, creating larger resonance frequency enhancements, with the largest enhancement occurring at the positive edge of the locking range.

The 3 dB modulation bandwidth of the slave shows a similar pattern as the resonance frequency and the corresponding maps of the slave laser's 3 dB modulation bandwidth under external optical injection is presented in Figure 4.11(a), and (b). One important point to notice here is that we enhanced the modulation bandwidth of the slave laser for the given injection parameters from it's intrinsic value of $\sim$ 6 GHz to $\sim$ 22 GHz. This large improvement in the modulation response of the slave laser is the direct consequence of external optical injection.

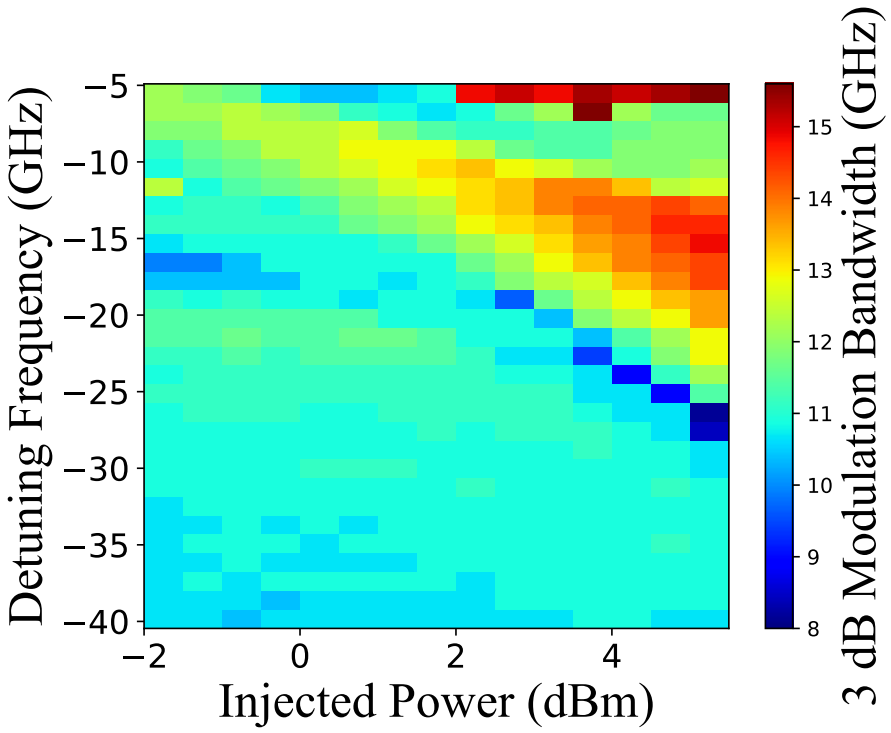


(a)

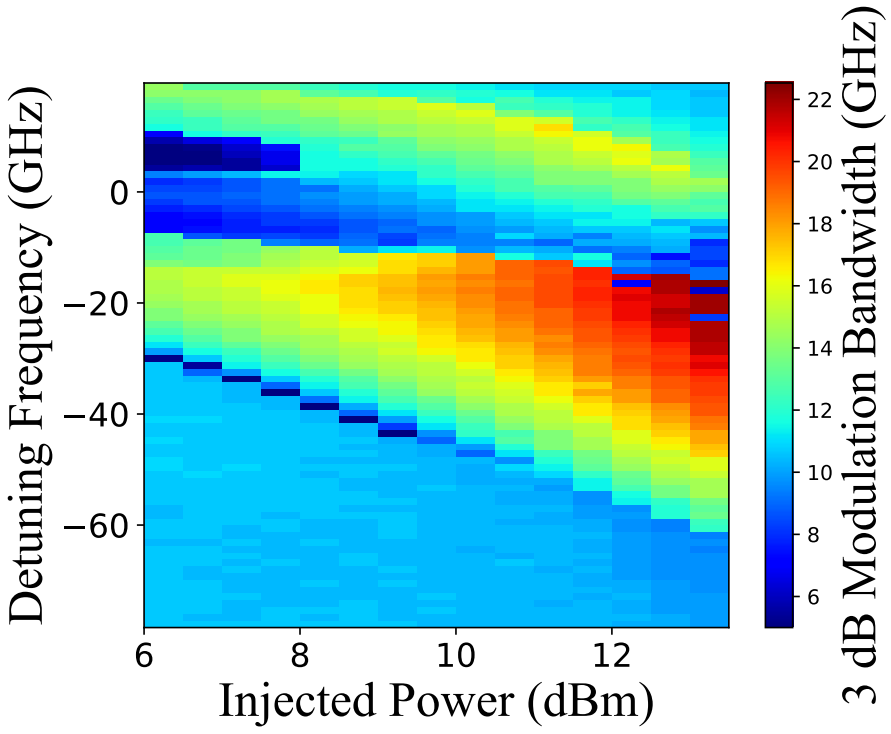


(b)

Figure 4.10: Locking map showing the resonance peak for (a) low injected power, and (b) high injected power, for the mentioned detuning.



(a)



(b)

Figure 4.11: Locking map showing 3 dB modulation bandwidth for (a) low injected power, and (b) high injected power, for the mentioned detuning.

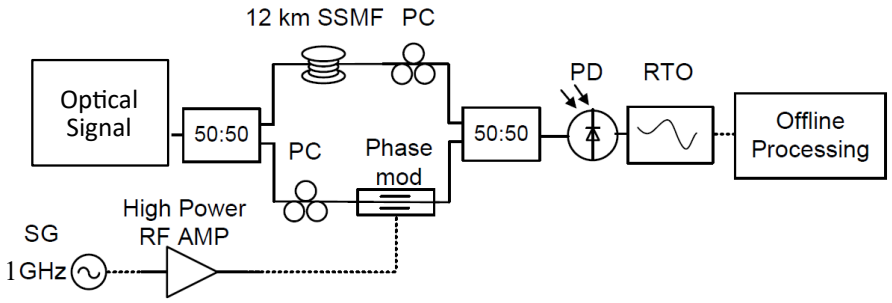


Figure 4.12: Experimental set up for phase noise measurements using the modified delay selfheterodyne detection method. SSMF: standard single mode fiber; PC: polarization controller; SG: signal generator; RF AMP: RF amplifier; Phase mod: phase modulator; PD: photodiode, RTO: real time oscilloscope.

4.3.4 Noise Reduction

The phase noise of a semiconductor laser diode is an important parameter in coherent communication systems and in the systems employing high order optical modulation formats. For these high speed modulation formats, the phase noise of the light must be low. Due to optical signals undergoing dispersion within a fiber, a narrow linewidth is desirable to minimise this effect. In this work, the noise in the optical signal is characterised by measuring the Frequency-Modulated (FM) - noise spectrum, discussed in detail in section 2.9.5, which fully describes the noise processes contributing to the overall phase noise [75, 77]. The optical linewidth is then calculated through the flat white noise component of the FM-noise spectrum.

The experimental characterisation of the FM-noise spectrum is performed via a phase noise measurement method previously developed [75], whose set up is presented in Figure 4.12. The technique used here to measure the phase noise of the optical signal is based on the technique presented in [75], and is known as modified delayed self heterodyne. The optical signal to be measured is split into two equal parts using a 50:50 coupler. One of the part is de-correlated to the original/other signal by delaying it using a 12 km of standard single mode fiber (SSMF). The other part is phase modulated, using a phase modulator driven by a high power 1 GHz signal to achieve second order harmonics. The light from both the arms are then recombined using another 50:50 coupler. The recombined signal is then passed to the photodetector. The detected heterodyne signal will present copies of the doubled-linewidth at 1 GHz harmonics, which are captured with a real time oscilloscope. The differential phase

information is then recovered offline by following the procedure explained in section 2.9.5. Phase noise can be quantified by the Power Spectral Density (PSD) of the differential phase, $S_{\Delta\phi_n}(f)$, having units of rad^2/Hz. Phase noise is directly related to the frequency noise, as the instantaneous frequency, f_{ins}, is basically the time derivative of the phase, $\phi_n(t)$:

$$f_{ins} = \frac{1}{2\pi}\frac{d\phi_n(t)}{dt} \tag{4.8}$$

The PSD of the instantaneous noise frequency, $S_F(f)$, can be found from the PSD of differential phase, $S_{\Delta\phi_n}(f)$, using equation 4.9 [104]:

$$S_F(f) = \left(\frac{f}{2sin(\pi fT)}\right)^2 S_{\Delta\phi_n}(f) \tag{4.9}$$

here, T is the time delay in the 12 km of SSMF. The unit of the PSD of the instantaneous frequency noise, as can be seen in equation 4.9, is Hz^2/Hz. Now, for a white FM-noise, the single-sided PSD of the noise frequency can be written as:

$$S_F(f) = \frac{\delta f}{\pi} = S_0 \tag{4.10}$$

This leads to a double-sided field spectrum, $S(f)$, having the Lorentzian shape [104]:

$$S(f) = \frac{\delta f}{2\pi\left[f^2 + \frac{\delta f}{2}^2\right]} \tag{4.11}$$

Thus δf in equation 4.10 represents the full width at half maximum (FWHM) of the field spectrum (optical spectra). Hence the linewidth can be extracted from the flat portion of the FM-noise spectrum (PSD of instantaneous noise frequency). In our measurement, the linewidth extracted from the FM-noise spectra plot is given by - FWHM $= \frac{\pi}{2} S_0$. The factor of 2 is added since the local oscillator light output and the signal are equally noisy.

Figure 4.13(a), shows the FM-noise spectrum of the slave laser which appears to be completely flat because its resonance peak lies far outside the observed frequency range. The measured linewidth from the flat white FM-noise component of the slave laser is of the order

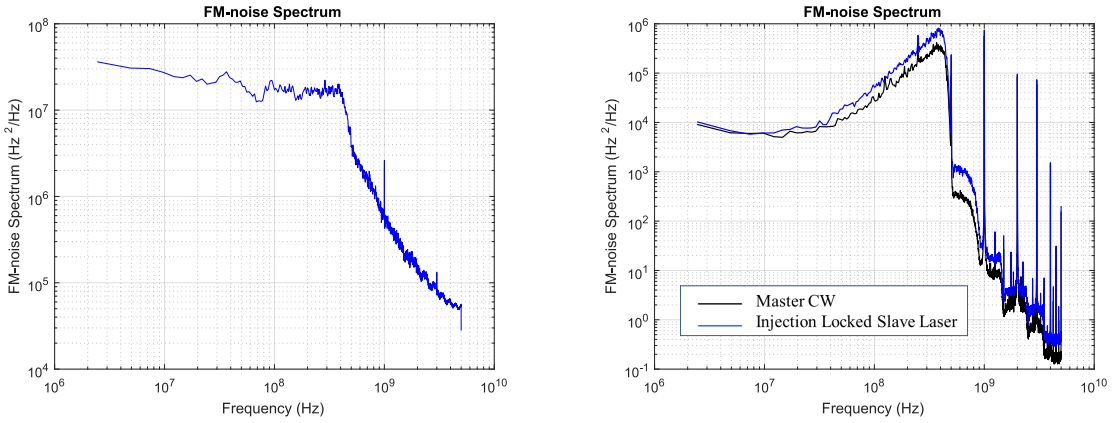


Figure 4.13: Measured FM-noise spectrum of (a) Free running slave laser, and (b) master laser, and injection locked slave laser.

of tens of megahertz. Such a large linewidth makes the usability of higher modulation format challenging if not completely redundant and the dispersion in fiber reduces the reach. Optical injection has been studied over years, and has shown to improve the noise characteristics of the injected laser [97, 98]. Injection from a highly spectral purity master under optimised injection conditions can lead to the generation of highly coherent output, equivalent to the master laser itself. Figure 4.13(b), shows the FM-noise spectrum of the master laser (black). The measured linewidth from the flat white FM-noise component is $\sim$ 20 kHz. Figure 4.13(b), also shows the FM-noise spectrum of the slave laser under external optical injection, with master laser operating at a detuning of -20.8 GHz and the injected power was 7 dBm. As expected, the external optical injection resulted into a superior performance in terms of noise. The FM-noise spectrum of the injected slave laser is equivalent to the master laser with a measured linewidth of $\sim$ 20 kHz.

Figure 4.14(a), plots the SMSR map of the externally injected slave laser, showing the stable locking regime in red (SMSR $>$ 40 dB). Figure 4.14(b), plots the corresponding linewidth map of the slave laser under external injection for the given detuning and injected power. As evident from the linewidth map, a linewidth of less than 60 kHz is obtained for all the points in the locking range. Also, as predicted in [98], for a given detuning, the laser linewidth continuously improves with the increased injected power. Also, the laser linewidth seems to improve with negative detuning as predicted in [98].

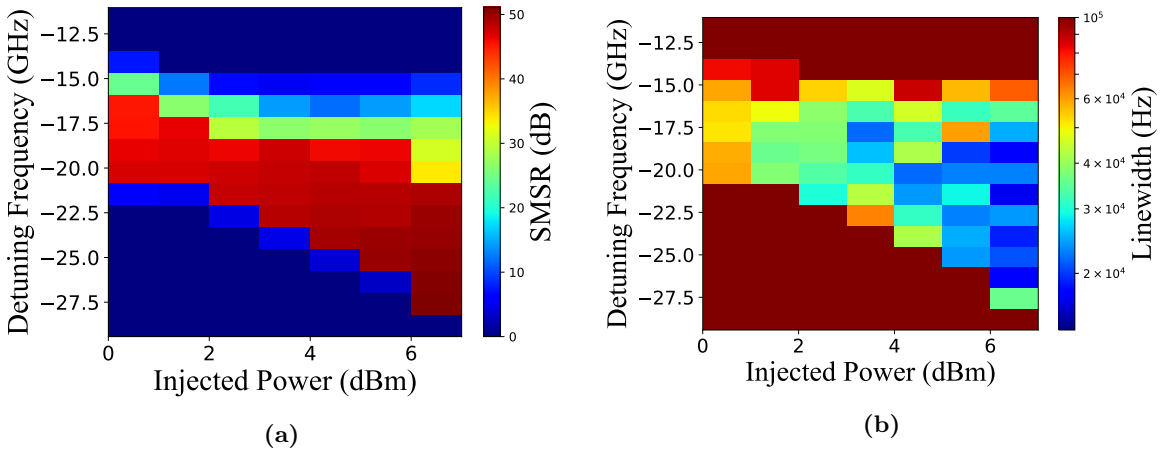


Figure 4.14: Locking map for various detuning and injection ratio, showing steady state (a) SMSR, and (b) linewidth.

4.4 Gain Switched Optical Frequency Comb

4.4.1 Experimental Set Up and Device Characterisation

The schematic diagram of the experimental set-up used to generate the gain switched optical frequency comb (GS OFC) is presented in Figure 4.15. The slave laser used is a commercially sourced Fabry-Perot laser (FP) from Fraunhofer Heinrich Hertz Institute. The sourced device is packaged in an optically un-isolated and temperature controlled high-speed butterfly package. The P-contact of the laser diode is wire-bonded to the RF connector through an internal 47 Ω sheet resistor for proper impedance matching. The RF connection to the laser was designed to provide low loss flat frequency response up to 40 GHz. The packaged device contains a 10 kΩ thermistor and a thermoelectric cooler (TEC) for sensing, controlling and stabilising the laser diode temperature. The optical light from the FP laser is collected using a polarisation maintaining (PM) fiber.

As shown in Figure 4.16(a), the FP laser exhibited a threshold current of ∼ 10 mA at 20 ^{o}C. The output emission of the FP laser is in C and L band with the emission peak around 1572.5 nm when biased at 50 mA at 20 ^{o}C, as shown in Figure 4.16(b). The small signal modulation response of the FP laser at 20, 40 and 60 mA of injection current is recorded in Figure 4.16(c). We observed a relaxation oscillation frequency of 5, 9, 10 GHz at 20, 40, and 60 mA of bias current respectively. The observed small signal 3-dB modulation bandwidth at 60 mA of injection current is ∼ 13 GHz.

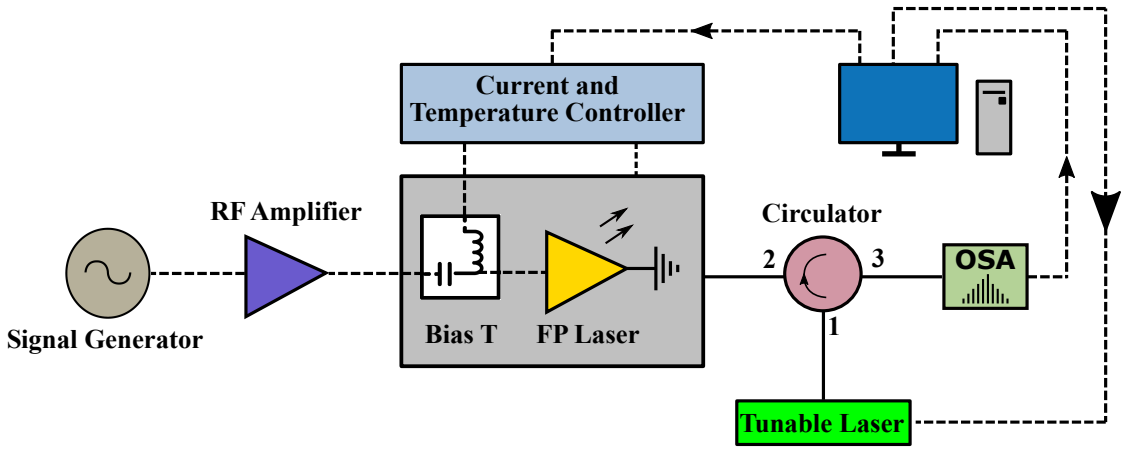


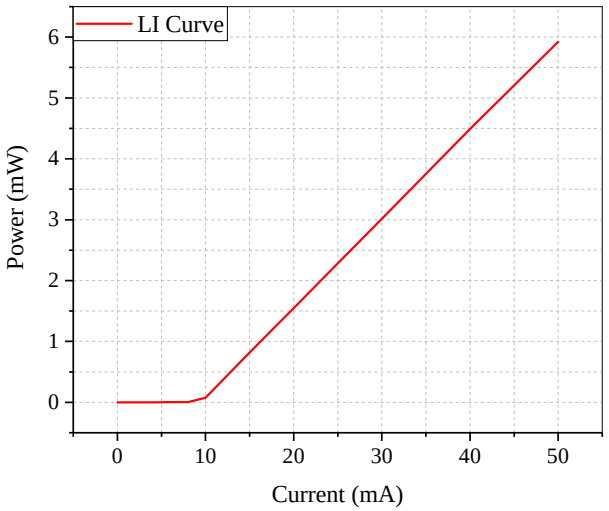
Figure 4.15: Schematic diagram of the experimental set-up used to generate Gain-Switched Optical Frequency Comb (GS-OFC).

The low linewidth tunable laser used in the previous section is used here as well as a master laser to provide external injection through a PM circulator. The effect of optical injection on the output characteristics of the slave laser is already characterised in detail and presented in the previous sections. Figure 4.17 shows the optical spectrum of the master laser at the specified wavelengths showing a full C-band coverage.

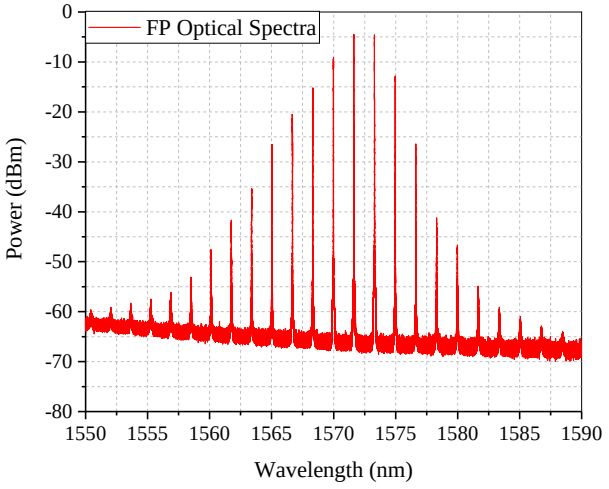
An external Bias T with a bandwidth of 26 GHz, is used to provide the DC bias and the gain switching signal to the slave laser as shown in Figure 4.15. Thorlabs LDC205C laser diode controller is used to provide the DC bias to the slave laser. Gain switching is achieved by applying an amplified RF sinusoidal signal ($\sim$ 24 dBm) to the high speed SMA connector of the Bias T. The RF sinusoidal signal was generated by the Rhode and Schwarz SMR40 signal generator and amplified by HP 83020A RF amplifier which has bandwidth ranging from 2 GHz to 26.5 GHz. The output optical signal of the injected and gain-switched FP laser is then transferred to a very high resolution (20 MHz/0.16 pm) optical spectrum analyser, Apex Technologies AP2083A, for spectral measurements.

4.4.2 Generation of GS-OFC without External Optical Injection

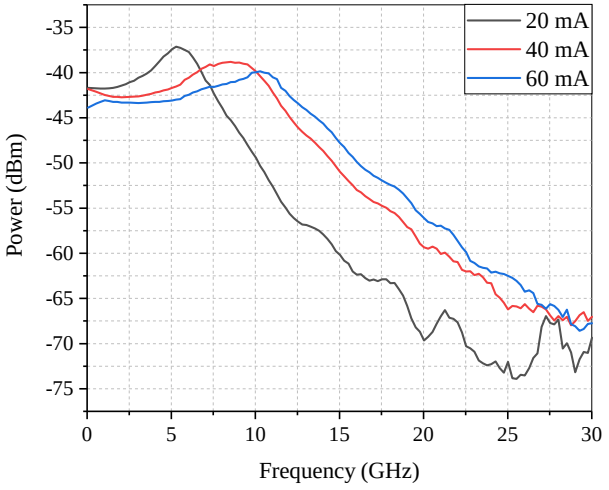
Figure 4.18(a) shows the optical spectrum of the gain switched FP laser without external injection, gain-switched at 12.5 GHz. As expected, due to lack of any mode selectivity, all the longitudinal modes of the FP laser are present in the optical output. The application of a large sinusoidal signal ($\sim$ 24 dBm) resulted in the generation of optical frequency comb



(a)



(b)



(c)

Figure 4.16: FP laser CW characterisation at 20 ^{o}C: (a) LI curve, (b) Optical spectrum at 50 mA, and (c) small-signal modulation response at 20, 40 and 60 mA.

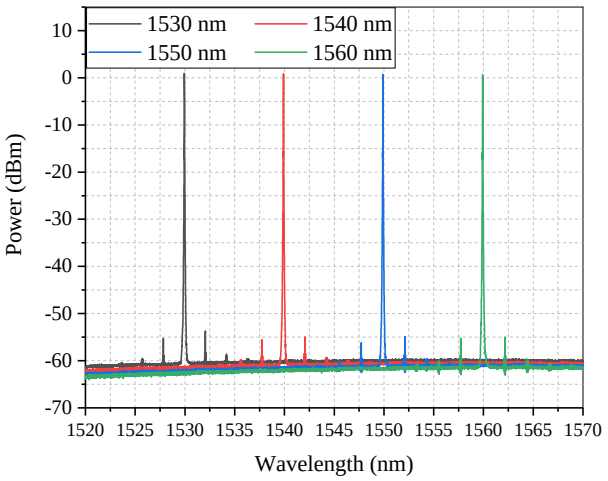


Figure 4.17: Optical Spectrum of the Tunable laser used as master for optical injection, at 1530, 1540, 1550, and 1560 nm.

at some modes (modes with higher power) and broadening of the other modes (modes with lower power). Due to lack of optical injection or stabilisation the optical output still carries a high mode-partition noise of the FP laser along with the large temporal jitter and chirp across the generated pulse associated with the gain switching technique. As shown in Figure 4.18(a), the OFC generated at the dominating longitudinal modes of the FP cavity showed very poor flatness and a carrier to noise ratio of < 30 dB was observed for all the modes, which is below the acceptable value. Figure 4.18(b) focuses on the extreme modes of the optical output of Figure 4.18(a), further away from the gain peak of the FP laser. In contrast to the dominating modes, gain switching of the extreme modes resulted in a significantly broadened spectrum with no discernible comb tones. All these factors make such system practically inefficient/useless for all the applications including WDM and all optical OFDM.

4.4.3 Generation of GS-OFC with External Optical Injection

The challenges mentioned above can be mitigated by employing optical injection. Optical injection has been earlier shown to suppress the mode partition noise [95] to provide single mode performance with high SMSR [91, 94] and enhanced modulation bandwidth [91, 94, 105, 106].

Figure 4.19 illustrates the mode-selectivity obtained through optimised optical injection. By applying an optical injection through the master laser into the cavity of the FP laser at 1564.6 nm, a single mode performance with a SMSR > 60 dB is obtained. Application

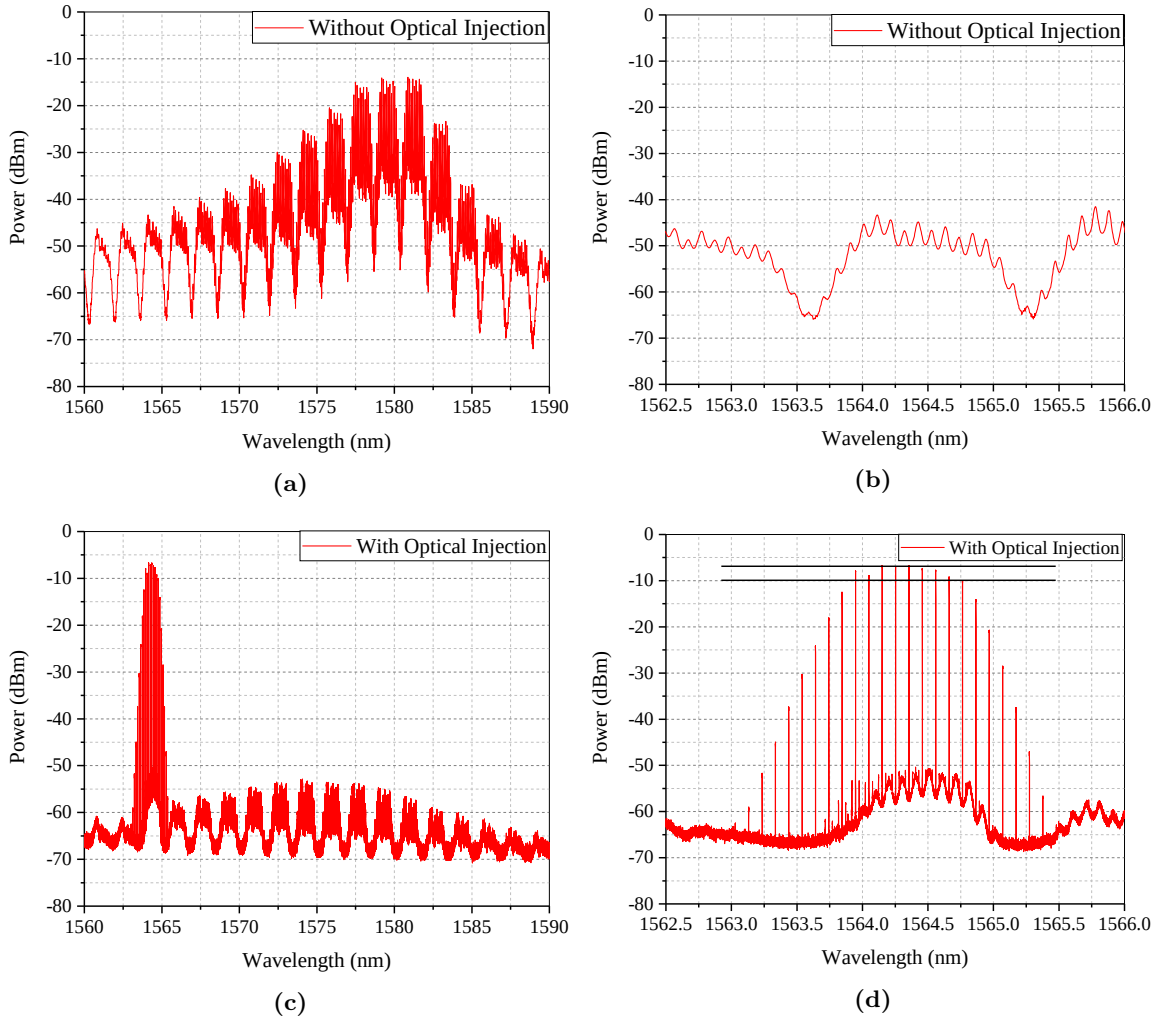


Figure 4.18: Optical spectra of gain switched optical frequency comb at a gain switching frequency of 12.5 GHz: (a) without external injection, (b) without external injection, focussing on the non-dominating mode of the FP laser, (c) with optical injection, showing the excellent mode selectivity, and (d) with optical injection, focussing on the generated optical frequency comb with 9 lines in the 3 dB bandwidth.

of gain switching signal at 12.5 GHz to the slave laser at these operating points resulted in the generation of highly coherent frequency combs as shown in Figure 4.18(c) and 4.18(d). The generated OFC showed very good flatness with a full width at half the maximum of around 0.8 nm, having 9 comb tones in the top 3 dB window, with a free spectral range of 12.5 GHz. An SMSR and carrier to noise ratio (CNR) of more than 40 dB is achieved. This indicates excellent pulse-to-pulse phase stability, phase co-relation of the emitted pulses, and reduction in the linewidth considerably. Each of these generated frequencies can be treated as an independent channel for data transmission, which removes the requirement of separate transmitters for each channel. These generated channels can then be separated using an

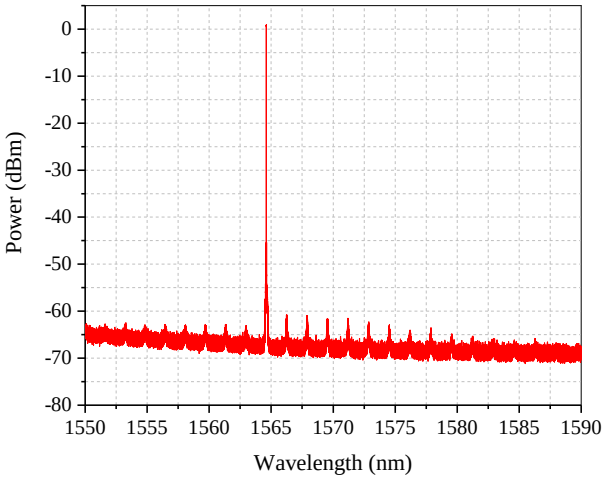


Figure 4.19: Injection locked master-slave laser, showing excellent mode selectivity with an SMSR of > 60 dB.

optical demultiplexer. This reduces the cost of implementing a multicarrier transmitter in an access network substantially.

4.4.4 FSR Tunability

One of the major advantages of GS-OFCS apart from its simplicity, cost-efficiency, and stability, is its ability to achieve FSR tunability only restricted by the device's modulation response which can be significantly enhanced by optical injection. Since, in a GS-OFCS, the frequency spacing between adjacent comb tones is set by the frequency of the applied gain-switching signal, precise and flexible FSR can be easily achieved.

Figure 4.20 reports the generated GS-OFCS with FSR ranging from 6.25 to 25 GHz. This flexibility in the FSR is achieved by simply changing the frequency of the applied gain switching signal. Gain switching at these frequencies resulted in the generation of the OFC with 2-17 clearly discernible and phase correlated comb tones in the 3 dB bandwidth. A carrier to noise ratio of > 40 dB is observed for all the generated OFCs. These results are obtained under the application of external injection from the master laser at 1564.05 nm. The intensity of applied optical injection was varied from 6 to 13.5 dBm to keep the frequency of relaxation oscillation close to the required FSR value, this resulted in the generation of an optimised comb with low temporal jitter [107].

In Figure 4.21(a), the variation of the number of comb tones generated in the 3 dB bandwidth against the free spectral range (FSR) is plotted. Due to the applied large amplitude

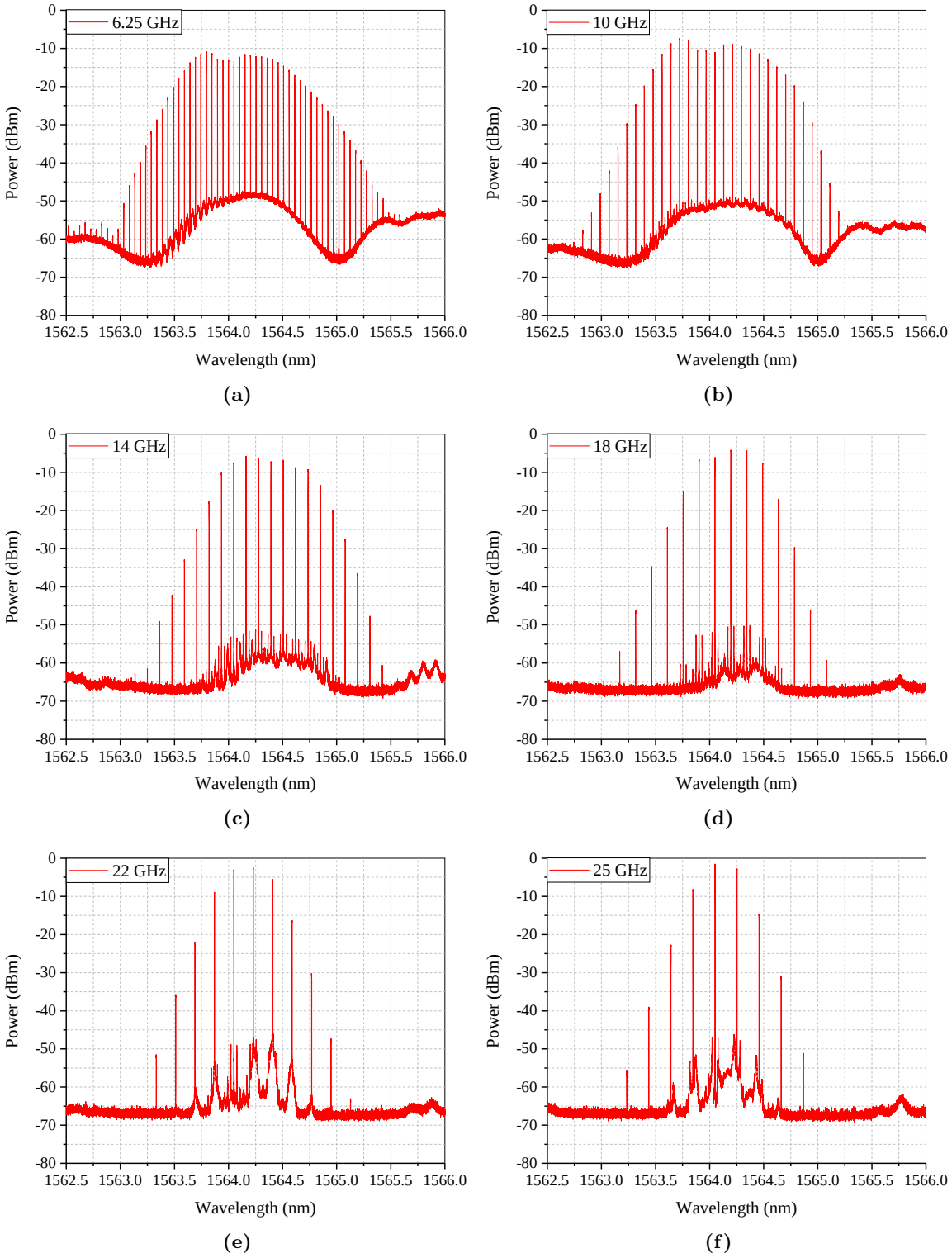


Figure 4.20: Optical spectra of the GS-OFCS generated with different FSRs: (a) 6.25 GHz, (b) 10 GHz, (c) 14 GHz, (d) 18 GHz, (e) 22 GHz, and (f) 25 GHz. OSA resolution is 0.16 pm.

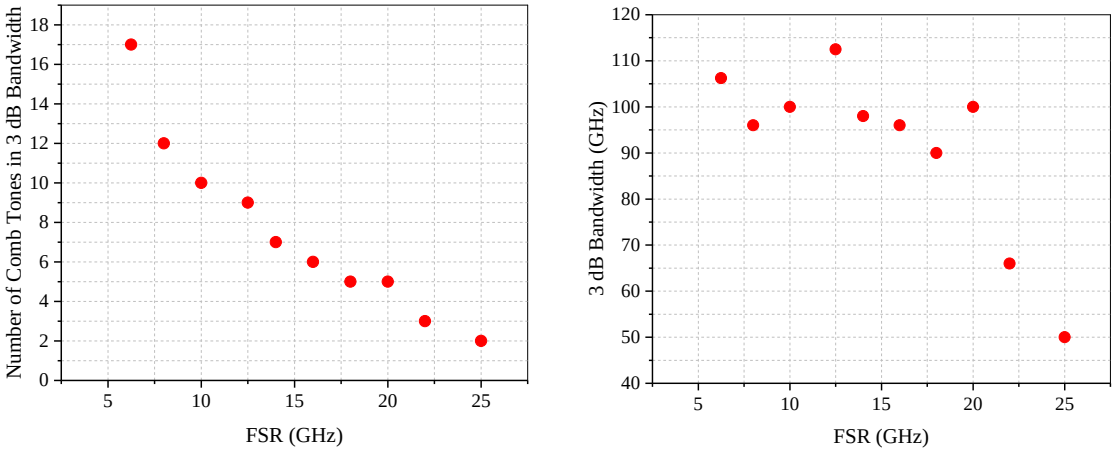


Figure 4.21: Variation of (a) number of comb tones in the 3 dB bandwidth, and (b) 3 dB bandwidth versus free spectral range (FSR).

gain switching signal to the slave laser, the carrier concentration experiences large variation which causes variation in the refractive index of the active region. This variation in the refractive index translates into the change in output instantaneous wavelength and the output laser spectrum is chirped. This chirp is given by equation 4.12 [67].

$$\Delta v(t) = \frac{\alpha}{4\pi}\left[\Gamma g_o(N - N_t) - \frac{1}{\tau_{ph}}\right] \tag{4.12}$$

here, $\Delta v(t)$ is the frequency chirp, Γ is the confinement factor, N - N_t is the swing in the carrier concentration, g_o is the differential gain and τ_{ph} is the photon lifetime. The bandwidth of the generated OFC is directly related to the frequency chirp caused by the large amplitude modulation of the slave laser. Hence, the bandwidth of the generated OFC is constant. In Figure 4.21(b), the variation of the 3 dB bandwidth of the generated OFC against the free spectral range (FSR) is plotted. As illustrated in Figure 4.21(b), the 3 dB bandwidth of the generated OFC remains in the range of 100 $\pm$ 10 GHz upto 20 GHz. Since the overall bandwidth of the generated OFC is fixed, the number of comb tones in the 3 dB bandwidth decreases as the FSR increases, as illustrated in Figure 4.21(a). The sudden reduction in the bandwidth of the generated OFC post 20 GHz comes from the limited modulation bandwidth of the slave laser. Degraded modulation response of the slave laser at FSR $>$ 20 GHz, results in the reduced swing in the carrier concentration, which in turn reduces the frequency chirp. Hence a reduced modulation response results in reduced bandwidth, lesser number of comb

tones and poorer flatness.

4.4.5 Wavelength Tunability

As shown in Figure 4.19, precise injection into a particular FP mode results into a single mode with an SMSR in excess of 60 dB. So by carefully injecting into different FP modes which are separated by 1.66 nm (see Figure 4.16(b)), a single mode operation on all the longitudinal modes of the FP laser can be achieved. Gain-switching at these operating points results in the generation of highly coherent optical frequency combs. In Figure 4.22(a), the overlapped spectra of these generated OFCs under a 20 GHz applied gain-switching signal is plotted, showing a quasi continuous wavelength tuning from 1552 nm to 1583 nm, covering 31 nm. By carefully designing the FP laser, this wavelength span can be moved to the C-band or any other band of interest. The generated OFCs on all the modes consists of 5 clearly resolved comb tones separated by 20 GHz, one such OFC is shown in Figure 4.22(b). Furthermore, finer wavelength tunability can be achieved by temperature tuning the slave laser and then carefully injecting into the desired FP mode as shown in [108].

4.4.6 Phase Noise

The experimental characterisation of the FM-noise spectrum is performed using a phase noise method developed in [75]. The experimental setup is the similar to as presented in Figure 4.12. In this case, the optical signal (GS-OFC) is first passed to a narrow optical band

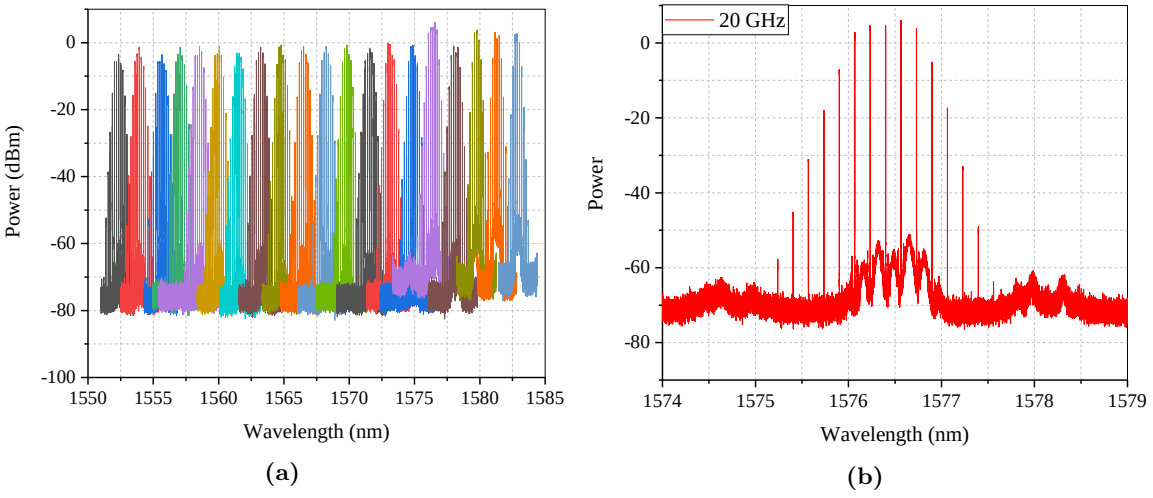


Figure 4.22: Optical spectra of: (a) overlapped GS-OFCs with an FSR = 20 GHz covering wavelength range from 1552 nm to 1583 nm, and (b) GS-OFC with an FSR = 20 GHz with a central wavelength around 1576.5 nm having 5 lines in the 3 dB bandwidth.

pass filter (OBPF) that selects the individual comb line. Here, we have used Yenista Optics XTM-50 tunable filter with adjustable bandwidth. The OBPF used operates in the 1450 to 1650 nm wavelength range with a minimum bandwidth of 6.25 GHz and an insertion loss of 5 dB. The filtered comb line is then passed through an erbium doped fiber amplifier in order to compensate for the losses in the OBPF. We have used IPG Laser Fiber Amplifier (Model-20-C-30) for amplification. It has an optical bandwidth of 1533-1567nm with a gain of 20 dB and a noise figure of < 5 dB. The saturation output power is ~ 30 dBm. The EDFA was set to amplify the input light to 3 dBm. The amplified optical signal was then passed to the modified-DSH setup for phase noise characterisation.

Figure 4.23(a), shows the generated GS-OFC under external injection with an FSR of 10 GHz, for phase noise analysis. The phase noise measurement is carried on the marked comb lines in Figure 4.23(a). These measurements are then compared with the phase noise characteristic of the master laser at those specific wavelengths. As shown in Figure 4.24(a), the FM-noise spectrum of the master laser is dominated by the flat white FM-noise component which corresponds to a linewidth value of 20 kHz.

The filtered comb lines at each wavelength have similar FM-noise spectrum as the master at lower frequencies, as shown in Figure 4.24(a). The slight increment in the phase noise of the comb lines at lower frequency can be attributed to the noise introduced in the optical signal by the EDFA. The corresponding linewidth for all the filtered comb tones is observed

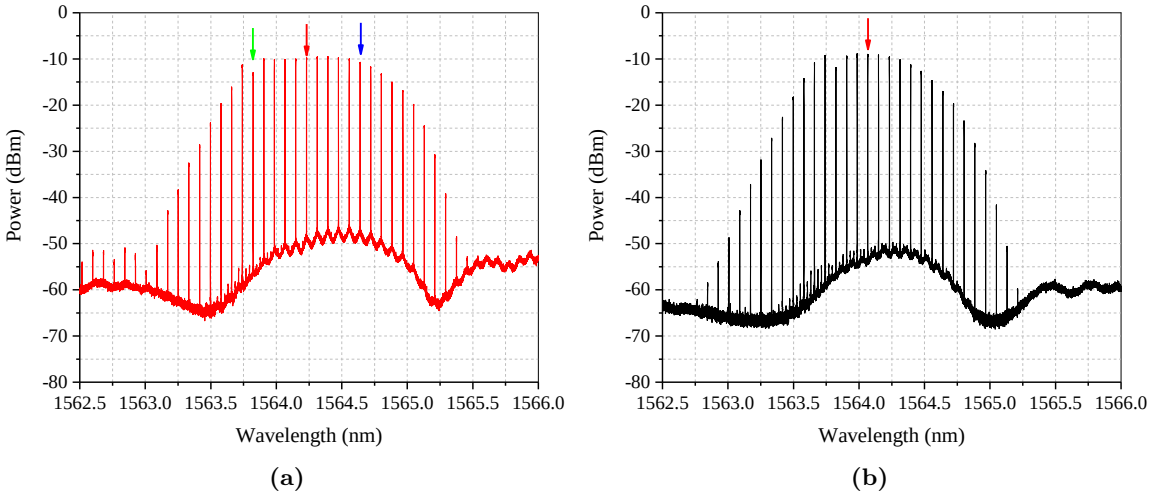


Figure 4.23: Optical spectra of GS-OFC with external optical injection optimised for (a) flatness, and (b) low noise.

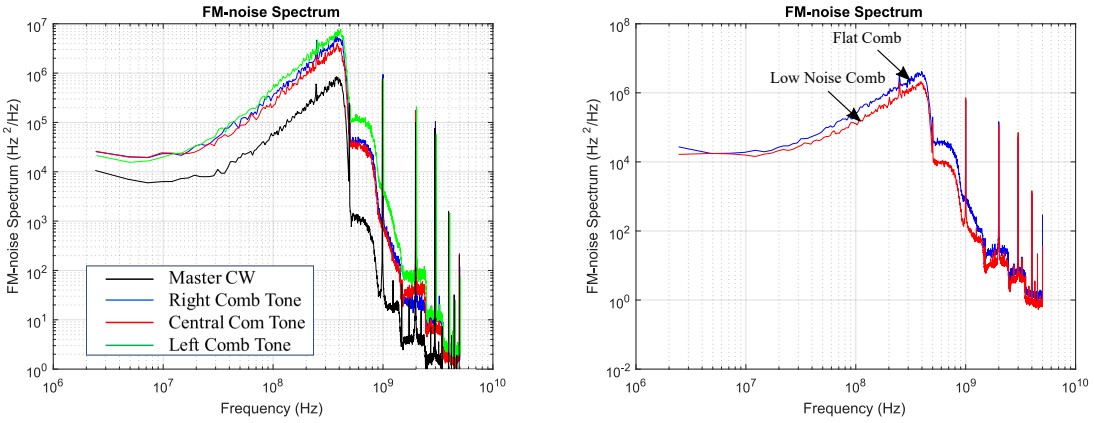


Figure 4.24: Measured FM-noise spectrum for (a) master laser and the 3 comb tones marked in Figure 4.23 (a), and (b) comparison of the phase of the cenral comb tone of the 2 combs shown in Figure 4.23 (marked with red arrow).

to be $\sim$ 40 kHz. At high frequencies the phase noise of the filtered comb lines presents an acceptable deviation from the master laser. This deviation was studied in [77] and is a consequence of residual phase noise from the slave laser, which depends on the injection parameters used (injected power and wavelength detuning). As pointed out earlier and illustrated in Figure 4.11, and 4.14(b), with negative (positive) detuning, the modulation response decreases (increases), and linewidth also decreases (increases). Hence, the noise in the optical comb lines can be further improved by negatively detuning the master - slave laser. But this leads to a reduced modulation response which reduces the overall flatness and 3 dB bandwidth of the comb. So there exist a trade-off between phase-noise at higher frequencies and overall flatness of the comb and the injection parameters should be chosen wisely according to the application at hand.

Figure 4.23(b), shows a generated GS-OFC under external injection and with an FSR of 10 GHz. The slave laser was negatively detuned (by increasing the operating temperature of slave) relative to master. As pointed out earlier, this resulted in a reduced modulation response and hence, a relatively narrower and less flatter comb compared to the one in Figure 4.23(a). Figure 4.24(b), compares the phase noise of the central comb lines (marked by red arrow in Figure 4.23(a), and (b)) in these two cases. The 2 filtered comb lines have an almost identical FM-noise spectrum at lower frequencies. The comb line with increased negative detuning shows lower phase noise at higher frequencies as expected from the discussion earlier and as pointed out in [77].

From the results presented in Figures 4.23 (a), and (b), the deviation in the FM-noise spectrum is acceptable hence suggesting optimum injection parameters for the generated GS-OFC. These results indicate that the comb tones would impose small penalties (compared to the master) when being employed in a coherent communication system [77].

4.5 Conclusion

Networks incorporating flexible channel spacing to maximise the spectral efficiency by adapting to the demand of the network are gaining a lot of attention recently. Implementation of such networks calls for specialised transmitters capable of generating number of carriers, with high flatness, flexible channel-spacing, wavelength tunability, high SMSR, low-noise and cost and power efficiency. Currently in WDM PON, transmitters based on either a bank of independent lasers or a bank of externally injected Fabry-Pérot laser diodes are used. Such systems require a dedicated temperature control for wavelength stabilisation along with a large inventory which increases the power and overall cost budget. In this work, we presented an innovative multicarrier transmitter, Gain Switched Optical Frequency Comb source (GS-OFCs), which can play a vital role in the implementation of flexible networks. The presented GS-OFCs takes advantage of external optical injection to generate optical frequency comb with clear multiple discernible comb tones with very high spectral purity, equivalent to the injecting laser (master). The spacing between the generated comb tones is governed by the frequency of the applied high power sinusoidal signal - this provides a huge range of Free spectral Range (FSR) achievable. We presented a complete characterisation of the generated OFC including FSR tunability – from 6.25 GHz to 25 GHz, wavelength tunability – covering 31 nm, and low linewidth – 40 kHz, and a carrier to noise ratio of > 40 dB. We also present a detailed experimental study of external optical injection. We provided experimental verification of various benefits reaped from optical injection including single mode performance with high SMSR, wavelength stabilisation, resonance frequency and modulation response enhancement and noise reduction. The presented GS-OFCs employing external optical injection satisfies most of parameters required from the flexible networks and can prove critical in the implementation of such systems.

Chapter 5

Chirp Compensated Directly Modulated PIC for Next Generation Access Networks and Uncooled DWDM

5.1 Introduction

The International Telecommunication Union (ITU) [109] standardised the operating channel wavelength and channel spacing. The channel spacing is the frequency separation between two adjacent wavelengths. This is decided by taking the information bandwidth and guard bands into consideration. These are the unused part of the spectrum to prevent adjacent channels interfering – which could result in loss of information and poor performance.

Figure 5.1 plots the transmission losses in various telecommunication optical wavelength bands. Due to low transmission losses and the availability of EDFAs, C-band (1530-1565 nm) became one of the most widely used optical band for metro, long-haul, ultra-long-haul, and submarine optical transmission systems combined with Wavelength Division Multiplexing (WDM) technologies. Currently deployed WDM systems typically operate at a 50 GHz grid spacing, standardised by the International Telecommunication Union (ITU) [109] and referred to as Dense WDM (DWDM). This means that the C-band is divided into multiple operating channels spaced by 0.4 nm (50 GHz). The ever increasing demand for the bandwidth driven by consumers is forcing the network providers to adopt spectrally efficient technologies to use the bandwidth limited C-band more effectively.

Due to the emergence of WDM, optical communication systems saw rapid capacity growth [110] because of its ability to transmit multiple bit streams simultaneously over the same optical fiber. For a typical WDM system, see Figure 1.2, with N channels, each transmitting at a bit rate, B, the system capacity is enhanced by a factor of N.

$$System\ Capacity\ =\ NB \tag{5.1}$$

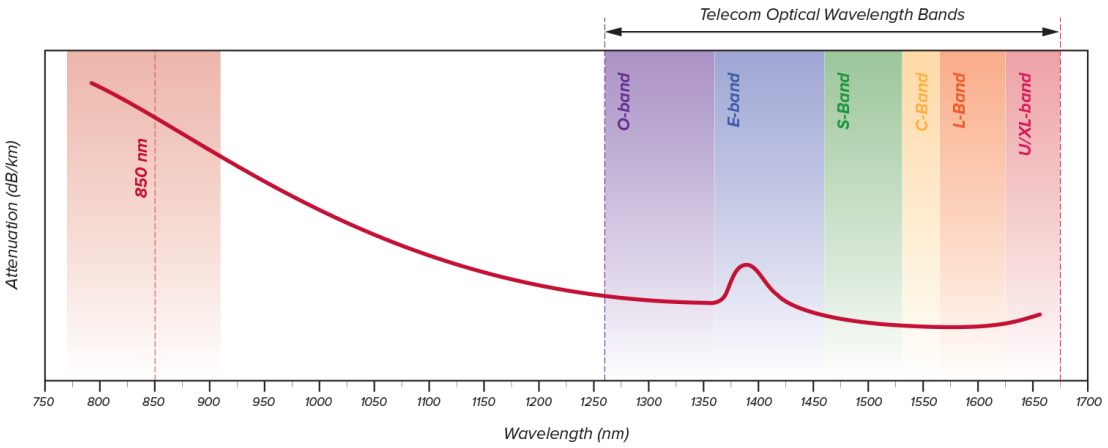


Figure 5.1: Transmission loss of silica fiber and optical communication wavelength bands. *Image courtesy: Laser 2000*

For a WDM system with channel spacing of Δf,

$$System\ Bandwidth\ =\ N\Delta f \tag{5.2}$$

$$Spectral\ Efficiency\ =\ \frac{B}{\Delta f} \tag{5.3}$$

The total system efficiency of a WDM system depends on 2 factors,

1. Data rate per channel, B, and its transmission over certain distance, l, without using any optical amplification . This can be mathematically written as Bl, and
2. Number of available optical carriers (channels), N.

Then, system efficiency can be given by,

$$System\ Efficiency\ \propto\ (Data\ Rate\ per\ Channel\ \times\ Transmission\ Distance) \tag{5.4}$$

$$System\ Efficiency\ \propto\ (Number\ of\ available\ Channels) \tag{5.5}$$

Figure 5.2(a) illustrates a typical schematic diagram of a WDM system with a grid spacing, Δf of 50 GHz. The length of the carrier in the schematic diagram signifies the system's efficiency of transmitting a data rate, B, over a transmission distance, l, without using an optical amplifier. Due to exponential growth of global data traffic, the optical transmissions systems are facing a capacity crunch due to filling up of the C-band. In order to accommodate the need of existing users and include new users, optical communication systems need to evolve continuously. As suggested by equation 5.4 and 5.5, in order to improve the system efficiency, the communication system should evolve towards

- Higher data rates per channel and its transmission over longer distances.
- Denser channel spacing, $\Delta f < 50$ GHz.

Figure 5.2(b) captures this idea and is the focus of research in this chapter. Firstly, in this chapter we will focus our attention on improving the Bl factor. This is achieved by using a directly modulated 4 section laser with a master-slave configuration, which exhibits chirp reduction, linewidth reduction and enhanced modulation bandwidth through optical injection. We demonstrate, for the first time, this PIC under direct modulation as a 10 Gbit/s transmitter achieving an error free performance after 37 km of fiber transmission. Then, we will discuss the main challenges in moving towards denser channel spacing. As the

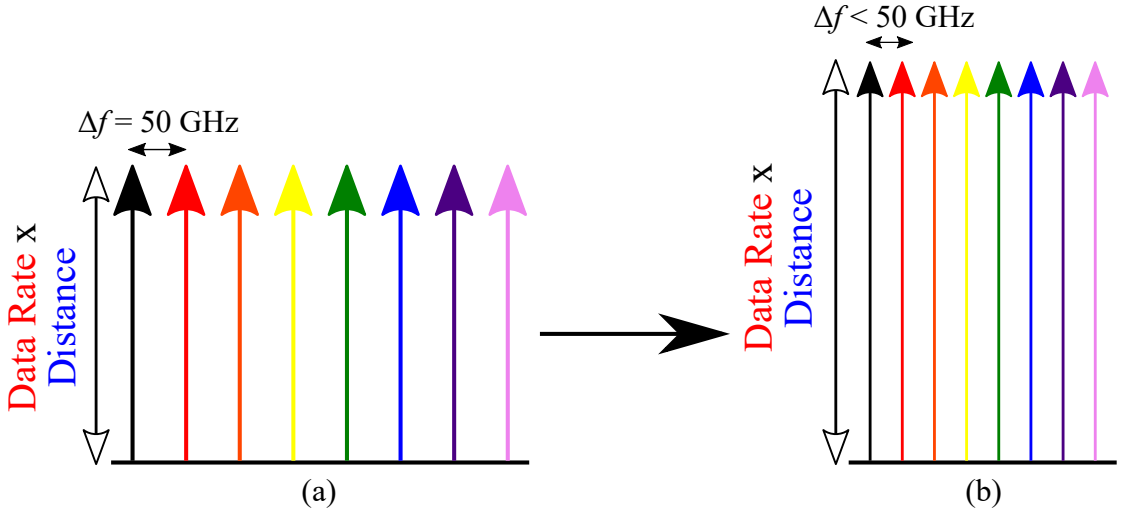


Figure 5.2: (a) Typical WDM grid with channel spacing of 50 GHz. The length of the channel signify the BL product, and (b) improved grid with narrower channel spacing and increased BL product enhancing the overall system efficiency.

system moves towards denser channel spacing, wavelength stability becomes one of the most crucial aspects. Typically this is attained by controlling the temperature of the devices using thermoelectric coolers (TECs). However, such a solution increases packaging costs and energy consumption. In this chapter we present an alternative solution to wavelength stability by athermalising the laser diode which makes it's wavelength insensitive to temperature changes through control of self-heating.

5.2 Direct Modulation and it's Challenges

In order to meet the ever growing demand for bandwidth, continual industry innovation is needed. For the optical access network, next generation passive optical network 2 (NGPON2) is an ambitious ITU standard developed to drive such innovation [111]. Time and wavelength division multiplexing (TWDM) has been chosen for the NGPON2 standards [112] and it poses stringent requirements on the optical network unit (ONU) transmitters, including high side mode suppression ratio (SMSR), high optical output power, wavelength tunability, burst mode operation, transmission distances of up to 40 km, high data rate per channel (2.5 or 10 Gb/s), and low cost. Externally modulated lasers comfortably meet most of these requirements. A system incorporating external modulation requires continuous wave lasers followed by a electro-optic modulators, or an integrated electro-absorption modulators. These modulators usually suffer from high insertion loss which is detrimental for a passive optical network (PON) system. In order to manage insertion losses, a high power laser is generally required. Due to the requirement of a high power laser and modulators, the power consumption and cost profile of such systems presents challenges.

An alternative is to use Directly Modulated Lasers (DMLs) for simplicity and cost efficiency. When operated above threshold, the intensity of emitted light from a laser is linearly proportional to the applied bias current, until some saturation is reached for high bias current values. Direct modulation exploits this dependence of the laser diode output power on the bias current. As shown in Figure 5.3, for a laser under direct modulation, the message signal can be encoded onto the light output by simply modulating the injected current. Due to its simplicity and ease of operation, directly modulated lasers provide a cost effective optical transmitter for access networks.

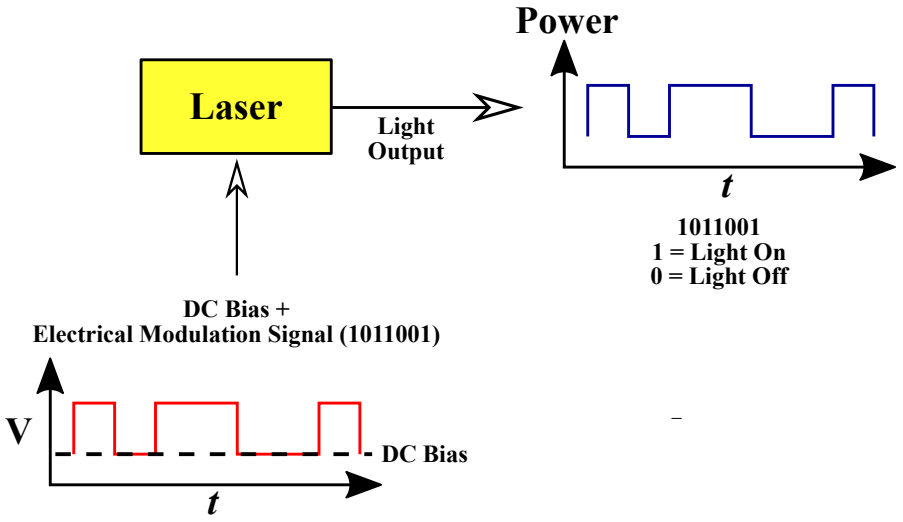


Figure 5.3: Schematic diagram of a laser under direct modulation.

Direct modulation provides a simple, cost-efficient, small-footprint and energy efficient optical transmitter. But there are a few drawbacks associated with the DMLs. One such drawback is the introduction of frequency fluctuations onto the optical carrier through direct modulation. In a laser under direct modulation, a change in the bias current leads to a change in the carrier density, which in turn leads to a change of the refractive index of the semiconductor material. The lasing wavelength of a semiconductor laser is determined from the feedback condition in the laser cavity and is dependent on the refractive index. Since in DMLs, the bias current is continuously varying, the instantaneous frequency of the emitted signal is a time variable signal. Such an optical signal is called chirped and the frequency chirp, $\Delta v(t)$ is given by [2]:

$$\Delta v(t) = \frac{\alpha}{4\pi}\left[\Gamma g_o(N - N_t) - \frac{1}{\tau_{ph}}\right] \tag{5.6}$$

Chirped signal are more susceptible to the dispersion effects in the fibre. The group velocity through an optical fibre is frequency dependent. Different frequency components of the spectrum of a pulse injected at the fibre input will travel at different speeds, hence leading to pulse broadening. When a directly modulated signal is transmitted, the information pulses spreads out of their allocated time slots, leading to inter-symbol interference, which can in turn introduce errors at the decision circuit and lead to a degraded bit-error-rate. Another drawback associated with DMLs is the dependence of the maximum data rate achievable on

the modulation response of the laser diode. This is typically 3–7 GHz. Higher modulation responses can be achieved by shortening the cavity length of the laser. But this leads to poorer linewidth. This pulse broadening in DMLs and poor modulation response limits the bit rate - length product, *Bl*.

In cost sensitive applications like access networks, which cover short to medium range distances, DMLs are the optical transmitter of choice. At current speeds chirp doesn't limit performance significantly. However, due to the increased demand, the communication systems are moving towards higher data rate per channels (e.g. 10 Gb/s), then chirp becomes an important issue. These drawbacks eclipse the advantage of direct modulation and could potentially prevent service providers from adopting it in the access networks.

In order to reap the benefits of direct modulation in continuously evolving access networks, these issues need to tackled. Optical external injection [91, 94] is known to improve the output characteristics of the injected laser. Optical external injection consists in coupling light from an optically isolated external light source, usually named as *master laser*, into the cavity of a laser known as *slave laser* to improve its performance. As discussed in section 4.3, optical injection can be used for modulation response enhancement [105, 106], improved SMSR and reduced mode partition noise [95]. It can also be used to reduce the frequency chirp of the generated pulse under direct modulation as presented later in the chapter. Previously, optical external injection has been utilised in the directly modulated system to improve the system-performance and achieve higher *Bl* product [113–115]. In these systems, optical external injection is achieved by using an external master laser. In [116], the authors have presented an integrated 2-section discrete-mode laser in a master-slave configuration achieving high SMSR, low relative intensity noise, and enhanced modulation response.

In this work, in order to yield compactness, cost-efficiency and ease of fabrication we present a directly modulated 4 section laser with a master-slave configuration, which exhibits chirp reduction [32], linewidth reduction, enhanced modulation bandwidth, and improved noise properties through optical injection [94]. Due to the multi-section nature of this PIC, this design avoids the dependence of the SMSR on the cleaving error which won't be possible in the device presented in [116]. Here, we demonstrate, for the first time, this PIC under direct modulation as 10 Gbit/s transmitter achieving an error free performance after 37 km of

fiber transmission. In addition, we present the broad wavelength tuning of this PIC, enabling the generation of eight 50 GHz spaced channels with high SMSR. Finally, experimental results on enhancement of modulation response and reduction of linewidth and chirp are also shown.

5.3 Photonic Integrated Circuit (PIC) Design

Commercially available single mode semiconductor lasers, such as Distributed Bragg Reflector lasers (DBRs), have been previously demonstrated under direct modulation for the NGPON2 application [117, 118]. These devices are fabricated with periodic variations of the refractive index to form a low order grating. However, the fabrication of low order buried gratings require high resolution lithography and complex regrowth steps, which can reduce the yield and drive the cost up. In this work we demonstrate an alternative solution, with ease of fabrication which could potentially lead to improved cost. Our design does not require regrowth and employs a high order surface grating, etched into the ridge waveguide structure [40]. Such slotted lasers have been earlier exhibited in vernier and array devices for tunability across the C-band [27]. Also, in order to reap the benefits of optical injection to yield a chirp-compensated DML, photonic integration is employed.

The schematic diagram of the fabricated PIC is shown in Figure 5.4. The device is composed of 4 integrated, electrically isolated sections, with varying cavity lengths. The overall length of the device is ∼1.5 mm and the sections are arranged in a master-slave configuration. The material structure of the device is a standard 1550 nm laser material, previously described in section 2.8.1, with 5 strained AlGaInAs quantum wells in the active region, on an n-doped InP substrate. The PIC comprises of two integrated laser diodes in a master-slave configuration. These lasers are regrowth free Fabry-Pérot (FP) lasers that include mirror sections consisting of a number of slots, with different grating periods, that have been etched into the surface ridge waveguide and provide reflections and single mode operation with high SMSR. Although these slots can be patterned with standard photolithography, the fabrication process used e-beam lithography as a stepper was not available at the external foundry.

The master laser consists of a long gain section (depicted as master gain in Figure 5.4) and two reflector sections (depicted as master reflector and shared reflector in Figure 5.4) at either

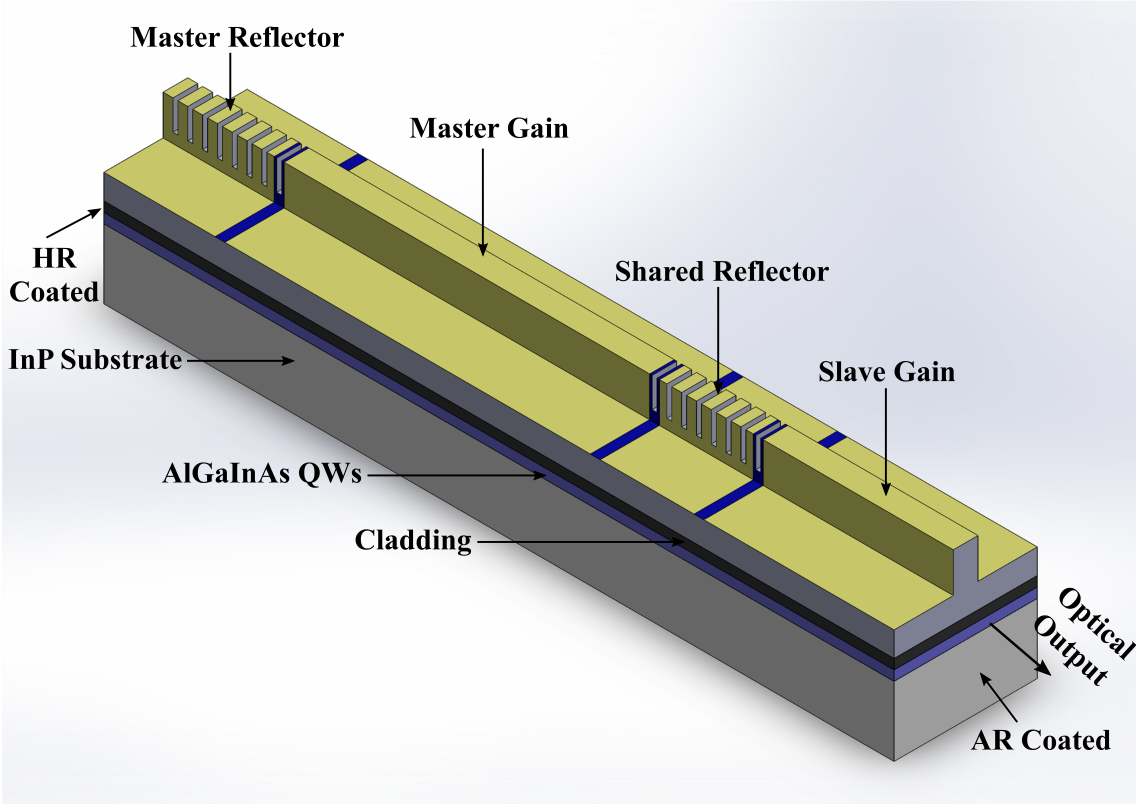


Figure 5.4: Schematic diagram of the 4 section InP PIC

side to create a resonating cavity for single mode operation, as shown in Figure 5.5. Both the mirror sections are 215 μm long and comprises of a 3-period high-order surface grating with 22 slots etched 1.395 μm deep into the ridge waveguide. Since, the lasing is independent of cleaved facet, such structures are suitable for monolithic integration with other photonic components in a single epitaxial growth. The reflector on the right end of the master gain section is shared by the slave cavity, effectively reducing the overall length of the PIC. The slave laser comprises a shorter gain section to attain better modulation response and shared reflector section for single mode operation as depicted in Figure 5.5. Figure 5.5 also proves that, even though the design of the fabricated PIC resembles a coupled cavity device due to lack of active isolation between master and slave laser, independent control of master and slave laser can still be obtained by carefully choosing the bias current. Four metal contacts were deposited to allow independent bias of the sections. The master-slave configuration of the chip delivers all the advantages of the optical injection, thus making our device suitable for directly modulated chirp compensated communication systems [33]. The fabricated PIC was packaged in a high-speed butterfly package with a Thermo-Electric Cooler (TEC) and

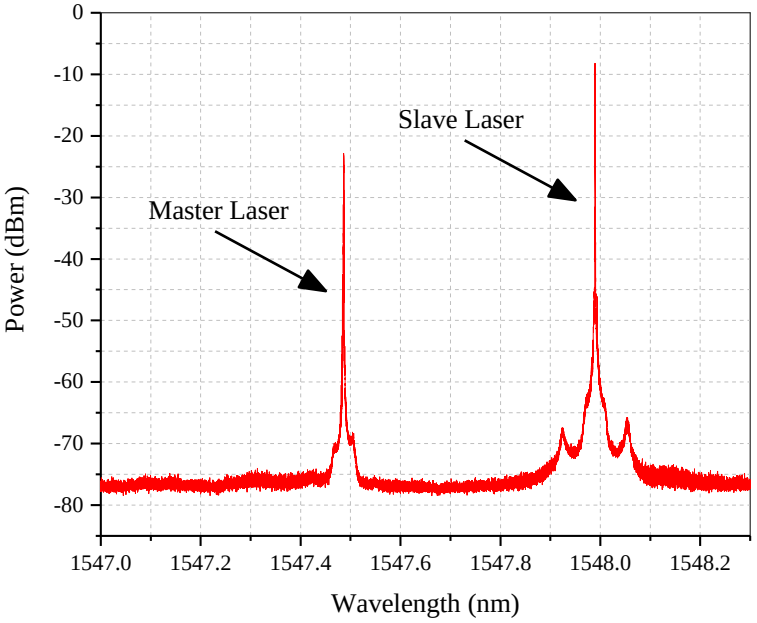


Figure 5.5: Continuous Wave (CW) optical spectrum of the two integrated lasers, Master section biased at 40 mA, Slave section biased at 70 mA.

a 10 kΩ thermistor for precise temperature control. In the next section we will present the Continuous Wave (CW) characterisation of this PIC.

5.3.1 CW Characterisation

Tuning maps at 20 ^{o}C are produced by sweeping the currents in all the sections and reading the peak wavelength, SMSR and peak power on an optical spectrum analyser (OSA), while maintaining the submount temperature constant. One such tuning map is presented in Figure 5.6 at 20 ^{o}C, when the master gain and slave gain section were biased at constant current of 34 mA and 65 mA respectively. Figure 5.6(a) shows the variation of the output peak wavelength of the PIC with respect to both the reflector currents. The measured threshold for the master gain and slave gain section is $\sim$ 30 mA for reflector bias (both) of 14 mA, so for the tuning maps in Figure 5.6, both master and slave laser are operating well above threshold. For the current specified in Figure 5.6(a), a tuning range of $\sim$ 2 nm is obtained. In order to find the region of good single mode performance for such master-slave configuration, an SMSR map becomes crucial. Figure 5.6(b) shows the variation of SMSR of the output spectra with respect to both the reflectors. As shown in Figure 5.6(b), there is large region where the output shows good single mode performance with SMSR in excess of 50 dB. Also, there are some regions of poor SMSR ($<$ 30 dB), which corresponds to multimode output

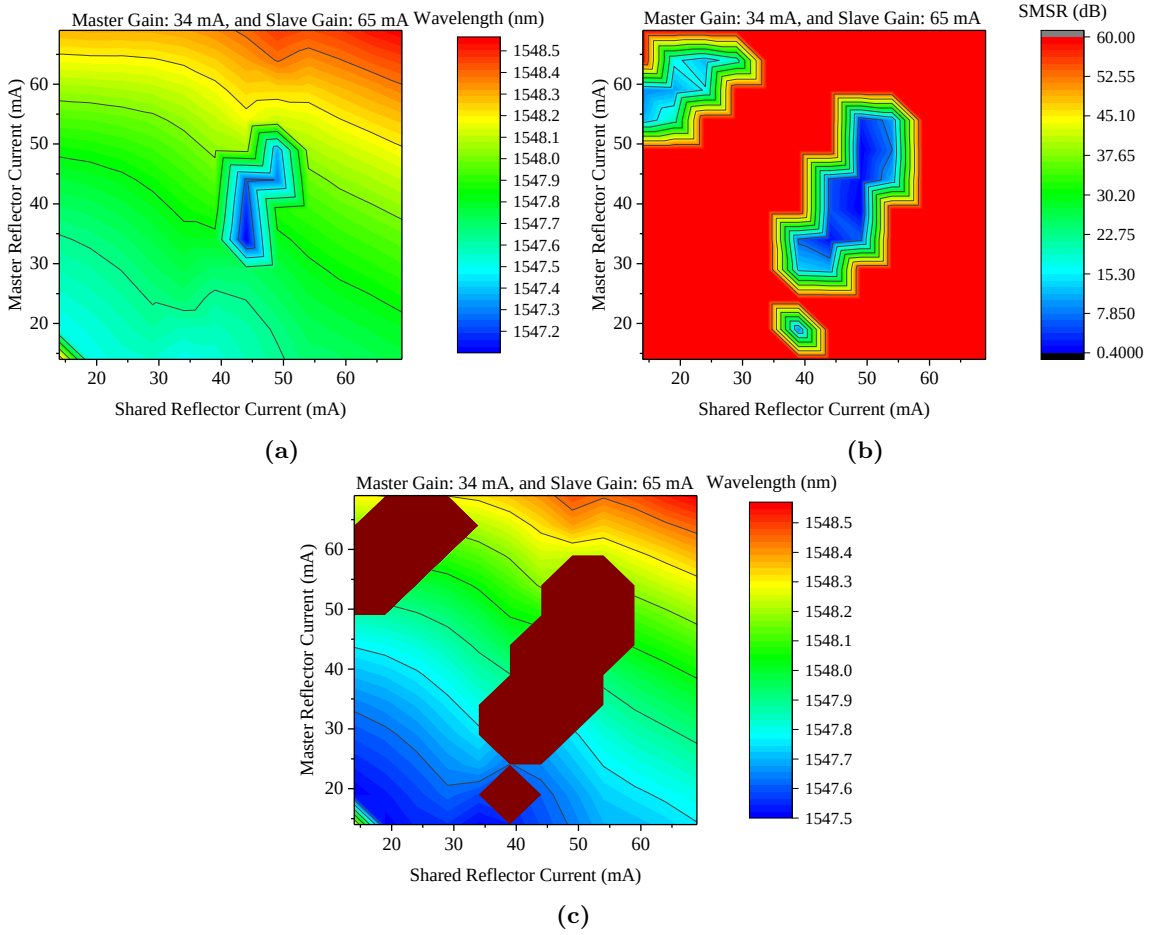


Figure 5.6: (a) Wavelength, (b) SMSR, and (c) Wavelength (for SMSR > 30) tuning maps at 20 ^{o}C for the master gain = 34 mA, and slave gain = 65 mA.

and should be avoided. Figure 5.6(c), plots the useful region of the wavelength map for single mode performance by getting rid of the operating points with SMSR < 30 dB. Detailed study of tuning maps can be found in [79, 119].

From the obtained tuning map, currents for different sections delivering wavelengths separated by 50 GHz (to meet the ITU requirements) are chosen. Figure 5.7 shows 8 such wavelengths. Table 5.1 indicate the bias currents to the various sections to attain these wavelengths. The measured SMSR for all the channels is > 50 dB. These wavelengths can be used as individual carriers in cost-effective short haul optical networks.

As explained in section 4.3, due to its unique master-slave configuration, this PIC improves critical characteristics of the device, including modulation response and optical linewidth. Figure 5.8(a) illustrates the enhancement in the modulation responses measured using a network analyser when the master gain bias is increased from 14 mA (below threshold, no

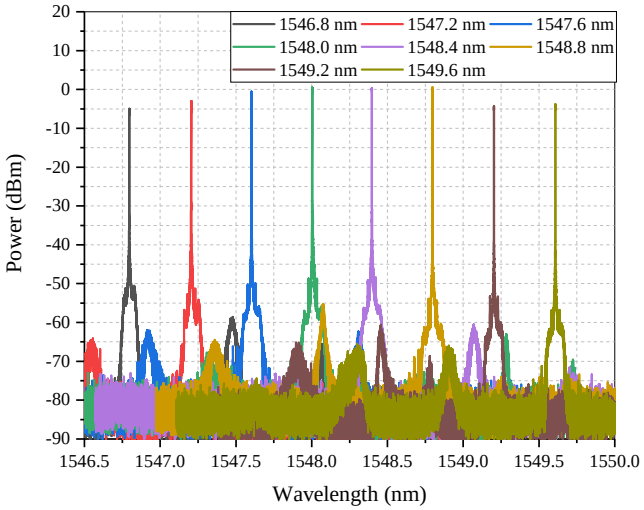


Figure 5.7: Overlapped optical spectra of 8 operating channels with emission wavelengths separated by 50 GHz

Table 5.1: Bias Currents for the various sections for the channels presented in Figure 5.7

Wavlength (nm)	Master Reflector (mA)	Master Gain (mA)	Shared Reflector (mA)	Slave Gain (mA)
1546.80	54.24	45.77	56.37	30.63
1547.20	34.23	42.02	33.58	35.00
1547.60	45.90	39.35	48.00	45.00
1548.00	59.40	57.43	63.52	49.90
1548.40	76.56	47.96	72.66	52.69
1548.80	33.80	82.20	43.70	64.00
1549.20	68.51	76.96	49.67	31.05
1549.60	41.56	71.93	53.69	57.24

injection) to 34 mA (above threshold, under optical injection). There is clear improvement in the modulation bandwidth by $\sim$ 2 GHz under optical injection. Figure 5.8(b) illustrates the optical linewidth measured using the delayed self-heterodyne (DSH) technique [74]. The test is performed for two cases: when the master laser is turned off (red) and when the master is turned on (black). As observed, the linewidth reduces from 1.6 MHz to 560 kHz, once the external optical injection from the master laser is applied into the cavity of the slave laser. The optical injection was turned off by simply unbiasing the master gain and master reflector section. The improvement in optical linewidth and modulation response is the direct consequence of the unique architecture of this PIC, which enables an optically-injected, injection-locked system. Now, in the next section we will assess the performance of this PIC under direct modulation - direct detection. Additional characterisation of this device is presented in later sections and in [120].

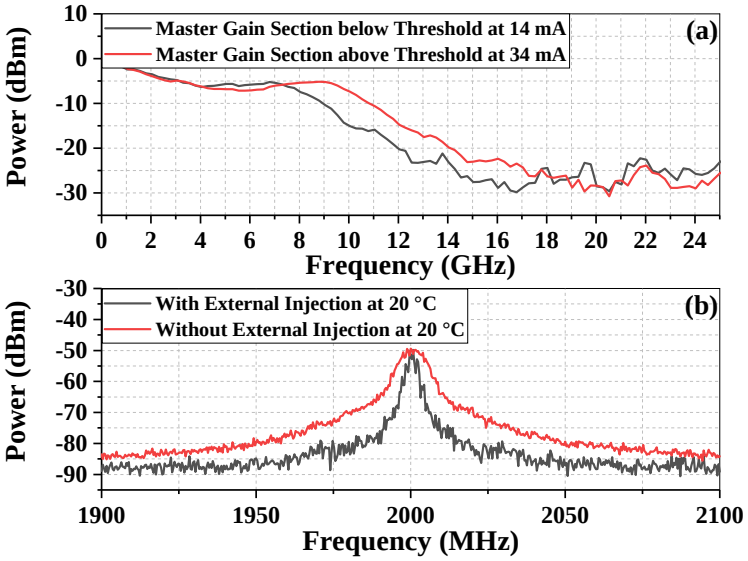
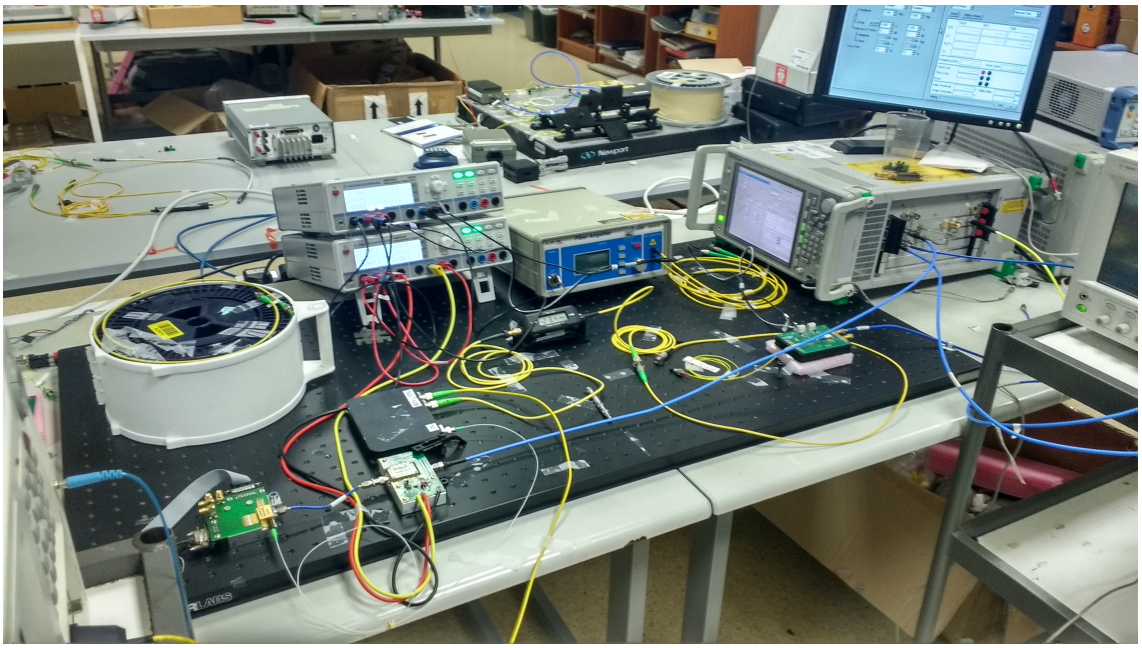


Figure 5.8: Measured (a) modulation response, and (b) linewidth

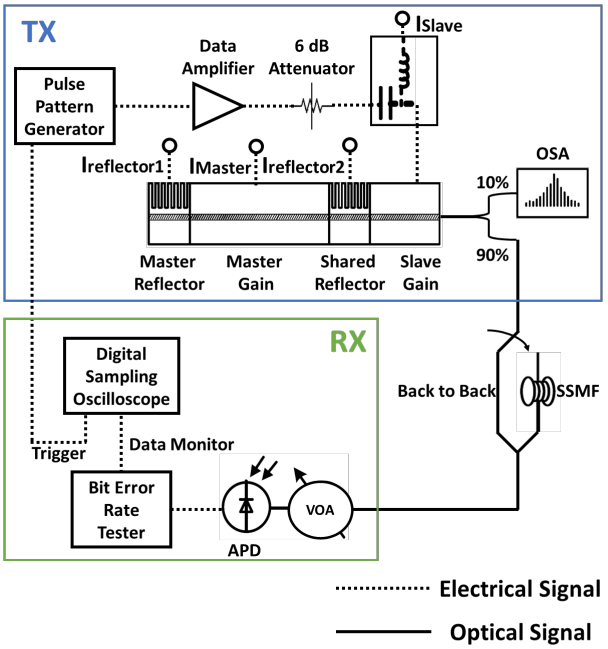
5.4 Transmission - *Towards improved Bl*

5.4.1 Transmission System

The experimental and the schematic setup for the direct modulation – direct detection system is illustrated in Figure 5.9(a), and (b), respectively. The PIC described in the previous section is used as the directly modulated light source. All 4 sections are dc biased, and the bias currents are chosen such that the output wavelengths are spaced by 50 GHz as shown in Figure 5.7. The dc bias of the slave gain section is combined with a pseudo random bit sequence (PRBS) signal (2^{15}-1) at 10 Gbit/s using a bias-T internal to the laser package. The PRBS signal is generated using a pulse pattern generator, which is then amplified using a data amplifier and then subsequently attenuated in order to maximise the extinction ratio of the modulated optical signal. The generated modulated optical output is then split using a 90-10 % coupler, where the 10 % tap is transferred to the OSA for monitoring the optical spectra and the remaining 90 % is either directly fed to the receiver (RX) or launched into a 37 km long standard single mode fiber (SSMF) before being passed to the receiver for direct detection. The scenario when the signal is directly fed to the receiver is famously known as back-to-back case. The receiver comprises a variable optical attenuator (VOA), which controls the received optical power (ROP) falling onto the avalanche photo diode (APD) for high sensitivity measurements. The output of the APD is then passed to a bit error rate tester



(a)



(b)

Figure 5.9: (a) Experimental, and (b) Schematic diagram of the set-up for the Transmission system.

(BERT) for measuring the number of errors. The qualitative performance of the system is monitored via an eye diagram with the aid of a digital sampling oscilloscope.

Before we present the performance of the fabricated PIC under direct modulation, it is important to discuss some basic terminology/performance parameters associated with the measurement to gain deeper understanding of the measurement:

- **Bit Error Ratio (BER):** In a fiber-optic transmission systems, bit errors are the number of received bits that have been altered due to noise, interference, distortion or bit synchronisation error. The Bit Error Ratio (BER) is the number of bit errors divided by the total transmitted bits during a given interval of time. For example: A BER $= 1 \times 10^{-6}$ signifies 1 bit error in every 1 million transmitted bits.

- **Error-Free:** Bit error ratio which can be tolerated without compromising the system performance. Typically, a BER of 1×10^{-9} is considered to be error-free.

- **Received Optical Power:** Optical power reaching the receiver (avalanche photo diode (APD), in this case).

- **Sensitivity:** Minimum received optical power required to achieve error-free performance.

- **Power Penalty:** Difference in the sensitivity in two different scenarios, e.g., back to back and over some length of SSMF.

- **Eye Diagram:** An Eye diagram is a graphical representation of the received data for qualitative analysis. It is formed by superimposing 2-3-bit long electrical sequence in the bit stream on top of each other. The resulting pattern is called an eye diagram because of it's appearance. Figure 5.10 shows an ideal eye diagram. Noise and timing jitter lead to a partial closing of the eye.

- **Forward Error Correction (FEC):** FEC is a error correction process in which a transmitter of digital data adds extra information known as check bits to the data stream. The receiver analyzes the check bit information to locate and correct errors in the useful data stream. Hence, in an FEC system, the receiver detects and corrects errors in real time as the data is being received. If 7% of the transmitted bits are check

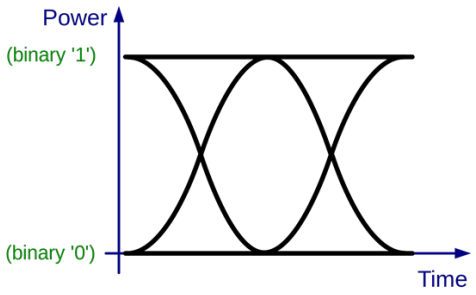


Figure 5.10: An ideal eye diagram.

bits then the BER required for error-free performance increases to 3.8×10^{-3} instead of 1×10^{-9}. FEC enhances the system performance by increasing the tolerance towards error and is extremely useful in transmitting data stream over noisy channels.

5.4.2 Transmission Performance

Figure 5.11 shows the plots of the bit error ratio (BER) as the function of received optical power, measured for the back-to-back case (shown in black squares), and after 37 km of SSMF transmission (in blue triangles). The performance in both the cases is well below 7 % forward error correction (FEC) limit (BER = 0.0038). We observed a receiver sensitivity of -20 dBm and -17.9 dBm at 7 % FEC limit for back-to-back and after 37 km transmission respectively.

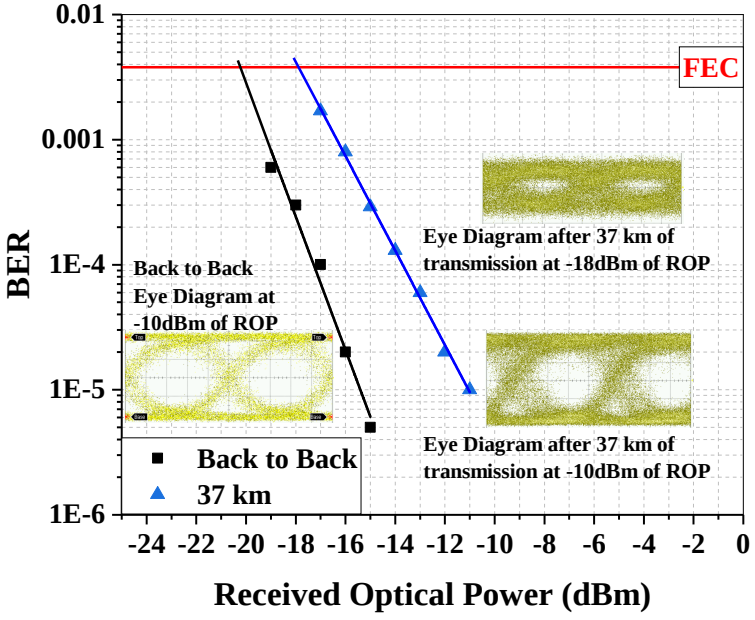
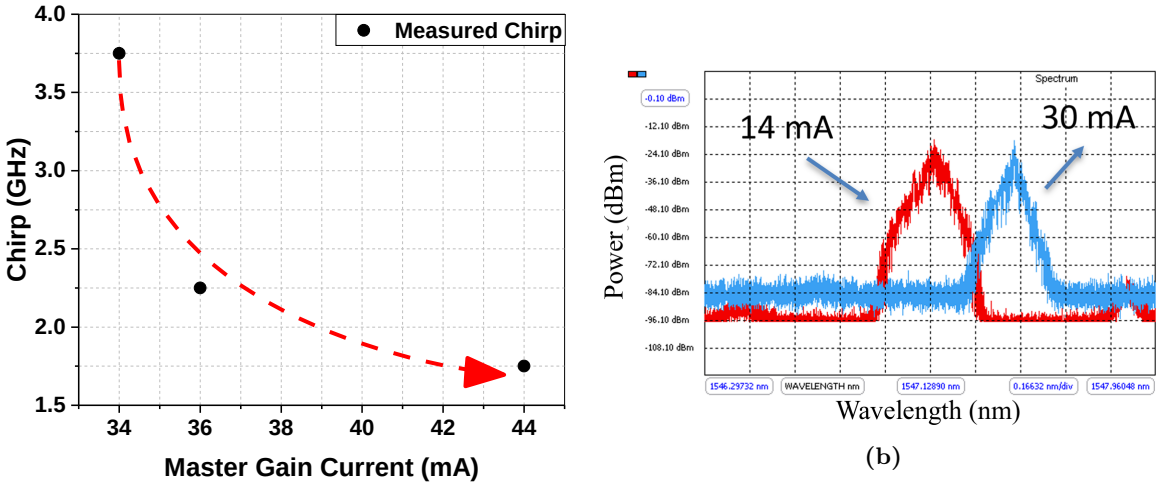
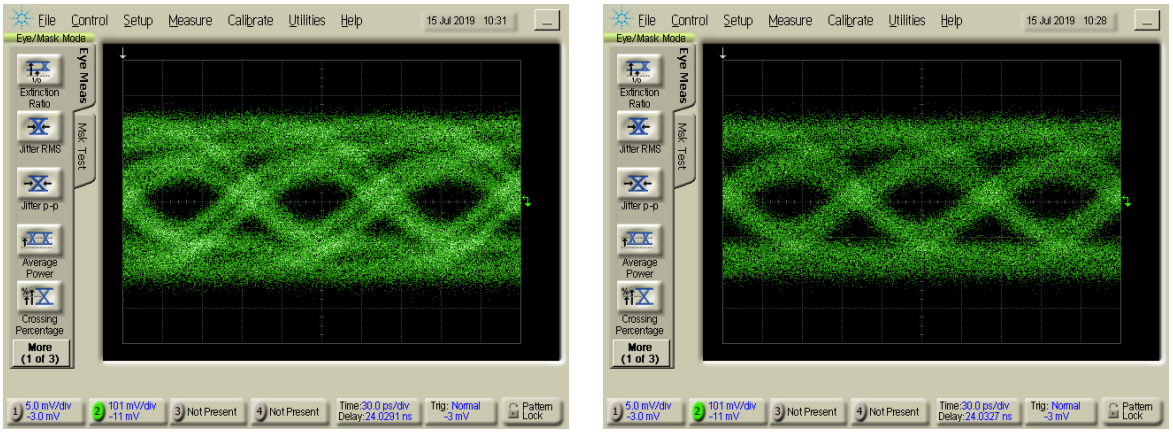


Figure 5.11: BER versus received power for back-to-back case, and after transmission through 37 km of SSMF, inset: eye diagram.



(a) (b)

Figure 5.12: Measured (a) chirp vs applied master gain current, and (b) optical spectrum at 2 different master gain current



(a) (b)

Figure 5.13: Eye-diagram measured back-to-back for (a) without, and (b) with optical injection.

This corresponds to only 2.1 dB of power penalty after transmission through 37 km of SSMF. The inset in Figure 5.11 also shows the eye diagrams for both the cases at different received optical powers.

The error-free transmission after 37 km of SSMF could only be achieved when the master sections were biased above threshold. This was attributed to a chirp reduction of the directly modulated signal due to the optical injection. We have confirmed this reduction, by measuring the chirp using the wavelength discrimination technique [121], we plot the peak chirp as a function of master gain current, for 3 different bias points above threshold in Figure 5.12a(a). As evident from the graph, the chirp reduces significantly as the master

gain current is increased. Figure 5.12b(b) shows the measured modulated optical spectrum at 2 different master gain biases. The spectral width clearly reduces, when the master gain bias changes from 14 mA (below threshold, no injection) to 30 mA (above threshold, under optical injection). Figure 5.13 qualitatively measure the effect of optical injection on the noise properties. Figure 5.13a, and 5.13b, shows the eye-diagram of the back-to-back signal without and with optical injection enabled respectively. It can be clearly seen that the "1" and "0" level are better distinguished and defined when the optical injection was enabled. Also, the eye crossing are well-defined when the optical injection is enabled which corresponds to lower timing-jitter. This is the direct consequence of the optical injection enabled by this PIC utilizing the master-slave configuration, and plays a critical role in achieving error-free data transmission over distances that are typically not achievable with standard DMLs.

5.5 Athermalised Wavelength Stabilization under Direct Modulation

The immense increase in bandwidth usage is driving all sectors of optical networks employing wavelength division multiplexed (WDM) technology towards denser channel spacing. Reduction of the channel spacing for increased data throughput imposes stringent requirements on the optical transmitters, which includes high power, high side mode suppression ratio (SMSR), and high wavelength stability. As current-biased semiconductor lasers suffer from self-heating, leading to a temperature variations, wavelength stability becomes one of the most crucial attributes required from any WDM based optical communication system. Typically this is attained by controlling the temperature of the devices using thermoelectric coolers (TECs). However, such a solution increases packaging costs and energy consumption. A solution to improved wavelength stability entails the athermalisation of the laser diode [79], making its lasing wavelength insensitive to temperature changes through control of self-heating. In order to athermalise a laser, it is necessary to control the thermal drift of mirror loss and cavity modes, and offset these against each other [122]. Although the design and fabrication of such lasers initially proved difficult [123], the performance and wavelength stability of athermal tunable lasers has improved significantly in recent years [124], with recent work by Zhu et al. achieving wavelength accuracy of ± 3 GHz over a 15-70 ^{o}C range [123].

This required control over the current supplied to 5 sections of the DS-DBR laser [123, 125–127] and feedback from a centralised shared wavelength locker [123, 127]. Previously, in our group an athermal bias current procedure based on thermal tuning was demonstrated for a low-cost, monolithic, 3-section slotted laser, achieving mode-hop free wavelength stability of ± 0.04 nm (5 GHz) over a temperature range of 8-47 ^{o}C [79]. In this work, we extend this athermalising scheme to the 4-section photonic integrated circuit (PIC), presented earlier in this chapter and illustrated in Figure 5.4.

In this work, we demonstrate a 4-section photonic integrated circuit (PIC), described earlier, as a directly modulated cost-efficient athermal transmitter, which employs a simpler fabrication process without any re-growth step. In this section we first present tuning maps of the PIC showing $>$ 6 nm of tunability with an SMSR of $>$ 50 dB. We then present results on the linewidth reduction due to external injection. Subsequently, results on the continuous wave (CW) athermalisation of this PIC showing a single mode performance over an athermal temperature range of 10-60 ^{o}C with a wavelength stability of 0.006 nm (750 MHz) with an SMSR $>$ 34 dB, is presented. We demonstrate a directly modulated athermal transmitter, modulated at 2.5 Gb/s achieving error free performance when transmitted over 37 km of standard single mode fibre (SSMF) over the temperature range 10-45 ^{o}C with wavelength stability of 0.01 nm (1.25 GHz). The key goal for this work is to extend the upper temperature range for transmission to 60 ^{o}C and higher.

5.5.1 CW Athermalisation

5.5.1.1 Experimental Setup

Figure 5.14 shows the schematic diagram of the experimental setup used to measure the spectral and output power characteristics of the 4-section PIC. The fabricated PIC was mounted on an AlN carrier and kept on a copper heat sink which in turn was mounted on a Peltier based thermo-electric cooler (TEC) for precise temperature control and attaining various chip temperatures to experimentally simulate the uncooled scenario. All 4 electrically isolated sections have separate probe contacts to provide independent current control using 4 independent current sources, ILX Lightwave: LDX3200. The PIC was fibre coupled for the collection of light. The collected light passes through a 90/10 beam splitter with 90% detected by an Agilent 86140B Optical Spectrum Analyser (OSA) and 10% detected by a Keithley

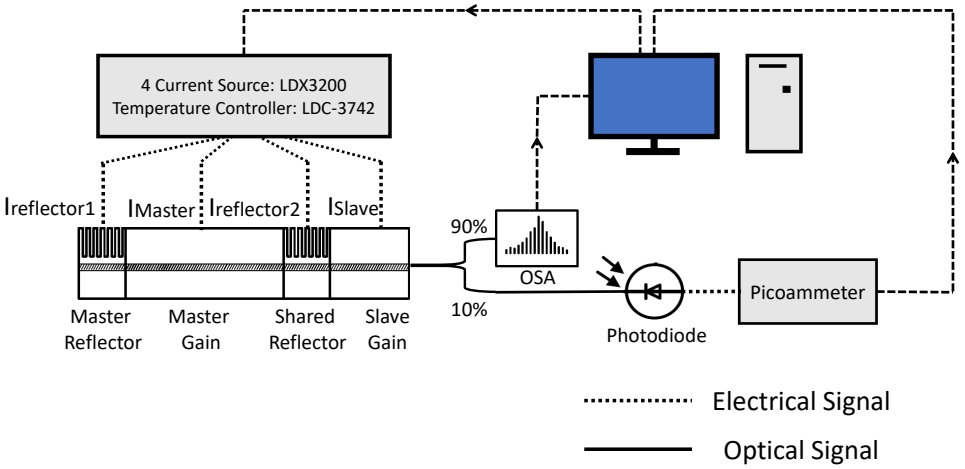


Figure 5.14: Experimental set up.

6485 Picoammeter. The power reading of the picoammeter is used to adjust the fibre position until maximum coupling efficiency is achieved. The output spectrum is recorded using an Agilent 86140B OSA with a maximum resolution of 0.06 nm being used with a sensitivity of -75 dBm.

5.5.1.2 Tuning Maps and Athermalisation Scheme

Due to complex nature of the device and 4 the independent sections, it becomes quite difficult to visualise the tuning maps and develop a current-based athermal scheme for the entire device. So, in order to simplify our understanding - we will first study the tuning maps and develop an athermal scheme for the slave laser. Then we will extrapolate our understanding to athermalise the entire device both in CW and under direct modulation.

In order to athermalize the laser one must control the thermal drift of the reflected wavelength (Bragg peak) of the grating in relation to the peak gain wavelength (longitudinal mode with the highest reflectivity). If the separation of these two wavelengths becomes greater than half the mode separation of the grating's reflectivity peaks, a mode hop occurs. In the current based athermalisation the redshift in the operating wavelength due to increased temperature, which is typically 0.1 nm/^{o}C is counteracted by changing the injected current to the device. Due to multi-section nature of this PIC, it becomes imperative to understand

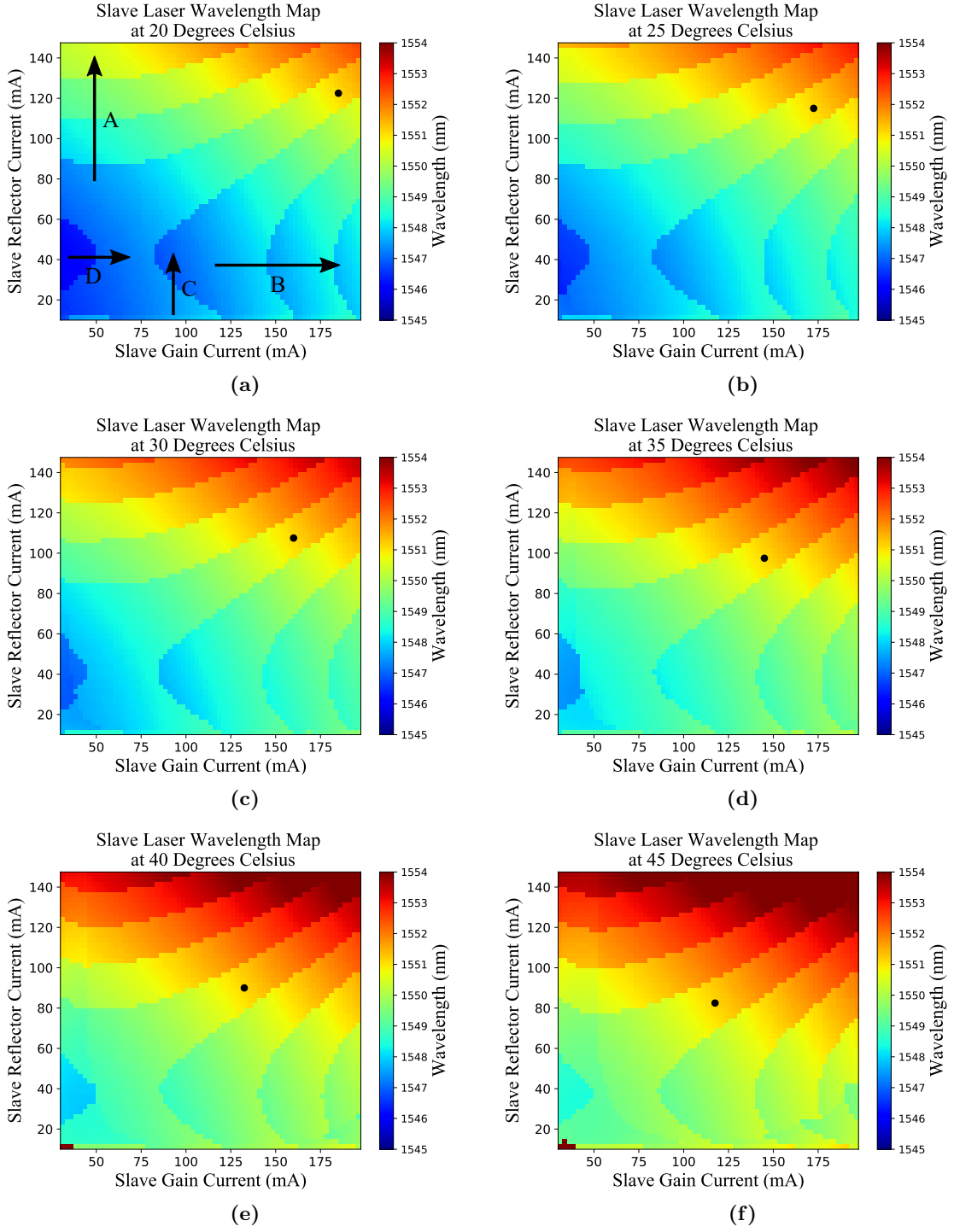


Figure 5.15: Wavelength tuning map of the slave laser at (a) 20 ^{o}C, (b) 25 ^{o}C, (c) 30 ^{o}C, (d) 35 ^{o}C, (e) 40 ^{o}C, and (f) 45 ^{o}C.

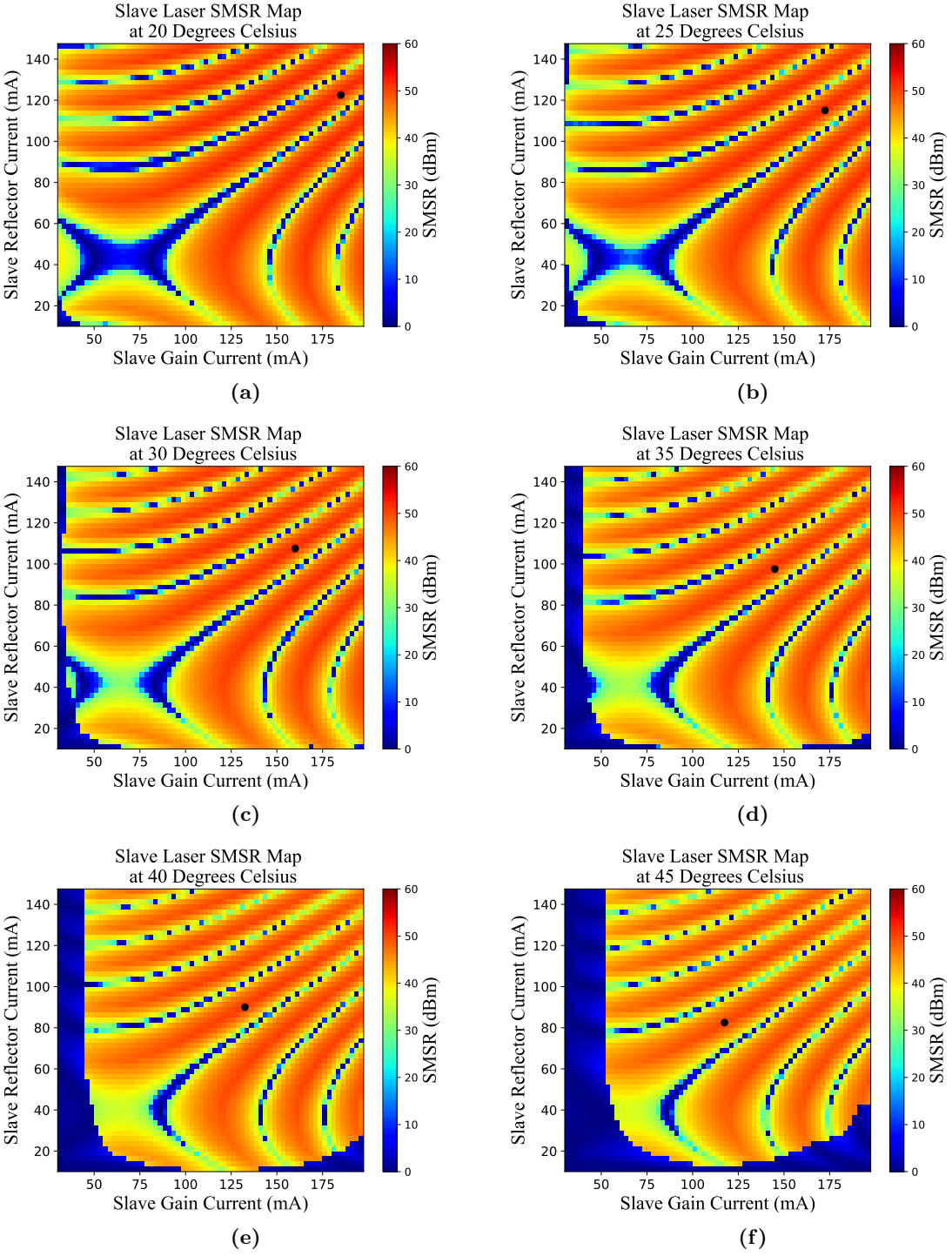


Figure 5.16: SMSR tuning map of the slave laser at (a) 20 ^{o}C, (b) 25 ^{o}C, (c) 30 ^{o}C, (d) 35 ^{o}C, (e) 40 ^{o}C, and (f) 45 ^{o}C.

the tuning maps in order to develop a robust athermal scheme. Figure 5.15 shows the shift in wavelength with respect to a range of shared-grating (slave-reflector) and slave-gain currents at the specified temperature. The tuning maps are recorded by sweeping the grating and gain currents and reading the peak wavelength on the optical spectrum analyser, while maintaining the submount temperature at the specified temperature using the TEC. The discontinuities in the tuning maps correspond to mode-hopping. These mode-hops are caused by the shift in either longitudinal modes or Bragg peak such that a side mode adjacent to the lasing mode coincides with the Bragg peak, resulting in a higher round trip gain for the competing side mode. Once the competing side mode has the highest round trip gain, it will start to lase resulting in the observed wavelength jump. Figure 5.16 shows the corresponding SMSR maps for the slave laser at the specified temperatures. It can be seen that the regions close to the mode-hops show poorer SMSR due to the mode competition. The wavelength tuning maps of the slave laser have four distinct regions where mode hopping occurs.

- At high grating section currents, as depicted by arrow-A in Figure 5.15(a), thermal effects are responsible for the mode-hopping. The increment in grating current here increases the temperature of the grating which results in the red shifting of the Bragg peak until the next longitudinal mode coincides with the Bragg peak, resulting in a mode-hop. This wavelength jump increases the lasing wavelength.

- At high gain section currents, as depicted by arrow-B in Figure 5.15(a), the increment in the gain current increases the temperature which results in the red shifting of the longitudinal mode. The lasing wavelength tune continuously until the adjacent lower wavelength mode coincides with the Bragg peak and results in a mode-hop. This causes a wavelength jump to a lower wavelength.

- At low grating section currents, as depicted by arrow-C in Figure 5.15(a), carrier density effects are responsible for the mode hopping. The increase in the carrier density results in the blue shifting of the Bragg peak until it coincides with the adjacent lower wavelength mode and results in the wavelength jump to a lower wavelength.

- Another distinct region of mode hopping is observed near low gain and grating section currents, as depicted by arrow-D in Figure 5.15(a). The increment in gain section

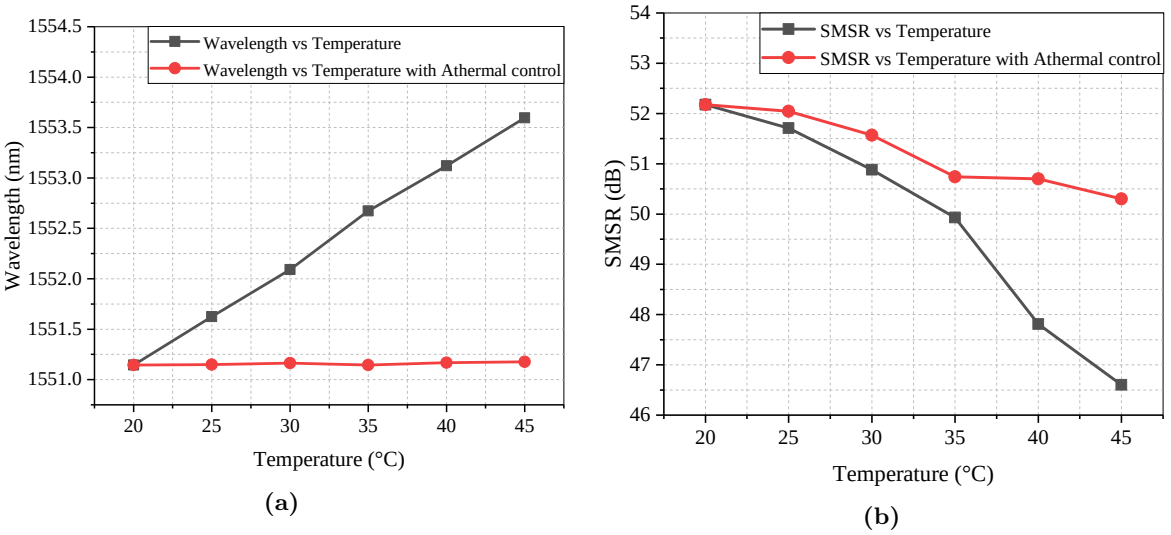


Figure 5.17: Comparison of (a) wavelength stability, and (b) SMSR, with (red) and without (black) athermal control.

current here results in a mode-hop to higher wavelength. Carrier density effects are responsible for this mode-hopping. The rise in the gain section injection current here increase the photon density in the grating section. This increment in the photon density in the grating region depletes the carrier density. The reduction in the carrier density in the grating section, red shifts the Bragg peak and causes a wavelength jump to higher wavelength once it coincides with adjacent higher wavelength mode.

Figure 5.15, and 5.16 captures the idea of the current based athermalisation. Figure 5.15 shows the variation of the overall wavelength of the slave laser with temperature at temperature ranging from 20 to 45 ^{o}C at an interval of 5 ^{o}C. As anticipated, with the rising temperature the longitudinal and Bragg peak redshifts, resulting in the redshifting of the entire tuning map. In order to counteract this effect, the injection current in both the sections needs to be properly tuned. Due to the multi section nature of this chip a correct balance in the tuning of the injected current to the different section needs to be found, in order to maintain good performance without a mode hop.

An obvious choice is to optimise for the highest SMSR achievable for the given temperature while maintaining the precise wavelength. This is the precise idea captured in Figure 5.15, and 5.16. As depicted in the tuning maps, as the temperature increases the wavelength for a given bias condition redshifts. The *black dot* on the wavelength and SMSR tuning maps

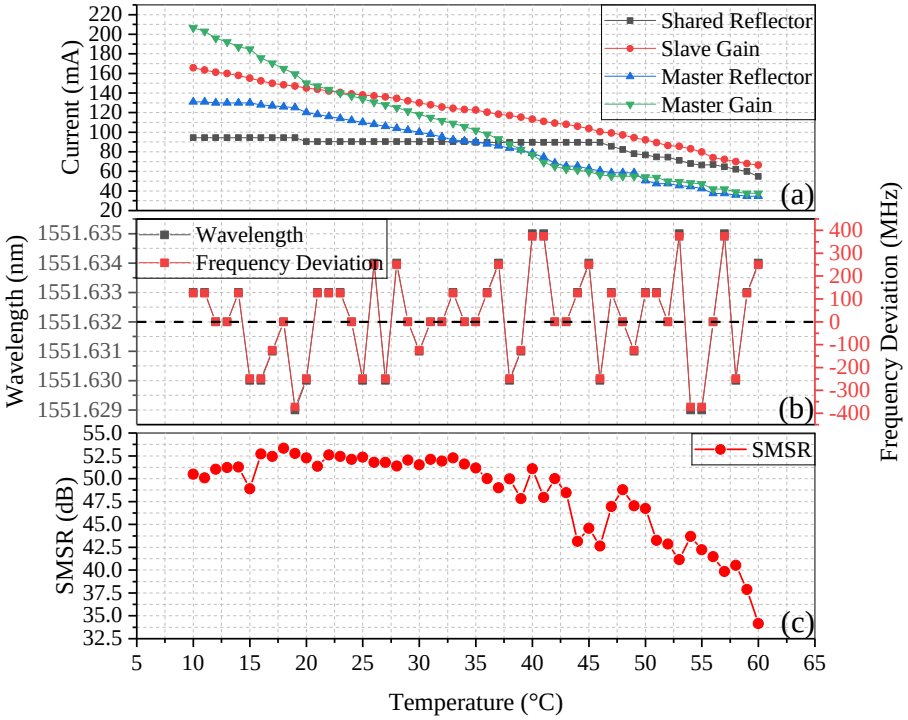


Figure 5.18: CW Athermalisation results: (i) applied Currents, (ii) emission wavelength, and (iii) SMSR versus Temperature

follows one such wavelength while maintaining the SMSR high. This is the core idea behind the developed athermal scheme - using current tuning to steer down the tuning map to counteract the effect of redshift caused by temperature rise. Figure 5.17 compares the output characteristics of the laser with and without athermal control at varying temperature. As is evident, application of athermal control provides high wavelength stability with high SMSR.

Now, we will apply this understanding to the entire PIC, with master laser on to enable the optical injection.

5.5.1.3 CW Athermalisation of PIC

Tuning maps from 20 ^{o}C to 45 ^{o}C at an interval of 5 ^{o}C, are obtained by sweeping the current in all sections and reading the peak wavelength along with the SMSR and the peak power on an optical spectrum analyser (OSA). Based on the measured tuning maps a continuous athermal scheme is developed, in which the wavelength redshift caused by the increased PIC temperature is compensated by blue-shifting the longitudinal mode by reducing the injected current density. Figure 5.18 shows the applied current to each section, peak wavelength, and SMSR versus the operating device temperature, which was precisely controlled through the

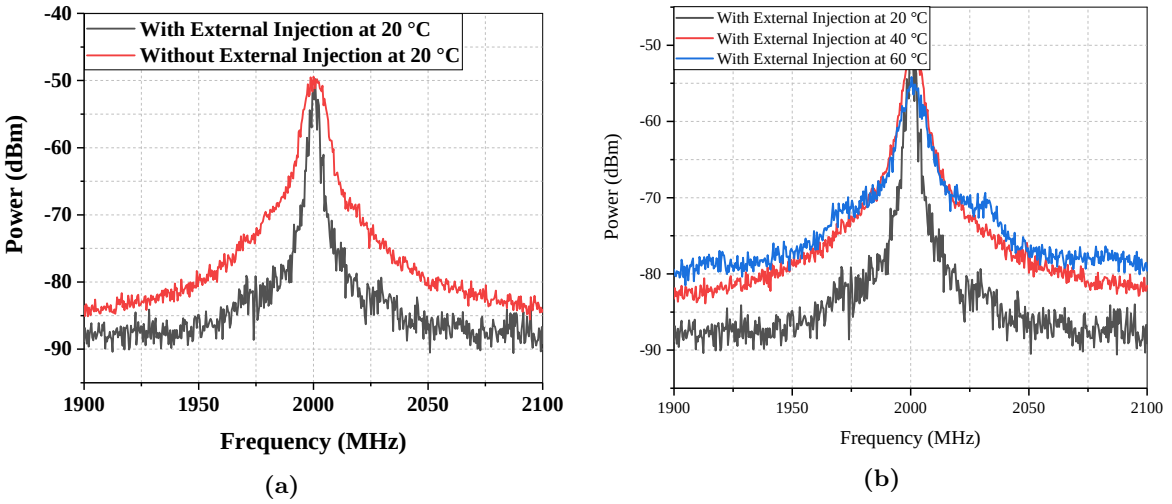


Figure 5.19: Optical Linewidth measurement; (a) Linewidth reduction through optical injection at 20 ^{o}C, and (b) Linewidth with optical injection at 20, 40, 60 ^{o}C for the operating currents shown in Figure 5.18(i) for the respective temperatures.

TEC. The current path is chosen to attain maximum wavelength stability without mode-hops while ensuring a high SMSR. Note that as the wavelength red-shifts with increasing temperature, the currents are reduced to compensate for the wavelength drift. As shown in Figure 5.18, a wavelength stability of ± 3 pm (± 375 MHz) is achieved with a SMSR greater than 34 dB over the temperature range 10-60 ^{o}C.

The operating current of the master and slave lasers section are chosen such that the wavelength of the master laser is always aligned with the operating wavelength of the slave laser. This results in an injection-locked laser system, with improved linewidth, enhanced modulation response, and reduced chirp under direct modulation. The optical linewidth is measured using the delayed self-heterodyne (DSH) technique, described in section 2.9.5. We observed a linewidth reduction from 1.6 MHz to 560 kHz through optical injection at 20 ^{o}C as shown in Figure 5.19(a). The optical injection was turned off by simply unbiasing the master gain and master reflector section. The measured linewidth at 20, 40 and 60 ^{o}C with optical injection was 560 kHz, 1.44 MHz and 3.2 MHz respectively. The bias current selected for these measurements are taken from Figure 5.18(a) for the respective temperature. The increment in linewidth with temperature as presented in Figure 5.19 (b), is attributed to two factor - (i) increased non radiative recombinations at higher temperatures, and (ii) reduction in the bias currents at higher temperature to attain athermalisation.

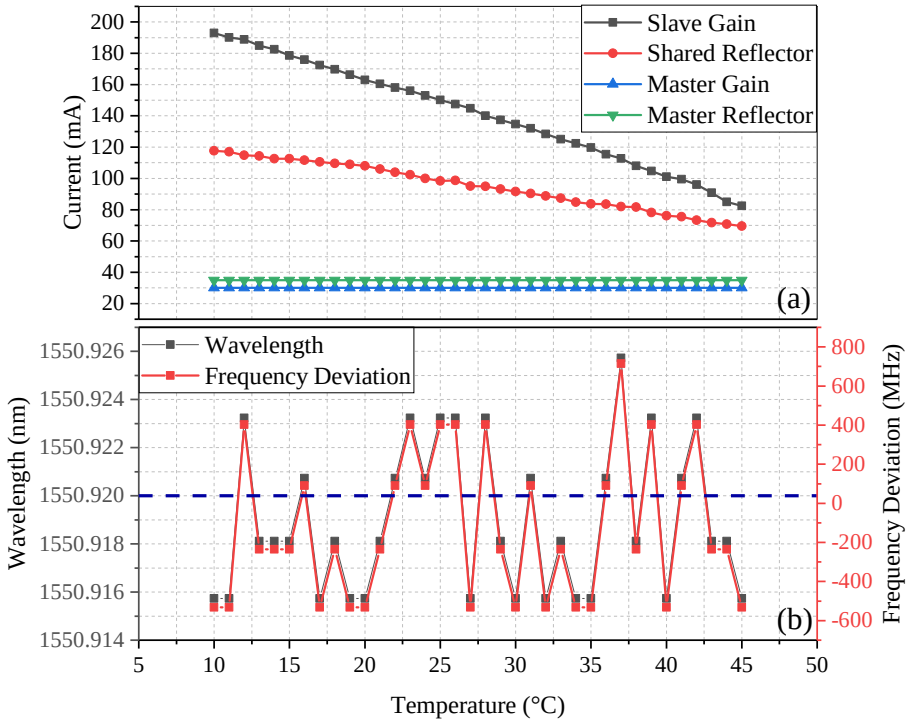


Figure 5.20: Athermal transmission results: (a) applied currents, and (b) emission wavelength versus temperature

5.5.2 Athermal Transmission

The experimental setup for athermalised direct modulation – direct detection system is the same used in the earlier section and is illustrated in Figure 5.9. Similar to the CW athermalisation scheme discussed in previous section, an equivalent scheme for directly-modulated athermalised transmission has been developed. The temperature of the chip is increased in steps of 1 ^{o}C using the TEC, the wavelength red-shift caused by the increased PIC temperature is compensated by blue-shifting the longitudinal mode by reducing the injected current density. The magnitude of the applied DC biases as shown in Figure 5.20(a) and the amplitude of the modulated signal at different chip temperatures is chosen such that the wavelength of the output modulated light lies on one of the DWDM ITU channel (1550.92 nm), while maintaining a high extinction ratio. A wavelength stability of 0.01 nm (1.25 GHz) is achieved as shown in Figure 5.20(b) over a temperature range of 10-45 ^{o}C, which is well within DWDM guard band requirements. The latter is achieved while transmitting the on-off keyed data at 2.5 Gb/s over 37 km of SSMF without observation any error floors at 1×10^{-9}.

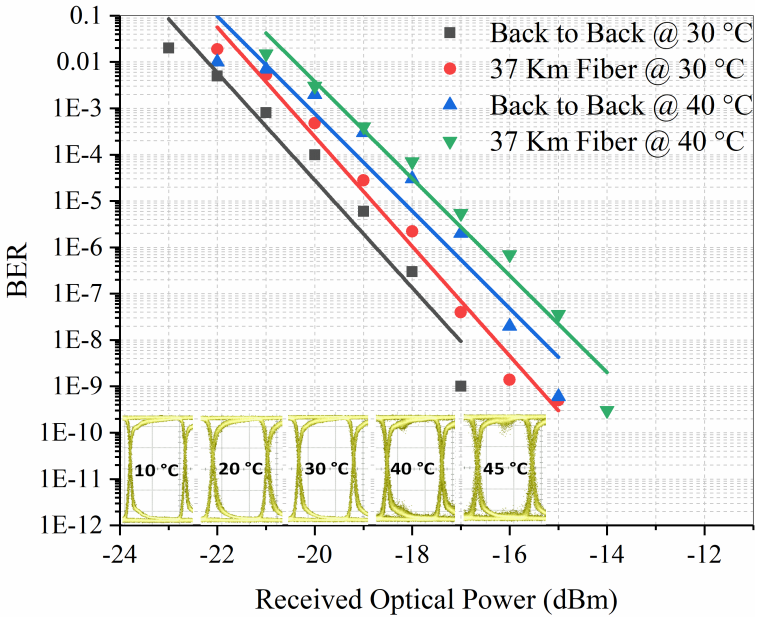


Figure 5.21: BER vs received power for back-to-back, and after transmission through 37 km of SSMF, at 30 and 40 ^{o}C, inset: Back-to-back eye diagram measured at 10, 20, 30, 40, 45 ^{o}C

Figure 5.21 shows the eye diagrams at 10, 20, 30, 40, and 45 ^{o}C captured for the back-to-back case. As evident from Figure 5.21, a clear eye opening is observed at each temperature. Fig 6 shows the performance of the athermalised 2.5 Gb/s directly modulated on-off keyed system, evaluated by carrying out bit error rate (BER) measurements as a function of received optical power. BER measurements are carried out for back-to-back case and 37 km SSMF transmission for 2 different temperatures, 30 and 40 ^{o}C. We observed a receiver sensitivity of -17 dBm and -16 dBm at a BER of 10^{-9}, measured back-to-back and after transmission over 37 km of SSMF at 30 ^{o}C. This corresponds to 1 dB power penalty after transmission over 37 km. The observed power penalty when the temperature is raised by 10 ^{o}C is 2 dB. The reason for this penalty is attributed to the coupled cavity nature of the device rather than a true master-slave configuration due to lack of isolation between master and slave laser. Due to this fact, we operated the master laser close to threshold in order to avoid multimode output and hence the optical injection was not optimum. Higher optical injection would have further reduced the chirp and resulted in lower power penalty. We are currently developing new devices with improved and controllable isolation between master and slave laser to take complete advantage of optical injection to further improve system performance.

5.6 Automation Of Athermalisation

In order to make the athermal transmitter viable for optical communication, it is imperative to automate the athermalisation process. The athermalisation achieved in the previous section was attained manually and it took hours and several trials to generate the look up table of the bias current to various sections for given temperature to achieve high wavelength stability. Also, due to the manual approach, there is a high possibility that the generated look up table is not optimised for the best performance, i.e., SMSR, temperature range etc. Also, due to the large number of transmitters required in any communication system, it becomes impractical if not impossible to obtain these look up table manually. Therefore, in this section we aim to develop an automated process for the athermalisation. We developed a reliable algorithm based on vector analysis to realise an athermal transmitter. The athermal algorithm developed here is for the slave laser (or any 2 section high order surface grating semiconductor laser) and can be potentially extended to the master-slave configuration as well.

5.6.1 Determination of Athermal Path

As explained in the previous section, Figure 5.15 captures the core idea of the current based athermalisation process. As the temperature is increased, the longitudinal and Bragg peak

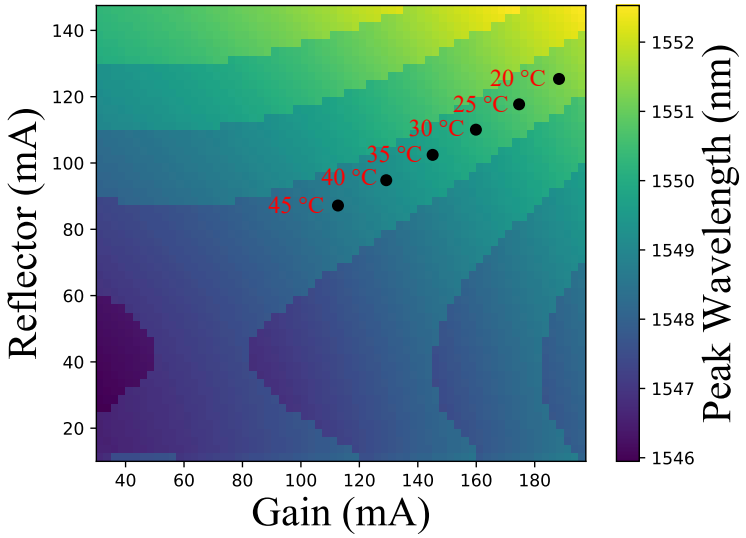


Figure 5.22: Wavelength map of the slave laser at 20 °C. The *black dot* points at the injection current required at mentioned temperature to keep the wavelength unchanged.

redshifts, resulting in the redshifting of the entire tuning maps. The *black dot* on the wavelength and SMSR tuning maps of slave laser in Figure 5.15, and 5.16 tracks a particular wavelength while maintaining a high SMSR for the mentioned device temperature. The movement of the *black dot*, suggests that in order to counteract the effect of temperature change on the operating wavelength, the injection current in the various sections needs to be properly tuned. In Figure 5.22, the movement of *black dot* (required bias current to keep the wavelength of the slave laser constant for the given temperature) on the wavelength map, at 20 ^{o}C is plotted. The movement of the *black dot* shows the athermal path that must be followed. An important consideration for any transmitter employed in a communication system is high SMSR. In Figure 5.23, a contour plot of SMSR of the slave laser at 20 ^{o}C is plotted. The plot shows several equipotential curves (constant SMSR). The features of the contour plot suggest that, the SMSR is highest for the central path between the mode boundaries. From Figure 5.22, and 5.23, moving along the path of highest SMSR, while appropriately changing the bias to various sections to counteract the effect of temperature change can lead to a stable output wavelength irrespective of the device and surrounding temperature with optimised performance.

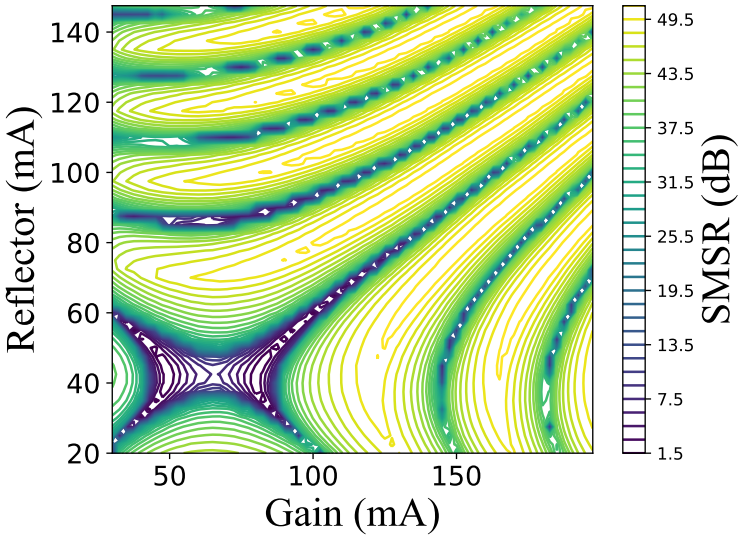


Figure 5.23: Contour plot of the SMSR map of slave laser at 20 ^{o}C.

5.6.2 Power Maps

An important consideration while developing the algorithm to realise athermalised transmitter was to reduce the complexity and total time required to find the look up table of operating current for various device temperatures to provide a constant wavelength output. Determining the athermal path through spectral measurements i.e., through wavelength and SMSR maps is a time consuming affair (subjected to spectral resolution of the measurement). In order to reduce the total run time of the process, the amount of spectral measurements needs to be limited.

In Figure 5.24, the power map of the slave laser at 20 ^{o}C is plotted. The map suggests that the power output of the slave laser reduces considerably at the mode boundary. As an example, this can be clearly seen in Figure 5.25, which plots the variation of peak power and wavelength of the emission with respect to the injected current in the reflector section at a constant gain current of 175 mA. As observed in Figure 5.24, Figure 5.25 also shows the reduction in the total power emission of the slave laser at the junction of two longitudinal mode. So the mode boundaries can be found through power maps. Hence the athermal path can be determined through power maps by locating the mode boundaries of a particular longitudinal mode of interest and then determining the central path between those mode boundaries.

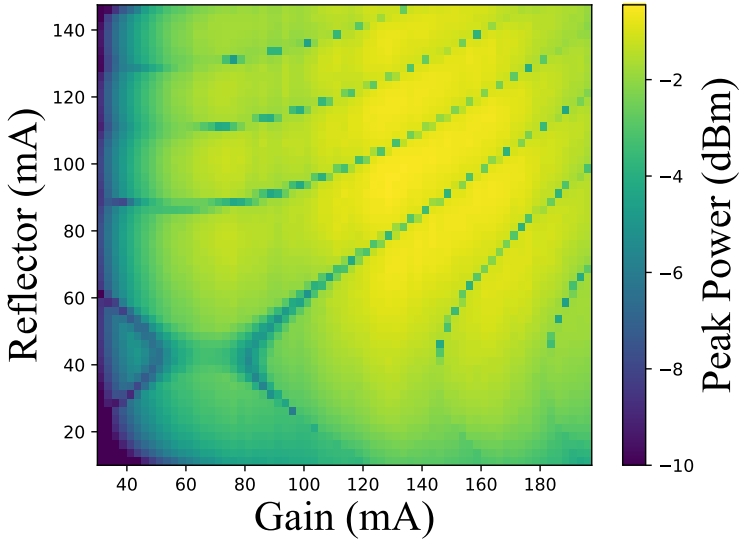


Figure 5.24: Power map of the slave laser at 20 ^{o}C.

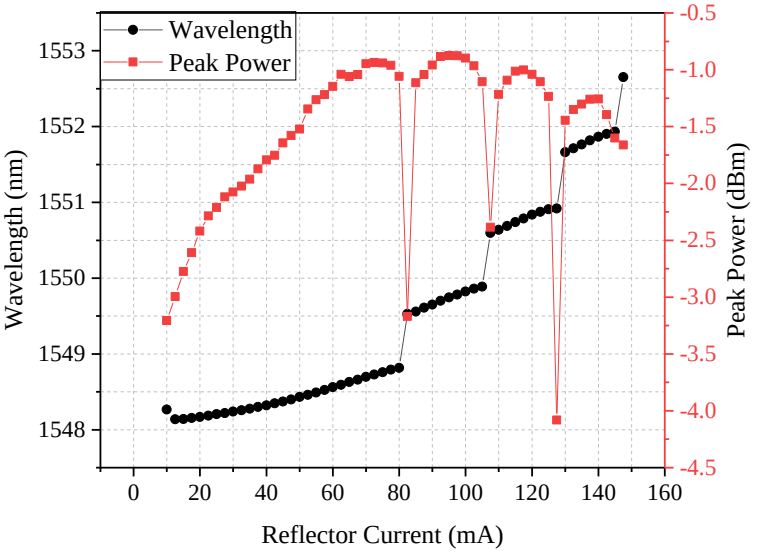


Figure 5.25: Variation of wavelength and peak power of slave laser with the reflector current at 20 ^{o}C, while the gain section is biased at 175 mA.

Now, power maps can be evaluated without any spectral measurements. Figure 5.26, shows a simple setup to evaluate the power map of the slave laser using a photodiode. The slave laser was biased using 2 current sources, ILX Lightwave: LDX3200. The optical output of the slave laser was passed to a photodiode, the generated photocurrent was detected and measured using a Keithley 6485 Picoammeter.

In Figure 5.27, the generated power map of the slave laser at 20 ^{o}C is plotted. The red curve is the estimated athermal path calculated by locating the mode boundaries corresponding to the chosen longitudinal mode. Measuring the power maps by the use of the

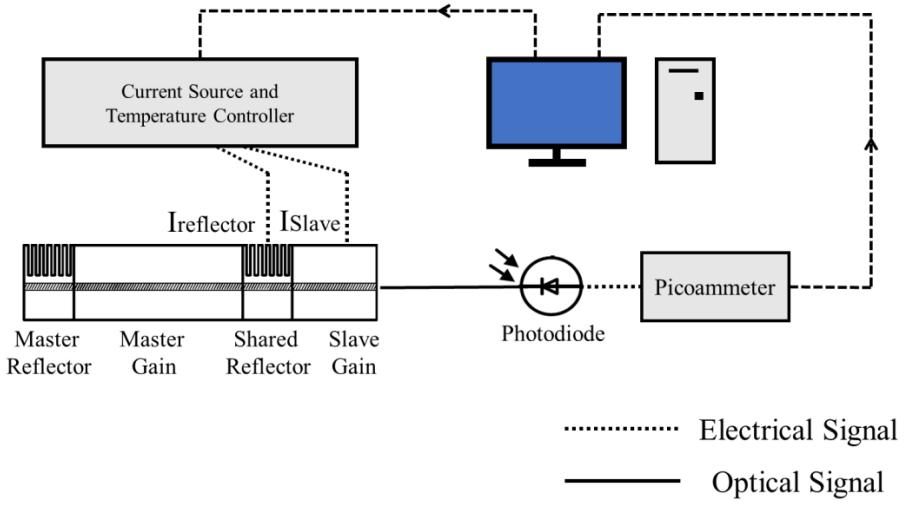


Figure 5.26: Experimental setup to determine the power map of the slave laser.

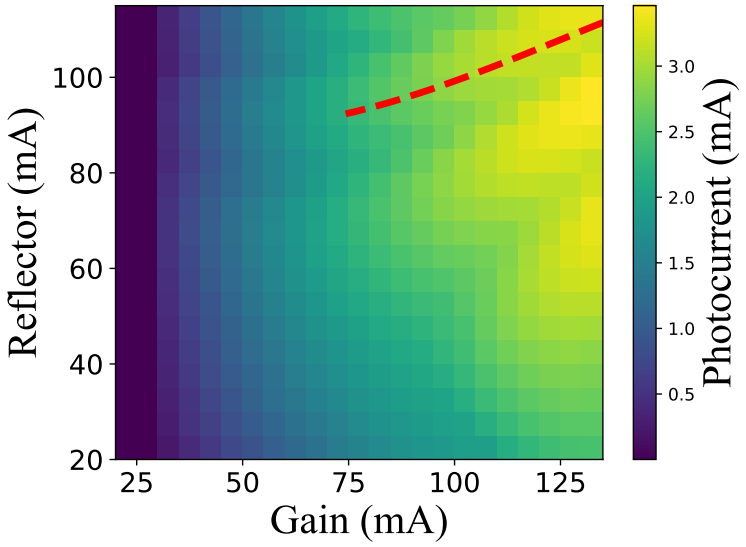


Figure 5.27: Generated power map of the slave laser at 20 ^{o}C using the experimental set up shown in Figure 5.26, which doesn't require any spectral measurement.

above mentioned setup reduces the time required to generate these maps from several hours to few minutes.

5.6.3 Generating Look-Up Table through Vector Analysis

As suggested in Figure 5.15, in order to compensate for temperature change, the bias currents to the 2 sections need to be properly adjusted to negate the effect of wavelength change through temperature variation. In this section, we will now develop a reliable and automated way to generate the look up table of required injection current to the gain and reflector sections of the slave laser for a given device temperature to attain wavelength stability with high SMSR.

The wavelength of a laser is highly sensitive to both temperature and bias current fluctuations and these effects need to be properly accounted for in order to generate a look up table. Within a mode boundary of interest, the change of wavelength with reflector current, gain current, and temperature can be written as:

$$\Delta\lambda_{reflector} = \frac{d\lambda}{dI_{reflector}}\Delta I_{reflector} = A\Delta I_{reflector} \tag{5.7}$$

$$\Delta\lambda_{gain} = \frac{d\lambda}{dI_{gain}}\Delta I_{gain} = B\Delta I_{gain} \tag{5.8}$$

$$\Delta\lambda_{T} = \frac{d\lambda}{dT}\Delta T = C\Delta T \tag{5.9}$$

Here, A, B, and C are the rate of change of wavelength with reflector current, gain current, and temperature. In order to athermalise the laser the overall drift in wavelength because of change in device temperature and bias current should be zero:

$$\Delta\lambda_{reflector} + \Delta\lambda_{gain} + \Delta\lambda_{T} = 0 \tag{5.10}$$

$$A\Delta I_{reflector} + B\Delta I_{gain} + C\Delta T = 0 \tag{5.11}$$

Equation 5.11 essentially relates the device temperature to the required bias currents in order to attain constant wavelength operation once the TEC is off or not present. In order to generate a look up table to relate the bias currents with device temperature, exact behaviour of the A, B, and C parameters needs to be defined on the athermal path determined earlier. Parameter A, and B can be found by measuring the rate of change of wavelength with respect to reflector and gain currents along the athermal path. Figure 5.28 illustrates this process. At a given point on the athermal path, i.e., $I_{gain} = I_{gain,0}$, $I_{reflector} = I_{reflector,0}$, $\lambda = \lambda_0$, and $T = T_0$, parameter A can be found by measuring the rate of change of wavelength at the chosen point with respect to the reflector current at constant gain current, i.e., $I_{gain} = I_{gain,0}$. This is given by the blue arrow in Figure 5.28. Similarly, parameter B can be found by measuring the rate of change of wavelength at the chosen point with respect to the gain current at constant reflector current, i.e., $I_{reflector} = I_{reflector,0}$. This is given by the green arrow in Figure 5.28. So at any point on the athermal path, parameter A, and B can be written as:

$$A = \frac{\partial\lambda}{\partial I_{reflector}} = \frac{\lambda_1 - \lambda_0}{I_{reflector,1} - I_{reflector,0}} \tag{5.12}$$

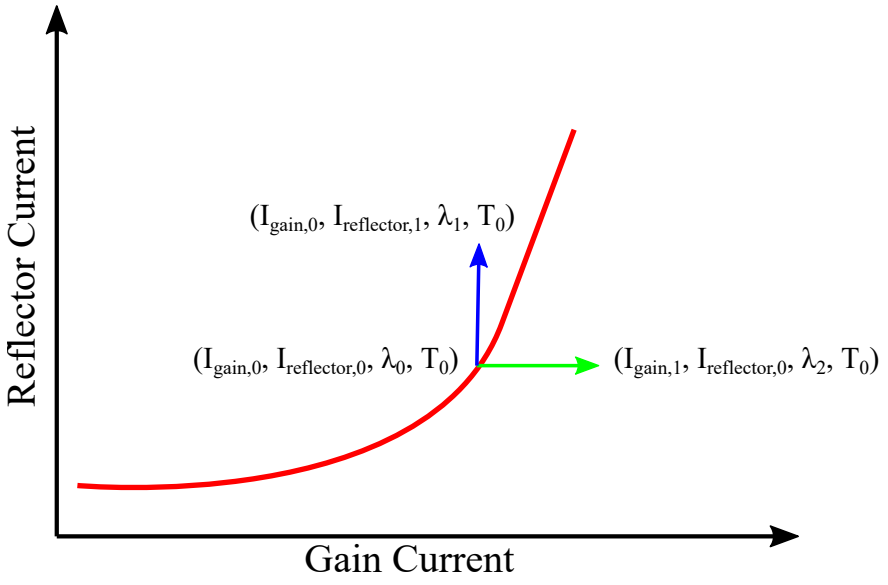
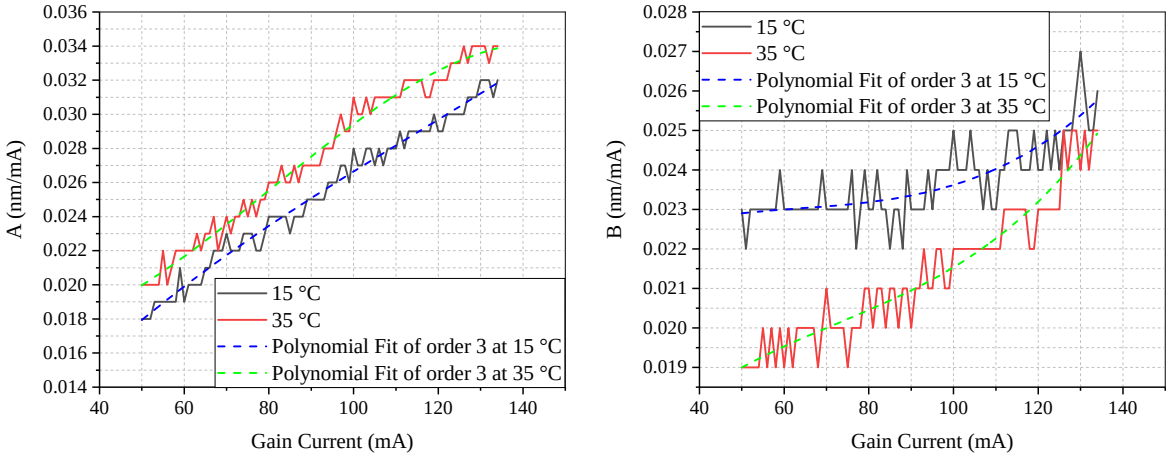


Figure 5.28: Determination of A and B parameter.

$$B = \frac{\partial \lambda}{\partial I_{gain}} = \frac{\lambda_2 - \lambda_0}{I_{gain,1} - I_{gain,0}} \tag{5.13}$$

By using equation 5.12, and 5.13, a look up table of parameter A and B can be found at a given temperature. In this study we have considered A and B to be a function of temperature as well to attain a higher level of wavelength stability. In Figure 5.29, the variation of A and B as a function of gain current at 15 and 35 ^{o}C is plotted, the relationship with reflector current can be simply found using the athermal path determined earlier. As shown in Figure 5.29, the data is fitted to a polynomial of order 3 allowing approximate knowledge of the parameter at any position along the athermal path. We have assumed that the A and B parameters vary linearly with temperature. From the measurements done at 15 and 35 ^{o}C, a slope can be found through which the value of A and B parameter can be determined at any temperature along the athermal path. Parameter C can be simply found by measuring the rate of change of wavelength with respect to temperature along the athermal path. Parameter C is given by equation 5.14, where λ_1 and λ_0 are the emission wavelength at temperature T_1, and T_0, respectively at any point along the athermal path. The variation of parameter C along the athermal path is illustrated in Figure 5.30.



(a) **(b)**

Figure 5.29: Variation of Parameter (a) A, and (b) B with the gain current at the mentioned temperatures.

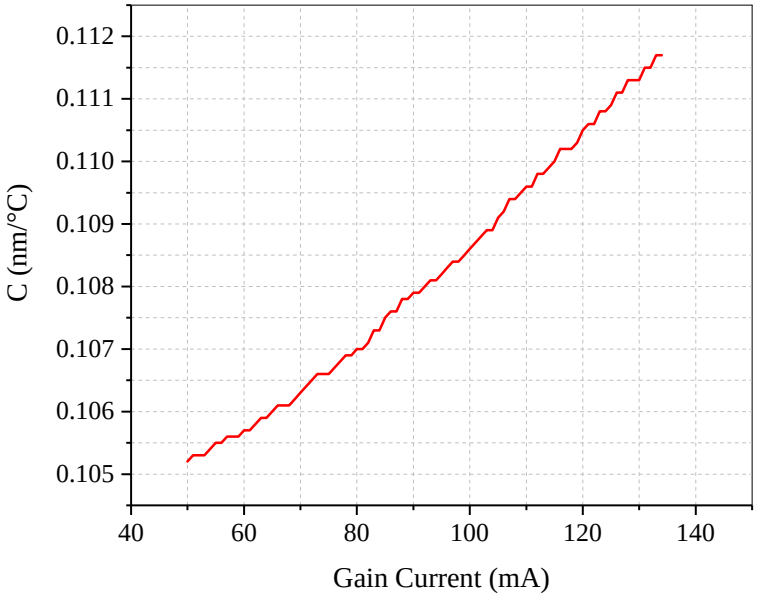


Figure 5.30: Variation of Parameter C with the gain current.

$$C = \frac{\partial \lambda}{\partial T} = \frac{\lambda_1 - \lambda_0}{T_1 - T_0} \tag{5.14}$$

In Figure 5.31, the variation of the emission wavelength of the slave laser along the athermal path at 15 ^{o}C is plotted. Depending on the requirement of the application, any wavelength on the athermal path can be chosen to be athermalised. Also, it should be noted that other wavelengths can also be achieved by carefully choosing the appropriate longitudinal mode in Figure 5.22. The wavelength requirements sets the initial condition on I_{gain}, $I_{reflector}$,

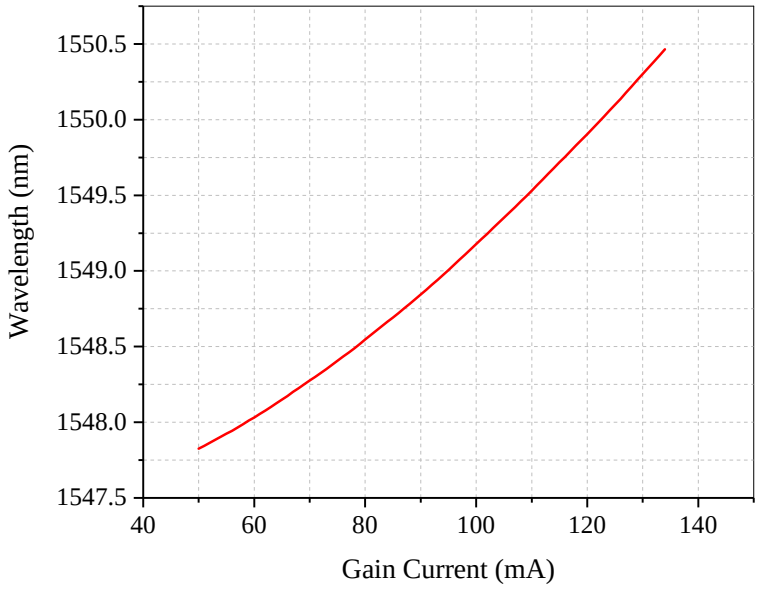


Figure 5.31: Variation of the wavelength of the slave laser along the athermal path at 15 ^{o}C.

and T (15 ^{o}C in this case). For these initial values of gain current, reflector current, and temperature, equation 5.11 can be solved to generate a look-up table of the injection current required versus the device temperature to athermalise the chosen wavelength. Table 5.2 shows the example of one such look-up table found to athermalise the DWDM channel at 1550.12 nm. The look up table found is for the temperature range 15 to 35 ^{o}C at an interval of 0.5 ^{o}C. A look-up table for a larger temperature range (this depends on the maximum temperature the device can operate on with reasonable performance) with a finer interval can be found by following the process defined in this section.

Since we determined the athermal path through power map, this reduces the overall time required to generate these look up tables for any unknown 2 section high order surface grating laser. Measuring a sufficiently detailed power map and determining the athermal path takes approximately 5 minutes. Then doing the spectral measurements to determine A, B, and C parameters takes another 3-4 minutes. So the entire process of generating look up tables for these devices take only $\sim$ 10 minutes.

5.6.4 TEC Free Operation

In this section, we will assess the performance of the generated look up tables for various wavelengths on the DWDM grid supported on the athermal path. In order to simulate the

Table 5.2: Look-up table found to athermalise DWDM channel at 1550.12 nm.

Temperature (^oC)	Gain Current (mA)	Reflector Current (mA)	Temperature (^oC)	Gain Current (mA)	Reflector Current (mA)
15	125.473	108.03	25.5	94.3906	97.474
15.5	124.07092	107.53	26	92.78762	96.998
16	122.66287	107.02	26.5	91.16779	96.528
16.5	121.24869	106.51	27	89.52995	96.063
17	119.82823	106	27.5	87.87289	95.605
17.5	118.40128	105.49	28	86.19527	95.153
18	116.9676	104.98	28.5	84.49573	94.708
18.5	115.52695	104.46	29	82.77268	94.271
19	114.07902	103.95	29.5	81.02439	93.843
19.5	112.62349	103.44	30	79.24909	93.425
20	111.15997	102.93	30.5	77.44482	93.017
20.5	109.68809	102.43	31	75.60934	92.62
21	108.20739	101.92	31.5	73.74038	92.236
21.5	106.71741	101.42	32	71.83531	91.866
22	105.21762	100.91	32.5	69.89135	91.511
22.5	103.70746	100.41	33	67.9053	91.174
23	102.1863	99.914	33.5	65.87388	90.855
23.5	100.6535	99.419	34	63.79321	90.558
24	99.10831	98.927	34.5	61.65929	90.284
24.5	97.55001	98.439	35	59.46768	90.038
25	95.97773	97.954			

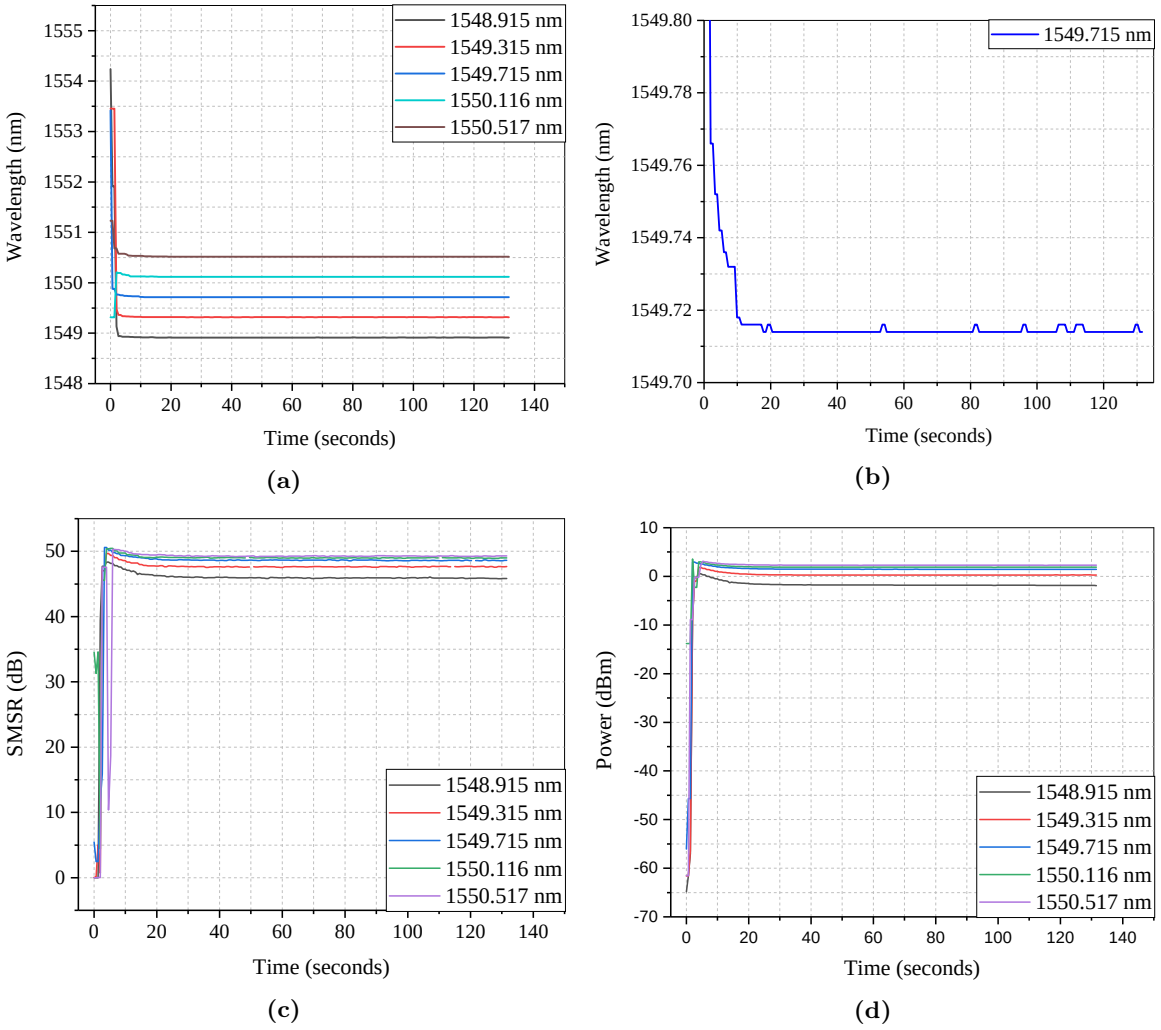


Figure 5.32: Performance of the developed athermalisation algorithm at a constant ambient temperature of 20 ^{o}C, athermalising 5 wavelengths on the DWDM grid spaced by 50 GHz/ 0.4 nm.

TEC free operation in our experimental setup, we have turned off the heating/cooling of the laser by turning off the TEC. Also, in order to simulate the ambient temperature we placed the laser inside a temperature chamber which can control the ambient temperature of the laser with high precision. The ambient temperature was maintained at 20 ^{o}C until unless mentioned otherwise. Both sections of the slave laser were initially biased at an arbitrary current values. Then in order to athermalise the laser, the temperature of the slave laser is continuously monitored through the thermistor and according to the look-up table generated for the given wavelength, the bias current were changed corresponding to the measured device temperature.

Figure 5.32(a) illustrates the performance of the look up table generated for 5 wavelengths

which lie on the generated athermal path at an ambient temperature of 20 ^{o}C. These wavelengths lies on the DWDM grid (DWDM ITU channel 33.5, 34, 34.5, 35, and 35.5) and are 50 GHz/0.4 nm spaced. Figure 5.32(b), focuses on the channel at 1549.715 nm, as illustrated the slave laser reaches the required channel wavelength in $\sim$ 10 seconds (the timing measurement was limited by the sweep speed of the optical spectrum analyser, the actual time was lower than 10 seconds). Once settled, the laser operates at the channel wavelength with a measured accuracy of $\pm$ 2 pm ($\pm$ 250 MHz), although this is at our limit of detection. In Figure 5.32(c), and (d) the SMSR and peak power of the corresponding channel in Figure 5.32(a) is plotted. An SMSR of $>$ 45 dB with peak power of $>$ -2 dBm is achieved for all the channels. The peak power can be further boosted by integrating a semiconductor optical amplifier (SOA) with the laser as shown in [79].

Since the measured stability of the emission wavelength of the athermalised laser is so precise, this technique can be successfully implemented for even smaller channel spacing suitable for flexible optical network. In Figure 5.33, the performance of the athermalised slave laser set for emission wavelengths mentioned with a channel spacing of 12.5 GHz/ 0.1 nm is plotted. As measured in the previous case, the measured wavelength stability here is also $\pm$ 2 pm ($\pm$ 250 MHz).

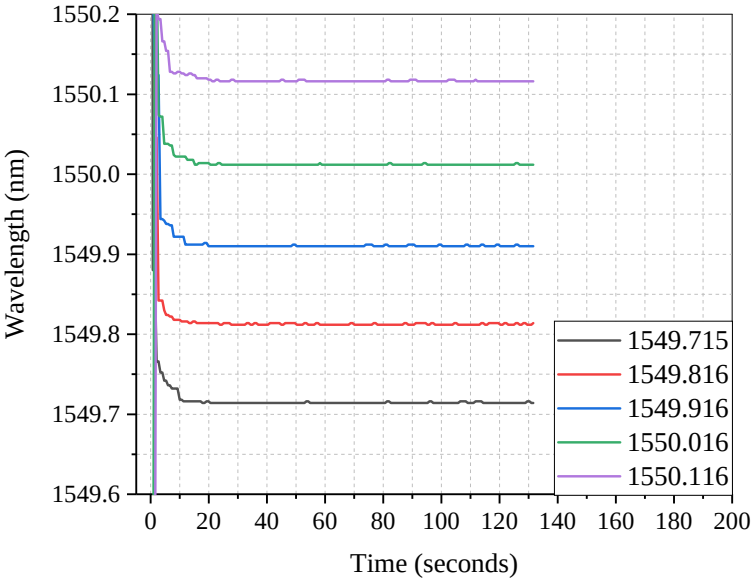


Figure 5.33: Performance of the developed athermalisation algorithm at a constant ambient temperature of 20 ^{o}C, athermalising 5 wavelengths spaced by 12.5 GHz/ 0.1 nm, confirming the suitability of the developed algorithm for finer grid spacing.

In access networks, data centres, customer premise etc. the ambient around the transmitter is not controlled and can vary significantly. So one of the major requirement from any transmitter is to maintain its emission wavelength fixed irrespective of the ambient temperature. In Figure 5.34, we record the performance of the athermalised scheme developed with continually varying ambient temperature. The ambient temperature was changed by sweeping the temperature of the temperature-chamber from 15 to 35 ^{o}C. A wavelength stability of $\sim$ 0.014 nm/ 1.5 GHz is achieved over the swept temperature range, as shown by the red curve in Figure 5.34. This corresponds to a wavelength drift of 0.7 pm/^{o}C, which is $\sim$ 140 times smaller than the intrinsic drift of 100 pm/^{o}C. The variation in the output wavelength in this case is due to the approximation used earlier to derive the variation of A and B parameter with temperature. We have linearly approximated the variation of A and B with temperature, but a polynomial approximation would result in better stability.

However, with the drift measured, and knowing the parameter A and B values along the path we can improve this drift. By simply multiplying the B (or A) parameter by the difference between the measured curve and the target wavelength and by making the resulting small adjustment to the lookup table we can completely eliminate the drift. The black curve in Figure 5.34 shows the measured wavelength after readjusting the look-up table. A wavelength stability of $\pm$ 2 pm ($\pm$ 250 MHz) is now measured which is limited by the detection limit of the optical spectrum analyser used.

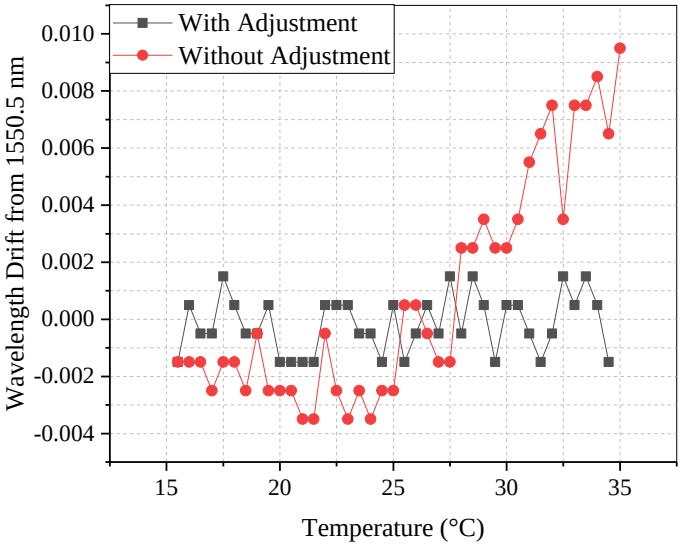


Figure 5.34: Performance of the developed algorithm with varying ambient temperature with and without adjustment of the look-up table.

5.7 Conclusion

A novel 4-section integrated optical transmitter has been demonstrated. The unique architecture of the chip, employing a master-slave configuration, enables a significant reduction in the chirp caused by direct modulation, enhances the modulation response, and reduces the optical linewidth significantly. As a result, an error-free transmission of a 10 Gb/s on-off keyed signal over a transmission on 37 km of standard single mode fiber (SSMF), with only 2 dB penalty vs. the back-to-back case, has been achieved. The device also offers wavelength tunability, enabling the generation of 8 channels placed on a 50 GHz grid. We then demonstrated an athermal bias current procedure on this novel PIC to illustrate an athermal transmitter for uncooled WDM systems based on current-tuning. We demonstrated a steady state athermalisation scheme by utilising tuning maps and achieving a mode-hop free performance with a wavelength stability of $\pm$ 3 pm ($\pm$ 375 MHz) while maintaining an SMSR of $>$ 34 dB over the temperature range 10-60 ^{o}C. Subsequently, we demonstrated a directly modulated athermal transmitter, modulated at 2.5 Gb/s and showed error-free transmission through 37 km of SSMF over the temperature range 10-45 ^{o}C with wavelength stability of $\pm$ 5 pm ($\pm$ 625 MHz). We observed a receiver sensitivity of -16 dBm at 30 ^{o}C after 37 km of SSMF, which corresponds to a power penalty of 1 dB. The power penalty observed with varying temperature was 0.2 dB/^{o}C. Attaining athermalisation manually is a cumbersome process and take hours to generate the required look-up tables. Also, due to manual nature of the look-up table the generated look-up tables are often far from optimised for the maximum temperature range possible while maintaining a high SMSR throughout. In order to attain reliability, we developed an algorithm to generate look-up while keeping the SMSR high. We successfully presented the operation of the slave laser without any cooling/heating. We counteracted the effect of thermal redshifting by properly adjusting the biases to various sections according to the look up table generated through the developed algorithm. By doing so, we attained a wavelength $\pm$ 2 pm ($\pm$ 250 MHz). Also, automation of the athermalisation process has reduced the time required to generate these look-up tables from couple of hours to only few minutes. The exceptional performance of the PIC as a DML, and as an athermal transmitter, coupled with a simple fabrication process, makes the proposed PIC laser an attractive, cost, and power efficient solution for next generation optical access networks.

Chapter 6

Conclusions & Future Work

6.1 Conclusions

The central objective of this work was to develop technologies that can potentially improve spectral efficiency and reduce power consumption of a lightwave system. In that endeavour we explored 3 unique optical transmitters designs:

Semiconductor Lasers based on High Order Surface Gratings with Non Uniform Period

Semiconductors lasers based on simple fabrication were previously developed in the Semiconductor Photonics group of Trinity College Dublin led by Prof. John Donegan. In order to attain single mode operation, these devices employ high-order grating etched on the ridge waveguide structure. Etching a high-order surface grating simplifies the fabrication process as high-order gratings don't require high-resolution lithography techniques and employment of surface gratings removes the need of complex regrowth process from the fabrication. The first few runs of devices fabricated following this simple fabrication employed a high order surface grating with uniform slot period. The fabricated devices showed potential to be implemented as an *array of independent lasers* for applications requiring multicarrier transmitters. These fabricated lasers showed a very good single-mode performance with an SMSR in excess of 50 dB and an overall tunability of $\sim$ 3-4 nm. A complete C-band coverage was also achieved by using 11 such lasers on an array using temperature tuning. Even though the fabricated device was showing exceptional single-mode performance at lower temperature, the SMSR degraded significantly as the temperature was increased and even caused mode hopping beyond 60 ^{o}C. This degradation in the performance is due to the smaller Free spectral range (FSR) of high order gratings, typically $\sim$ 35-40 nm. The gain curve redshifts with the increased temperature, this results in the increased gain experienced by the adjacent mode which is one FSR away from the desired mode. This mode competition resulted in SMSR degradation and

eventually mode-hopping. In order to tackle this issue and improve over-temperature performance of these lasers, a new grating structure was designed which comprises of a non uniform grating, employing vernier effect to suppress the feedback experienced by modes adjacent to the desired mode. The suppression of undesired mode increased the maximum achievable temperature without mode hopping to up to 90 ^{o}C. Previously, efforts have been made to improve the SMSR of these devices, in this work we aimed to focus on threshold and slope-efficiency. We characterised over 100 devices employing non-uniform grating with 2, 3 and 4 periods. We found that the performance of these devices degrades as the non-uniformity increases with 2 period lasers performing best in terms of threshold and slope-efficiency while also improving the over-temperature performance. We then verified our finding by modelling the device characteristics using the scattering matrix method. We also found out that the slope efficiency and threshold of these 2 period grating lasers can be further improved by reducing the number of slots. Since reducing the number of slots results in the reduction of SMSR due to increment in the reflection bandwidth, a detailed modelling study was carried out. We also presented a way to select the configuration of slots so that the resulting device takes full advantage of the non-uniform grating while maintaining a high slope-efficiency and a high SMSR. Keeping this in mind - the simulated design benefiting from the advantages of non-uniform grating showed a slope-efficiency of 0.17 mW/mA, and threshold of $\sim$ 17 mA while maintaining an SMSR of $>$ 43.5 dB.

Gain Switched Optical Frequency Comb

Gain switched optical frequency comb sources (GS-OFCS) utilising external optical injection have shown considerable potential for their adoption in next generation, high capacity, and flexible optical networks. The credit goes to their ability to provide high spectral efficiency, flexibility, stability, and low noise characteristics which make them a perfect candidate for networks employing advance modulation formats. As a result, in this work, we considered externally injected gain switched optical frequency comb as a potential multicarrier transmitters for future optical networks. We presented an extensive experimental development and investigation of these sources. We first demonstrated the process of generation of an optical frequency comb based on the external injection of a gain switched Fabry-Pérot (FP) laser.

The presented GS-OFCS takes advantage of external optical injection to generate optical frequency comb with clear multiple discernible comb tones with very high spectral purity. We presented results on the free spectral range (FSR) tunability showing OFCS with comb tones spacing varying from 6.25 GHz to 25 GHz. The FSR of the generated OFC depends solely on the frequency of the applied high power sinusoidal signal (gain-switching signal), therefore very precise FSR can be attained. We then presented results on the quasi-continuous wavelength tunability of the generated OFC by injecting into various longitudinal modes of the FP laser. By doing so, we achieved a wavelength tunability of 31 nm. Furthermore, finer wavelength tunability can be achieved by temperature tuning the FP laser. We then presented results on the low-noise characteristics of the comb tones. All the comb tones in the OFC showed high spectral purity, equivalent to the master laser. The linewidth of the generated comb tones was measured through a phase noise setup and was 40 kHz. The high-spectral purity of the generated comb was direct consequence of the external optical injection. Since, external optical injection plays such a vital role in the generation of these OFCS, we studied it in great detail. We provided experimental verifications of the various benefits reaped from optical injection including single mode performance with high SMSR, wavelength stabilisation, high output power, enhancement of resonance frequency and modulation response, and low-noise.

Photonic Integrated Circuit (PIC) Employing a Master-Slave Configuration

In order to meet the ever increasing demand for bandwidth in the optical access networks, continual industry innovation is needed. Next generation passive optical network 2 (NG-PON2) is one such developed ITU standard. Implementation of such a standard requires transmitters capable of transmitting high speed data streams over longer distances at finer grid spacing ($\leq$ 50 GHz). Externally modulated lasers comfortably meets these requirements but their cost and power profile pose challenges. Direct modulation on the other hand despite being simple, small footprint, cost and energy efficient suffers from frequency chirp imposed on the signal. Chirped signals are more susceptible to dispersion effects in fiber and ultimately leads to intersymbol interferences, if the signal is to be transmitted over longer distances required by the modern optical access networks. In cost sensitive applications like access networks, directly modulated lasers are the transmitter of choice. At current speeds

chirp doesn't limit performance significantly but as the system is evolving towards higher data rates (10 Gb/s), chirp becomes critical. Optical external injection has been known to improve output characteristics of the injected laser. Previously, optical injection from an external laser has been utilised in directly modulated system to improve the system performance. In this work, in order to attain further compactness, cost-efficiency, and ease of fabrication while reaping the benefits of direct modulation, we developed a multi section PIC utilising optical injection by having 2 lasers in a master-slave configuration. We presented results on chirp reduction, modulation response enhancement, and linewidth reduction enabled by the unique architecture of the chip. We then presented transmission results showing an error free performance of a 10 Gb/s on-off keyed signal after transmission over 37 km of standard single mode fiber. We observed a receiver sensitivity of -17.9 dBm at 7 % FEC limit after 37 km of transmission and the observed power-penalty was 2 dB, compared to back-to-back case. We did complete spectral characterisation of the PIC and presenting tuning maps of wavelength, power and SMSR. Those maps were then utilised to identify 8 channels on a 50 GHz grid. Since access networks works on a narrow grid spacing, wavelength stability becomes one of the most critical parameters, which is highly temperature dependent. Presently, in order to achieve wavelength stabilisation, the temperature of the laser is continuously controlled by the use of a thermo-electric cooler. This increase the power-budget significantly and adds to the cost. In this work we developed a current based athermalisation technique to attain wavelength stability and to realise an athermal transmitter. We first demonstrated a steady state athermalisation achieving a mode-hop free performance with a wavelength stability of $\pm$ 3 pm ($\pm$ 375 MHz) while maintaining a SMSR of $>$ 34 dB over the temperature range of 10-60 ^{o}C. Subsequently, we presented results on athermal transmission, showing error free performance of a 2.5 Gb/s on-off keyed signal after transmission over 37 km of standard single mode performance over the temperature range of 10-45 ^{o}C with wavelength stability of $\pm$ 5 pm ($\pm$ 625 MHz). We observed a receiver sensitivity of -16 dBm at 30 ^{o}C after 37 km of fiber transmission which corresponds to a power penalty of 1 dB. The power penalty observed with temperature increment was 0.2 dB/^{o}C. Attaining athermalisation manually is a cumbersome and unreliable process and require hours to generate the look-up tables which are often far from optimised. This motivated us to develop an algorithm to simplify and optimised the athermalisation process. The developed algorithm then showed a wavelength stability of $\pm$ 2

pm (± 250 MHz) under TEC-free operation.

Now for deployment of a transmitter in NGPON2 cost will be a key consideration among others. In that regards communication industry is considering both direct and external modulation solutions. As discussed in section 5.2, both these solutions have their perks and drawbacks. DMLs provide a cost effective solution but suffers from chirp (hence require dispersion compensating components) and wavelength fluctuation under burst mode operation due to self heating on turn on. EMLs don't require dispersion compensation and usually performs well but are costly and have high insertion loss.

6.2 Future Work and Other Applications

6.2.1 Dynamic Free Spectral Range Sweep

As discussed in chapter 4, the gain-switched comb sources can have their free spectral range (FSR) tuned over a range of several gigahertz by simply tuning the frequency of the applied gain-switching signal. Figure 6.1(a) shows the superimposed comb spectra for four FSR settings, here the FSR was tuned from 7 to 10 GHz using a voltage controlled oscillator (VCO). One crucial aspect of gain-switched comb sources is their ability to repeatedly replay exact wavelength over every scan due to two reasons: firstly, irrespective of the applied gain switching frequency, the generated comb at every FSR setting has a common comb line, this

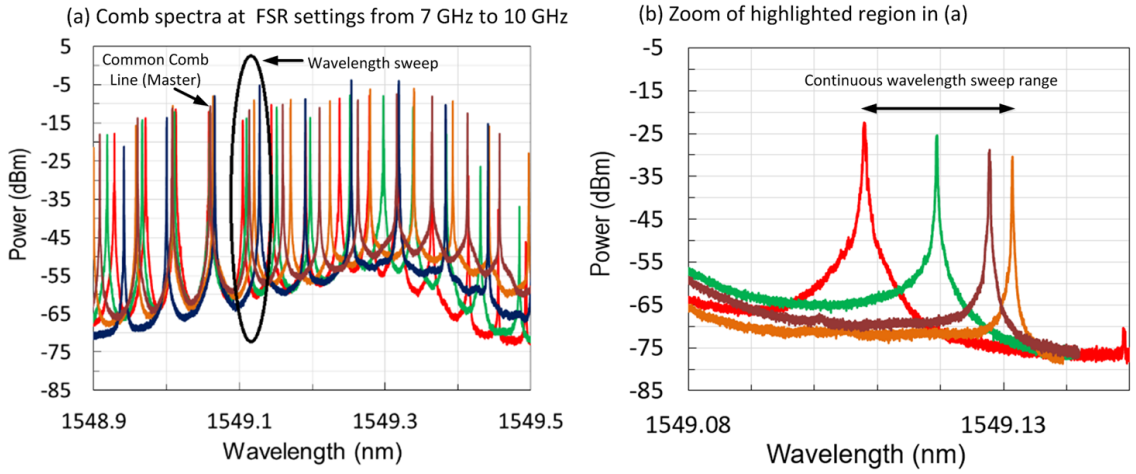


Figure 6.1: (a) Measured optical comb spectra for four different frequencies from the VCO. Note how one comb line (the master laser) remains fixed throughout the VCO sweep, marked with an arrow. (b) Zoom in on the relevant spectral region over which the linear frequency sweep will take place.

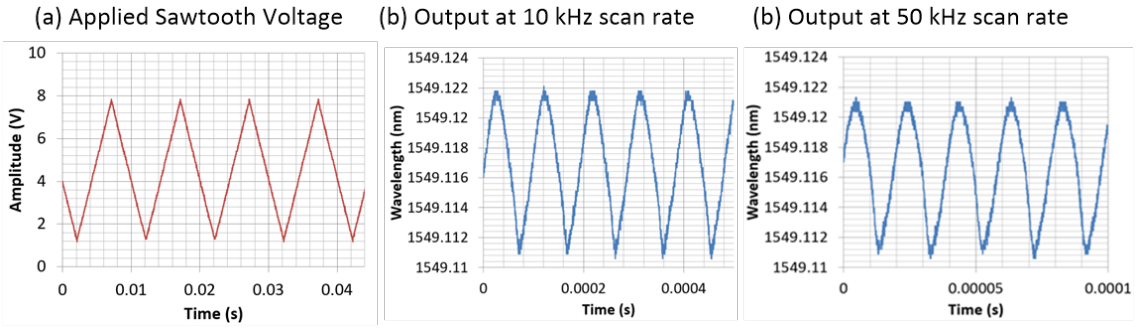


Figure 6.2: (a) Measured optical comb spectra for four different frequencies from the VCO. Note how one comb line (the master laser) remains fixed throughout the VCO sweep, marked with an arrow. (b) Zoom in on the relevant spectral region over which the linear frequency sweep will take place.

corresponds to the master laser and is explicitly indicated in Figure 6.1(a). Secondly, the next adjacent comb line must be one whole FSR away from the common line, therefore the spectral placement of this comb line is completely under the control of the VCO as shown in Figure 6.1(b), which can be easily filtered using an optical band pass filter. A continuous sweep (6 to 10 GHz, in this case) in the gain-switching frequency can be obtained by the application of an appropriate sawtooth signal to the VCO. This will then in turn sweep the FSR of the optical comb from 6 GHz to 10 GHz. The repetition rate of the sawtooth waveform is set to 10 kHz and 50 kHz. To emulate an optical fiber Bragg grating sensor we use an optical discriminator that converts wavelength to an easily detectable optical power. The time domain detector output is displayed on an oscilloscope in Figure 6.2, therefore we have the ability to see transduced changes in transmission of the optical filter/sensor on an oscilloscope. We have demonstrated this at a sweep rate of 50 kHz, which would allow for audio signals or other signals with similar rates of change to be detectable by an appropriate sensor. Even though we have demonstrated the FSR sweep at 50 kHz refresh rate, the limitation is imposed by the tuning speed of the VCO to adjust the output frequency. In principle this FSR sweeping technique could be applied to the laser at sweep speeds limited by the laser dynamics and thereby, the sweep rates could potentially approach hundreds of megahertz.

6.2.2 Dual-Comb Spectrometer

Dual-Comb spectroscopy is an emerging new spectroscopic tool that exploits the frequency resolution, frequency accuracy, broad bandwidth, and high power of optical frequency combs for high resolution, high sensitivity spectroscopy. Dual-comb spectrometry allows for an

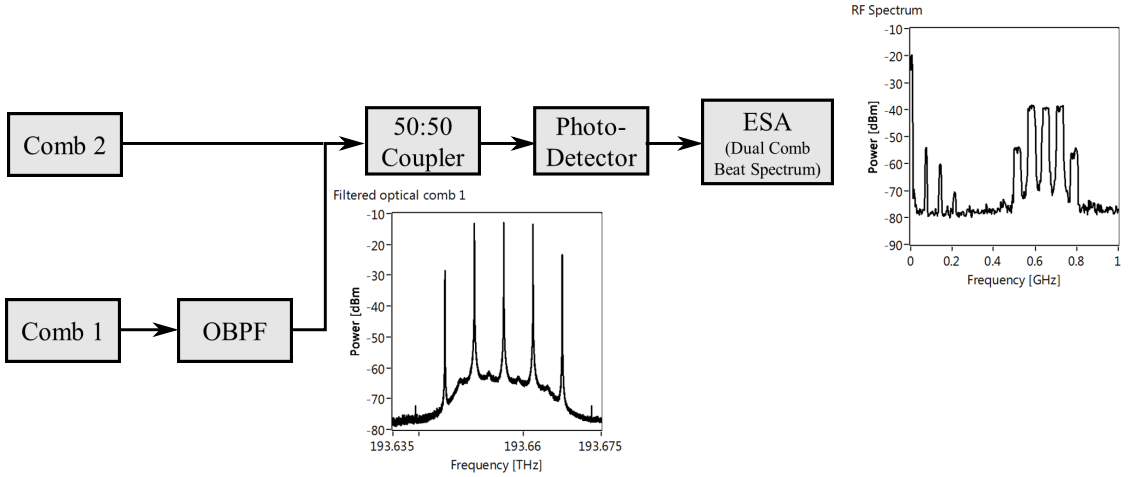


Figure 6.3: Experimental setup to create a dual comb spectrometer.

optical spectrum to be scaled and mapped to an easily detected electrical spectrum [128]. As the name suggests, in order to construct a dual-comb spectrometer, one needs two similar optical frequency combs (OFC) with slightly different FSR offsets. A gain switched OFC can be an ideal candidate for this because of their ability to attain a relatively flat comb with wide range of FSRs. The experimental set-up for the realisation of a dual-comb spectrometer is presented in Figure 6.3. We generated two gain-switched OFC with FSRs of 5.56 GHz and 5.5 GHz for comb 1 and comb 2 respectively. This corresponds to FSR offset, Ω, of 60 MHz. The combs are tuned in such a way that there is a common comb line at a frequency of 193.610 THz. As a proof of concept, we used an optical band pass filter (OBPF) to emulate a gas chamber and set out to detect the shape and bandwidth of the OBPF. Comb 1 passes through the OBPF with variable central wavelength and variable passband width (Yenista Optics XTM-50). The optical spectra of the filtered comb is shown in Figure 6.3. The modified comb 1 having passed through the OBPF is coupled with the unperturbed comb 2. The coupled combs are then mixed on a photodiode (PD) and then the output of the photodiode is observed on an electrical spectrum analyser (ESA). Note the similarity between filter optical comb and the detected beat spectrum. This shows the fundamental functionality of our dual-comb spectrometer using gain-switched lasers to be able to measure spectral changes in an optical medium. We still have many parameters to vary, to create FSRs around 100 MHz and this would allow us to measure spectral changes in an optical medium with femtometer resolution.

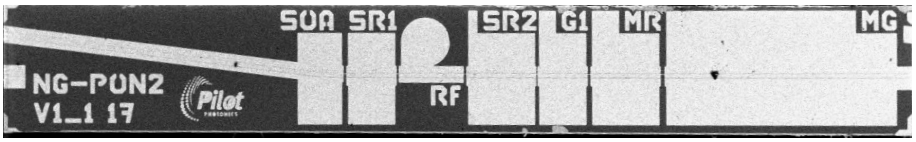


Figure 6.4: Improved PIC utilising optical injection through master-slave configuration with an attenuator section for improved isolation between master and slave laser.

6.2.3 Improved PIC Design

For a true master-slave configuration, any feedback/reflections from slave laser must be prevented from entering the cavity of the slave laser. In a discrete system, this is achieved by either integrating an isolator inside the master-laser package or by using an inline isolator after the master laser to avoid back reflections and feedback entering the cavity of master laser. These back reflections and feedback, if not controlled, can degrade the performance of the lightwave systems considerably [2]. It has been shown in [129] that even small levels of back reflections can deteriorate the performance of a semiconductor laser and can lead to excess noise in the transmitter output. The PIC presented in chapter 5, even though it benefits from optical injection due to its unique master-slave configuration, due to lack of isolation it suffers from back reflections and feedback in the cavity of the master-laser and doesn't take advantage of the optical injection to its full extent. Also, due to lack of isolation, the PIC acts like a coupled cavity laser if not controlled properly. Once the roundtrip gain compensates for the cavity and mirror losses, the entire PIC can potentially act as a single coupled cavity laser. This deteriorate the output significantly. This forced us to operate the master laser close to threshold to take advantage of optical injection but the extent of injection was limited to avoid the coupled cavity effects which usually results in unstable multimode optical output not ideal for a transmission system. In order to solve this issue, we redesigned the PIC as shown in Figure 6.4. An isolator/attenuator section, marked as *G1*, is included to provide better isolation between master-laser (comprises of a reflector, *MR*, and a gain section, *MG*) and slave-laser (comprises of a gain section, *RF*, and 2 reflector sections, *SR1* and *SR2*). Also, an SOA section is integrated to the PIC at a 7^o angle to reduce the effect of reflection on coupled cavity. The initial testing of the device looks promising though a detailed characterisation is necessary to assess the usefulness of such structure.

6.2.4 Burst Mode Operation

The rapid growth of high-speed data transmission services is increasing the demand for bandwidth and continual industry innovation is needed to meet this challenge. For the optical access networks, next generation passive optical networks 2 (NGPON2) is an ambitious ITU standard developed to drive such innovation. Time and wavelength division multiplexing (TWDM) has been chosen for the NGPON2 standard. For TWDM, the upstream transmission must occur in burst mode to allow multiple users to share a single upstream channel. These NGPON2 transmitters will be used in fiber-to-the-x (FTTx), including fiber-to-the-home (FTTH) systems and hence are to be deployed to every customer premises. Such wide network deployment places an extremely high level of importance on transceiver cost reduction – which can be achieved through the simplification of the manufacturing process. We introduce one such transmitter in chapter 3, which utilises simple fabrication i.e., high order grating etched on the ridge waveguide to attain single mode operation. In addition to low cost requirements, these burst mode transmitters must meet the stringent spectral excursion limit of ± 12.5 GHz for 50 GHz spaced channels which is necessary to avoid channel crosstalk. One key challenge in meeting this requirement is the large, time dependent thermal wavelength drift during bursts which is caused by the laser self-heating. While several schemes for compensating thermal wavelength drift have been proposed [130–132], they add extra complexity to the device fabrication process or operating procedure. Simple fabrication allows easy integration of components such as semiconductor optical amplifiers as shown in Figure 2.10. We are considering this device for burst mode transmission. We measured the performance of SOA blanking [133] to emulate burst mode on a fully integrated device. The initial results look promising where we achieved a wavelength stability of 0.0325 nm (4 GHz), however detailed characterisation and evaluation of transmission performance is required to assess the feasibility of such transmitters in a TWDM system.

6.2.5 Automation of Athermalised Transmission

As the the network traffic is increasing at a rapid rate, the power budget of the access networks and data centres are also increasing significantly and service providers are looking for newer technologies to tackle this problem. Laser cooling/heating is one of the major source of power consumption for the operation of an optical transmitter. This is required to

maintain the optical wavelength of the laser as drift in the wavelength can lead to failure in communication. In chapter 5, we introduced the concept of athermalisation which eliminate the requirement of thermo-electric coolers (TEC) to attain a constant wavelength operation. We presented an athermal transmitter attaining error free performance while transmitting a 2.5 Gb/s On-Off keyed signal over a distance of 37 km of SSMF and attaining a wavelength stability of ± 3 pm (± 375 MHz) over the temperature range of 10-45 ^{o}C. As indicated in chapter 5, this athermal performance was attained manually, hence the process was far from optimised, cumbersome, time-consuming and usually unreliable. This encouraged us to develop an algorithm to automate and optimise the athermalisation process and to reduce the time-required. We successfully achieved this which reduced the overall process time from several hours to few minutes. The algorithm was developed for a laser performing in CW. A similar algorithm can also be developed for a laser working under direct modulation by careful characterisation.

Bibliography

[1] A. Jones, *Historical Sketch Of The Electric Telegraph : Including Its Rise And Progress In The United States.* Publisher: George P. Putnam, 1852.

[2] G. P. Agrawal, *Fiber-Optic Communication System.* Wiley, 4th ed., 2010.

[3] A. G. Bell, "Improvement in Telegraphy - U.S. Patent no. 174,465," 1876.

[4] R. N. Hall, G. E. Fenner, J. D. Kingsley, T. J. Soltys, and R. O. Carlson, "Coherent Light Emission From GaAs Junctions," *Phys. Rev. Lett.*, vol. 9, pp. 366–368, Nov 1962.

[5] H. Kroemer, "A proposed class of hetero-junction injection lasers," *Proceedings of the IEEE*, vol. 51, pp. 1782–1783, Dec 1963.

[6] I. Hayashi, M. B. Panish, P. W. Foy, and S. Sumski, "Junction lasers which operate continuously at room temperature," *Applied Physics Letters*, vol. 17, no. 3, pp. 109–111, 1970.

[7] K. C. Kao and G. A. Hockham, "Dielectric-fibre surface waveguides for optical frequencies," *Proceedings of the Institution of Electrical Engineers*, vol. 113, pp. 1151–1158, July 1966.

[8] H. Kogelnik, "High-capacity optical communications: personal recollections," *IEEE Journal of Selected Topics in Quantum Electronics*, vol. 6, pp. 1279–1286, Nov 2000.

[9] R. J. Sanferrare, "Terrestrial lightwave systems," *AT T Technical Journal*, vol. 66, pp. 95–107, January 1987.

[10] T. Miya, Y. Terunuma, T. Hosaka, and T. Miyashita, "Ultimate low-loss single-mode fibre at 1.55 μm," *Electronics Letters*, vol. 15, pp. 106–108, February 1979.

[11] M. Yamada and Y. Suematsu, "A condition of single longitudinal mode operation in injection lasers with index-guiding structure," *IEEE Journal of Quantum Electronics*, vol. 15, pp. 743–749, August 1979.

[12] L. G. Cohen, C. Lin, and W. G. French, "Tailoring zero chromatic dispersion into the 1.5-1.6 μm low-loss spectral region of single-mode fibres," *Electronics Letters*, vol. 15, pp. 334–335, June 1979.

[13] R. J. Mears, L. Reekie, I. M. Jauncey, and D. N. Payne, "Low-noise erbium-doped fibre amplifier operating at 1.54 μm," *Electronics Letters*, vol. 23, pp. 1026–1028, Sep. 1987.

[14] X. Zhou, J. Yu, M. Huang, Y. Shao, T. Wang, L. Nelson, P. Magill, M. Birk, P. I. Borel, D. W. Peckham, and R. Lingle, "64-Tb/s (640 × 107-Gb/s) PDM-36QAM transmission over 320km using both pre- and post-transmission digital equalization," in *2010 Conference on Optical Fiber Communication (OFC/NFOEC), collocated National Fiber Optic Engineers Conference*, pp. 1–3, March 2010.

[15] V. Vujicic, *PhD Thesis - Optical multicarrier sources for spectrally efficient optical networks*. Dublin City University, 2015.

[16] R. Ramaswami and K. N. Sivarajan, *Optical Networks: A Practical Perspective*. Morgan Kaufmann, 2nd ed., 2001.

[17] L. G. Kazovsky, W. Shaw, D. Gutierrez, N. Cheng, and S. Wong, "Next-Generation Optical Access Networks," *Journal of Lightwave Technology*, vol. 25, no. 11, pp. 3428–3442, 2007.

[18] L. Kazovsky, S. Wong, T. Ayhan, K. M. Albeyoglu, M. R. N. Ribeiro, and A. Shastri, "Hybrid Optical–Wireless Access Networks," *Proceedings of the IEEE*, vol. 100, no. 5, pp. 1197–1225, 2012.

[19] R. Essiambre and R. W. Tkach, "Capacity Trends and Limits of Optical Communication Networks," *Proceedings of the IEEE*, vol. 100, pp. 1035–1055, May 2012.

[20] Cisco V. N. I. Forecast, "Cisco Visual Networking Index: Forecast and Trends, 2017–2022 White Paper." https://www.cisco.com/c/en/us/solutions/collateral/service-provider/visual-networking-index-vni/white-paper-c11-741490.html/, 2019. [Online; accessed 14-December-2019].

[21] Cisco Systems, "Internet traffic." https://en.wikipedia.org/wiki/Internet_traffic.

[22] S. Gringeri, E. B. Basch, and T. J. Xia, "Technical considerations for supporting data rates beyond 100 Gb/s," *IEEE Communications Magazine*, vol. 50, pp. s21–s30, February 2012.

[23] A. A. M. Saleh and J. M. Simmons, "Technology and architecture to enable the explosive growth of the internet," *IEEE Communications Magazine*, vol. 49, pp. 126–132, January 2011.

[24] Q. Y. Lu, W. H. Guo, R. Phelan, D. Byrne, J. F. Donegan, P. Lambkin, and B. Corbett, "Analysis of Slot Characteristics in Slotted Single-Mode Semiconductor Lasers

Using the 2-D Scattering Matrix Method," *IEEE Photonics Technology Letters*, vol. 18, pp. 2605–2607, Dec 2006.

[25] Q. Lu, W. Guo, D. Byrne, and J. F. Donegan, "Design of Slotted Single-Mode Lasers Suitable for Photonic Integration," *IEEE Photonics Technology Letters*, vol. 22, pp. 787–789, June 2010.

[26] Q. Lu, W. Guo, M. Nawrocka, A. Abdullaev, C. Daunt, J. O'Callaghan, M. Lynch, V. Weldon, F. Peters, and J. F. Donegan, "Single mode lasers based on slots suitable for photonic integration," *Opt. Express*, vol. 19, pp. B140–B145, Dec 2011.

[27] W.-H. Guo, Q. Lu, M. Nawrocka, A. Abdullaev, J. O'Callaghan, and J. F. Donegan, "Nine-channel wavelength tunable single mode laser array based on slots," *Opt. Express*, vol. 21, pp. 10215–10221, Apr 2013.

[28] A. Abdullaev, Q. Lu, W. Guo, M. J. Wallace, M. Nawrocka, F. Bello, A. Benson, J. O'Callaghan, and J. F. Donegan, "Improved performance of tunable single-mode laser array based on high-order slotted surface grating," *Opt. Express*, vol. 23, pp. 12072–12078, May 2015.

[29] J. L. Hall, "Nobel Lecture: Defining and measuring optical frequencies," *Rev. Mod. Phys.*, vol. 78, pp. 1279–1295, Nov 2006.

[30] T. W. Hänsch, "Nobel Lecture: Passion for precision," *Rev. Mod. Phys.*, vol. 78, pp. 1297–1309, Nov 2006.

[31] M. Imran, P. M. Anandarajah, A. Kaszubowska-Anandarajah, N. Sambo, and L. Potí, "A Survey of Optical Carrier Generation Techniques for Terabit Capacity Elastic Optical Networks," *IEEE Communications Surveys Tutorials*, vol. 20, pp. 211–263, Firstquarter 2018.

[32] G. Yabre, "Effect of relatively strong light injection on the chirp-to-power ratio and the 3 dB bandwidth of directly modulated semiconductor lasers," *Journal of Lightwave Technology*, vol. 14, pp. 2367–2373, Oct 1996.

[33] J. O'Carroll, P. M. Anandarajah, R. Zhou, R. Phelan, B. Kelly, J. O'Gorman, and L. P. Barry, "Transmission over 50 km using a directly modulated integrated two-section discrete mode laser at 1550 nm," in *2013 Conference on Lasers Electro-Optics Europe International Quantum Electronics Conference EUROPE/IQEC*, pp. 1–1, May

2013.

[34] L. D. Westbrook, "Measurements of dg/dN and dn/dN and their dependence on photon energy in λ =1.5 μm InGaAsP laser diodes," *IEE Proceedings J - Optoelectronics*, vol. 133, pp. 135–142, April 1986.

[35] M. Wallace, *PhD Thesis - Characterisation, Simulation and Optimization of Surface Etched Slotted Tunable Laser Diodes*. Trinity College Dublin, School of Physics, 2018.

[36] L. A. Coldren and S. W. Corzine, *Diode Lasers and Photonic Integrated Circuits*. Wiley, 1995.

[37] B. Corbett and D. McDonald, "Single longitudinal mode ridge waveguide 1.3 μm Fabry-Perot laser by modal perturbation," *Electronics Letters*, vol. 31, pp. 2181–2182, Dec 1995.

[38] D. C. Byrne, J. P. Engelstaedter, W. Guo, Q. Y. Lu, B. Corbett, B. Roycroft, J. O'Callaghan, F. H. Peters, and J. F. Donegan, "Discretely Tunable Semiconductor Lasers Suitable for Photonic Integration," *IEEE Journal of Selected Topics in Quantum Electronics*, vol. 15, pp. 482–487, May 2009.

[39] J. P. Engelstaedter, B. Roycroft, and B. Corbett, "Laser and detector using integrated reflector for photonic integration," *Electronics Letters*, vol. 44, pp. 1017–1019, Aug 2008.

[40] R. M. Lammert, J. S. Hughes, S. D. Roh, M. L. Osowski, A. M. Jones, and J. J. Coleman, "Low-threshold narrow-linewidth InGaAs-GaAs ridge-waveguide DBR lasers with first-order surface gratings," *IEEE Photonics Technology Letters*, vol. 9, pp. 149–151, Feb 1997.

[41] P. Bienstman, *PhD Thesis - Rigorous and efficient modelling of wavelength scale photonic components*. University of Ghent, Department of Applied Mathematics, Computer Science and Statistics, 2001.

[42] G. Bacher, N. Mais, M. Illing, A. Forchel, K. Schull, J. Nurnberger, and G. Landwehr, "ZnSe-based DBR-laser diode," *Electronics Letters*, vol. 31, pp. 2184–2185, Dec 1995.

[43] J. Fricke, F. Bugge, A. Ginolas, W. John, A. Klehr, M. Matalla, P. Ressel, H. Wenzel, and G. Erbert, "High-Power 980-nm Broad-Area Lasers Spectrally Stabilized by Surface Bragg Gratings," *IEEE Photonics Technology Letters*, vol. 22, pp. 284–286, March 2010.

[44] L. M. Miller, J. T. Verdeyen, J. J. Coleman, R. P. Bryan, J. J. Alwan, K. J. Beernink, J. S. Hughes, and T. M. Cockerill, "A distributed feedback ridge waveguide quantum well heterostructure laser," *IEEE Photonics Technology Letters*, vol. 3, pp. 6–8, Jan 1991.

[45] R. D. Martin, S. Forouhar, S. Keo, R. J. Lang, R. G. Hunsperger, R. C. Tiberio, and P. F. Chapman, "CW performance of an InGaAs-GaAs-AlGaAs laterally-coupled distributed feedback (LC-DFB) ridge laser diode," *IEEE Photonics Technology Letters*, vol. 7, pp. 244–246, March 1995.

[46] Jian Wang, Jian-Bo Tian, Peng-Fei Cai, Bing Xiong, Chang-Zheng Sun, and Yi Luo, "1.55-μm AlGaInAs-InP laterally coupled distributed feedback laser," *IEEE Photonics Technology Letters*, vol. 17, pp. 1372–1374, July 2005.

[47] M. Reinhardt, M. Fischer, M. Kamp, J. Hofmann, and A. Forchel, "1.3-μm GaInNAs-AlGaAs distributed feedback lasers," *IEEE Photonics Technology Letters*, vol. 12, pp. 239–241, March 2000.

[48] T. Bleuel, M. Muller, and A. Forchel, "2-μm GaInSb-AlGaAsSb distributed-feedback lasers," *IEEE Photonics Technology Letters*, vol. 13, pp. 553–555, June 2001.

[49] D. Hofstetter, H. P. Zappe, J. E. Epler, and P. Riel, "Monolithically integrated DBR laser, detector, and transparent waveguide fabricated in a single growth step," *IEEE Photonics Technology Letters*, vol. 7, pp. 1022–1024, Sep. 1995.

[50] J. Fricke, H. Wenzel, M. Matalla, A. Klehr, and G. Erbert, "980-nm DBR lasers using higher order gratings defined by i-line lithography," *Semiconductor Science and Technology*, vol. 20, pp. 1149–1152, oct 2005.

[51] C. Herbert, D. Jones, A. Kaszubowska-Anandarajah, B. Kelly, M. Rensing, J. O'Carroll, R. Phelan, P. Anandarajah, P. Perry, L. P. Barry, and J. O'Gorman, "Discrete mode lasers for communication applications," *IET Optoelectronics*, vol. 3, pp. 1–17, February 2009.

[52] S. O'Brien, F. Smyth, K. Shi, J. O'Carroll, P. M. Anandarajah, D. Bitauld, S. Osborne, R. Phelan, B. Kelly, J. O'Gorman, F. H. Peters, B. Roycroft, B. Corbett, and L. P. Barry, "Design, Characterization, and Applications of Index-Patterned Fabry–Pérot Lasers," *IEEE Journal of Selected Topics in Quantum Electronics*, vol. 17, pp. 1621–1631, Nov 2011.

[53] B. Kelly, R. Phelan, D. Jones, C. Herbert, J. O'carroll, M. Rensing, J. Wendelboe, C. B. Watts, A. Kaszubowska-Anandarajah, P. Perry, C. Guignard, L. P. Barry, and J. O'Gorman, "Discrete mode laser diodes with very narrow linewidth emission," *Electronics Letters*, vol. 43, Nov 2007.

[54] Y. Wang, Y. Yang, S. Zhang, L. Wang, and J. He, "Narrow Linewidth Single-Mode Slotted Fabry–Pérot Laser Using Deep Etched Trenches," *IEEE Photonics Technology Letters*, vol. 24, pp. 1233–1235, July 2012.

[55] Q. Lu, A. Abdullaev, M. Nawrocka, W. Guo, J. O'Callaghan, and J. F. Donegan, "Slotted Single Mode Lasers Integrated With a Semiconductor Optical Amplifier," *IEEE Photonics Technology Letters*, vol. 25, pp. 564–567, March 2013.

[56] Q. Lu, W. Guo, A. Abdullaev, M. Nawrocka, T. N. Huynh, J. O'Callaghan, M. Lynch, V. Weldon, L. P. Barry, and J. F. Donegan, "Two-section singlemode lasers based on slots suitable for photonic integration," *Electronics Letters*, vol. 48, pp. 945–946, July 2012.

[57] W. Sun, Q. Lu, W. Guo, and J. F. Donegan, "Short Cavity Single-Mode DBR Lasers Based on HighOrder Slotted Surface-Gratings Using Narrow Slot-Width," in *Asia Communications and Photonics Conference (ACPC) 2019*, p. T3D.4, Optical Society of America, 2019.

[58] H. Wenzel, J. Fricke, J. Decker, P. Crump, and G. Erbert, "High-power distributed feedback lasers with surface gratings: Theory and experiment," *IEEE Journal of Selected Topics in Quantum Electronics*, vol. 21, no. 6, pp. 352–358, 2015.

[59] J. H. den Besten, *PhD Thesis - Integration of multiwavelength lasers with fast electro optical modulators*. Dept. Elect. Eng., Eindhoven Univ. Technol., Eindhoven, The Netherlands, 2004.

[60] B. R. Bennett, R. A. Soref, and J. A. Del Alamo, "Carrier-induced change in refractive index of InP, GaAs and InGaAsP," *IEEE Journal of Quantum Electronics*, vol. 26, pp. 113–122, Jan 1990.

[61] M. Pantouvaki, C. C. Renaud, P. Cannard, M. J. Robertson, R. Gwilliam, and A. J. Seeds, "Fast Tuneable InGaAsP DBR Laser Using Quantum-Confined Stark-Effect-Induced Refractive Index Change," *IEEE Journal of Selected Topics in Quantum Electronics*, vol. 13, pp. 1112–1121, Sep. 2007.

[62] S. L. Woodward, U. Koren, B. I. Miller, M. G. Young, M. A. Newkirk, and C. A. Burrus, "A DBR laser tunable by resistive heating," *IEEE Photonics Technology Letters*, vol. 4, pp. 1330–1332, Dec 1992.

[63] M. C. Amann and J. Buus, *Tunable Laser Diodes*. Artech House, 1998.

[64] J. Weber, "Optimization of the carrier-induced effective index change in InGaAsP waveguides-application to tunable Bragg filters," *IEEE Journal of Quantum Electronics*, vol. 30, pp. 1801–1816, Aug 1994.

[65] J. E. Zucker, I. Bar-Joseph, B. I. Miller, U. Koren, and D. S. Chemla, "Quaternary quantum wells for electro-optic intensity and phase modulation at 1.3 and 1.55 μm," *Applied Physics Letters*, vol. 54, no. 1, pp. 10–12, 1989.

[66] T. Nakamori, H. Hashimoto, S. Endo, H. Machino, and M. Ishizu, "Semiconductor laser device having chip-mounted heating element - U.S. Patent no. 5,488,625," 1996.

[67] P. P. Vasil'ev, I. H. White, and J. Gowar, "Fast phenomena in semiconductor lasers," *Reports on Progress in Physics*, vol. 63, pp. 1997–2042, Dec 2000.

[68] Wikipedia, "Laser Linewidth." https://en.wikipedia.org/wiki/Laser_linewidth.

[69] V. Vujicic, J. Pfeifle, R. T. Watts, P. C. Schindler, C. Weimann, R. Zhou, W. Freude, C. Koos, and L. P. Barry, "Flexible terabit/s Nyquist-WDM superchannels with net SE $>$ 7bit/s/Hz using a gain-switched comb source," in *2014 Conference on Lasers and Electro-Optics (CLEO) - Laser Science to Photonic Applications*, pp. 1–2, 2014.

[70] K. Kikuchi, "Coherent optical transmission systems," in *Proceedings of OptoElectronics and Communications Conference (OECC)*, pp. 1–2, 2010.

[71] T. Pfau, S. Hoffmann, and R. Noe, "Hardware-Efficient Coherent Digital Receiver Concept With Feedforward Carrier Recovery for M -QAM Constellations," *Journal of Lightwave Technology*, vol. 27, no. 8, pp. 989–999, 2009.

[72] C. Henry, "Theory of the linewidth of semiconductor lasers," *IEEE Journal of Quantum Electronics*, vol. 18, pp. 259–264, February 1982.

[73] A. L. Schawlow and C. H. Townes, "Infrared and Optical Masers," *Phys. Rev.*, vol. 112, pp. 1940–1949, Dec 1958.

[74] S. Camatel and V. Ferrero, "Narrow Linewidth CW Laser Phase Noise Characterization Methods for Coherent Transmission System Applications," *Journal of Lightwave*

Technology, vol. 26, no. 17, pp. 3048–3055, 2008.

[75] T. N. Huynh, L. Nguyen, and L. P. Barry, "Phase Noise Characterization of SGDBR Lasers Using Phase Modulation Detection Method With Delayed Self-Heterodyne Measurements," *Journal of Lightwave Technology*, vol. 31, pp. 1300–1308, April 2013.

[76] K. Kikuchi, "Impact of 1/f-type FM noise on coherent optical communications," *Electronics Letters*, vol. 23, pp. 885–887, August 1987.

[77] R. Zhou, T. N. Huynh, V. Vujicic, P. M. Anandarajah, and L. P. Barry, "Phase noise analysis of injected gain switched comb source for coherent communications," *Opt. Express*, vol. 22, pp. 8120–8125, Apr 2014.

[78] W. Guo, Q. Lu, M. Nawrocka, A. Abdullaev, J. O'Callaghan, M. Lynch, V. Weldon, and J. F. Donegan, "Integrable Slotted Single-Mode Lasers," *IEEE Photonics Technology Letters*, vol. 24, pp. 634–636, April 2012.

[79] M. Wallace, R. O. Meehan, R. Enright, F. Bello, D. McCloskey, B. Barabadi, E. Wang, and J. F. Donegan, "Athermal operation of multi-section slotted tunable lasers," *Opt. Express*, vol. 25, pp. 14414–14426, Jun 2017.

[80] E. B. Desurvire, "Capacity Demand and Technology Challenges for Lightwave Systems in the Next Two Decades," *Journal of Lightwave Technology*, vol. 24, pp. 4697–4710, Dec 2006.

[81] P. J. Winzer and R. Essiambre, "Advanced Modulation Formats for High-Capacity Optical Transport Networks," *Journal of Lightwave Technology*, vol. 24, pp. 4711–4728, Dec 2006.

[82] O. Gerstel, M. Jinno, A. Lord, and S. J. B. Yoo, "Elastic optical networking: a new dawn for the optical layer?," *IEEE Communications Magazine*, vol. 50, pp. s12–s20, February 2012.

[83] J. Armstrong, "OFDM for Optical Communications," *Journal of Lightwave Technology*, vol. 27, pp. 189–204, Feb 2009.

[84] K. Christodoulopoulos, I. Tomkos, and E. A. Varvarigos, "Elastic Bandwidth Allocation in Flexible OFDM-Based Optical Networks," *Journal of Lightwave Technology*, vol. 29, pp. 1354–1366, May 2011.

[85] N. Cvijetic, "OFDM for Next-Generation Optical Access Networks," *Journal of Lightwave Technology*, vol. 30, pp. 384–398, Feb 2012.

[86] M. D. G. Pascual, V. Vujicic, J. Braddell, F. Smyth, P. Anandarajah, and L. Barry, "Photonic Integrated Gain Switched Optical Frequency Comb for Spectrally Efficient Optical Transmission Systems," *IEEE Photonics Journal*, vol. 9, no. 3, pp. 1–8, 2017.

[87] M. D. G. Pascual, J. Braddell, F. Smyth, and L. Barry, "Monolithically Integrated 1x4 Comb De-multiplexer Based on Injection Locking," in *18th European Conference on Integrated Optics 2016*, 2016.

[88] M. D. G. Pascual, *PhD Thesis - Development and Investigation of Optical Frequency Combs for Photonic Communication Systems*. Dublin City University, 2017.

[89] P. Torphammar and S. T. Eng, "Picosecond pulse generation in semiconductor lasers using resonance oscillation," *Electronics Letters*, vol. 16, pp. 587–589, July 1980.

[90] P. M. Anandarajah, R. Maher, Y. Q. Xu, S. Latkowski, J. O'Carroll, S. G. Murdoch, R. Phelan, J. O'Gorman, and L. P. Barry, "Generation of Coherent Multicarrier Signals by Gain Switching of Discrete Mode Lasers," *IEEE Photonics Journal*, vol. 3, pp. 112–122, Feb 2011.

[91] R. Lang, "Injection locking properties of a semiconductor laser," *IEEE Journal of Quantum Electronics*, vol. 18, pp. 976–983, June 1982.

[92] F. Mogensen, H. Olesen, and G. Jacobsen, "Locking conditions and stability properties for a semiconductor laser with external light injection," *IEEE Journal of Quantum Electronics*, vol. 21, pp. 784–793, July 1985.

[93] Linlin Li, "Static and dynamic properties of injection-locked semiconductor lasers," *IEEE Journal of Quantum Electronics*, vol. 30, pp. 1701–1708, Aug 1994.

[94] E. K. Lau, L. J. Wong, and M. C. Wu, "Enhanced Modulation Characteristics of Optical Injection-Locked Lasers: A Tutorial," *IEEE Journal of Selected Topics in Quantum Electronics*, vol. 15, pp. 618–633, May 2009.

[95] K. Iwashita and K. Nakagawa, "Suppression of mode partition noise by laser diode light injection," *IEEE Journal of Quantum Electronics*, vol. 18, pp. 1669–1674, October 1982.

[96] A. Murakami, K. Kawashima, and K. Atsuki, "Cavity resonance shift and bandwidth enhancement in semiconductor lasers with strong light injection," *IEEE Journal of*

Quantum Electronics, vol. 39, pp. 1196–1204, Oct 2003.

[97] N. Schunk and K. Petermann, "Noise analysis of injection-locked semiconductor injection lasers," *IEEE Journal of Quantum Electronics*, vol. 22, pp. 642–650, May 1986.

[98] P. Spano, S. Piazzolla, and M. Tamburrini, "Frequency and intensity noise in injection-locked semiconductor lasers: Theory and experiments," *IEEE Journal of Quantum Electronics*, vol. 22, pp. 427–435, March 1986.

[99] T. B. Simpson, S. Wieczorek, B. Krauskopf, and D. Lenstra, "Mapping the Complex Dynamics of a Semiconductor Laser Subject to Optical Injection," *AIP Conference Proceedings*, vol. 676, no. 1, pp. 375–375, 2003.

[100] T. B. Simpson, J. M. Liu, A. Gavrielides, V. Kovanis, and P. M. Alsing, "Period-doubling route to chaos in a semiconductor laser subject to optical injection," *Applied Physics Letters*, vol. 64, no. 26, pp. 3539–3541, 1994.

[101] V. Annovazzi-Lodi, S. Donati, and M. Manna, "Chaos and locking in a semiconductor laser due to external injection," *IEEE Journal of Quantum Electronics*, vol. 30, pp. 1537–1541, July 1994.

[102] C.-H. Lin and F.-Y. Lin, "Four-wave mixing analysis on injection-locked quantum dot semiconductor lasers," *Opt. Express*, vol. 21, pp. 21242–21253, Sep 2013.

[103] T. B. Simpson, J. M. Liu, and A. Gavrielides, "Small-signal analysis of modulation characteristics in a semiconductor laser subject to strong optical injection," *IEEE Journal of Quantum Electronics*, vol. 32, pp. 1456–1468, Aug 1996.

[104] K. Kikuchi, "Characterization of semiconductor-laser phase noise and estimation of bit-error rate performance with low-speed offline digital coherent receivers," *Opt. Express*, vol. 20, pp. 5291–5302, Feb 2012.

[105] J. Wang, M. K. Haldar, L. Li, and F. V. C. Mendis, "Enhancement of modulation bandwidth of laser diodes by injection locking," *IEEE Photonics Technology Letters*, vol. 8, pp. 34–36, Jan 1996.

[106] Xue Jun Meng, Tai Chau, and M. C. Wu, "Experimental demonstration of modulation bandwidth enhancement in distributed feedback lasers with external light injection," *Electronics Letters*, vol. 34, pp. 2031–2032, Oct 1998.

[107] P. M. Anandarajah, S. P. Ó Dúill, R. Zhou, and L. P. Barry, "Enhanced optical comb

generation by gain-switching a single-mode semiconductor laser close to its relaxation oscillation frequency," *IEEE Journal of Selected Topics in Quantum Electronics*, vol. 21, pp. 592–600, Nov 2015.

[108] M. D. G. Pascual, R. Zhou, F. Smyth, P. M. Anandarajah, and L. P. Barry, "Software reconfigurable highly flexible gain switched optical frequency comb source," *Opt. Express*, vol. 23, pp. 23225–23235, Sep 2015.

[109] International Telecommunications Union (ITU), "G.694.1 spectral grids for WDM applications: DWDM frequency grid." https://www.itu.int/rec/T-REC-G.694.1-201202-I/en, 2012.

[110] G. P. Agrawal, *Lightwave Technology: Telecommunication Systems*. Wiley, 2005.

[111] International Telecommunications Union (ITU)), "40-Gigabit-capable passive optical networks 2 (NG-PON2): Physical media dependent (PMD) layer specification." https://www.itu.int/rec/T-REC-G.989.2-201708-S!Amd2.

[112] Y. Luo, X. Zhou, F. Effenberger, X. Yan, G. Peng, Y. Qian, and Y. Ma, "Time- and Wavelength-Division Multiplexed Passive Optical Network (TWDM-PON) for Next-Generation PON Stage 2 (NG-PON2)," *Journal of Lightwave Technology*, vol. 31, pp. 587–593, Feb 2013.

[113] Z. Liu, G. Hesketh, B. Kelly, J. O'Carroll, R. Phelan, D. J. Richardson, and R. Slavík, "Optical Injection-Locked Directly Modulated Lasers for Dispersion Pre-Compensated Direct-Detection Transmission," *Journal of Lightwave Technology*, vol. 36, pp. 4967–4974, Oct 2018.

[114] S. Mohrdiek, H. Burkhard, and H. Walter, "Chirp reduction of directly modulated semiconductor lasers at 10 Gb/s by strong CW light injection," *Journal of Lightwave Technology*, vol. 12, pp. 418–424, March 1994.

[115] X. J. Meng, T. Chau, D. T. K. Tong, and M. C. Wu, "Suppression of second harmonic distortion in directly modulated distributed feedback lasers by external light injection," *Electronics Letters*, vol. 34, pp. 2040–2041, Oct 1998.

[116] P. M. Anandarajah, S. Latkowski, C. Browning, R. Zhou, J. O'Carroll, R. Phelan, B. Kelly, J. O'Gorman, and L. P. Barry, "Integrated two-section discrete mode laser," *IEEE Photonics Journal*, vol. 4, no. 6, pp. 2085–2094, 2012.

[117] Y. Liu, J. D. Ingham, R. G. S. Plumb, R. V. Penty, I. H. White, D. J. Robbins, N. D. Whitbread, and A. J. Ward, "Directly-modulated DS-DBR tunable laser for uncooled C-band WDM system," in *2006 Optical Fiber Communication Conference and the National Fiber Optic Engineers Conference*, pp. 3 pp.–, March 2006.

[118] Y. Matsui, W. Li, H. Roberts, H. Bulthuis, H. Deng, L. Lin, and C. Roxlo, "Transceiver for NG-PON2: Wavelength tunablity for burst mode TWDM and point-to-point WDM," in *2016 Optical Fiber Communications Conference and Exhibition (OFC)*, pp. 1–3, March 2016.

[119] F. Bello, M. J. Wallace, R. McKenna, G. Jain, Q. Y. Lu, W. H. Guo, and J. F. Donegan, "Athermal Tuning for a Two-Section, All-Active DBR Laser With High-Order Grating," *IEEE Photonics Journal*, vol. 10, pp. 1–11, Oct 2018.

[120] M. N. Hammad, A. Kaszubowska-Anandarajah, M. D. G. Pascual, P. Landais, P. D. Lakshmijayasimha, G. Jain, and P. M. Anandarajah, "Characterization and Direct Modulation of a Multi-Section PIC Suited for Short Reach Optical Communication Systems," *Photonics*, vol. 7, no. 3, 2020.

[121] G. Simon, F. Saliou, P. Chanclou, B. L. Guyader, L. Guillo, J. Konopacki, F. Bourgart, and D. Erasme, "Focus on Time-Dependent Wavelength Drift of DMLs Under Burst-Mode Operation for NG-PON2," *Journal of Lightwave Technology*, vol. 34, pp. 3148–3154, July 2016.

[122] J. Bovington, S. Srinivasan, and J. E. Bowers, "Athermal laser design," *Opt. Express*, vol. 22, pp. 19357–19364, Aug 2014.

[123] J. Zhu, A. Wonfor, S. H. Lee, S. Pachnicke, M. Lawin, R. V. Penty, J. Elbers, R. Cush, M. J. Wale, and I. H. White, "Athermal Colorless C-Band Optical Transmitter System for Passive Optical Networks," *Journal of Lightwave Technology*, vol. 32, no. 22, pp. 4253–4260, 2014.

[124] S. H. Lee, A. Wonfor, R. V. Penty, I. H. White, G. Busico, R. Cush, and M. Wale, "Self-configuring athermal tunable DS-DBR laser for passive optical networks," in *CLEO/QELS: 2010 Laser Science to Photonic Applications*, pp. 1–2, 2010.

[125] L. Ponnampalam, C. C. Renaud, R. Cush, R. Turner, M. J. Wale, and A. J. Seeds, "Simplified wavelength control of uncooled widely tuneable dsdbr laser for optical access networks," in *39th European Conference and Exhibition on Optical Communication*

(ECOC 2013), pp. 1–3, 2013.

[126] L. Ponnampalam, C. Renaud, M. Fice, R. Cush, R. Turner, P. Firth, M. Wale, and A. Seeds, "High temperature operation of athermal widely tuneable laser with simplified wavelength control for WDM-PON systems," *Opt. Express*, vol. 22, pp. 24405–24410, Oct 2014.

[127] J. Zhu, A. Wonfor, R. Cush, M. J. Wale, S. Pachnicke, R. V. Penty, and I. H. White, "High temperature athermal colorless laser for low-cost backhaul networks," in *2014 Conference on Lasers and Electro-Optics (CLEO) - Laser Science to Photonic Applications*, pp. 1–2, 2014.

[128] I. Coddington, N. Newbury, and W. Swann, "Dual-comb spectroscopy," *Optica*, vol. 3, pp. 414–426, Apr 2016.

[129] R. Tkach and A. Chraplyvy, "Regimes of feedback effects in 1.5-μm distributed feedback lasers," *Journal of Lightwave Technology*, vol. 4, pp. 1655–1661, November 1986.

[130] H. Debregeas, R. Borkowski, R. Bonk, R. Brenot, J. Provost, S. Barbet, and T. Pfeiffer, "TWDM-PON Burst Mode Lasers With Reduced Thermal Frequency Shift," *Journal of Lightwave Technology*, vol. 36, pp. 128–134, Jan 2018.

[131] G. Simon, F. Saliou, P. Chanclou, L. Anet Neto, and D. Erasme, "Experimental Demonstration of Low Cost Wavelength Drift Mitigation for TWDM Systems," in *ECOC 2016; 42nd European Conference on Optical Communication*, pp. 1–3, Sep. 2016.

[132] V. Houtsma, D. van Veen, S. Porto, N. Basavanhally, C. Bolle, and H. Schmuck, "Investigation of 100G (4×25G) NG-PON2 Upgrade using a Burst Mode Laser based on a Multi-Electrode Laser to enable 100 GHz Wavelength Grid," in *2018 Optical Fiber Communications Conference and Exposition (OFC)*, pp. 1–3, March 2018.

[133] E. Connolly, A. Kaszubowska-Anandarajh, L. P. Barry, J. Dunne, T. Mullane, and D. McDonald, "Cross-channel interference due to wavelength switching events in wavelength packet switched WDM networks," in *2005 31st European Conference on Optical Communication, ECOC 2005*, vol. 3, pp. 359–360 vol.3, Sep. 2005.

Appendix A

List of Publications

The following is the list of publications included in this work.

A.1 Referred Journal Paper

1. **Gaurav Jain**, Michael J. Wallace, Robert Mckenna, Kevin Brazel, Frank Bello, Qiaoyin Lu, Weihua Guo, and John F. Donegan, "Design Optimization for Semiconductor Lasers With High-Order Surface Gratings Having Multiple Periods", in *Journal of Lightwave Technology*, vol. 36, no. 22, pp. 5121-5129, 15 Nov, 2018.

A.2 Referred Conference Papers

1. *(Oral)* **Gaurav Jain**, Michael J. Wallace, and John F. Donegan, "Multi Period Surface Grating Semiconductor Laser", in *Photonics Ireland*, Galway (Ireland), 2017.

2. *(Poster)* **Gaurav Jain**, Michael J. Wallace, Qiaoyin Lu, Wei-Hua Guo, and John F. Donegan, "Design Optimization for Semiconductor Lasers with High-Order Surface Gratings having Multiple Periods", in *Conference on Lasers and Electro-Optics (CLEO)*, San Jose (USA), 2018.

3. *(Oral)* **Gaurav Jain**, Maria Deseada Pascual Gutierrez, Jules Braddell, Gavin King, Chris Leonard, Frank Smyth, and Seán Ó Dúill, "Photonic Integrated Optical Combs for Structural Health Monitoring in Space", in *European Conference on Spacecraft Structures, Materials and Environmental Testing (ECSSMET)*, Noordwijk (Netherlands), 2018.

4. *(Oral)* **Gaurav Jain**, Michael J. Wallace, Frank Smyth, Jules Braddell, and John F. Donegan, "Athermal Operation of Multi Section Comb PIC", in *Photonics Ireland*, Cork (Ireland), 2018.

5. *(Poster)* Robert J. McKenna, Michael J. Wallace, **Gaurav Jain**, and John F. Donegan, "Optimisation of High Order Surface Gratings for Semiconductor Lasers", in *Photonics Ireland*, Cork (Ireland), 2018.

6. *(Poster)* **Gaurav Jain**, Michael J. Wallace, M. Deseada Gutierrez Pascual, Robert McKenna, Frank Smyth, Jules Braddell, Prince M. Anandarajah, and John F. Donegan, "Athermal Operation of Multi-Section PIC", in *Conference on Lasers and Electro-Optics (CLEO)*, San Jose (USA), 2019.

7. *(Poster)* **Gaurav Jain**, Deseada Gutierrez-Pascual1, Sean O'Duill1, Prince M. Anandarajah, Aleksandra Kaszubowska, Frank Smyth, Liam P Barry, John F Donegan, and Jules Braddell, "Directly Modulated Photonic Integrated Multi-Section Laser for Next Generation TWDM Access Networks", in *European Conference on Optical Communication (ECOC)*, Dublin (Ireland), 2019.

8. *(Poster)* **Gaurav Jain**, Prince M. Anandarajah, Robert McKenna, Deseada Gutierrez-Pascual, Frank Smyth, Jules Braddell, and John F. Donegan, "Athermal Chirp-Compensated Directly-Modulated PIC for Uncooled DWDM", in *Photonics West*, San Francisco (USA), 2020.

A.3 Other Publications Arisen from the PhD Research

A.3.1 Journal Papers

1. Frank Bello, Michael J. Wallace, Robert McKenna, **Gaurav Jain**, Qiaoyin Y. Lu, Weihua H. Guo, John F. Donegan, "Athermal Tuning for a Two-Section, All-Active DBR Laser With High-Order Grating", in *IEEE Photonics Journal*, vol. 10, no. 5, 26 Sept, 2018.

2. Michael J. Wallace, **Gaurav Jain**, Robert Mckenna, Frank Bello, and J. F. Donegan, "Tuning behaviour of slotted vernier widely tunable lasers", in *Opt. Express*, vol. 27, no. 12, pp. 17122-17137, 2019.

3. Michael J. Wallace, Sepideh. T. Naimi, **Gaurav Jain** , Robert McKenna,Frank Bello, and John F. Donegan, "Genetic algorithm optimization of high order surface etched grating tunable laser array", in *Opt. Express*, vol. 28, no. 6, pp. 8169-8184, 2020.

4. M. N. Hammad, A. Kaszubowska-Anandarajah, M. D. G. Pascual, P. Landais, P. D. Lakshmijayasimha, **G. Jain**, and P. M. Anandarajah, "Characterization and Direct Modulation of a Multi-Section PIC Suited for Short Reach Optical Communication Systems," *Photonics*, vol. 7, no. 3, 2020.

A.3.2 Conference Papers

1. *(Oral)* Prince M. Anandarajah, **Gaurav Jain**, M. Deseada Gutierrez Pascual, Jules Bradell, and Frank Smyth, "Integrated Optical Frequency Combs", in *19th International Conference on Transparent Optical Networks (ICTON)*, Girona (Spain), 2017.

2. *(Poster)* Michael J. Wallace, Robert McKenna, **Gaurav Jain**, Frank Bello, David McCloskey, and John F. Donegan, "Athermal Operation of High-Order Slotted Lasers for Communications Applications", in *21st International Conference on Transparent Optical Networks (ICTON)*, Angers (France), 2019.

3. *(Oral)* Mohab Nabil Hammad, **Gaurav Jain**, Aleksandra Kaszubowska, Prince Anandarajah, and Pascal Landais, "Characterisation of a Novel InP Photonic Integrated Circuits for Direct Modulation Applications", in *21st International Conference on Transparent Optical Networks (ICTON)*, Angers (France), 2019.

4. *(Poster)* Prajwal D. Lakshmijayasimha, Prince M. Anandarajah, Deseada G. Pascual, **Gaurav Jain**, Jules Braddell, Pascal Landais, and Aleksandra Kaszubowska-Anandarajah, "Optical Generation of mmW and THz Signals Using PICs", in *21st International Conference on Transparent Optical Networks (ICTON)*, Angers (France), 2019.

5. *(Oral)* Dovydas Mickus, **Gaurav Jain**, Sepideh T. Naimi, Robert Mckenna, Caolán Murphy, John Donegan, "Athermal Operation of Multi-Section Surface Grating Lasers for Applications including Burst-Mode for TWDM-PONs", in *Conference on Lasers and Electro-Optics (CLEO)*, San Jose (USA), 2020.